Unsteady Phenomena and Realistic Geometry Effects at the Combustor-Turbine Interface of a Large Gas Turbine



Faisal Shaikh

Worcester College

A thesis submitted for the degree of

Doctor of Philosophy

Hillary Term 2020

Acknowledgements

Most of all, I would like to thank my supervisor, Budimir Rosic, for his wisdom and guidance over the years.

This work was funded by Mitsubishi Heavy Industries. Regular communication with turbine design team was extremely helpful for choosing which research directions to pursue. In particular, thanks to the project lead, Mizukami Satoshi, and also to Tanimoto kouichi, Uchida Sumiu and Ito Eisaku for their feedback and expertise.

I must thank Wesley Ramm for his assistance in instrumentation and in running experiments, as well as all the staff at the Oxford Thermofluids Institute.

The community of Worcester College MCR have made the past four years all the more enjoyable. I won't list individuals, though I will single out the cohort of 2017 as an extra special bunch.

Ultimate credit must go to my parents, who always encouraged all my interests.

This thesis is for Clare.

Abstract

Gas turbines in combined cycle are the cleanest and most efficient form of large-scale thermal power generation, and their use is expected to increase in the future. The most arduous conditions within a turbine are faced by the first stage nozzle guide vanes (NGV). These are located immediately after the combustion chamber and face the highest thermal loads, as well a a complex flow field influenced by combustor conditions. For this thesis, experiments and computational methods are developed and used together to investigate steady and unsteady heat transfer and aerodynamics in the nozzle guide vanes It is beneficial to reduce the heat transfer to components in order to increase efficiency and maximise component life.

Improvements were developed to experimental methods which could be carried out in a scale experimental rig, which operated at realistic Reynolds number and Mach number. Thin film gauges were developed for heat transfer measurements at higher sensitivity and spatial resolution than has been possible in the past. The use of a large numbers of unsteady pressure sensors has been pioneered successfully.

Improved experimental techniques are applied to optimising heat transfer and aerodynamics resulting from realistic features which are often overlooked in simplified studies. Several combustor chamber geometries are compared, finding that a combustor design that minimised length scales of turbulence structures reduces NGV heat transfer coefficients significantly. This shows the benefits which can be achieved by designing combustor and turbine together in a holistic manner.

The unsteady effects of large-scale flow structures generated in the combustion chamber were observed in detail by high resolution unsteady measurements and LES. Instantaneous flow phenomena which occur are measured experimentally, and are explained physically with the support of LES. Instantaneous heat transfer events are found to be sufficient to cause potentially damaging temperature fluctuations to thermal barrier coatings, despite being disguised in time-averaged measurements.

The impact of the mid-passage gap between vane platforms on heat transfer and aerodynamic efficiency is measured. An analytical model is developed, which can be used to assess the importance of such gaps in the general case. It is found that great improvements are possible if gap sizes are reduced below a critical threshold. The optimum distribution of cooling flows required to prevent ingress can be calculated by means of a one-dimensional equation, with no need for iterative optimisation.

Ingress into circumferential gaps is also investigated, and found to cause damaging local heat transfer. A measurement campaign investigating surface texturing effects on heat transfer is also presented.

Contents

List of Figures **vi**

Nomenclature and acronyms **x**

Equation variables by chapter **xii**

1 Introduction **1**

1.1 Gas turbines for the future 1

1.1.1 Introduction to gas turbines 1

1.1.2 Operation of power generation gas turbine 3

1.1.3 Thermodynamic cycle 4

1.1.4 Limitations and areas of improvement 7

1.2 Thesis objectives 8

1.3 Overview of thesis 10

2 Experimental and computational techniques **12**

2.1 Experimental facility 13

2.1.1 Swirlers 13

2.1.2 Vane geometry 16

2.1.3 Test pieces 17

2.1.4 Overview of measurement techniques 17

2.1.5 Traverse 18

2.2 Measurement of heat transfer in nozzle guide vanes 18

2.3 Infra-red camera 19

2.3.1 High speed infra-red camera 20

2.3.2 Processing of infra-red 20

2.3.3 Flow visualisation with infra-red 21

2.4 Heat transfer measurements using thin film gauges . . . 21
2.4.1 Historical use of thin film gauges . . . 22
2.4.2 Development of high density thin film gauges on flexible substrate . . . 24
2.4.3 Accuracy and operation of thin film gauges . . . 26
2.4.4 Post-processing of thin film gauge data . . . 30
2.4.5 Experimental campaign in gas turbine linear cascade . . . 33
2.5 Unsteady pressure transducers . . . 35
2.5.1 Unsteady pressure measurement techniques . . . 35
2.5.2 Low cost pressure transducers . . . 35
2.5.3 Natural frequency of cavity . . . 36
2.5.4 Fabrication of test piece . . . 36
2.5.5 Data acquisition and processing . . . 38
2.5.6 Experimental measurement campaign . . . 39
2.6 Data acquisition and analysis . . . 39
2.6.1 Labview integrated data acquasition . . . 39
2.6.2 Matlab data manipulation and comparison . . . 41
2.6.3 Paraview visualisation . . . 42
2.7 Tblock flow solver . . . 42
2.7.1 Parallelisation . . . 43
2.7.2 Total pressure limiter . . . 43
2.7.3 Non-uniform cooling flows . . . 43
2.7.4 Large eddy simulation study . . . 43

3 Steady-state combustor turbine interactions 46

3.1 Introduction and literature review . . . 46
3.1.1 Flow through nozzle guide vanes . . . 47
3.1.2 Secondary flow . . . 47
3.1.3 Can combustor with swirl . . . 49
3.2 Measured heat transfer coefficients . . . 54
3.2.1 Differences between swirlers . . . 55
3.3 New midspan secondary flow . . . 58
3.3.1 Physical explanation . . . 58
3.3.2 RANS study . . . 59
3.3.3 Detailed Analysis of pressure loss but no swirl . . . 61

3.3.4 Comparison of CFD cases . . . 61
3.4 Summary . . . 63

4 Unsteady combustor turbine interactions 65

4.1 Introduction . . . 65
4.1.1 Influence of the inlet flow field on nozzle guide vanes . . . 66
4.2 Experimental and computational methods . . . 67
4.3 Precessing swirl core . . . 68
4.3.1 Swirl core through passage . . . 69
4.3.2 Vane surface unsteady pressure measurements . . . 70
4.3.3 Variation in vane loading distribution . . . 72
4.4 Unsteady heat transfer on vanes - measurement results . . . 75
4.4.1 High speed infra-red camera . . . 75
4.4.2 Comparison of swirler results . . . 75
4.5 Thin film gauges on vane surfaces . . . 79
4.5.1 Turbulence grid . . . 79
4.5.2 Swirl generator . . . 82
4.5.3 Clean inflow . . . 86
4.5.4 Unsteady fluctuating heat transfer . . . 89
4.5.5 High frequency endwall thin film gauge results . . . 89
4.6 Fluctuating horseshoe vortex near vane leading edge . . . 93
4.6.1 Importance of horseshoe vortex area . . . 93
4.6.2 Instability of horseshoe vortex near leading edge . . . 95
4.6.3 Self-excited instability of horseshoe vortex . . . 96
4.6.4 Influence of incoming flow on horseshoe vortex of unshielded vane . . . 98
4.7 Analysis of unsteady passage vortex . . . 100
4.7.1 Passage vortex and secondary flow unsteadiness . . . 100
4.7.2 Passage vortex on endwall . . . 101
4.7.3 Large eddy simulation results showing unsteady passage vortex . . . 104
4.8 Vortex shedding from combustor wall . . . 107
4.8.1 Can combustor geometry . . . 109
4.8.2 Leading edge measurements . . . 109
4.9 Summary and conclusion . . . 113

5 Effects of unsteady heat flux on component life **115**

5.1 Introduction . . . 115

5.1.1 Thermal barrier coating literature . . . 116

5.1.2 High frequency change in surface temperature . . . 116

5.1.3 Non-dimensional numbers and engine scaling . . . 120

5.1.4 Increase in surface temperature due to measured unsteadiness . . . 121

5.1.5 Effect of temperature fluctuation on component life . . . 122

5.2 Separating unsteady HTC from unsteady temperature fluctuations . . . 123

5.2.1 Separation technique . . . 124

5.2.2 Application to measured data . . . 125

5.2.3 Possible future improvements to method . . . 125

6 Flow within the midpassage gap **127**

6.1 Midpassage gap literature review . . . 128

6.2 Experimental set up . . . 130

6.3 CFD simulation of midpassage gap . . . 131

6.4 Overview of flow within gap . . . 133

6.5 Low order analysis of flow in gap . . . 134

6.5.1 Derivation of equation for mass flow within midpassage gap . . . 134

6.5.2 Solution of equation for mass flow within midpassage gap . . . 136

6.5.3 Derivation of critical threshold for gap flow . . . 137

6.6 Aerodynamic losses due to midpassage gap . . . 139

6.7 Comparison of predicted loss to experiments . . . 141

6.8 Additional heat load to vane platform due to gap . . . 141

6.8.1 Measured distribution of heat transfer coefficient within gap . . . 144

6.9 Control of ingress using purge flows . . . 145

6.10 Effect of gap flow on endwall HTC . . . 147

6.11 Effect of chamfered edges and other geometrical modifications . . . 148

6.12 Estimate of gap influence . . . 149

6.13 Conclusions and recommendations . . . 150

7 Ingress into stationary ring segment cavity **151**

7.1 Introduction . . . 151

7.2 Turbine ring cavity literature review . . . 152

7.3 Experimental setup . . . 154
7.4 CFD domain . . . 157
7.5 Experimental and CFD results within cavity . . . 157
7.5.1 External heat transfer coefficient . . . 157
7.5.2 Pressure within cavity . . . 157
7.5.3 Heat transfer coefficient within cavity . . . 158
7.5.4 Flowfield within cavity . . . 160
7.6 Explanation of flow into and out of cavity . . . 161
7.7 Downstream cavity with purge flows . . . 161
7.8 Conclusion . . . 164

8 Surface texturing to reduce heat transfer 165
8.1 Introduction . . . 165
8.2 Experimental specification and methods . . . 166
8.3 Results . . . 168
8.4 Discussion . . . 170

9 Conclusion 172
9.1 Introduction . . . 172
9.2 Experimental techniques . . . 172
9.3 Applications of experimental techniques to nozzle guide vanes . . . 174
9.4 Final remarks . . . 177

A Temperature fluctuations appendix 178

B Midpassage gap appendices 181
B.1 Alternative ODE derivation . . . 181
B.2 Coupled temperature equation . . . 183
B.3 Numerical solution to equation with Matlab . . . 184

Bibliography 191

List of Figures

1.1 Power generation in 2040 (IEA) 2
1.2 Gas turbine in combined cycle T-S diagram 4
1.3 Combined cycle ideal and real efficiency 6
1.4 Gas turbine and NGV 8

2.1 MHI high speed linear cascade 14
2.2 Measured inflow total pressure field 15
2.3 Swirl generators 16
2.4 Traverse mechanism and working section 18
2.5 Vane endwall with 48 TFG 22
2.6 Heat flux gauges with coverlay apertures 23
2.7 New gauge design using zero-height vias 24
2.8 Schematic of new gauges 25
2.9 Ideal noise of TFG 27
2.10 New connector designs for TFG 29
2.11 Post-processing for unsteady HTC 31
2.12 Thin film gauges instrumented on vane surface 34
2.13 Resonant frequency of pressure sensors 37
2.14 Vane with 48 unsteady pressure sensors 37
2.15 Natural frequency of pressure sensors 38
2.16 Measurement processing with automated DAQ 40
2.17 Unsteady pressure in transition section and NGV 45

3.1 Swirl stabilised combustion features 50
3.2 HTC of NGV 53
3.3 Clean endwall HTC 55
3.4 Comparison of HTC with inlet conditions 57

3.5 Pressure contours showing formation of midspan vortex 59
3.6 midspan vortex 60
3.7 Midspan vortex with different inflows 62

4.1 Unsteady flows in NGV 66
4.2 Unsteadiness on endwall and vane surfaces 68
4.3 Unsteady position of swirl core 70
4.4 Unsteadiness of incoming flow field 71
4.5 Unsteady pressure with different inlets 73
4.6 Variation of vane loading 74
4.7 Instantaneous high speed IR HTC 76
4.8 IR HTC plotted along suction surface line 77
4.9 Unsteady PS HTC with turbulence grid inflow 80
4.10 Unsteady SS HTC with turbulence grid inflow 81
4.11 Unsteady PS HTC with swirl inflow 83
4.12 Unsteady SS HTC with swirl inflow 84
4.13 Comparison of LES to TFG measurements 85
4.14 Unsteady PS HTC with clean inflow 87
4.15 Unsteady SS HTC with clean inflow 88
4.16 HTC unsteadiness for different inflows 90
4.17 Detailed unsteady HTC on endwall 92
4.18 Summary of unsteady HTC on endwall 93
4.19 Frequency of horseshoe vortex 94
4.20 Self-excited unsteadiness of horseshoe vortex 97
4.21 Externally excited oscillation of horseshoe vortex 99
4.22 Variation of secondary flow lift off 101
4.23 Schematic of passage vortex HTC enhancement 102
4.24 Unsteady endwall HTC with swirling inflow 103
4.25 Instantaneous variation in passage vortex 104
4.26 Analysis of passage vortex 106
4.27 Instantaneous midspan vortex from LES 107
4.28 Combustor wall vortex shedding 110
4.29 Vortex shedding with different inflows 112

5.1 Transient conduction in boundary layer . . . 117
5.2 Unsteady surface temperature . . . 122
5.3 Increase in unsteady endwall surface temperatures . . . 122
5.4 Unsteady heat flux gauges data showing the different components of heat flux . . . 124
5.5 Separating components of unsteady heat flux . . . 125

6.1 Gas turbine vanes and mid-passage gap . . . 128
6.2 Test piece used for measurements of midpassage gap . . . 130
6.3 Flow into midpassage gap . . . 132
6.4 Static pressure within gap . . . 134
6.5 Model used to derive 1-D equation for gap flow . . . 135
6.6 Comparison of CFD and 1-D model for gap flow . . . 137
6.7 Total pressure downstream of gap . . . 139
6.8 Losses due to gap . . . 141
6.9 Heat transfer within gap . . . 144
6.10 HTC distribution in gap . . . 145
6.11 Purge flow used to cool midpassage gap . . . 146
6.12 Endwall HTC with and without midpassage gap (RANS) . . . 148
6.13 Static pressure within the gap with and without a chamfered edge . . . 149

7.1 Stationary ring segment . . . 152
7.2 Downstream cavity experimental flow domain . . . 154
7.3 Downstream cavity test pieces . . . 156
7.4 HTC near downstream cavity . . . 158
7.5 Static pressure within downstream cavity . . . 159
7.6 HTC within downstream cavity . . . 159
7.7 Velocity distribution within downstream cavity . . . 160
7.8 Flow ingress and egress from downstream cavity . . . 161
7.9 Cooling distribution to prevent ingress into cavity . . . 162
7.10 Ingress with optimum cooling compared to uniform cooling . . . 163

8.1 CMC samples . . . 166
8.2 Test pieces used for CMC study . . . 167
8.3 Surface texture of CMC test pieces . . . 168
8.4 CMC heat transfer results . . . 169

8.5 Variation of HTC with CMC angle 170

B.1 Alternative derivation of 1-d equation for gap flow 181

Nomenclature and acronyms

ABS	Acrylonitrile Butadiene Styrene: a tough thermoplastic polymer
BL	Boundary Layer
CFD	Computational Fluid Dynamics
CMAS	Calcium-magnesium-alumino-silicate
CMC	Ceramic Matrix Composite
DAQ	Data Acquisition
FIR	Finite Impulse Response function
HTC	Heat Transfer Coefficient ($Wm^{-2}k^{-1}$))
HV	Horseshoe Vortex
IR	Infra-Red
LES	Large Eddy Simulation
LE	Leading Edge
LIC	Line Integral Convolution: a technique for visualising vector field such as velocity
MHI	Mitsubishi Heavy Industries
NGV	Nozzle Guide Vane: the first row of stator vanes, after the combustion chamber
NOx	Nitrogen oxides NO and NO_2, a form of air pollution
Nu	Nusselt number
ODE	Ordinary Differential Equation
Pr	Prandlt number
PS	Pressure side
PV	Passage Vortex
q	Heat Flux
RANS	Reynolds Average Navier-Stokes equations
Re	Reynolds number
rms	Root Mean Square
SLA	Stereo-Lithography [Apparatus]: a form of 3D printing

SNR	Signal to Noise Ratio
SS	Suction Side
St, Str	Strouhal Number
Stn	Stanton Number
TBC	Thermal Barrier Coating
TE	Trailing Edge
TFG	Thin Film heat flux Gauge
T	Temperature
uHTC	Unsteady HTC ($Wm^{-2}k^{-1}$))
VS	Vortex Shedding
YSZ	Yttria Stabilised Zirconia: a common TBC material

Equation variables by chapter

Chapter 1: Introduction

c_p	Specific heat capacity at constant pressure
p	Pressure
q	Heat flux
T	Temperature
w	Work
γ	Ratio of specific heat
η	Turbine efficiency
PR	Pressure ratio

Chapter 2: Experimental and computational techniques

A	Area
c	Specific heat capacity
$\mathbf{c}$	Speed of sound
f	Frequency
h	impulse response function
k_B	Boltzmann constant
k	Thermal conductivity
L	Length
P	Power
q	Heat flux
R	Resistance
t	Time
T	Temperature

$uhtc$	Unsteady heat transfer coefficient
V	Volume
V_s	Signal voltage
V_n	Noise voltage
V_{JN}	Johnson-Nyquist noise
V_{DAQ}	Data acquisition system noise
x	Depth into surface
α	Thermal diffusivity
a	Temperature coefficient of resistivity of material
δ	Dirac impulse function
Δf	Frequency range
ΔT	Amplitude of temperature fluctuations
η	Cooling effectiveness
ρ	Density

Chapter 4: Unsteady Combustor-turbine interactions

f	Frequency
L	Length
Re	Reynolds number
St	Strouhal number
v	velocity
μ	Dynamic viscosity
ρ	Density

Chapter 5: Effects of unsteady heat flux on component life

$d_{0.5}$	Depth with 0.5 of surface temperature change
f	Frequency
h	Unsteady heat transfer coefficient
H	Amplitude of unsteady HTC
k	Thermal conductivity
P	Period
t	Time

T	Temperature
$\bar{T}$	Time-averaged wall surface temperature
T_∞	Adiabatic wall temperature
y	Depth
α	Thermal diffusivity
ω	Angular frequency, $\omega = 2\pi f$

Chapter 6: Flow within the midpassage gap

A	gap cross sectional area
c_p	specific heat at constant pressure
C_τ	Skin friction coefficient
d	gap depth
F_τ	Wall shear force per unit length
h	Heat transfer coefficient
I	Momentum flux
L	gap length
m	Mass flux
p	Static pressure
q	Heat flux into wall per unit area
R	Gas constant
s	Entropy
T	Static temperature
u	Velocity
u^*	Ingressing velocity
w	gap width
x	distance along gap
α	angle between gap and mainstream
μ	Dynamic viscosity
ρ	Density

Subscripts and superscripts

$'$	differential with respect to x

$_0$ Stagnation quantity

$_1$ upstream condition

$_2$ downstream condition

$_f$ main flow quantity

$_g$ gap quantity

Chapter 1

Introduction

1.1 Gas turbines for the future

Industrial gas turbines for power generation provide a significant part of the world's energy supply, and this is expected to increase for the foreseeable future. The need to provide energy cleanly and in increasing quantity as part of worldwide sustainable development requires gas turbines to become more flexible and efficient in operation, while keeping capital and maintenance costs are kept to a minimum. This will be achieved by component optimisations, enabled by new materials, manufacturing and an increased understanding of detailed physical phenomena.

1.1.1 Introduction to gas turbines

Gas turbines are often categorised into three types; the first is the aero-engine and aero-derivative turbines. These form the core of aircraft engines, and in other applications where a compact size, low weight and high operational flexibility are important. Small and medium industrial gas turbines are used to provide mechanical and electrical power to industrial processes.

Large frame industrial gas turbines are the largest gas turbines in both power output and physical size, and are used for grid-scale electrical power generation. These turbines may be up to 500MW, and when used in combined cycle are the cleanest and most efficient practical thermal power plants, with efficiencies of above 62% achieved, and higher efficiencies targeted for the next generation of turbines. [2]. It is these turbines which are primarily considered in this project, though many of the conclusions could be applied more widely.

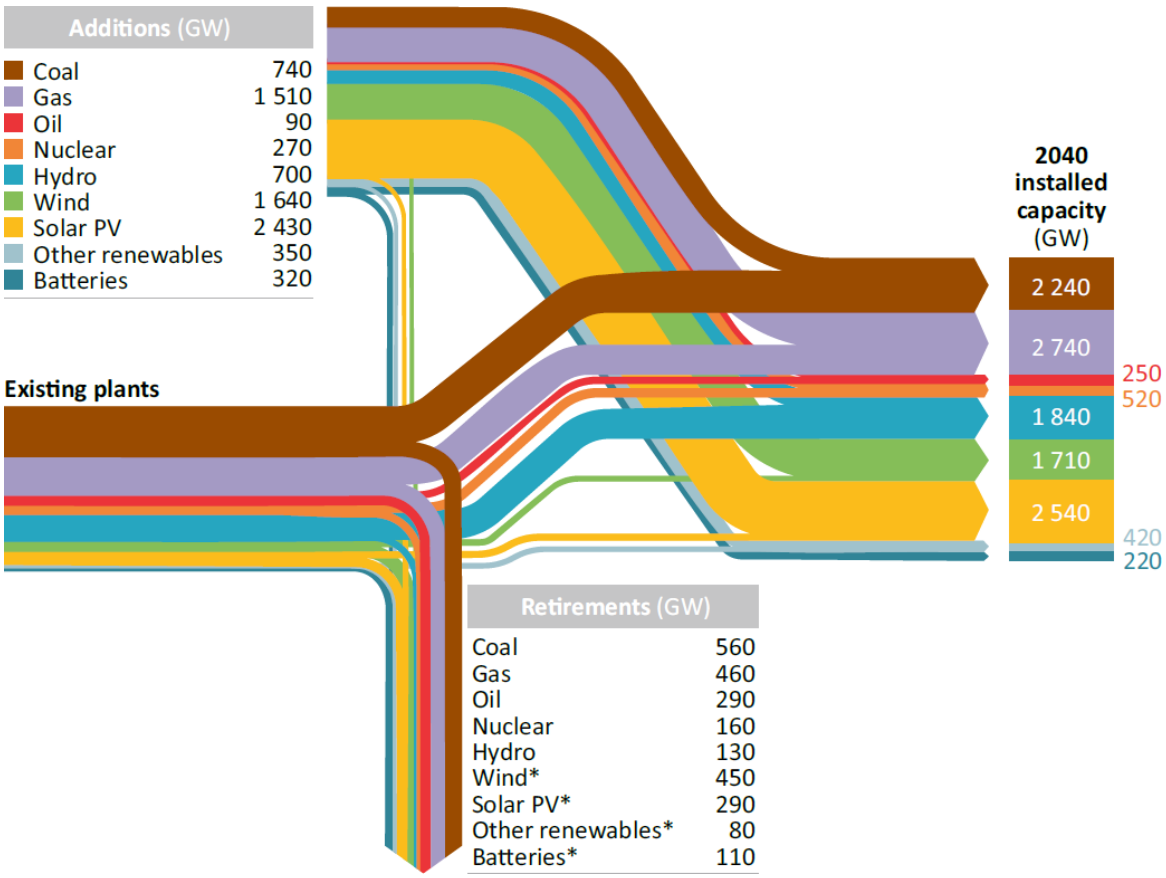


Figure 1.1: Installed capacity and expected additions and retirements by 2040 (reproduced from [1])

future of power generation

As the share of renewables increases in the energy mix, gas turbine generators will be a necessary complement for their load absorbing capabilities. According to the predictions of the International Energy Agency [1], although the share of renewables will increase greatly by 2040, the increasing total demand for electricity worldwide will ensure that fossil fuel power generation will continue to increase in absolute terms from currently installed capacity. Increasing electrification, especially in Africa and Asia will lead to all forms of power generation, except oil, increasing in capacity, shown in figure 1.1. Gas is expected to have the largest increase in installed capacity, this will mostly be converted to power by large frame gas turbines. In addition, some coal generation may used in integrated gasification (IGCC) plants, which use a gas turbine core. These are preferred as they produce fewer emissions and have higher efficiency, as well as a tolerance for low-grade coal [3]

Therefore, it is important that new gas turbines be as efficient as possible, to reduce fuel usage and emissions. Existing gas turbines may also be retro-fitted with new blades, vanes and combustors to increase efficiency and reliability [4].

In the future, there is the prospect of using hydrogen powered gas turbines for carbon free generation,with hydrogen generated using surplus wind or solar power at times of low demand [5]. Alter-

natively biomass replacing coal in IGCC could provide a long-term use for gas turbines in a carbon neutral world.

1.1.2 Operation of power generation gas turbine

The overall operation of a large power generation turbine, intended to run primarily in combined cycle, is described in this section, using the Mitsubishi Hitachi Power Systems M/701J as an example. This is one of the newest developed, state of the art gas turbines. Total power output is around 500MW for the turbine alone, with an additional 200MW generated in the steam bottoming cycle.

The gas turbine alone is 6.5m diameter, and weighs 550 tons.

Approximately 1000kg/s of air enters the turbine, and is compressed to 25 times atmospheric pressure through 15 stages of axial compressor. This compressed air enters one of 22 separate can combustors, is mixed with fuel and is combusted, raising the temperature to 1650°C. This hot gas is next expanded through four stages of turbine. A portion of the mechanical work thus produced drives the compressor, while the rest drives a generator to give 500MW of electrical power to feed into the national grid.

Since the temperature of hot gas entering the turbine stages is 1650°C, while the maximum working temperature of metal alloys is generally less than 1000°C, continuous cooling of turbine components is necessary. This is achieved by both internal and external film cooling of turbine component. Cooling is achieved using air which is diverted from the compressor, cooled (with waste heat feeding into the bottoming steam cycle), and then further compressed in a boost compressor before being re-introduced to the turbine through film cooling holes. This keeps turbine components at acceptable temperatures, but requires additional power for compression, and represents a irreversibility when it is mixed with the hot gasses in the turbine. Therefore the amount of cooling air used is kept to the minimum levels possible.

After expansion back to atmospheric pressure through the turbine, the temperature of the exhaust gas stream is around 650°C. At this point, 45% of the fuel heating value has been converted into electric power. In a combined cycle the exhaust gas of the turbine is then passed through a heat recovery steam generator, which heats pressurised water into supercritical steam. The supercritical steam is then passed through a steam turbine, generating an additional 200MW of electricity.

These large turbine power plants are used exclusively for grid-scale electrical power generation, as there are no single applications which require such large amounts of mechanical power.

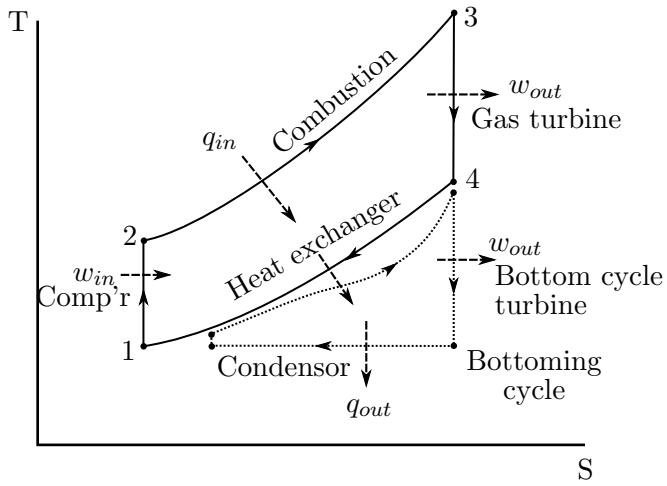


Figure 1.2: Thermodynamic cycle of the gas turbine is based on the Brayton cycle. In a combined cycle, remaining heat in the gas turbine exhaust is used to drive a bottoming cycle. A near ideal working fluid is pictured, but steam is used in reality, giving lower efficiency

1.1.3 Thermodynamic cycle

In the ideal, the gas turbine engine follows a Brayton cycle. The Brayton cycle consists of an adiabatic compression, isobaric heat addition, adiabatic expansion, and isobaric heat rejection, as shown in figure 1.2. This gives a theoretical efficiency dependant only on the compression ratio and is given by equation 1.1.

$$\eta = 1 - \frac{1}{(p_2/p_1)^{(\gamma-1)/\gamma}} \tag{1.1}$$

In the case of a real cycle with compressor and turbine adiabatic efficiencies <1, then efficiency is also dependent on temperature ratio.

Combined cycle

Even the ideal Brayton cycle has an efficiency less than that of a Carnot cycle. This is due to the fact that both at the top of the cycle and the bottom, heat transfer is not occurring at the maximum or minimum temperature. The bottom irreversibility can be removed by operating the Brayton cycle together with a 'bottoming' cycle, usually a Rankine cycle, and this is often done in practice in combined cycle power plants. The bottoming cycle uses heat rejected from the turbine exhaust gas to produce work, itself rejecting heat at a single lower temperature by a condensation process.

An ideal bottoming cycle would have a working fluid which could accept heat input at the same temperature as the gas turbine exhaust, but then be expanded to a saturated state and so allow heat rejection by condensation at a constant temperature. In practice, a steam cycle is normally used, which gives a less than ideal efficiency, as there will be large temperature differences across the heat recovery steam generator, resulting in an irreversible process.

However, even the ideal combined cycle still has an efficiency less than that of a Carnot cycle operating at the same maximum temperature, as analysed below:

$$\eta = \frac{w}{q_{in}} \tag{1.2}$$

$$T_3 = T_2 + \frac{q_{in}}{c_p} \tag{1.3}$$

$$w_{rev} = \left(1 - \frac{T_c}{T_h}\right) q_{in} \tag{1.4}$$

In the ideal Brayton cycle with bottoming cycle, heat input between stages 2 and 3 occurs at a temperature $T = T_2 + q/c_p$. By considering the maximum work that can be generated by each unit of heat input, the total work generated can be calculated as in equation 1.6.

$$w_{rev} = \int_0^{q_{in}} 1 - \frac{T_c}{T_2 + q/c_p} dq \tag{1.5}$$

$$= q_{in} - T_c c_p \ln\left(1 + \frac{q_{in}}{T_2 c_p}\right) \tag{1.6}$$

$$\eta_{rev} = 1 - T_c \frac{\ln T_3 - \ln T_2}{T_3 - T_2} \tag{1.7}$$

By substituting equation 1.6 into 1.2, the ideal combined cycle efficiency can be derived as in equation 1.7. Assuming ideal gas and isentropic compression, pressure ratio can be given in terms of temperature ratio in equation 1.8. Substituted into equation 1.7, this gives equation 1.9 for efficiency in terms of pressure ratio, and minimum and maximum temperatures.

$$\mathrm{PR} = \frac{p_2}{p_1} = \left(\frac{T_2}{T_1}\right)^{\frac{\gamma}{\gamma - 1}} \tag{1.8}$$

$$\eta_{rev} = 1 - T_c \frac{\ln T_h - \ln T_c \mathrm{PR}^{\frac{\gamma-1}{\gamma}}}{T_h - T_c \mathrm{PR}^{\frac{\gamma-1}{\gamma}}} \tag{1.9}$$

The ideal efficiency of a combined cycle with constant pressure heat addition and perfect bottoming cycle is given by equation 1.9. This is plotted for several pressure ratios, along with the Carnot efficiency to compare, in figure 1.3. Ideal gas turbine efficiency can be improved by increasing firing temperatures, and by increasing pressure ratios, but as shown by figure 1.3, a great deal of discrepancy exists between the ideal efficiencies and those realised in practice.

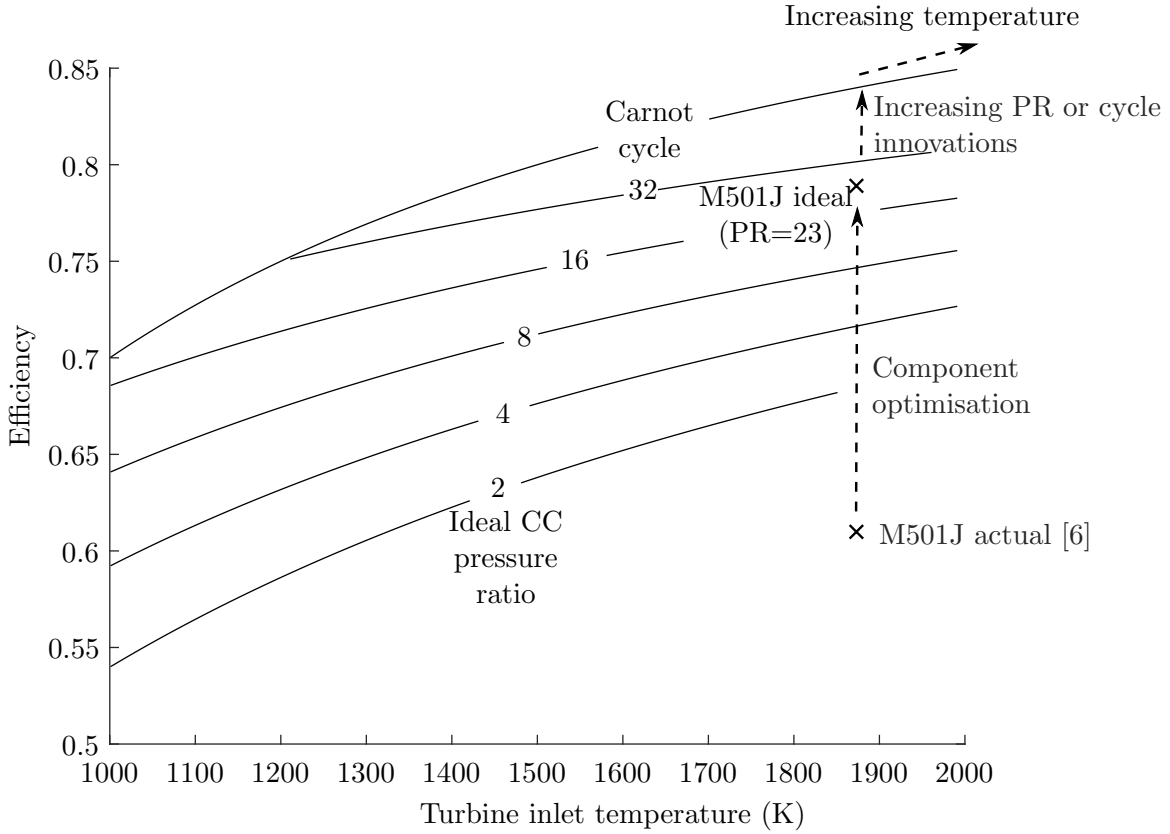


Figure 1.3: Efficiency of an ideal combined cycle at various pressure ratios and turbine inlet temperatures, compared to the efficiency of a reversible cycle with the same maximum temperature.

Real efficiency

There are significant differences between both ideal combined cycle and the Carnot cycle of the same temperature, and between real and ideal cycles. The ideal cycle assumes isentropic compression, expansion, and overall isentropic heat exchange in the heat recovery stream generator. In reality, each of these processes will be irreversible, and so reduce efficiency.

To use a real example, the Mitsubishi Heavy Industries (MHI) M501J is a advanced gas turbine intended to be used as part of a combined cycle. This machine has a pressure ratio of 23, and turbine inlet temperature of 1873K [6]. The measured efficiency is 61%, compared to a theoretical maximum of 79% for an ideal combined cycle with the same compression ratio and turbine inlet temperature.

This means that in general improvements can be made by: cycle innovations or increasing pressure ratio to move towards Carnot efficiency; increasing turbine inlet temperatures to increase efficiency, and component optimisation to move realised machines towards the ideal. This project will assist with the latter two of these goals, component optimisation to reduce losses, and to enable higher firing temperatures.

1.1.4 Limitations and areas of improvement

Past improvements to efficiency of gas turbines has mainly come through increasing turbine inlet temperatures, and to some extent this will continue. The newest commercially operating gas turbines have a turbine inlet temperature of 1600C. The next generation of gas turbines will have an inlet temperature of 1700C. This will require an increased understanding and better measurement and prediction of heat transfer, to prevent equipment failure [7].

There are two limits on firing temperatures. This first is metallurgical constraints, firing temperature must not cause damage to turbine components. This may be partially overcome by film cooling, and advanced high temperature ceramics. Modern gas turbines rely on film cooling to maintain acceptable component temperatures. Bogard and Thole [8] give an overview of the use of film cooling in gas turbines. In some industrial gas turbines, cooling air is not drawn directly from the high pressure compressor, but additionally passes through an intercooler and boost compressor before being used. This makes it even more desirable to reduce the cooling air requirements of the turbine.

Ceramic thermal barrier coatings are now commonly used to protect high temperature parts. TBC structure is engineered to be very low conductivity and high porosity. However this does create a vulnerability to unsteady surface heat loads, as a fluctuating heat transfer may cause significant, and potentially damaging fluctuations in surface temperature. An analysis of this issue is presented in chapter 5.

Beyond thermal barrier coatings, full ceramic hot gas path components may see an introduction into large turbines, especially ceramic matrix composites (CMC). A brief investigation into heat transfer of CMC is given in chapter 8. If cooled ceramic components are introduced, it would be even more important to have uniform coolant coverage, as small hot spots could result from any non-uniformities in cooling, whereas in metal components heat conduction within the component is greater.

The second constraint on temperature is NOx emission limits. NOx emissions are kept within acceptable levels by keeping combustor temperatures low, so the effective cycle temperature can be increased by reducing the amount of cooling air used, and so both power output and efficiency are increased by reductions in cooling air use. Lowering NOx emissions while increasing turbine inlet temperature can also be achieved by achieving a more uniform combustion in a lean burn combustor. Combustor systems are an active area of development, and future combustors may use different geometries which produce different flow fields. An overview of lean-burn swirl premixed combustors is given in section 3.1.3. A more homogeneous temperature profile means near endwall temperatures have increased, making endwalls of especial interest.

Computational Fluid Dynamics (CFD) methods for evaluation of heat transfer in nozzle guide

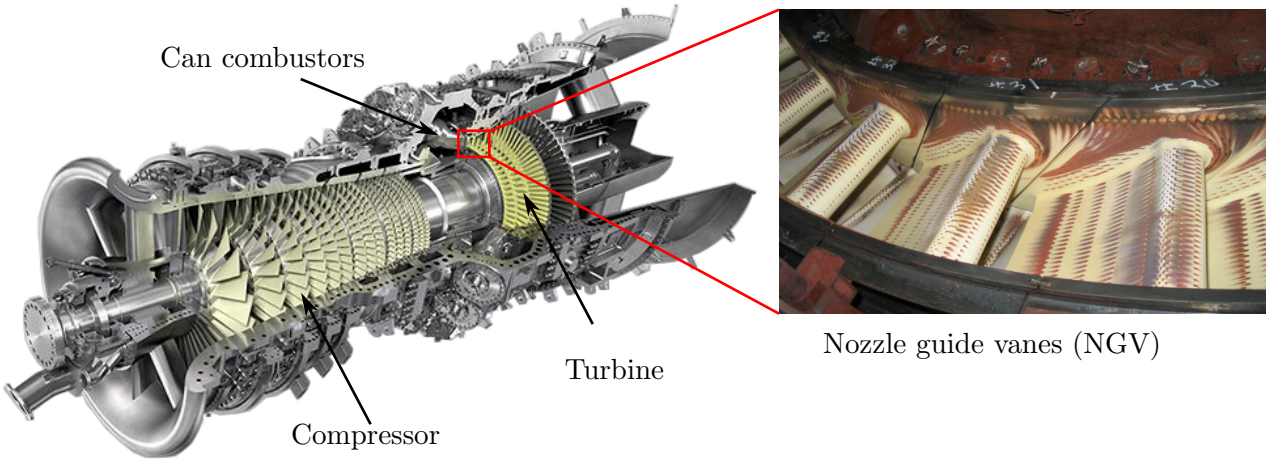


Figure 1.4: Gas turbine with NGV highlighted [10],[11]

vanes are not yet developed sufficiently for use by turbine designers, with empirical correlations based on experience of real equipment still being widely used. However, with increasing turbine inlet temperature, accurate numerical simulation, and comprehensive measurements will be required [9]

Beyond increasing turbine inlet temperatures, as shown in figure 1.3 the greatest capacity for efficiency improvements is in component optimisation to reduce irreversibilities which occur within turbines. Despite the great amount of resources which has gone into gas turbine research over the years, there are still doubtless many improvements to be discovered.

Bunker [12] reviewed the opportunities for step changes in turbine heat transfer design. There is a possibility of step changes in efficiency by novel design. The opportunities raised which are touched on in this thesis include using high temperature materials such as ceramic matrix composites, micro-3-D structures for modifying heat transfer behaviour in the gas path, and the interaction between the secondary air system leakage flows with the main flow path.

1.2 Thesis objectives

There are continuing efforts by turbine designers to continue to increase the turbine inlet temperatures of gas turbines. The limiting factor of turbine inlet temperature is the need to cool components to within acceptable temperature levels. The area which faces the highest temperatures, and thus is the limiting factor to further temperature increases are the combustion chamber and the nozzle guide vanes, which are directly behind the combustion chamber. The location of the NGV within the gas turbine is shown in figure 1.4.

A secondary constraint on temperature is the need to minimise NOx emission, in accordance with legislation to prevent air pollution. Since NOx production increases exponentially with temperature, emissions may be kept acceptably low by reducing the peak firing temperature which occurs in the

combustor. This can be achieved by making use of lean pre-mixed combustors. Combustion stability is typically achieved with the use of swirl generators.

Experimental studies have shown that the effects of the combustor flow field on heat transfer and aerodynamics in the nozzle guide vanes can be significant, and design should take this into account.[13] It is possible that modifications to a combustor may reduce cooling requirements of NGV significantly, making integrated design of combustors and NGV desirable for efficient gas turbines. In order to fully optimise heat transfer and aerodynamics in the NGV combustor and turbine should be considered in an integrated manner.

It has also been found that the combustion chamber flow has a high levels of unsteadiness, which causes unsteady fluctuations of the flow within the NGV[14]. It is important to understand the nature and causes of this unsteadiness, and especially whether it is likely to cause component damage in the turbine.

Realistic geometry features present in the real turbine NGV area, such as gaps and discontinuities between vane platforms, can cause damaging localised heat transfer. These features have been implicated in failures in real machines, and so understanding these phenomena is essential to improving the next generation of turbines.

The objective of this thesis was to investigate these problems in the combustor-turbine interface area, and to suggest solutions. It was decided to use both experiments and CFD together to carry out the investigations. Experiments were used to gain accurate steady and unsteady data, and to validate CFD, while CFD results can be used to show full flowfield phenomena which are difficult to measure directly.

Experiments were carried out using an existing experimental rig, which has been used for past studies of steady-state combustor-turbine interactions. Instrumentation was developed with the aim of taking a high density of unsteady heat flux and unsteady pressure measurements.

It was set out to investigate areas of observed damage in the NGV, by measurement and simulation, in order to gain a full understanding of the root causes. It was further aimed to then give concrete suggestions for improvement which could be acted on by turbine designers to improve the next generation of gas turbines.

Relevant literature is reviewed for each chapter individually, rather than as a single literature review.

1.3 Overview of thesis

It was set out to develop appropriate instrumentation and measurement techniques to investigate heat transfer particularly in scale models, and then to apply this to the problem areas identified in real machines. In this, a close industrial partnership was crucial to identify areas of investigation. Regular meetings with turbine designers, in both England and Japan, ensured that the results of these investigations were rapidly communicated back to turbine design teams, and that investigations could be focused on priority areas in the development of the next generation of turbines.

Over the course of the project, many experiments have been carried out in a linear cascade, both speculative wide area measurements to see what is observed, and others focused on specific areas. A large eddy simulation (LES) was carried out to provide a full set of matching data to go with experiments. Many supplementary RANS studies were performed to investigate specific phenomena.

The test facility used, instrumentation and development of measurement techniques, as well as CFD methods, are described in chapter 2.

Chapter 3 describes the steady flow field in the NGV, and heat transfer measured. The effects of different swirling inlet conditions are reported. A newly observed secondary flow like structure near to the midspan of the vanes is examined in detail, both using experiments and a supplementary RANS study to confirm the conditions for its formation.

Chapter 4 describes many of the unsteady flow phenomena which were observed using high speed measurements, including a comparison between swirlers. Where possible these have been explained physically with reference to the LES study results. An unsteady area map of endwalls and vane surfaces is shown, giving characteristic frequencies measured in each area.

It is shown in chapter 5 that unsteady effects measured can have a potentially damaging effect on component life.

The second half of this thesis focuses on realistic assembly features in the NGV, and heat transfer which results, as well as ways to mitigate these harmful effects. While these were carried out using the same NGV geometry, the results are likely to be more widely applicable to other stator vanes.

Chapter 6 details improvements which can be made to the midpassage gap between adjacent vane platforms, an area of turbine design which appears to have been largely overlooked so far. It has been observed in real machines that damaging heat transfer can occur in this area. This was experimentally investigated, with the first heat transfer measurements in this area. A RANS study was also performed, with a good agreement. A one-dimensional analytical approximation was constructed, which allows estimation of the effect of the gap on both heat transfer and aerodynamic loss. This can be used to predict the impact of the midpassage gap for and machine, and so whether mitigating action is

necessary. The ideal distribution of purge flow to eliminate ingress into the cavity was calculated directly from the one-dimensional model.

Chapter 7 investigates the related but physically quite distinct situation of a gap or cavity downstream of the vanes. This occurs in the real machine between adjacent casing ring segments. Heat transfer was measured within the cavity and on endwalls, with results matching observed damage in real machines. A way to more efficiently mitigate this damage is suggested, and simulated with CFD, with promising results.

Chapter 8 looks at one of the possible side effects of using ceramic matrix composites for stators in future. Test pieces were made with the same surface texture as CMC, with various orientations, and heat transfer compared.

Finally, chapter 9 gives some concluding remarks, summary and some suggestions for designers based on this work. It is also suggested and speculated on other fields where the techniques developed could be applied.

Chapter 2

Experimental and computational techniques

Experimental measurements in scaled test facilities are the major method to take detailed measurements of heat transfer and aerodynamics of turbine components, since CFD is still not sufficiently advanced to give routine prediction of flows and heat transfer within a gas turbine. It is likely that this will continue for the foreseeable future, as the mesh requirements for a fully resolved direct numerical simulation of a gas turbine are prohibitive even for supercomputers. This makes continual development to improve experimental techniques necessary.

The test rig and working section used to carry out experiments is described below. It is necessary to measure heat transfer at a high sensitivity, at high frequency, and as high a spatial resolution as possible. To do this, we advanced the use of thin film gauges (TFG). High density arrays of thin film gauges were used to take 384 measurement points on a NGV.

To investigate unsteady flow phenomena in the NGV, and validate LES which was carried out, the use of high density of unsteady pressure transducers was pioneered. 48 pressure transducers were spread over the vane surface, with a frequency response above 2000Hz achieved.

An infra-red (IR) camera was also used to measure heat transfer in the test rig. The advantage of IR is that full surface coverage can be achieved (aside from optical dead spots), and without the difficulties of instrumenting each test piece. However, sensitivity and speed do not match that achieved by thin film gauges. A state of the art high speed IR camera was used for the first time in this facility.

Data acquisition and processing is described. A suite of Matlab functions was created to automate processing of experimental data.

CFD was used to support experimental measurements. CFD was carried out using a modified version of the Tblock solver. Modifications made to the solver are described briefly.

Full results and analysis are presented later in the relevant chapters.

2.1 Experimental facility

The experimental facility used was the MHI High Speed Linear Cascade at the Oxford Thermofluids Institute, shown in figure 2.1. Two can combustors and four nozzle guide vane passages were modelled in a linear cascade with a Mach number matched to the real machine and Reynolds number 42% of the real machine value. A compressed air supply passed through an upstream regulator and orifice to give a constant mass flow for around 2 minutes. Details of the facility are given by Luque et al.[15] and Aslanidou [16].

The MHI High Speed Linear Cascade facility at the University of Oxford was constructed to measure heat transfer and aerodynamic measurements in nozzle guide vanes with modelled can combustors. Experiments were performed to measure the heat transfer coefficients using an infra-red camera and step response heater mesh in a transient technique. The modular nature of this facility allowed different geometries to be easily experimented upon with good repeatability.

The working section was contained within a pressure vessel. It was protected by three safety valves and a bursting disk.

The vanes were made using 3-D printing technology, allowing for experimentation on different geometries quickly and economically. Past use of the rig include a study made of the influence of swirling flows in the combustor on aerothermal performance of the first vanes using infra-red camera and five hole probe traverse [13]. More recently, this facility has been used in conjunction with thin film heat transfer gauges instrumented on the nozzle guide vanes, in order to extract unsteady results [17].

2.1.1 Swirlers

Inlet conditions were changed by means of replaceable upstream cassettes, which hold various turbulence grids or swirlers. Six different inlet conditions were used for different experiments, shown in figure 2.3. The swirlers used were: a clean inflow with low turbulence level; a highly turbulent inflow generated by a grid; a swirling flow generated by a single swirler with a bypass; a swirling flow with one pilot swirler and eight main swirlers; a swirling flow with one pilot swirler and twelve main swirlers; and a mirror image of the single swirler to give a reversed swirl direction.

The inlet conditions to the vanes were measured using a five-hole probe on an automated two-axis traverse mechanism. Figure 2.2 shows the measured inlet conditions for the experimental cases of the single swirler and the eight-core swirler.

Vane exit Mach number	0.65
Inlet total temperature	310-335K
Reynolds number	1.6×10^6
Vane true chord	150mm
Vane axial chord	89mm
Vane pitch	120mm
Vane span	104mm
Geometric scaling factor	0.62
Mass flow per passage	1.2kgs^{-1}
Inlet total pressure	$1.55 \times 10^5\text{Pa}$
Outlet static pressure	$1.19 \times 10^5\text{Pa}$

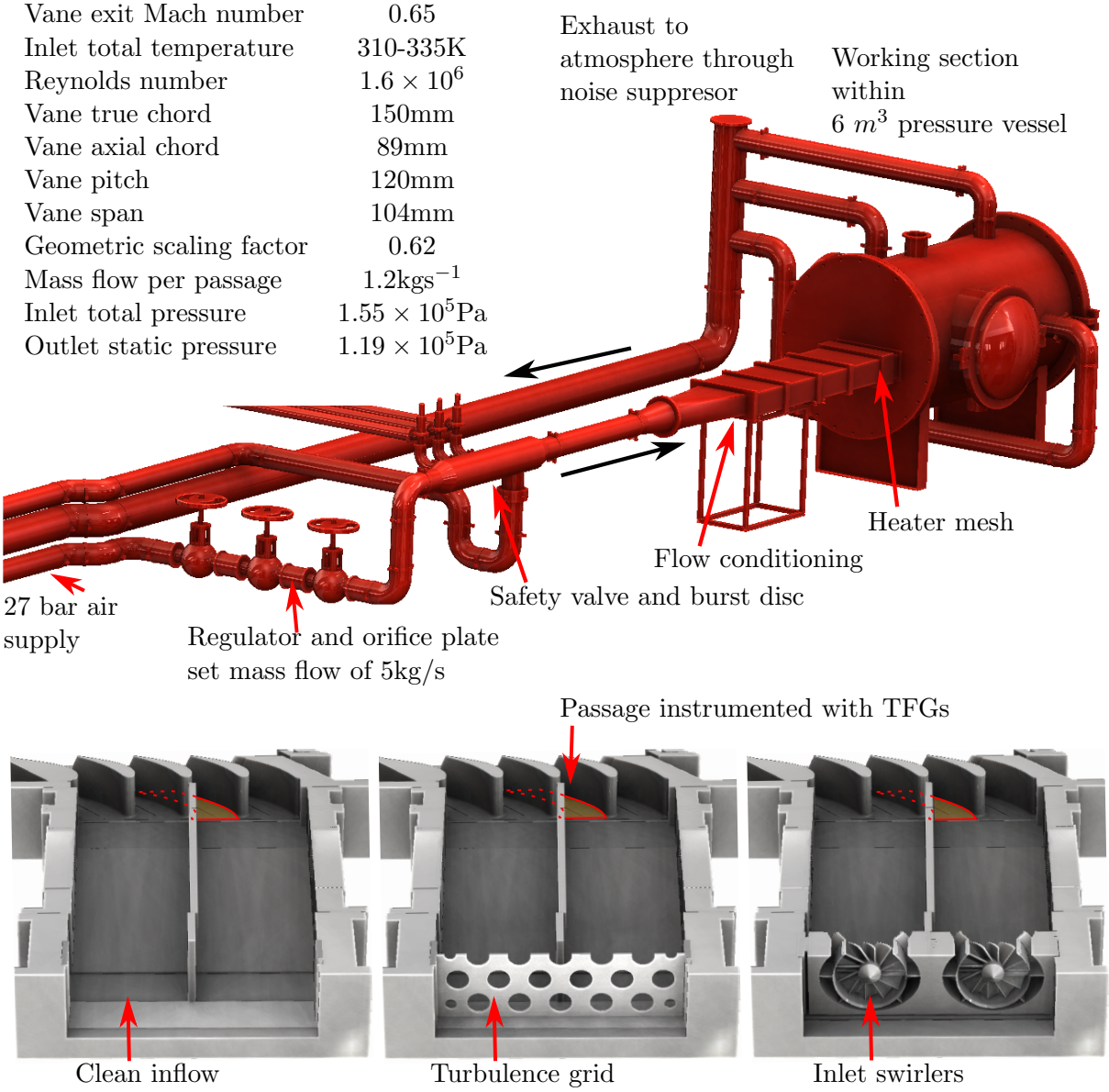


Figure 2.1: Experimental facility. The MHI high speed linear cascade provides a flexible platform for performing tests on NGV geometries with different combustor inflow models. Top: Illustration of experimental facility. Bottom: working section showing position of inlet conditioning cassettes and instrumented NGV

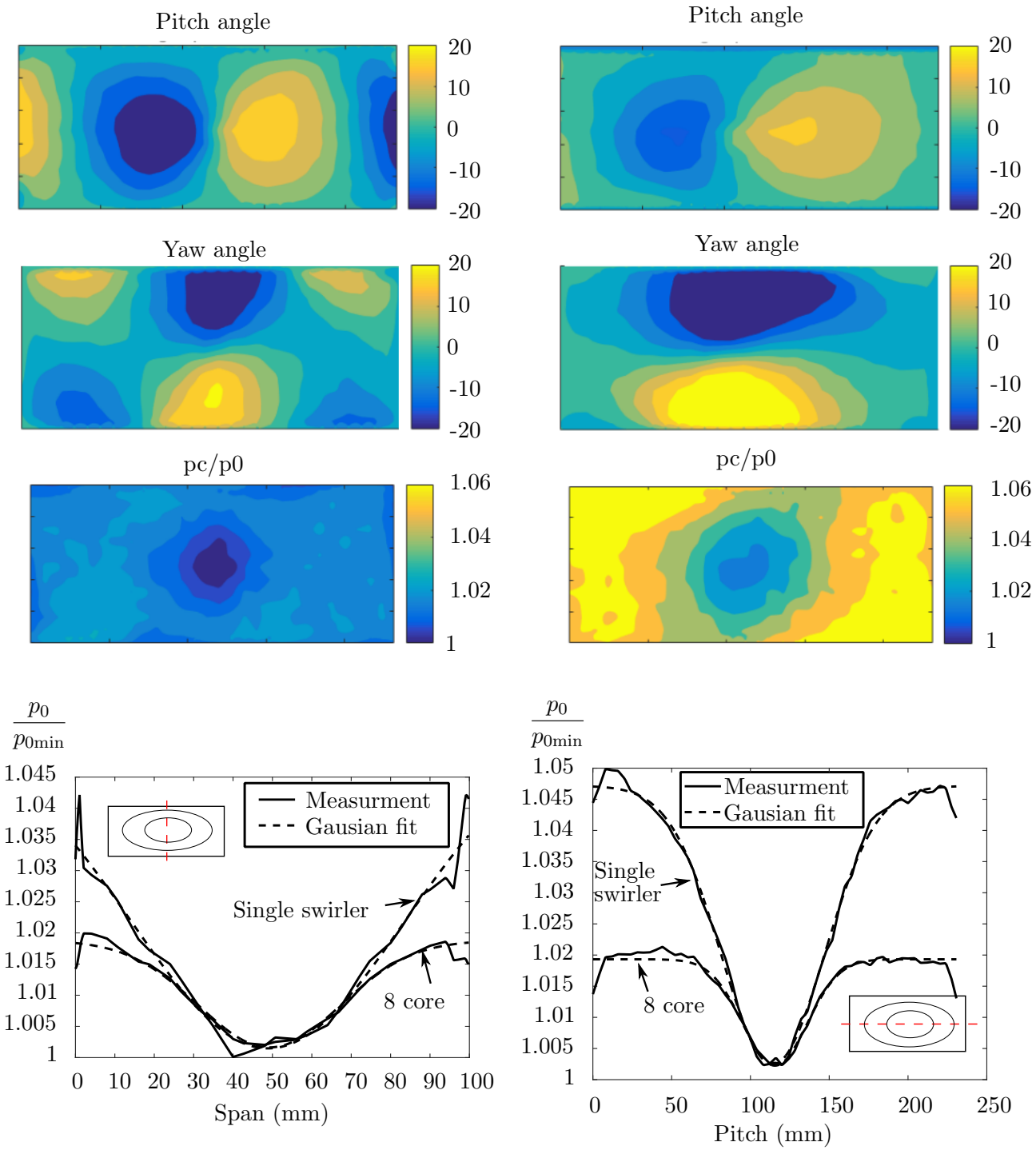


Figure 2.2: Left: Pitch, yaw and non-dimensional total pressure measured upstream for 8 core swirler case. Right:Pitch, yaw and non-dimensional total pressure measured for single swirler. Bottom: Simplified inlet conditions used for CFD boundary

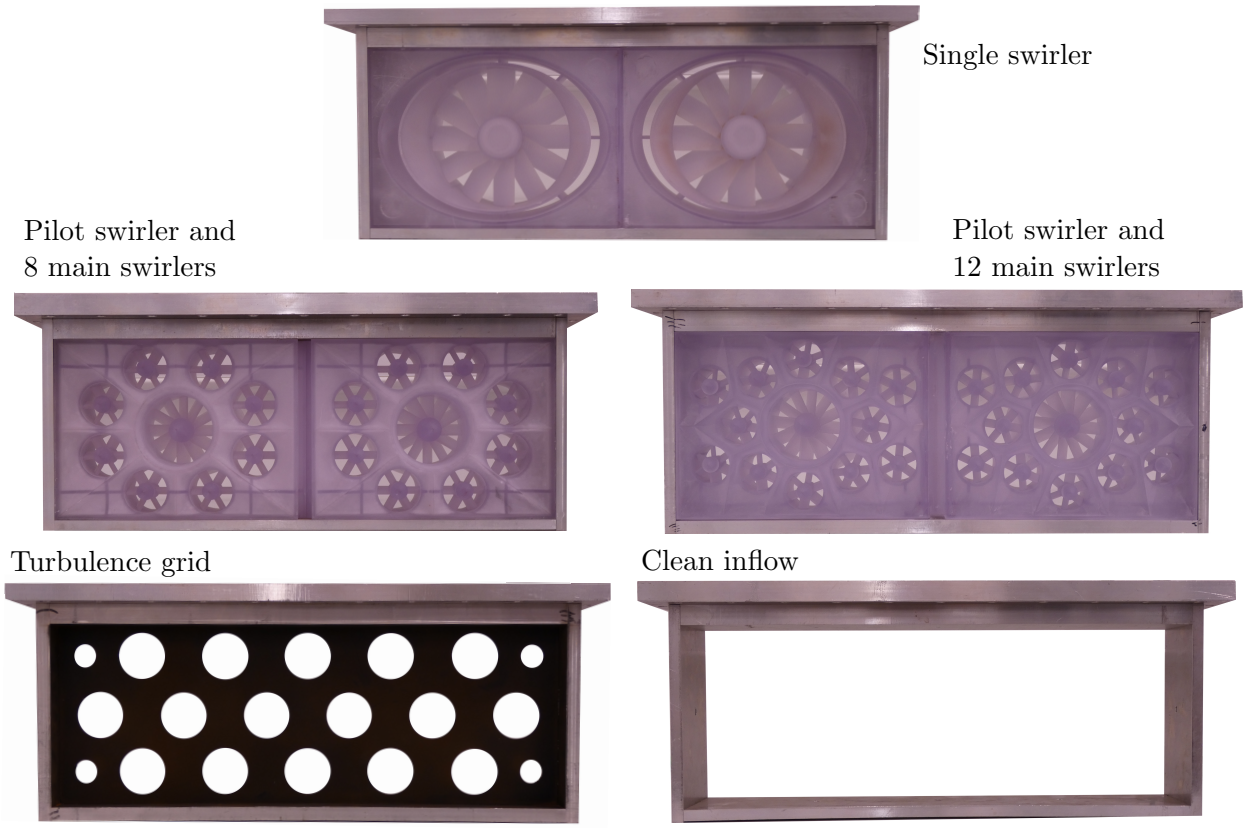


Figure 2.3: Swirl generators used to create various inlet conditions. Top: single swirler gives highest levels of swirl and largest structures. Middle left: 8 core swirler gives lower level of swirl and smaller flow structures. Middle right: 12 core swirler gives smaller turbulent structures. Bottom left: Turbulence grid. Bottom right: empty cassette for low turbulence inflow.

The turbulence grid was designed following the empirical correlations given by Roach[18] in order to give a mainstream turbulence level of about 12%. It consisted of a plate with circular apertures 15mm in diameter.

The swirlers were designed by Jacobi [13], and provided a mean swirl angle of 8 deg at vane inlet.

Figure 2.2 shows the total pressure along the midlines of the simplified inlet conditions. The experimentally measured inlet conditions were found to be well fitted by a Gaussian function. Swirl is defined as the ratio of angular momentum to axial momentum, as measured using the five-hole probe traverse. Pressure drop is the difference between the mean and the minimum inlet absolute total pressure. Total pressure and flow direction at inlet were used as boundary conditions input into Tblock. A Matlab script was created to take experimental data from the traverse and convert it into the correct format for Tblock entry.

2.1.2 Vane geometry

The vane geometry used for these experiments was based on a linearised version of an MHI F-class NGV, reduced to 60% of actual size. The vane had a chord length of 150mm and height of 104mm.

There were two vanes for each can combustor, so that each vane was either directly in the path of a swirler, or was behind a combustor wall. In this configuration the vane leading edge was directly behind the combustor wall, this vane is referred to as the shielded vane. Although the shielding effect of the combustor wall reduces velocity impinging onto the leading edge, it also increases turbulence levels, and there may be von Karmann vortex shedding from the combustor wall impinging onto the vane. If not otherwise specified, all data presented in this thesis refers to the unshielded vane.

2.1.3 Test pieces

The vanes under test are manufactured out of a polymer resin using stereo lithography (a form of 3-d printing), with a resolution of 0.1mm. Component surfaces were hand finished to ensure a smooth surface. The resin used is SL7870.

The use of 3-D printing allows test pieces to be rapidly designed and fabricated in order to test different effects. Tests measuring external heat transfer can be carried out in a matter of weeks from conception from results, using an IR camera. Other instrumentation takes longer to implement.

2.1.4 Overview of measurement techniques

Several measurement techniques are used in this facility. Steady state measurements are carried out using static pressure tappings connected by flexible tubing to a digital sensor array. A five-hole probe and one-hole probe traverse is used for low-speed aerodynamic measurements. Thermocouples are used to measure freestream temperatures. An IR camera is used for steady state surface heat transfer coefficients. A high speed IR camera has been trialled for unsteady full surface measurements, at a medium frequency response. For even higher frequency response, thin film heat flux gauges are used. Thin film gauges are also used for heat transfer measurements in areas which do not have good optical access. Unsteady pressure tappings have also been developed for use in this facility, giving a more detailed coverage than ordinary methods. Development of thin film gauges and unsteady pressure tappings is described in detail in section 2.4 and 2.5. The high speed IR is commercially available technology, but it is not yet commonly used in facilities of this kind, so some discussion is included in section 2.3.1.

All heat transfer measurements performed in this facility, whether using an IR camera or thin film gauges, rely on a transient heat transfer technique. Upstream of the working section is a heater mesh, which provides a rapid rise in freestream temperature of up to 30°C.

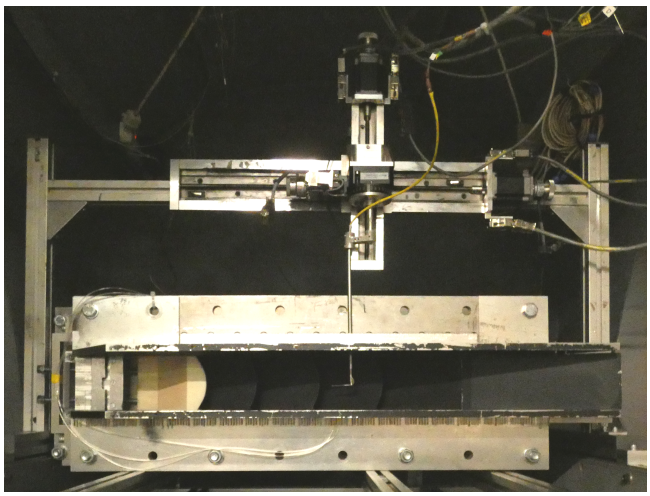


Figure 2.4: Working section and traverse mechanism used for aerodynamic measurements

2.1.5 Traverse

A traverse system was used to take aerodynamic measurements over an area downstream of the vanes. It was also used to measure vane inlet conditions. A five hole probe is used to measure static and total pressure, and flow angles. The five-hole probe was calibrated in a specialised facility by rotating it by fixed angles of pitch and yaw in a jet, to create a map of coefficients. This process is described for this facility by Aslanidou [19]. The uncertainty of pressure measurements is ±50Pa, which is limited by the measurement accuracy of the data acquisition system. Statistical analysis of the probe calibration indicated an uncertainty of ±0.32 deg to within 95% confidence for the yaw angle and ±0.3 deg to within 95% confidence for the pitch angle.

The traverse follows a list of co-ordinate locations and automatically takes data from each location. The traverse was manually repositioned to a marked zero point between runs. A feeler gauge was used to set the distance from the bottom wall, while the horizontal position corresponded to a marked point on the cascade. This gives a estimated uncertainty in positioning of ±0.1mm in the vertical direction (the thickness of the feeler gauge), and ±0.5mm in the horizontal direction (based on the operator lining up the marked points).

A 2 second dwell time at each point ensures that pressure can settle before measurement is taken. The traverse mechanism installed in the rig is shown in figure 2.4.

2.2 Measurement of heat transfer in nozzle guide vanes

There have been many measurements of steady heat transfer to the endwall using a variety of techniques. Papa et al.[20] compared CFD to experimental measurements of an endwall using a mass transfer analogue. Laveau et al.[21] measured endwall heat transfer distributions over a vane endwall

using IR. Harvey and Jones[22] used thin film gauges (TFG) to take measurements of a NGV endwall in a piston facility, with realistic Re, M and temperature ratio, using thin film gauges painted onto a ceramic vane. Spencer et al.[23] made measurements of endwall heat transfer using a transient liquid crystal technique. Barringer et al.[24] used seven thin film gauges to measure the effect of combustor exit profiles on NGV endwall heat transfer. Qureshi et al.[25] used thin film gauges to measure endwall HTC.

Laveau et al.[21] have made a set of extremely high resolution first vane endwall heat transfer coefficient measurements with an infra-red camera photographing a constant temperature vane covered in an insulating layer of polyimide, with measurements taken from several view angles combined using projective geometry to give a full coverage map, with a repeatability of +-5%. However, they do state that an uncertainty of +-1.3% is required to give an uncertainty in component life of +-10%, so there are still large improvements to be made.

In general, full surface heat transfer coefficients are calculated by measuring surface temperature. Either with a constant heat flux surface [26, 27], or a constant temperature substrate below a known thickness of insulator [21, 28], which is allowed to reach steady state before surface temperature is measured and HTC calculated. Or a transient technique can be used, calculating HTC from the change in surface temperature with time on a surface with known thermal properties, for example [13, 29, 15].

The common techniques for measuring the surface temperature are using an Infra-red camera [21, 27, 15, 13], or using liquid crystals [28, 29]. Both of these methods need optical access to the area being measured.

The thin film heat flux gauge (TFG) can give accurate high frequency measurements at frequencies up to 100kHz [30].

2.3 Infra-red camera

Steady state heat transfer coefficients are measured by using an infra-red camera. Surface temperature is measured by the camera, then HTC is calculated using the same transient technique as detailed in section 2.4.4. Two different IR cameras were used in this project. A low speed IR camera for time-averaged heat transfer coefficients has been used in this facility before by Jacobi [31] and Aslanidou [19]. An advanced, high speed IR camera was used for the first time for measurement of unsteady heat transfer into the vane surface. The high speed IR camera was also used as a means of unsteady flow visualisation.

Low speed infra-red

For time-average heat transfer measurements, a FLIR A655sc infra-red camera is used. This IR camera samples at 50Hz at full frame of 640 × 480 pixels, or up to 200Hz at reduced frame size. There is also a significant level of noise, so that this camera is only used for essentially steady state measurement. A zinc selenide window is used to give optical access into the working section. The window includes an anti-reflection coating made for the wavelength used by the camera. A full description of the calibration and use of this IR camera in the facility is given by Luque et al. [15]. The measurement uncertainty of heat transfer coefficient was found to be ±4.79 %.

After observing the very low frequency of unsteady phenomena which occurred in the nozzle guide vanes (see chapter 4), it was attempted to use a high-speed IR camera to observe unsteadiness over the full surface.

2.3.1 High speed infra-red camera

A high speed infra-red camera was used to measure unsteady heat flux in the cascade of NGV. Investigations using thin film gauges to measure unsteady heat flux revealed that many of the unsteady processes taking place in this area were at a frequency of below 500Hz. This allows the possibility of measuring these unsteady processes using a high speed IR camera. A FLIR X6900sc camera was used to measure unsteady temperature of vane surfaces and endwalls. With an integration time of 1ms, a maximum sampling frequency of 1000Hz was be achieved. This gives a Nyquist frequency of 500Hz, allowing many of the unsteady flow features to be visualised.

The camera uses a cooled indium antimonide sensor, giving an extremely low level of noise.

2.3.2 Processing of infra-red

Temperature was converted into heat flux and unsteady HTC in the same way as thin film gauge data, using the transient method described in section 2.4.4. This conversion was carried out for each pixel independently. Due to the extremely large amount of data created by recording a full run at 1000Hz, the processing was only carried out on a section of data from immediately before the heater mesh was switched on until approximately 1 second afterwards. Since the assumption of an initially isothermal substrate is not strictly achieved, the absolute values of HTC may not be accurate.

Unsteady HTC can be shown in movies, and snapshots are shown as still images. Time averaged statistics, such as RMS values of fluctuation in heat flux are also reported throughout this thesis.

In the raw signals there is a large amount of camera shake. This is due to the vibrations of the entire test facility under operation. The X6900sc camera was quite heavy at 6.3kg, and tended to shake

at a low natural frequency, even when stiffened to the greatest degree possible with the mountings available.

Since heat transfer calculations rely on analysing the temperature history of each pixel, for this to be accurate it is essential that the movement of the imaging area is eliminated. This could be achieved post-run in software. A Matlab script was created which used point recognition to identify features in each image frame and compare them to the same features in subsequent frames. In this way the motion between each frame could be adjusted for, allowing the accurate calculation of heat flux. While this works well for some datasets, when the flow is relatively steady, when there are large changes to flow pattern from frame-frame, then automatic point recognition may wrongly interpret this as being a changing camera position. This may be solved by using filters on the data to extract specific features which are not related to the flow, and which show true camera position. For example, a horizontal line filter may be used to extract the top of the working section, which then gives a reliable guide. This does mean that the script must be somewhat tuned for different cases though.

2.3.3 Flow visualisation with infra-red

The high resolution of this IR camera allows much of the surface texture of the test piece to be visible. It is observed that HTC tends to 'streak' in the direction of flow behind small obstacles or surface discontinuities. On a rough surface it is therefore possible to see the flow direction in the IR image. This may be a useful method of flow visualisation in some cases, even if HTC is not in itself of any direct interest. Unlike oil and pigment flow vis, unsteady flow visualisation may be achieved, and also requires less preparation. It also requires less preparation and causes less flow disruption than using tufts attached to the surface.

It is relatively straightforward to observe flow directions by inspection of a movie of IR data. Creating a still image that objectively quantifies this information is more difficult, but has been attempted, at least for steady state. A Matlab function has been created to extract the pattern of streaks showing flow direction from the unsteady dataset. This must be done for each frame, and then averaged, since the smaller streaks are unsteady, and so are smoothed out in the time-averaged case.

2.4 Heat transfer measurements using thin film gauges

This film gauges have often been used at Oxford and elsewhere for heat transfer measurements. They can make high speed measurements up to frequencies of 100 kHz or higher, and their sensitivity and accuracy is superior to other measurement techniques. Additionally, they can be used even when there is no optical access to the measurement location. This was a significant advantage in this case as

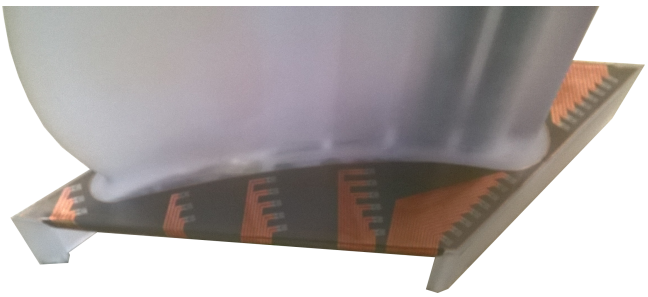


Figure 2.5: First iteration of thin film gauges on endwall. 48 gauges were used, limited by the size of connecting tracks.

previously it had been impossible to take measurements of the entire endwall area in this facility, due to the available viewing angles of the IR camera. Measurements were also taken within small gaps and cavities which would be impossible to view with an IR camera, or any other technique which relied on optical access. However, they cannot match the optical techniques for resolution of measurement, since tens of thousands would be required on a surface for the same level of spatial resolution.

An endwall has been instrumented with 192 thin film gauges, which as far as is known is by some margin the most detailed measurement of an engine realistic endwall with this technique.

Thin film gauges are fabricated on a flexible polyimide substrate, designed specifically for the geometry under test. Manufacturing broadly followed the technique of Collins et al. [32], with additional improvements developed over the past three years, which are described fully below. The number of thin film gauges which can be used has been increased dramatically, as well as the sensitivity and reliability of measurements.

Time averaged heat transfer coefficients (HTC) have been calculated using a transient technique of measuring surface temperature in response to a fast rise in freestream temperature created by an upstream heater mesh. This can provide an increase in temperature of approximately 30K.

2.4.1 Historical use of thin film gauges

Thin film heat transfer gauges are extensively used for high fidelity, high frequency heat transfer measurements. Usually in transient facilities, and sometimes to make time resolved measurements. The Osney laboratory has significant experience and expertise in their manufacture, application, calibration and use, as a result of the presence of the Oxford Turbine Research Facility [33].

Basic descriptions are given by Epstein et al. [30], and compared to other techniques by Sieverding et al. [34].

The gauges are manufactured on a polyimide substrate using photo-lithography techniques. A layer of photoresist is applied using a mask to etch a network of copper traces in a pre-laminated copper-polyimide sheet. A second layer of photoresist is then applied over the etched copper. Platinum

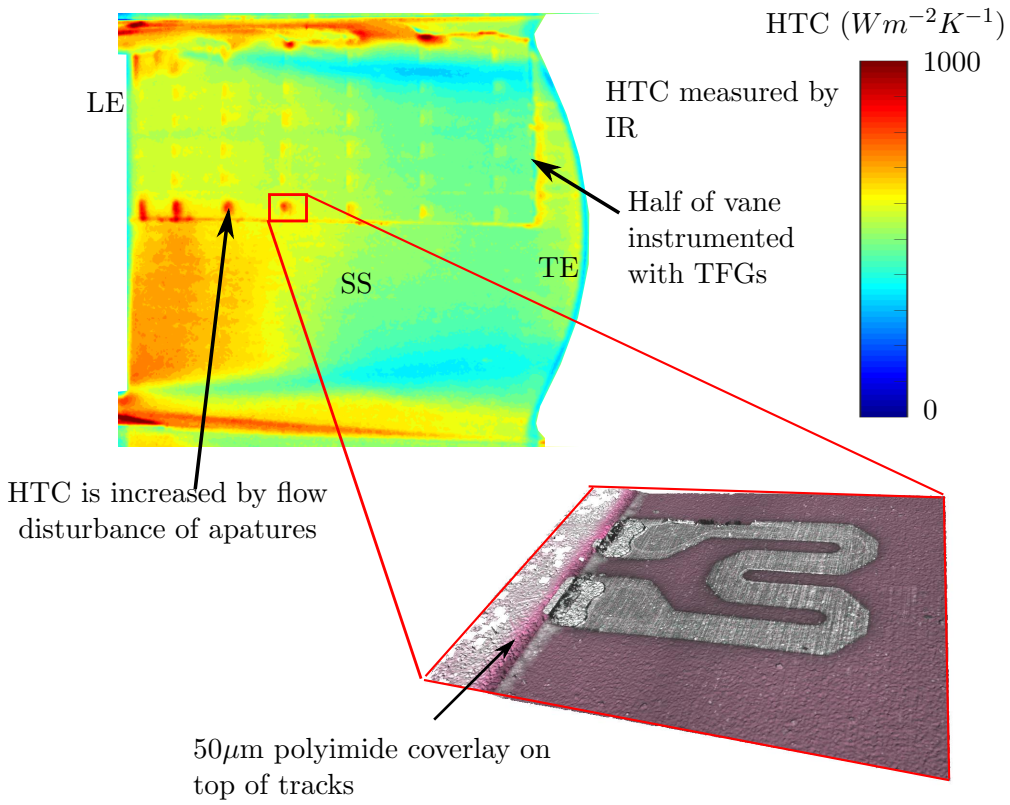


Figure 2.6: Second iteration of thin film gauge development used coverlay to protect 100 μm tracks, but apertures in coverlay cause modification to HTC, as shown by IR imaging of instrumented vane.

is sputtered over the entire surface, and the photoresist then removed leaving platinum only in the desired areas. This allows the creation of gauges of an arbitrary layout, with robust connecting track which can be safely bent around narrow radii. Gauges are calibrated using an automated water bath calibration rig created by Collins and Povey [32]. This steps through several temperatures, uses thermocouples to detect when the work-piece has become isothermal, and measures the resistance of each gauge once isothermal conditions have been reached. This produces a family of curves for each gauge giving their resistance-temperature relationship. These are highly linear and so can be fully characterised only by their gradient and intercepts [32].

A common method of converting surface temperature to heat flux is by using the impulse response method of Oldfield [35]. An assumption of one-dimensional conduction into a semi-infinite substrate is made. The impulse response method makes use of the fact that the response of any linear time invariant system can be characterised fully by its impulse response: $q(t) = T(t) * h(t)$, where $h(t)$ is the impulse response, h (t) may be found by deconvolving any known pair of T - q histories. In general this T - q pair may be found analytically, experimentally, or numerically with finite elements. The analytical solution of the response of a 1-d, semi-infinite substrate to a step in surface heat flux is normally used, which is a parabolically increasing temperature. T is measured in the experiment, and q is calculated by the convolution of this signal with the impulse response. The details of an actual

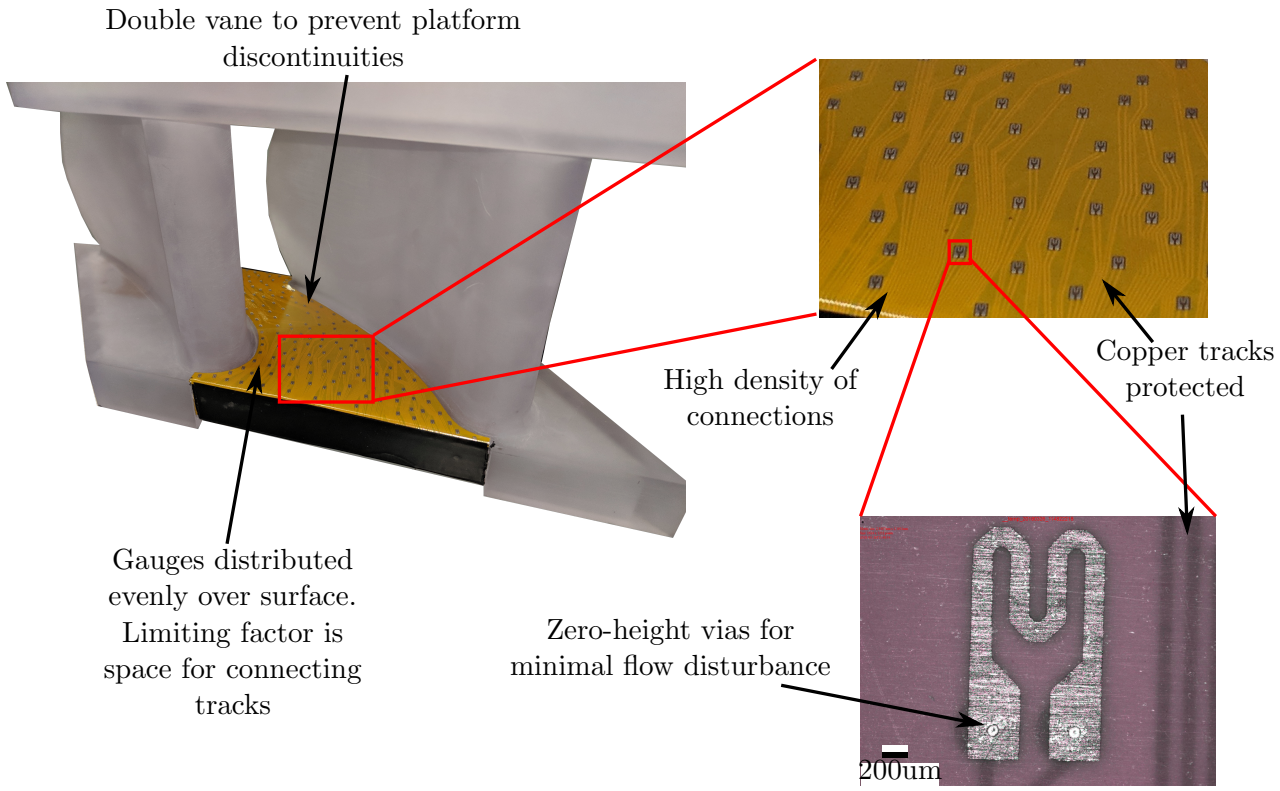


Figure 2.7: New gauge design using zero-height vias demonstrated with high-resolution endwall study. 192 gauges were placed on an endwall, with space for the connecting tracks being limiting factor.

implementation of this method in MATLAB is given by Oldfield [36].

Other techniques have recently been developed by Bertolazzi et al. [37] with alleged superior properties, but there is very little published validation of these methods or use with experimental data other than that provided in their own paper.

Other than the basic design of a thin film gauge, more complicated variants are used by some groups. Fralick et al. [38] developed a method of arranging four gauges in a Wheatstone bridge, with two of them covered by an additional thermal resistance, in order to increase the magnitude of the output signal. However, this technique then leads to the gauges only being usable above a certain frequency, and requires significant extra manufacturing and data processing.

Zribi et al. [39] have designed a process for the fabrication of individual double sided thin film sensors, each mounted on a small square of borosilicate glass. These sensors have an absolute uncertainty on temperature determination of 0.14K.

2.4.2 Development of high density thin film gauges on flexible substrate

There have been many advancements in electronics manufacturing over the years, and multi-layer flexible circuits can routinely be fabricated commercially. This gives an opportunity to increase the density and reliability of thin film gauges. In many applications, the limiting factor of number of gauges which

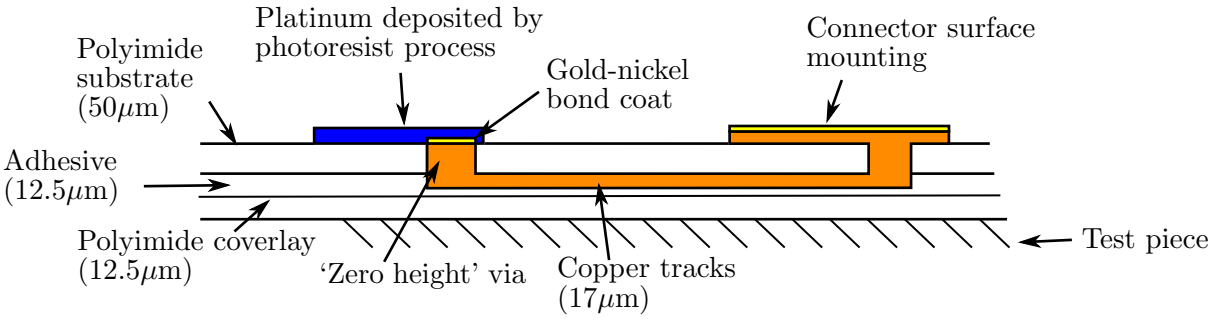


Figure 2.8: New gauges with connections made through zero height through hole vias. Copper connecting tracks are protected by polyimide on both sides, allowing smaller track and gap widths, down to 100μm

can be deployed is the ability to make connections. For example, figure 2.7 shows the instrumented endwall of a NGV, showing most of the available area covered by connecting tracks. Copper tracks can be manufactured with a 100μm track and gap width, but this can lead to unreliability when used in a lab environment, as tracks can be damaged, or short-circuited by small pieces of dust and debris, and when a fault is suspected the tracks are too small to allow unaided visual inspection. By covering the tracks with a layer of polyimide, they are protected from damage and contamination, and reliability is increased. This protective layer of polyimide is known as a coverlay. This in turn allows smaller track sizes to be used with confidence. Extensive automated quality control by a mature commercial manufacturer ensures that there are no pre-existing faults before the protective coverlay is applied.

An initial attempt to make use of this technology used apertures cut into the coverlay to deposit the gauges into, as shown in figure 2.6. This achieved the aims in terms of improved reliability gage density and reliability, but the presence of cut apertures was shown to affect the local heat transfer coefficients around the gauges by disrupting the boundary layer. Figure 2.6 shows this affect by looking at a vane using an IR camera to measure HTC. The apertures are visible as areas of higher HTC.

A second generation of gauges used so-called 'zero height vias' to connect from copper tracks sandwiched between two layers of polyimide, to platinum gauges on the top surface. A 'via' is a drilled hole though one or more layers in the flex circuit, which is then filled with copper to create connections between different layers. Zero height vias cause much less of a discontinuity in surface height (though not zero, despite the name), so less modification to the boundary layer and surface HTC. A gauge manufactured with this method is shown in figure 2.8.

2.4.3 Accuracy and operation of thin film gauges

Maximum signal to noise ratio possible

The sensitivity of thin film gauges is governed by the signal to noise ratio of the measurements. As measured, noise had an RMS level of $10.5\mu V_{rms}$, which corresponded to a noise level in T of $0.04\mathrm{K}_{\mathrm{rms}}$. This is a great improvement over previous use of TFG in this facility and has been made possible by a series of improvements in manufacturing, experimental procedure and data acquisition techniques.

This noise has three main contributions: electro-magnetic interference from the surrounding, noise generated within the signal processing equipment itself (including ADC discretisation noise), and the intrinsic Johnson-Nyquist thermal noise generated by the thin film resistive element itself. Interference has been minimised by using shielded, twisted pair cables from the test piece to the signal processing equipment.

The noise generated by the signal processing equipment is the largest contributor. Data acquisition is performed using National instruments PXIe-4330 bridge input modules, which are a great improvement over previous data acquisition systems, and appear to be current state of the art. This contribution to noise cannot currently be reduced further, as far as commercial solutions are concerned at least.

However, the signal to noise ratio can still be reduced by increasing gauge resistance, which will increase the absolute value of the temperature signal, while noise will remain constant. Johnson-Nyquist noise is generated by the motion of charge carriers in a resistive element, and is therefore inevitable and unavoidable and provides a hard limit on SNR (for a given gauge power dissipation and operating temperature). It currently only contributes 2% of noise so a 50-fold further improvement in sensitivity is in theory possible before this limit is reached.

Maximum sensitivity

The easiest way to increase sensitivity of TFG is to increase the power supplied to the gauges. However, high powers supplied to the gauges result in gauge self-heating. This means that the measured temperature is not the same as the surface temperature would be without the gauges. This is especially detrimental in transient facilitates, as starting the flow results in a rapid change to HTC, so causing the gauges to change temperature independently of any temperature differences between the fluid and the substrate. Generally, an excitation power is used such that the gauge self-heating is kept below 1K.

$$V_s = \sqrt{P}\sqrt{R}a\Delta T \tag{2.1}$$

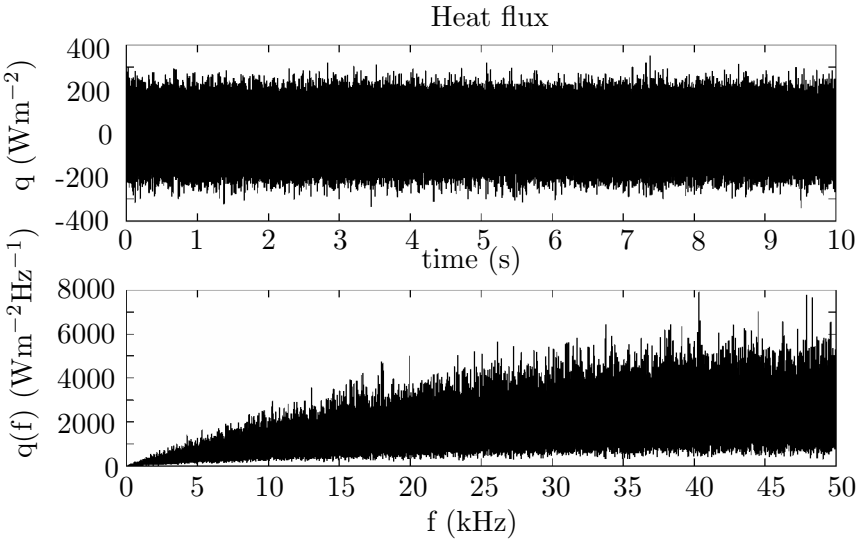


Figure 2.9: Simulated best case noise in ideal case. White noise in temperature signal is amplified in heat flux signal for higher frequencies

$$V_n = V_{\mathrm{JN}} + V_{\mathrm{DAQ}} \tag{2.2}$$

$$V_{\mathrm{JN}} = \sqrt{4k_B T R \Delta f} \tag{2.3}$$

$$\mathrm{SNR} = \frac{V_s}{V_n} = A\left[\frac{1}{1 + B/\sqrt{R}}\right] \tag{2.4}$$

$$A = \frac{\sqrt{P}a\Delta T}{\sqrt{4k_B T \Delta f}} \tag{2.5}$$

$$B = \frac{V_{\mathrm{DAQ}}}{\sqrt{4k_B T \Delta f}} \tag{2.6}$$

Since A and B are mostly fixed by experimental conditions and the data acquisition systems available, the only remaining way to increase SNR is to use gauges of higher resistance. This will continue to give improvements to sensitivity until the limit $B/\sqrt{R} \ll 1$, when the maximum sensitivity is reached of:

$$\mathrm{SNR}_{\mathrm{max}} = \frac{\sqrt{P}a\Delta T}{\sqrt{4k_B T \Delta f}} \tag{2.7}$$

In temperature noise levels are equal at every frequency (white noise). When transformed to heat flux however, the higher frequencies are amplified more than the lower frequencies, as shown in figure 2.9. SNR can also be increased by increasing gauge excitation power, or by using a material with a higher temperature coefficient of resistivity, α.

An attempt was made to manufacture a new generation of high-resistance gauges, which would have higher SNR without increasing gauge footprint. A resistance of 1000Ω was targeted, compared to typical gauge resistance of 50Ω, therefore giving a 4.5 times improvement to SNR. A highly serpentine gauge was designed with 25μm platinum tracks, with 100μm gaps. While there was some success with

test samples, manufacturing at this scale was found to be too unreliable, and gauges with this fine detail were extremely susceptible to damage. It is hoped that in future more careful manufacturing could allow these high sensitivity gauges to be fabricated more reliably.

Absolute accuracy and calibration

While the previous section shows the high sensitivity which can be achieved with thin film gauges, the absolute accuracy is dependent on the quality of the calibration, and is also subject to drift over time so gauges must be regularly re-calibrated. Differences in connector resistance between calibration facilities and experiments give additional offset errors. An ideal calibration for absolute accuracy of temperature measurement would therefore be repeated before and after experiments, to check for drift, and take place in situ using the same equipment, to remove the effect of connector resistances. This is usually not practical, so methods to reduce the dependence on calibration are desirable. For many purposes, it is possible to entirely remove the need for calibration, for both calculations of time averaged and unsteady HTC, and cooling effectiveness.

Given a linear error in calibration, such that T is measured as T'

$$q(t) = h(t) * T(t) \tag{2.8}$$

$$T'(t) = aT(t) + b \tag{2.9}$$

$$q'(t) = h(t) * T'(t) = h(t) * (aT(t) + b) = aq(t) + b \tag{2.10}$$

$$\mathrm{HTC}' = \frac{\Delta q'}{\Delta T'} = \frac{a\Delta q}{a\Delta T} = \frac{\Delta q}{\Delta T} = \mathrm{HTC} \tag{2.11}$$

This also applies to unsteady HTC.

Depending on the procedure for calculating it in a given facility, it may also be possible to remove the effects of mis-calibration in calculation of cooling effectiveness. In the Oxford MHI high speed linear cascade, heat transfer measurements are taken on a transient basis with a heater mesh providing two different mainstream flow temperatures. For each mainstream flow temperature an adiabatic wall temperature can be measured, both with and without cooling. A cooling effectiveness can then be calculated as:

$$\eta = 1 - \frac{T_{awc1} - T_{awc2}}{T_{awu1} - T_{awu2}} \tag{2.12}$$

This relies on the ability to repeatably create the same change in mainstream temperature however. If the mainstream temperature is measured accurately, this can be additionally corrected for variation

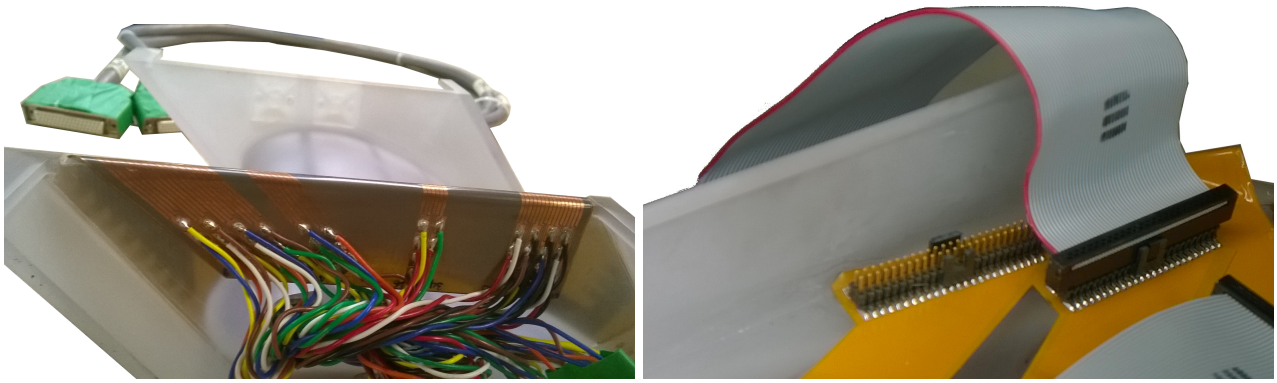


Figure 2.10: Left: connection using soldered connection to 50-pin cables. Right: push fit ribbon cable connectors allow greater density of connections and easier manufacturing.

in test conditions between runs:

$$\eta = 1 - \frac{T_{awc1} - T_{awc2}}{T_{awu1} - T_{awu2}} \cdot \frac{T_{fu1} - T_{fu2}}{T_{fc1} - T_{fc2}} \tag{2.13}$$

Connector development

Initially, gauges were each individually soldered using varnished wire to BNC connectors which connected to a co-axial cable. Co-axial cable does not in fact provide shielding in this application, as the outer sheath is being used as a current carrying element. This soldering process was extremely slow and difficult technical task, involving soldering under a microscope sometimes 100s of individual wires, as such it was the main bottleneck in gauge manufacture. These soldered connections also caused disturbance to the flow if they were made in a flow path. The need to connect and disconnect 10s or 100s of individual connectors, and verify each of these connections, each time a test was to be performed also severely impacted test turnaround time.

Directly soldering the wires to a 50-pin connector reduced the cable count by 25 times, so improving test turnaround time hugely. The need to make the soldered connections was still a bottleneck in manufacturing however. Making an integrated flex-circuit connector, in which the same polyimide sheet on which the gauges are formed also forms a flex connector, which can be connected to a cable some distance from the test article. This was partially successful, and several experimental campaigns were carried out using this method. Manufacturing times were hugely improved by this method, and it was sometimes possible to carry out the whole process of design-test in 1 week.

However, in the environment of a high speed wind tunnel, and repeated testing in different configurations, these connectors all eventually underwent mechanical failure by low-cycle fatigue. Attempts to add further reinforcement only accelerated this process by causing stress concentrations at the interface of the reinforced parts.

The final solution, which has been highly successful, is to use push-fit connectors surface mounted onto the test article connecting to ribbon cables which allow flexibility in rig set-up, before connecting to twisted pair cables to the DAQ. This is shown in figure 2.10.

2.4.4 Post-processing of thin film gauge data

Time averaged heat transfer coefficients (HTC) have been calculated using a transient technique of measuring surface temperature in response to a fast rise in freestream temperature created by an upstream heater mesh. This can provide an increase in temperature of approximately 30K. Unlike some other transient methods, there is no requirement for the rise in freestream temperature to be a perfect step, only for it to be known.

Heat flux has been calculated using the Oldfield technique [36]. Surface temperature is measured and using the assumptions of isothermal initial conditions and a semi-infinite substrate, time-history of heat flux can be calculated. The theory behind this method is briefly given below:

The data which is measured with thin films is surface temperature as a function of time. Heat flux cannot be measured directly, but using some knowledge of the body on which the surface temperature is measured, it can be calculated from temperature history.

Heat conduction in a solid is governed by Fourier's law of conduction. In 1-d this is:

$$q = \rho c \frac{dT}{dt} = k \frac{dT^2}{dx^2} \tag{2.14}$$

This is a linear, time invariant system, so for example:

$$T(q_1 + q_2) = T(q_1) + T(q_2) \tag{2.15}$$

and

$$\text{if } \; T(q_1(t)) = T_1(t) \text{then } \; T(q_1(t+\tau)) = T_1(t+\tau) \tag{2.16}$$

The fact that it is linear and time invariant means that the techniques of impulse response processing are applicable.

$$q(t) = \int q(t) \times \delta(t-\tau) d\tau \tag{2.17}$$

$$T(t) = f(q(t)) \tag{2.18}$$

$$f(q(t)) = \int q(t) \times f(\delta(t-\tau)) d\tau \tag{2.19}$$

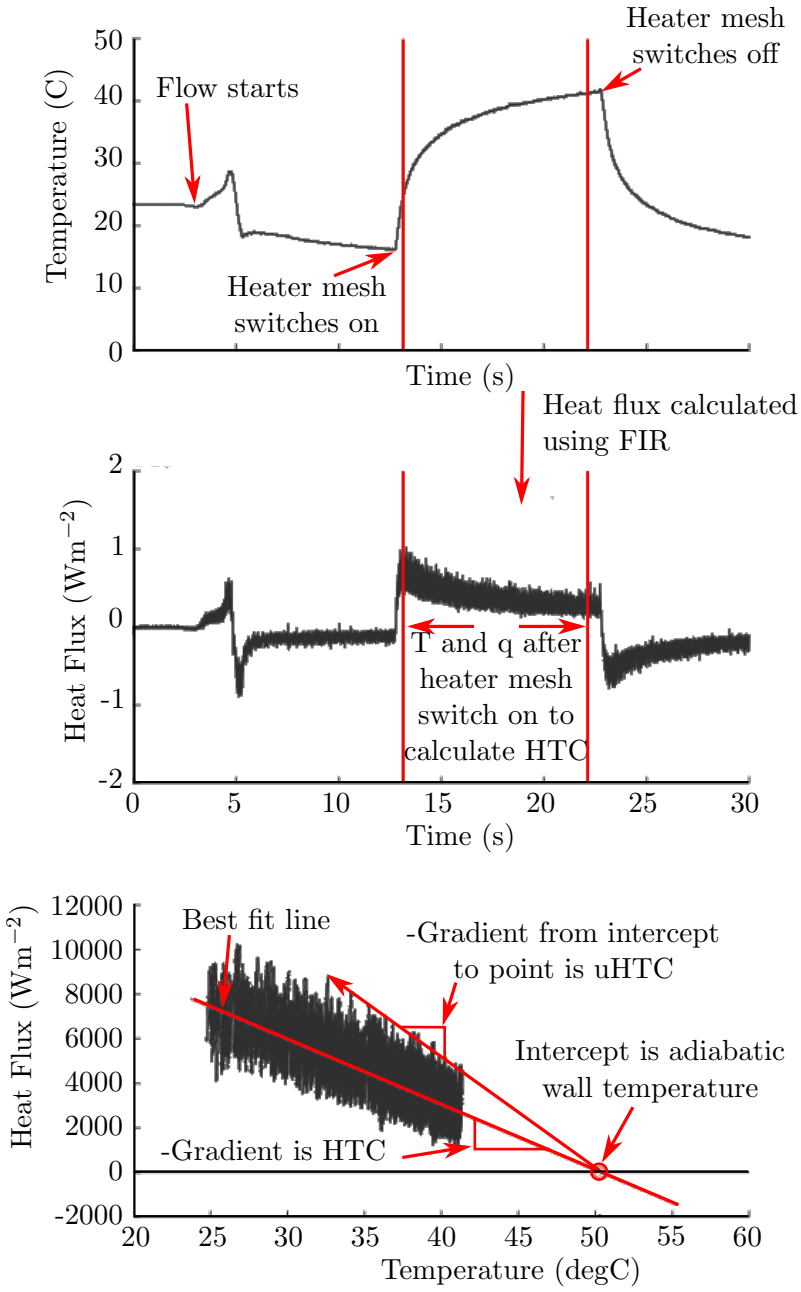


Figure 2.11: Illustration of post-processing procedure to convert measured surface temperature into heat flux, HTC and adiabatic wall temperature. Top: raw temperature as measured, middle: heat flux calculated using Oldfield method, bottom: linear regression of heat flux against temperature to give HTC and adiabatic temperature

Define $h(t) = f(\delta(t))$, called the impulse response function. Then:

$$T(t) = \int q(t) \times h(t - \tau) d\tau \tag{2.20}$$

$$T(t) = q(t) * h(t) \tag{2.21}$$

$h(t)$ is a function only of the body in which the conduction is taking place. $h(t)$ can be found from any matching pair of $T(t)$ and $q(t)$. In general, this could be an analytical solution, an experimentally measured temperature response to known imposed heat flux, or a numerical solution by finite elements. In this case, the analytical solution to a step change in surface heat flux onto a one-dimensional semi-infinite body was used. This gives the solution of a parabolicly increasing temperature for a constant heat flux applied at time $t = 0$. The solution is deconvolved to give a finite impulse response function of the same sampling speed and length as the measured temperature signal. This is then convolved numerically with the measured temperature to give surface heat flux.

A set of MATLAB functions have been written to process large datasets simultaneously.

The test pieces are constructed out of SLA resin. This has a low enough conductivity that the semi-infinite assumption is valid for the 10s required to take measurements of the heat flux. Penetration depth can be calculated as $d = 4\sqrt{\alpha t}$ [40].

Heat transfer coefficient

HTC is then calculated using a transient method of calculating a linear regression between heat flux and temperature. This is illustrated in Figure 2.11. An unsteady HTC (uHTC) has also been defined shown below. That is to say, it is the negative of the gradient of the line drawn between any point on the $q - T$ graph and the adiabatic temperature intercept.

$$\text{uhtc}(t) = \frac{q(t)}{T(t) - T_{\text{adiabatic}}} \tag{2.22}$$

The advantage of using an unsteady heat transfer coefficient as defined above is firstly that it does not change as the run progresses, as heat flux does, since heat flux will begin high, and become lower in magnitude as the wall temperature approaches the adiabatic temperature. Secondly, the unsteady heat transfer coefficient is not affected by linear calibration errors, as shown in equation 2.11. This is in contrast to heat flux, which must be carefully calibrated if it is to be accurate.

Since the calculation of HTC by regression uses a great number of sample points, this gives a high accuracy of HTC calculation. The 95% confidence interval of the calculate HTC was found to be within $\pm 0.5\%$ or less for all gauges. A greater uncertainty in the calculated value of HTC is the uncertainty in

the thermal product of the substrate. The thermal product of polyimide was measured by Piccini [41], with an estimated uncertainty of ±4.2%. Any error in this value would be a systematic error affecting all gauges equally, so while changing absolute values of measured HTC, qualitative comparisons would not be affected.

One potential issue of calculating unsteady heat flux in this way is that it is very difficult to separate the effect of changing HTC from that of changing driving temperature. Since the unsteady data is stochastic, there is no way to confirm with certainty whether any given heat flux event is caused by a change in HTC, or a change in driving temperature. A brief investigation of this issue is reported in section 5.2, with the conclusion that most unsteadiness is indeed caused by unsteady HTC, so that use of equation 2.22 is justified. This might not always be the case in other situations however.

2.4.5 Experimental campaign in gas turbine linear cascade

Several campaigns have been carried out successfully in the MHI linear cascade using thin film gauges, demonstrating the improvements developed.

An endwall has been instrumented with 192 thin film gauges, which as far as is known is by some margin the most detailed measurement of an engine realistic endwall with this technique. The endwall instrumentation is shown in figure 2.7. Another vane has also been fabricated instrumented with 192 thin film gauges placed regularly spaced over the vane pressure surface, leading edge and suction surface, as shown in figure 2.12. The limiting factor in the number of gauges used in this case is the available data acquisition system. Since the intention was to observe large unsteady structures on the vane surfaces, it was decided that at least half the vane should be measured in synchonicity. 96 gauges may be measured simultaneously, due to data acquisition limits so it was decided to have 96 gauges spread over the pressure side, and another 96 on the suction side.

Heat flux was measured at a frequency of 10 kHz. Higher frequencies up to 100 kHz were initially used, but it was found that there was little frequency content above 5 kHz. This high resolution both temporally and spatially allows for detailed study, and visualisation, of unsteady flow structures in time over the endwall and vane surfaces; as well as the overall time averaged levels of HTC.

It was decided to space gauges evenly over the surface of the vane, and of the endwall rather than pre-empt where areas of interest were expected to be and concentrate gauges only in those areas. Using this approach means that data for the large structures over the entire vane have been able to be seen. However, more localised structures such as passage vortex lift-off, or details of the leading edge, are not well-resolved with sufficient spatial resolution; specialist vanes concentrating only on

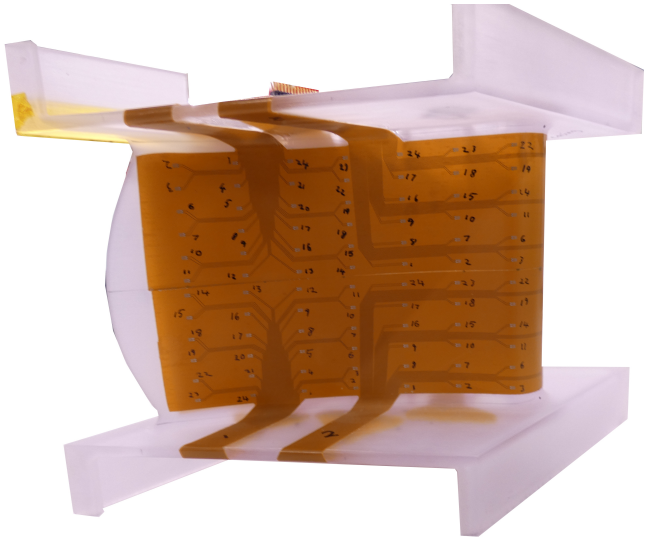


Figure 2.12: Thin film gauges instrumented on vane surface

these areas would be necessary for this.

A challenge associated with instrumenting a curved surface such as the vane surface is that it is in theory impossible without stretching to conform a flat sheet to a surface which curves in two dimensions. To mitigate this, the gauges were fabricated over four different sheets, which could then be glued to the vane separately. A Solidworks tool was used to calculate the amount of stretching which would be required to conform the flat sheet to a curved surface, to confirm that the design was acceptable. It was necessary to make some small cuts in the flex substrate in places, which introduced steps in the surface of up to 75μm. The effect of these surface steps can be seen in figure 3.2, as the spurious areas of high and low HTC. Although time-averaged HTC is affected by this, instantaneous variation in HTC does not seem to be highly affected. The only other methods of overcoming this problem would have been to use a different, 2d, vane geometry, or to use a thinner gauge substrate material, which has more compliance.

Additionally, high density TFG on the vane endwall allowed more comprehensive measurements than had been previously possible. Whereas in the past in this facility, IR camera measurements were limited in their viewpoint so not all of the endwall could be measured, thin film gauges allowed a full surface coverage regardless of any need for optical access. This advantage is balanced against the lower spatial resolution possible with discrete gauges compared to a full surface map however. In the case of vane endwall measurements, the spatial resolution seemed to be sufficient, and high speed IR imagery revealed no more significant flow structures which were too small or localised to have been measured using TFG coverage.

Thin film gauges were also used to take measurements of a region where no optical access et all was possible. The interior of mid-passage and downstream slits were instrumented with TFG and

HTC measurements taken, for the first time as far as is known. This revealed a flow field and pattern of HTC which had not been investigated in any detail before. A reasonably high level of detail was possible, and it was possible to instrument this area without causing excessive disturbance to the surface.

2.5 Unsteady pressure transducers

Unsteady surface pressure measurements can also help with physical understanding of the flow field, and validation of unsteady CFD, although it is of less direct interest to designers than heat transfer. Ainsworth et al. [42] give an overview of the state of the art in piezoresistive pressure sensors. It is usual for e.g. a Kulite sensor to be secured flush with the surface to be measured. Bandwidths of up to 500 kHz can be achieved, manufacturing is complex and expensive however.

There is often a need to measure time-varying surface static pressure. However, most measurement techniques suffer from both low spatial resolution and an extremely high cost. High spatial resolution techniques such as using pressure sensitive paint operate at extremely low frequencies. On the other hand, high temporal resolution pressure sensors become extremely expensive when used in large numbers, and require specialist fabrication to be attached to the test pieces.

For use in this rig, an intermediate solution was required. A moderately high measurement frequency up to around 2000Hz was aimed for, with as high a spatial resolution as practicable.

2.5.1 Unsteady pressure measurement techniques

There are three main techniques commonly used for surface static pressure measurements. The first is the use of a pressure sensitive paint (PSP), this allows a high spatial resolution of measurements, but can be used only at a low frequency. Secondly, surface pressure tappings may connect to a separate pressure sensing apparatus. This is used extensively in this rig for steady state pressure measurement. However, this is again only possible for the lowest frequencies, as the pressure waves are damped out over the length of tubing connecting the tappings to the sensing equipment. The third method is to have pressure sensors in place as part of the test item. The sensor may be mounted flush with the surface, which allows very high frequencies to be measured, limited only by the natural frequency of the sensing element.

2.5.2 Low cost pressure transducers

In this application, a higher frequency than was possible with pressure sensitive paint or remote sensing was required, but the high cost of these sensors would have limited the spatial resolution to a handful

of measurement points, and the highest frequencies of a flush-mounted sensor were not necessary.

By compromising between these techniques slightly, it was possible to use an array of 48 low cost pressure transducers placed inside the test piece, but instead of being flush mounted had a sufficiently small length communicating with the surface that frequencies up to 2000Hz could be measured.

Honeywell NBP series of pressure transducers were chosen, as they were found to respond in the required frequency range, compared to a range of alternatives.

2.5.3 Natural frequency of cavity

The limiting natural frequency of the sensing element is the natural frequency of the tube communicating with the sensor, and the internal cavity within the transducer. The natural frequency of the silicon sensing element itself was expected to be extremely high, and not an issue.

The resonant frequency of a long tube closed at one end, which is a appropriate model for a pressure tapping connected by a tube to a sensor, is given by:

$$f = \frac{n\mathbf{c}}{4L} \tag{2.23}$$

Where $n = 1, 3, 5...$ etc. and c is the speed of sound. In order to measure frequencies up to 1500Hz, the resonant frequency should be a minimum three times this, 4500Hz, in order to guarantee a flat frequency response. Using equation 2.23, this gives a maximum tubing length of 19mm. This is far insufficient to use any kind of remote sensors away from the test piece, so that the pressure sensors must be integrated into the test piece itself.

A second resonant frequency equation applies to an internal volume communicating through a tube.

$$f = \frac{\mathbf{c}}{2\pi}\sqrt{\frac{A}{VL}} \tag{2.24}$$

This contains three parameters which can each easily vary independently by orders of magnitude, making it difficult to make generalised estimates. For specific cases though, the resonant frequency can be calculated. Figure 2.13 illustrates the calculation of resonant frequency for the design chosen. Using equation 2.24 gives a natural frequency of 4800Hz, which is sufficient for the purpose.

2.5.4 Fabrication of test piece

A test vane was fabricated in two sections using SLA. Cavities to receive the pressure sensors were printed into the test piece, with a good distribution over the surface. Small tappings connected the pressure sensing elements to the surface of the vane. These tappings were first printed in, then drilled

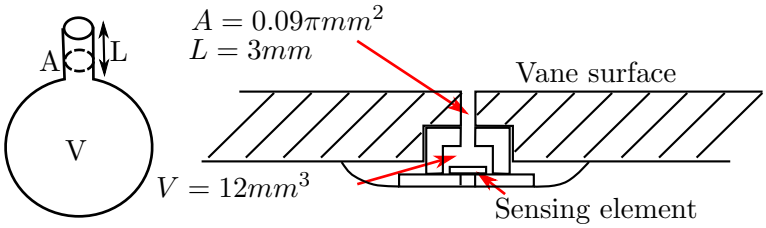
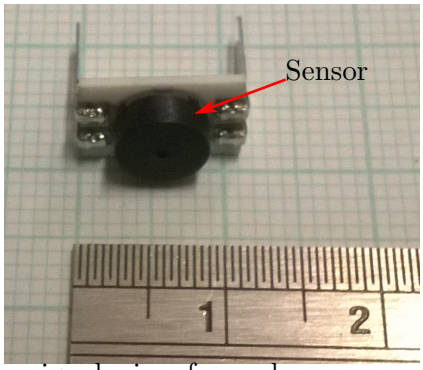
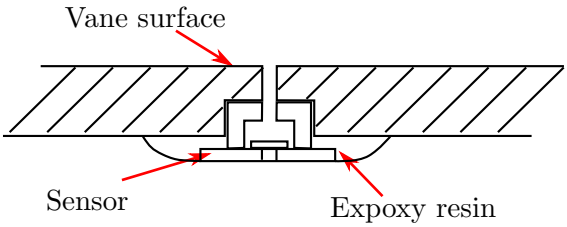


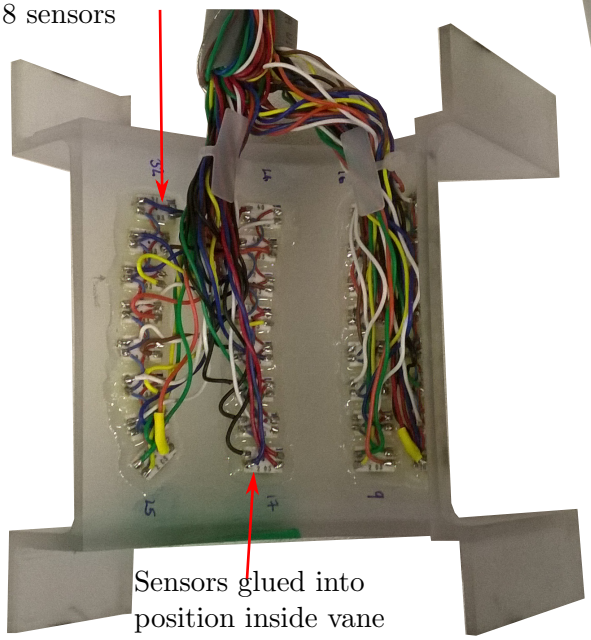
Figure 2.13: Approximation of sensor as internal volume with narrow tube allows calculation of resonant frequency



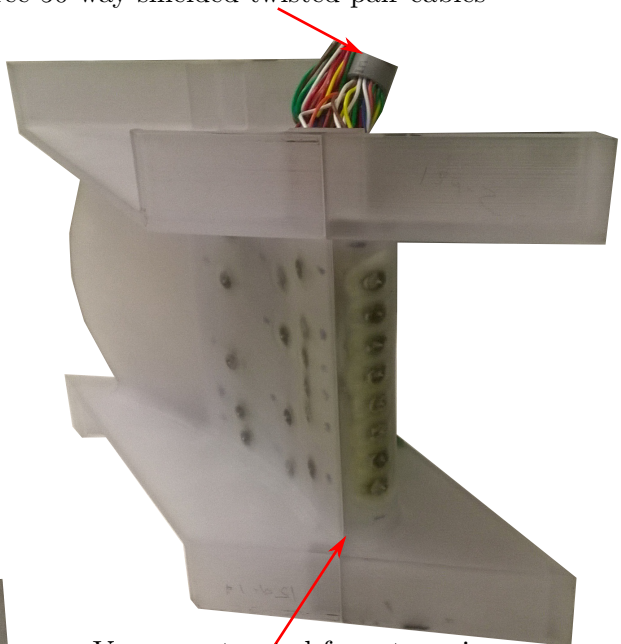


Excitation and signal connected through three 50-way shielded twisted pair cables

Two signal wires for each sensors. Excitation shared in parallel between 8 sensors



Sensors glued into position inside vane



Vane constructed from two pieces bonded together

Figure 2.14: Construction of vane with 48 unsteady pressure measurement points. Pressure sensors are secured inside a two part vane which was then bonded together. The length from the surface tapping to the sensing element is small enough to give a sufficient frequency response.

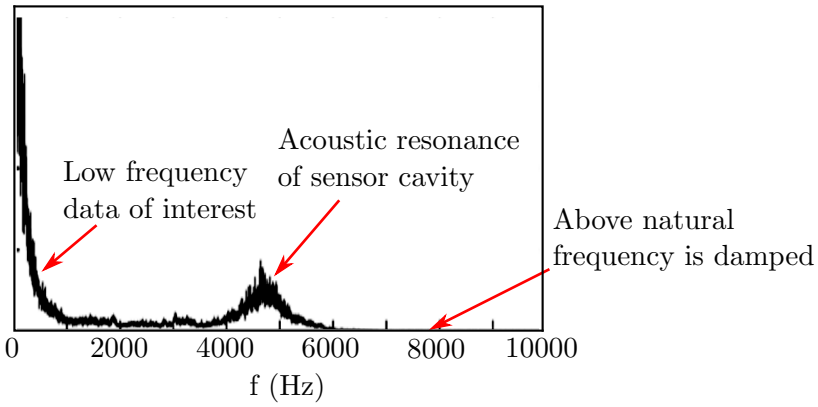


Figure 2.15: Example spectral plot of measured pressure. The natural frequency of the cavity is as predicted, but low in amplitude so that there is no danger of saturation.

through to give a consistent size. Sensors were attached in place with epoxy resin, and fully sealed around the edges. The sensors had soldered leads connected before being glued into place. Once all sensors were in place, the two halves of the vane were connected together and sealed. The internal cavity of the vane was fully sealed with epoxy resin. A static pressure tapping was included so that the internal cavity pressure could be measured, and set to a value. The construction of the test vane is shown in figure 2.14.

Signal connections to the sensors were made using three 50-way twisted pair cables. Each cable supported 16 pressure transducers. The two measurement points for each sensor were connected to a single twisted pair. The excitation points of the sensors were connected in parallel in groups of eight to a single twisted pair. Excitation was provided by the NI controller, which provided a clean power source to prevent added electrical noise. The cable shield drain was likewise connected to the same ground as the shield of the NI DAQ. With these precautions, electrical noise was reduced to negligible levels.

2.5.5 Data acquisition and processing

Data acquisition was carried out using three general purpose National instruments PXIe-6363 data acquisition cards. The sampling rate was in excess of the natural frequency of the gauges, which gives confidence that there is margin for downsampling to ensure there is no frequency aliasing.

The sensors measure gauge pressure, so that measured pressure is relative to downstream plenum static pressure. The data was normalised to the time averaged pressure. This means that linear errors in calibration are cancelled in the non-dimensional results which are presented. The accuracy based on the manufacturer's data is $\pm 0.25\%$. Electrical noise and other data acquisition noise was found to be negligible compared to signal levels.

Figure 2.15 shows a typical frequency spectra produced by the sensor from a test run. The natural frequency is clear as a resonant peak, with all higher frequencies damped out. The data of interest is the lower frequency data, below 2000Hz, which should be transmitted through the acoustic system and measured accurately.

2.5.6 Experimental measurement campaign

The vane and associated data acquisition system was robust and reliable, and measurements could be rapidly taken for all different inlet conditions and vane positions. Measurements showed the intense unsteadiness in the NGV area, often thought of as a steady state area. Various results are analysed in detail in section 4.3.2

The use of these sensors in this way was considered highly successful, and would certainly be recommended for use in future campaigns in this facility, and elsewhere provided the required frequency range is similar.

2.6 Data acquisition and analysis

When conducting experimental campaigns, it is common to spend as long or longer on data processing, analysis and presentation as on the design and running of the experiments themselves. It has been described how experimental methods have been streamlined so that a campaign of measurements on a novel geometry may be conducted from conception to execution in a matter of weeks. However, processing, analysis and interpretation of these results may take this time again or longer. Therefore there is a great advantage in automating these tasks to the greatest extend possible.

Three main software packages are used for data acquisition and analysis of experimental results. Labview is used first for acquisition of the raw data from the data acquisition hardware. Matlab is then used as the main programme for data processing, as well as calculating comparisons between cases, and production of plots and graphs. Paraview is used finally for examination and plotting of 3D and time-varying datasets.

The general sequence of processing used is shown in figure 2.16. For most of the common experimental methods used, this process is now almost fully automated, from acquiring and processing the measurement data to the generation of 3D surface plots and animations.

2.6.1 Labview integrated data acquasition

A Labview integrated data acquisition script was written, with the aim of simultaneously measuring all required flow quantities. This ensures that all measured quantities are synchronised, although they

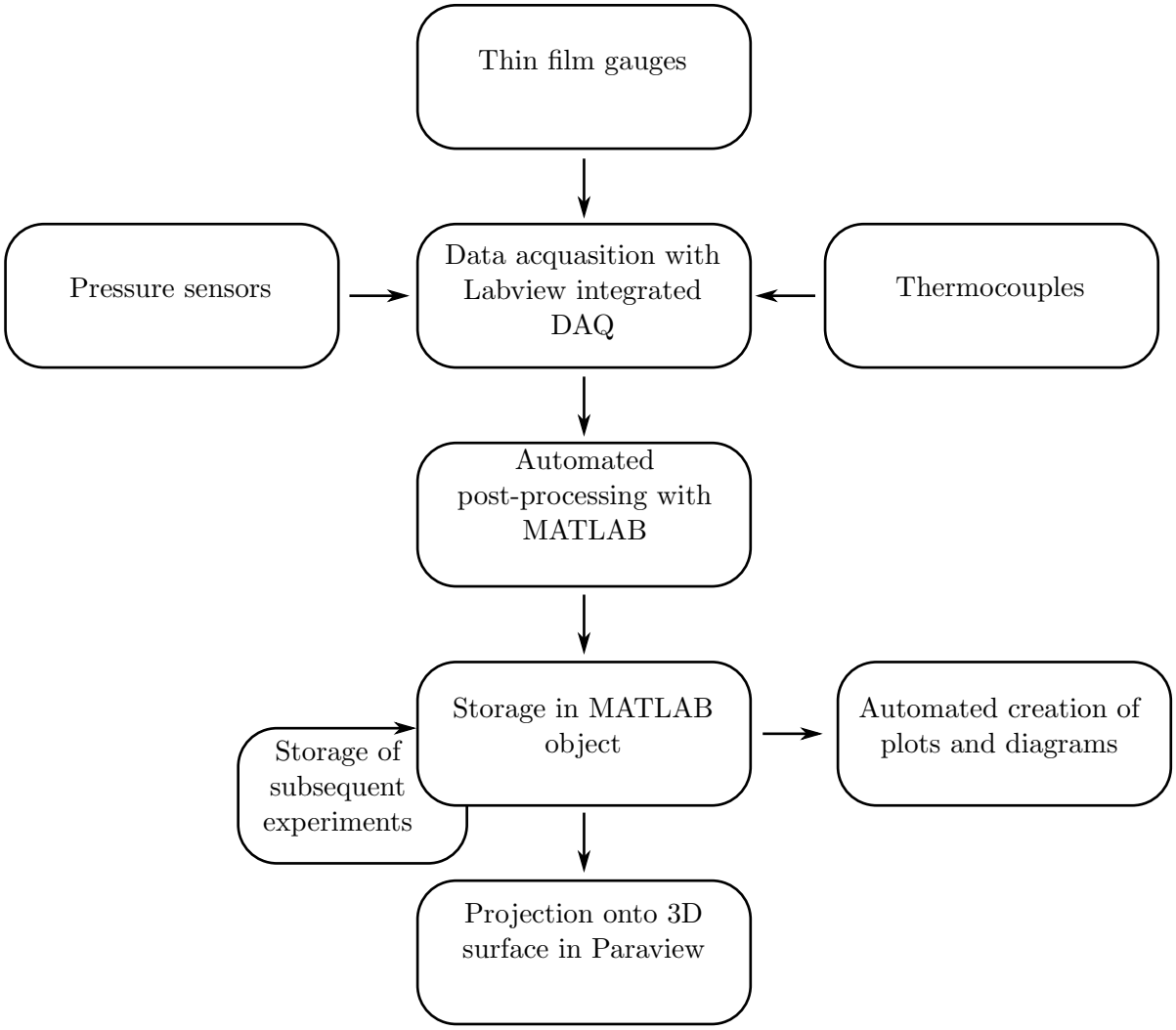


Figure 2.16: Sequence of measurement processing with automated DAQ

come from different data acquisition devices, such as thermocouples, pressure sensors and thin film gauges. Integrating these measurements within one piece of software ensures that all data that may be required is available, and is automatically arranged in a rational file structure, thereby streamlining both the experimental run process, and subsequent data analysis.

2.6.2 Matlab data manipulation and comparison

Object oriented data analysis and comparison

Object-oriented programming in Matlab has been used to create interactive datasets including measurements over many different cases, which can then be compared automatically. Object-oriented MATLAB classes have been created to both store and process experimental data. The object-oriented programming paradigm is that data and the associated methods, containing the manipulations and processing which are likely to be applied to it, should be organised together in 'objects'. In some cases this paradigm has advantages over a traditional functional programming style. When a script which performs some particular manipulations upon a dataset which is too specific to conceivably be applied to any other type of dataset, it is logical to be intimately associated with that dataset rather than stand-alone.

Functional programming has been used for all 'lower level' processing, such as conversion of raw temperature data into heat flux and heat transfer coefficients. Object-oriented programming is used for production of plots and output.

For example, a thin film gauge dataset object contains the experimental data for several runs, and all of the manipulations which may want to perform. Rather than having to manually retrieve data from different locations and then plot this, the fact that data is stored in a fixed format along with methods allows this process to be done only with interactive pop-up menus.

Traverse point generation

Traverses with a five-hole probe are an essential tool used to measure aerodynamics in this rig. However, it is also one of the most time-consuming measurements to take and this is a major limitation to its use. To maximise the utility of measurements, a MATLAB script was created to automate the generation of measurement points into the optimal configuration. This is based on a hexagonal packing of points. Additionally, since it is often necessary to have higher spatial resolution in an area of interest, but lower resolution over a larger area, an object-oriented MATLAB class was created to automate the filling in of a generated grid with a denser set of points, and also to deal with data acquisition of these points. This increases the utility of the limited number of traverse measurements

which can be taken.

2.6.3 Paraview visualisation

All experimental data, after processing, is projected back onto a 3D CAD model of the test geometry. This greatly assists in visualisation and interpretation of experimental data, and allows side by side comparisons with corresponding CFD data. The projection onto a 3D surface mesh for visualisation is done in Matlab.

A Matlab function has been created to read in a surface mesh previously created from CAD, and to interpolate onto this experimental data given the 3D co-ordinates of sensor positions, again taken from CAD. This is done in the correct format to be read by paraview and displayed. Unsteady data can be displayed similarly, by the interpolation being repeated from each timestep, which can then be read by paraview and be animated as a time-series.

2.7 Tblock flow solver

For CFD the Tblock flow solver created by Denton is used. This is a multiblock structured grid solver created for turbomachinery applications. It has capabilities for turbulence modelling using the mixing length model, or the Spalart-Allmaras model, or LES. Thermal wall functions were implemented into Tblock by Mazzoni [43], and verified against experimental data for HTC prediction.

The Tblock solver was developed by John Denton as a CFD flow solver, specialised for turbomachinery applications. Throughout, the Tblock solver is optimised for speed; some of the features which give this high speed are reviewed.

Tblock is also highly robust to low mesh quality, and extreme cell skewness. Meshes can either be generated by the solver automatically, or can be explicitly input as a list of point co-ordinates. Generally in this project the Ansys ICEM meshing tool was used to generate meshes, which are then converted to the correct format for Tblock by a small Fortran script.

Tblock is written in Fortran 77. All main variables are contained in a shared common block. This helps speed, as variables do not need to be copied to functions and subroutines. It does require some care on the part of editors however, that a variable is not modified when it is needed elsewhere. A modified version of this solver has been used for all CFD presented in this thesis. Several modifications were made to the Tblock solver over the course of this project.

2.7.1 Parallelisation

Tblock-15 was modified to run over many different processors. This allows for faster simulation on a multi-core desktop machine, or allows larger meshes to be used on clusters with distributed memory. Tblock meshes are block based anyway, with each block consisting of a hexahedral structured mesh. In parallel, multiple processes are used, with each process possessing one or more blocks. Each block is solved each timestep exactly as normal, but MPI communication is necessary to communicate periodic boundary conditions between patches, and other information which is needed by other blocks.

2.7.2 Total pressure limiter

Some of the meshes used during this project had a problem with a very small number of cells slowly diverging towards non-physical solutions, even with very low CFL numbers and high residual smoothing. This problem was solver by the addition into Tblock of a total pressure limiter. When total pressure exceeded a given value, input by the user, the density, velocity and energy variables for those cells are reduced by the amount required to lower total pressure below the limit. This process does not satisfy the conservation equations, but it does appear effective in increasing stability when problems are occurring in only a very small number of cells. To minimise impact on speed, this subroutine is only called every 5 timesteps. If no total pressure limit is specified the subroutine is not called, so that there is no impact on speed unless it is being made use of, and existing input files will function with no change.

2.7.3 Non-uniform cooling flows

In order to investigate non-uniform cooling flows in cavities and gaps as a way to efficiently prevent hot gas ingress (see chapters 6 and 7), an option to input spatially varying cooling flow rates was implemented. Cooling flow conditions were calculated using the average conditions over the cooling patch, as in existing versions of Tblock. The local cooling mass flow rate is then scaled as required, with total mass flow rate through the patch matching what is specified. Any number of input points may be specified, and mass flow will be interpolated between them, using Tblock's existing interpolation subroutine.

2.7.4 Large eddy simulation study

An LES study was conducted to support experimental measurements, and provide full flowfield data to help provide understanding of the phenomena observed. The use of Tblock for LES is described in detail by Klostermeier [44].

The LES was carried out using a mesh created by Jacobi [13]. The mesh consists of approximately 120M points in a blocked structured mesh. The near wall mesh was not fully resolved, instead wall functions were used to calculate shear stress and heat flux. This was necessary to allow the full domain to be modelled, as mesh requirements for fully wall resolved LES for a domain of this size would have been prohibitive.

The domain consists of a swirler, can combustion chamber and two nozzle guide vanes, there is a combustor wall separating upstream, while downstream of the vanes is periodic. The flow conditions are those of the experimental linear cascade, this is to allow direct comparisons between the experimental data and LES. The whole of the domain simulated is shown in figure 2.17. Contours of instantaneous pressure deviation are shown, to give an impression of the kinds of large scale flow structures that are formed in the combustion chamber. Flow first passes through a swirler. This imparts a bulk swirl velocity into the flow, but also creates large-scale unsteady structures (analysed in detail in chapter 4). This unsteady flow then is accelerated through the NGV passages, and is exhausted through a non-reflecting pressure boundary condition.

The time varying data was stored, though in order to not take an unacceptable storage space only every fourth mesh point(1/64th of total 3-D mesh points) and every 50th timestep was stored, and only the blocks around the vanes had data stored rather than the whole domain (1/5th of all blocks). This reduced the storage space required for the simulation results by a factor of approximately 16,000, allowing time varying results to be saved for a full three flow-through times (or 30 flow through times through the vane passage), for all flow variables. Pressure and heat flux on solid surfaces was also saved every 50th timestep, for the entire surface mesh. The spatial and time resolution was still acceptable for analysis.

Visualisation of velocity fields was done using the technique of line integral convolution [45], as it is implemented in the Paraview post-processing software.

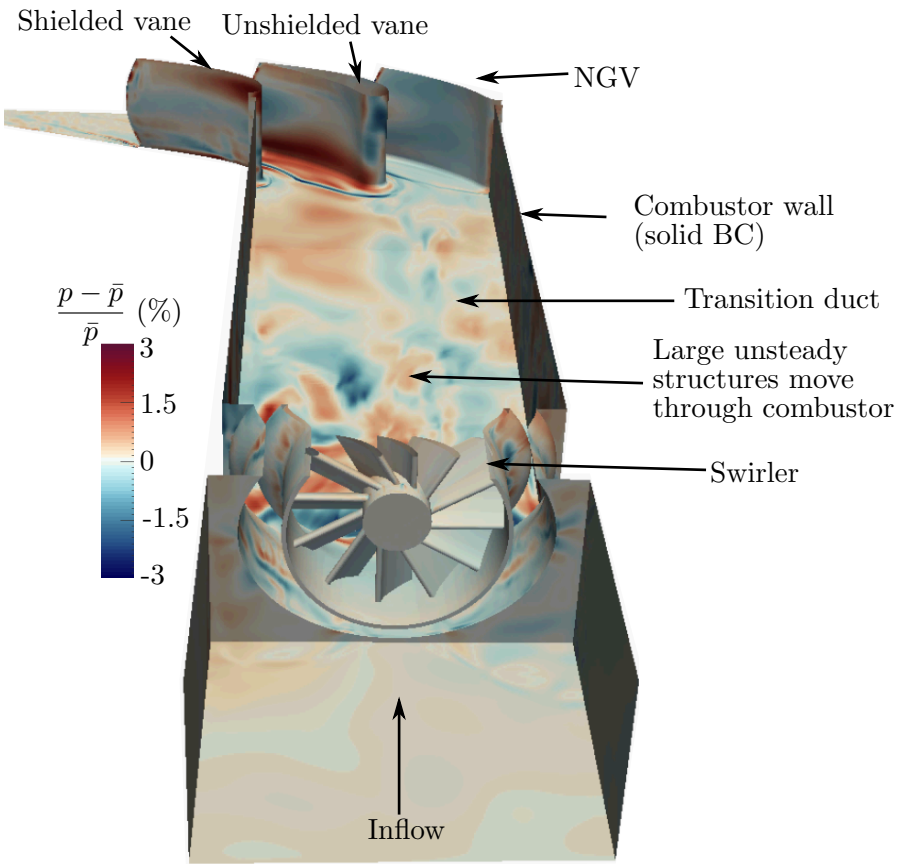


Figure 2.17: Instantaneous surface pressure deviation from time mean throughout domain

Chapter 3

Steady-state combustor turbine interactions

3.1 Introduction and literature review

This chapter describes the time-averaged, steady flow field within the nozzle guide vanes. The method of calculating heat transfer coefficient(HTC) using thin film gauges developed in chapter 2 has been applied to perform high-resolution measurements of a NGV. The influence of various realistic swirling inlet conditions on heat transfer is investigated. It is shown that the swirling inflow can have a significant effect on heat transfer levels. While combustion chambers are normally designed in isolation, with bulk flow properties targeted, the fact that heat transfer in the NGV can be reduced by combustion chamber design suggests that greater optimisation could be achieved by designing combustors and first vanes together.

Large industrial gas turbines operate with fluid temperature far in excess of metal temperatures. This is maintained by continuous internal and external cooling of components. An accurate knowledge of local heat transfer rates can allow optimisation of cooling design, both to keep metal temperatures below acceptable levels and to avoid excessive internal stresses which may reduce component life. Increasingly thick thermal barrier coatings (TBC) lead to the need for even more accurate measurements of local HTC, as reduced conductivity can lead to local spots of high temperature if there is a locally high HTC.

Experimental measurements in cascades remain important to gain data to inform design. An important factor affecting heat transfer in the NGV is the nature of the flow field exiting from the combustor. This has been measured experimentally using thin film gauges. The steady-state results of five different inlet conditions with different combustor models are compared.

In this chapter, steady state flow is considered. A literature review is given of flow through the NGV, and the effects of combustion. Results of the measurement campaign using TFG are then presented for the baseline case of a turbulent but non-swirling inflow. The effects of swirler models simulating the combustion chamber is shown by comparing measurements to the baseline case. It is shown that heat transfer can be improved by using smaller length scales of the swirler. Finally, a phenomena of an additional midspan secondary flow caused by swirl is examined with the aid of a steady state CFD study. Unsteady flow effects are discussed later, in chapter 4.

3.1.1 Flow through nozzle guide vanes

Primary flow

NGV turn and accelerate hot gas from the combustion chamber, converting enthalpy into external kinetic energy which then provides shaft work in the first stage rotor. Fluid is turned through 70 deg, as flow is turned, a narrowing passage area acts as a nozzle and accelerates the flow, to a maximum at the throat. In aero-engines there is normally a maximum Mach number of 1, but this is not necessary in industrial turbines, as there is no strong requirement to minimise size and weight. Beyond the throat there is a diffusion region in which flow decelerates. In this turbine there is a Mach number at the throat of 0.85, and an exit Mach number of 0.65.

Around half of vane aerodynamic loss can be explained in terms of this primary flow [46]. Entropy is generated whenever there is a shear stress in a fluid. Thus skin friction on vane surfaces causes loss, as does the wake behind the trailing edge.

Likewise, the most pertinent features of observed heat transfer distribution are caused by this primary flow. HTC is relatively high on the leading edge of the vane, where flow is impinging. Following the flow downstream over the PS, HTC first decreases as the boundary layer grows, then increases towards the throat due to acceleration of the flow. On the suction side flow rapidly accelerates and reaches a maximum HTC. Over the diffusion region the boundary layer grows and HTC reduces. On the pressure side HTC is reduced compared to the leading edge as the boundary layer grows, while velocity is still low. Flow then accelerates and HTC increases to a maximum near the trailing edge. On the endwall there is again a generally increasing HTC towards the throat, but additionally with a large influence of secondary flows.

3.1.2 Secondary flow

As well as the essentially two dimensional, primary flow field, there are also 3-D flow effects, known as secondary flows. The secondary flows have the greatest effect on the endwall region. These secondary

flows lead both to aerodynamic losses, and increased heat transfer coefficients by stripping away the boundary layers of the endwall and vane surfaces.

A horseshoe vortex is formed whenever flow over a surface encounters a significant protrusion from that surface, in this case a vane protruding from the hub or casing. It is caused by the fact that incoming flow velocities are not radially uniform, but rather are zero at the wall, increasing through the boundary layer to the freestream value. The boundary layer therefore has a vorticity normal to the main flow direction. Just upstream of the leading edge of the vane, flow is brought to stagnation by the vane pressure field. The vorticity from the incoming boundary layer then forms the horseshoe vortex near to the leading edge of the vane. From the leading edge, the two sides of the HV extend around the pressure and suction sides of the vane, the horseshoe like shape giving the usual name of the horseshoe vortex (HV). This ordinary, steady-state explanation is given in standard texts, such as [47]

Secondary flows in turbines is the subject of well known reviews by Sieverding [48] and Langston [49]. Since the boundary layer is in shear it also contains a large amount of vorticity aligned perpendicular to the flow. After turning a large component of this vorticity become aligned with the streamwise direction. From pressure side to suction side there is a cross-passage pressure gradient within the boundary layers. By the endwall velocity is lower than the mainstream and so this fluid is turned even more than the mainstream. The result is a cross-passage migration of boundary layer fluid from pressure side to suction side. As a result the boundary layer thickens near to the suction side, and is thinned near to the pressure side of the endwall. Usually the boundary layer separates under the influence of the adverse pressure gradient, and forms a passage vortex. This is usually also associated with the pressure side leg of the horseshoe vortex created at the leading edge.

Langston concluded that routine prediction of secondary flows has not yet been achieved, and that turbulence models used for industrial RANS modelling of guide vanes are inadequate for accurate predictions of secondary flows. The popular k-epsilon model gives worse results than the simple mixing length. It is suggested that more basic experiments are necessary to study secondary flows, and that CFD can be improved best by following experimental results.

Harrison [50] used hot films, oil drops and detailed five-hole probe measurements to measure endwall shear stresses and secondary flows. Oil flow visualisation shows a clear lift-off line created by the horseshoe vortex/passage vortex on the endwall, and on the blade suction surfaces Based on intermittency of hot film signals the boundary layer behind the horseshoe vortex is shown to be laminar, before it transitions to turbulence again further downstream.

A numerical investigation by Denton and Pullan [51] to find the sources of secondary flow loss

found that loss was not from any single dominant source, but rather that many areas contributed significant amounts of loss. The passage vortex separation line coincides with a line of reduced heat transfer on the endwall.

Gaugler and Russell [52] provided early evidence of the effect of secondary flows on the endwall heat transfer, with a superposition of measured heat transfer data with bubble flow visualisation. As a result of endwall boundary layer thickening near to the suction side, and thinning near to the pressure side of the endwall, there is an increased HTC near to the pressure side and reduced HTC by the suction side.

Simon and Piggush [53] reviewed the literature up to 2006 on turbine secondary flows, and their effect on heat transfer. The distribution of HTC over the endwall is explained in terms of secondary flows, with a wedge shaped area of low HTC in the leading edge where the thick inlet boundary layer exists. Behind this is an area of higher HTC due to the boundary layer having been swept into the horseshoe vortex. There is also a spot of very high HTC in the wake. It is suggested that among the areas requiring further study are the steps and gaps which exist in real turbines for manufacturing reasons, and their effect on secondary flows.

There is also some effect of secondary flows on the vane suction surface. The endwall BL is transferred onto the suction surface and then lifts-off at a particular point, creating a distinct line of low HTC that is easily identified in experiments. This is described in section 4.4

3.1.3 Can combustor with swirl

Combustion dynamics is a specialist subject, and combustion chambers are typically designed and tested in isolation, with little reference to the downstream turbine, except through the targeted bulk flow properties. There has been recently an increasing appreciation for the benefits which could be gained from considering combustors and turbines in an integrated manner.

A large industrial gas turbine typically uses a ring of several can combustors. For example the Mitsubishi F-series uses 16 combustor cans for a 60Hz model or 20 cans in a larger 50Hz model. Several discreet combustion chambers are spaced annularly around the turbine, each operating independently. Combustors are kept separated mainly in order to reduce combustion instabilities which occur in larger combustors. Additionally, discreet combustors allow for maintenance or replacement of individual combustor cans, and allows the same combustors to be used in both 60Hz and larger 50Hz machines, by simply increasing the number of cans. This is weighed against the disadvantages of can combustors, which is increased weight compared to a single annular combustor, which is the reason they are not generally used in aero engines, and the increased internal surface area, which requires additional

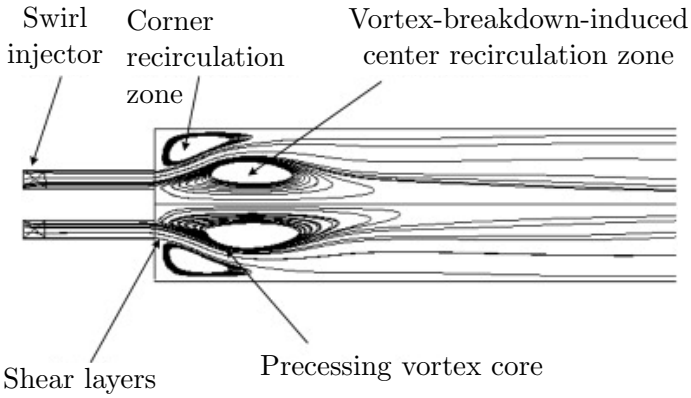


Figure 3.1: Generic swirl-stabilised combustor [54]. The central recirculation zone created by swirl stabilised combustion creates low total pressure core in inflow to vanes.

cooling.

In order to reduce NOx emissions, most modern industrial gas turbines use lean premixed, swirl stabilised combustion. This lowers the flame temperature, which reduces the formation of NOx. This is in contrast to a traditional burner with a diffusion flame which will have some stoichiometric regions as the fuel and air mix, which will be high temperature, and thus produce large amounts of NOx. The swirl is necessary to mix and stabilise the flame, and prevent flashback, or backfiring.

A recirculation zone is created downstream of the swirler which results in a lower total pressure swirl core impinging onto the unshielded vane. This central low pressure core is not simply the 'wake' of the swirler centre body, but rather is created by so-called vortex breakdown of the swirl in the expanding transition duct. A similar geometry to the swirler, but with axial vanes which impart no turning, does not result in any significant central low total pressure core; any wakes created by the vanes or centrebody are fully mixed out by the end of the transition duct. The presence of the swirler also produces large scale flow structures in the combustion chamber, particularly the so called precessing vortex core (PVC) [54] [55] [56] [57].

A review by Huang and Yang [54] presents many of the features of the flow field produced by swirl-stabilised combustion system. Figure 3.1 shows the formation of a central recirculation zone as a result of swirl. It is this recirculation zone which causes the low total pressure core which interacts with the NGV. This low pressure core is not always exactly central, but precesses with a particular frequency.

Syred [57] shows the large impact that the presence of a swirling flow can have on heat transfer and cooling in first stage NGV. This is a flow field characterised by large scale, low frequency, unsteady flow structures. The effect of these on cooling and aerodynamics is not yet well understood.

Combustion does make some difference to the flow field and structures which are created in the combustion chamber [58]. Nevertheless, due to the difficulty of performing experiments with combust-

ing flows, and the extra complexity of including reactions in a CFD code, this is a factor which will not be pursued further in this project.

The swirlers used were designed by Jacobi [13] to model those used in an MHI F-class gas turbine. Details are given in section 2.1.1.

Effect of swirl on NGV

There have been several studies over the past decade investigating the effect of aggressive inlet swirls on the flows through the NGV. Turrell et al. [59] show the increased surface temperature that occurs on the vane immediately downstream of the swirler compared to other vanes, they also carry out a CFD analysis of swirler assembly and NGV and found that a highly rotating swirl core in convected through the vanes, causing a lift-off of coolant on the vane suction side and consequentially high temperatures.

Pyliouras et al. [60] conducted a detailed CFD study of the effect of non-uniform combustor exit flows on turbine aerodynamics, with the conclusion that swirl can cause large efficiency penalties and significantly modify secondary flow patterns.

Schmid et al. [61] and Werschnik et al. (2017) [62, 63] found large efficiency penalties as a result of swirl, and increased heat transfer and reduced film cooling effectiveness.

Giller and Schiffer [64] performed experiments comparing an axial inflow to an inflow with swirl, using five hole probe traverses and film cooling effectiveness measurements. The addition of swirl can make a massive difference to both the film cooling, and the flow field through the vanes. Downstream loss cores present in the axial inflow case completely disappeared in the swirling inflow case, and were replaced with different loss cores. The swirling flow persists through the vanes, and is still visible downstream of the NGV.

Qureshi et al. [25] conducted experiments on the effect of inlet swirl on heat transfer using a light piston tunnel, and also found a significant effect on first vane heat transfer coefficients. Heat transfer coefficients were mostly increased, though in some areas were decreased.

Numerical studies also indicate there is an effect on HTC from swirl. Jacobi [13] performed an in depth study of the effect of swirl on the aerodynamics and heat transfer of NGV using the MHI High Speed Linear Cascade. Again, the findings were that the inclusion of engine-realistic inlet conditions makes a large difference to both heat transfer, and aerodynamics compared to clean inflow conditions.

Inlet turbulence can have a large effect on heat transfer. Radomsky and Thole[65] reported increase in endwall heat transfer coefficients compared to lower turbulence inflows. It was also found that the horseshoe vortex was pushed closer to the vane in a higher turbulence case.

Ames et al. [26] measured the effect on turbulence on endwall heat transfer of first vanes, and found that the effect of high turbulence is to weaken the impact of the secondary flows on the heat transfer coefficient patterns, though they report that the high heat transfer in the wake and around the leading edge due to the horseshoe vortex is still present.

Several LES based studies using realistic inlet flow conditions have produced results significantly diverging from the secondary flow model produced by low speed studies.

Experiments and simulations performed by Cha et al. [66] showed that the high turbulence levels at the turbine inlet caused by the combustor has a significant effect on the flow around the first stage vanes. Vortex visualisations of LES performed showed differences from the traditional picture. High Reynolds number turbulence with no dominant direction enters the turbine, as the flow passes through the turbine a pattern of counter rotating vortices aligned with the flow direction develops through stretching of the vortices. Instead of one dominant passage vortex being generated per endwall, there were many, densely packed, stream wise vortices, counter-rotating in no particular pattern. It is suggested that this puts into doubt the use of two equation turbulence models for RANS simulation of NGV.

Overall, most researchers have found with different geometries that swirl and turbulence at the turbine inlet have significant effects. Highly turbulent of swirling inflow conditions in general increase heat transfer, though in some localised areas it can be decreased.

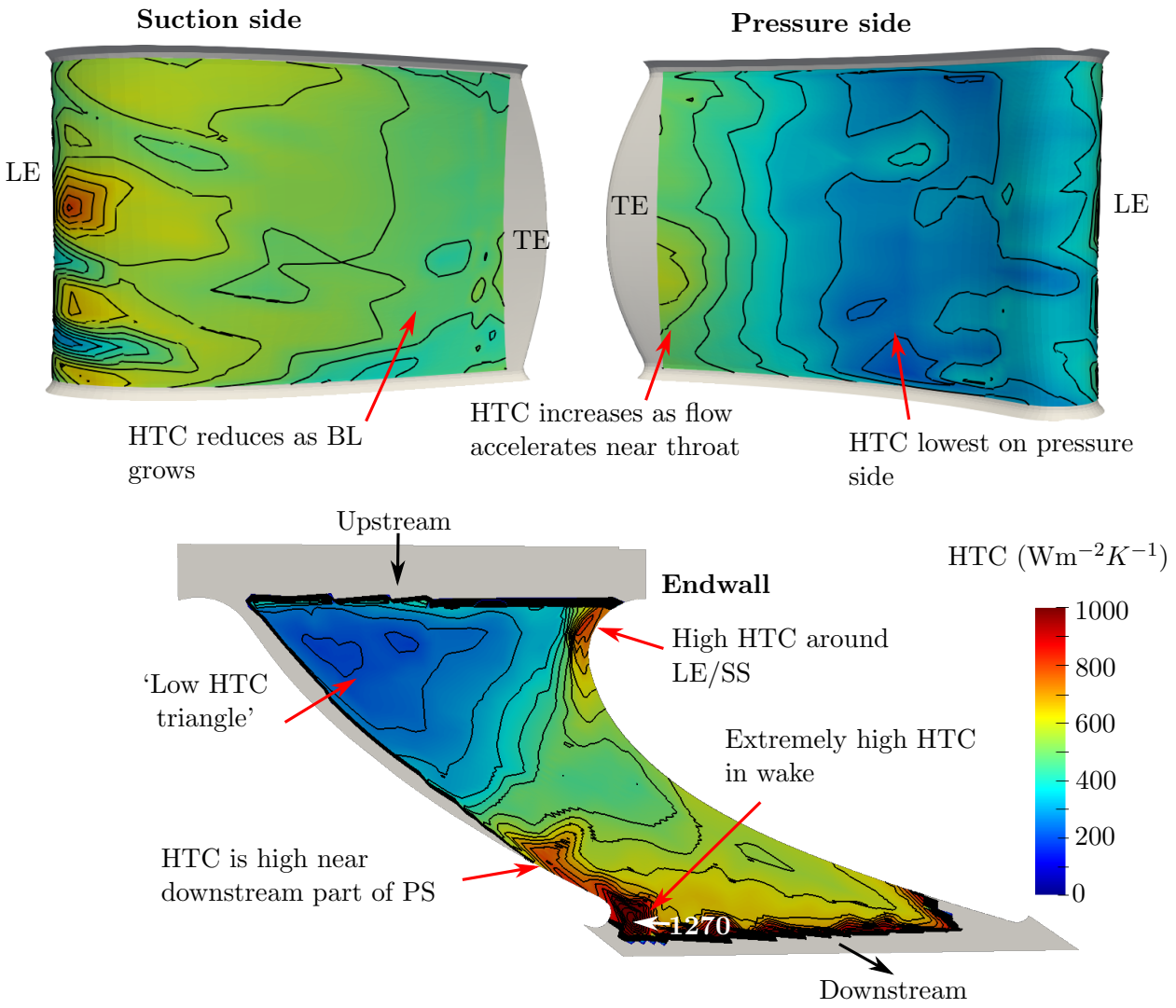


Figure 3.2: Time average HTC of vane surfaces and endwall in with turbulence grid inlet, measured with thin film gauges

3.2 Measured heat transfer coefficients

Experiments were carried out with NGV test pieces instrumented with high density thin film gauges, developed in chapter 2. 192 gauges on the endwall and 192 gauges on the vane surfaces were used for a total of 384 thin film gauge measurement points per vane. The test pieces used are described in more detail in section 2.1.3.

Time averaged heat transfer results are shown on the endwalls and vane surfaces in Figure 3.2 for the case of turbulence grid inflow.

Considering the vane surfaces only, heat transfer is greatest on the suction side, and lower on the pressure side. Far along the pressure side approaching the throat HTC begins to increase due to acceleration. There are some distinct hot and cold streaks visible in the HTC data near the leading edge. It is thought that these are due to small surface irregularities from the thin film gauge substrate. It is seen regardless of inlet condition.

The most interesting phenomena occur on the endwalls. Both the highest and lowest local heat transfer coefficients are found on the endwall, rather than the vane surfaces. There is a large low heat transfer triangle covering most of the upstream part of the passage. This is a result of both comparatively low flow velocities combined with an thick inlet boundary layer transferring from the transition duct.

On the endwall close by to the stagnation point of the vane and around the first part of the suction side surface, there is a much higher HTC. This is due to the horseshoe vortex at the leading edge causing flow to directly impinge on the endwall surface, resulting in extremely high heat transfer.

Further down the passage towards the throat, flow is accelerated, the increasing velocity results in an increased HTC. Additionally, since the boundary layer does not have time to fully develop, HTC is higher than would be calculated by fully developed flow correlations.

HTC on the endwalls is highest near to the pressure side and lowest near to the suction side. This is due to there being a thinner boundary layer near to the pressure side behind the passage vortex. The highest HTC occurs in the wake behind the trailing edge of the vane. This local HTC at this point is double the HTC at the midpoint of the throat, and 10$\times$ the lowest heat transfer areas.

In the case of a clean inflow only, there is a narrow band of reduced HTC caused by the lift-off of the passage vortex, as shown in figure 3.3. In the turbulent inflow case the passage vortex lift off is not so distinct, though the gradient of the HTC contours at the throat, increasing from suction side to pressure side, suggest it may still be present, though spread over a larger area. This is investigated in chapter 4

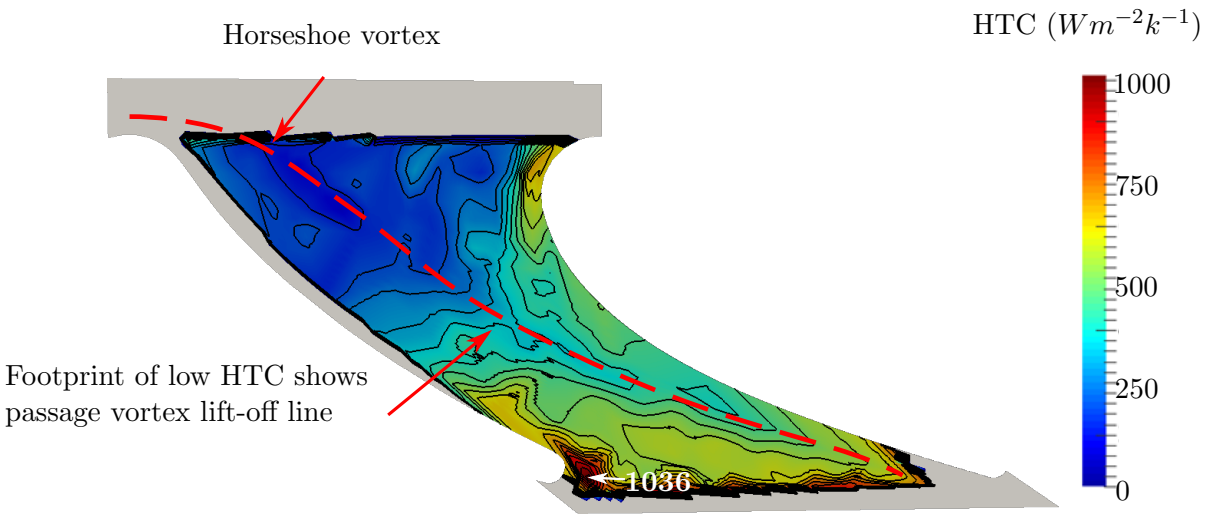


Figure 3.3: Endwall HTC with clean inflow showing footprint of passage vortex lift-off line, measured by thin film gauges. This clear lift-off line is not present in the case of turbulent or swirling inflow.

3.2.1 Differences between swirlers

Five different inlet conditions were compared, as detailed in section 2.1.1. The same operating conditions were used in all cases, only the swirl generator was changed between tests. The turbulence grid inflow case has been used as a reference and the percentage difference of HTC of the other cases is compared. The difference in HTC is therefore locally calculated for each gauge as:

$$\frac{\mathrm{HTC} - \mathrm{HTC}_{\text{with turbulence grid inflow}}}{\mathrm{HTC}_{\text{with turbulence grid inflow}}} \tag{3.1}$$

The inlet condition makes a significant difference to the level of HTC measured. Table 3.1 shows the difference between the five different cases, split between the three main areas of the vane. The overall picture is that a clean inflow gives lowest HTC, followed by the 12 core swirler, eight core swirler, turbulence grid then finally single swirler. These figures disguise much greater local re-distribution of HTC however. An almost 30% reduction from an already low HTC level on the pressure side in the clean inflow case is thought to be from partial re-laminarization of the pressure side. The twelve core swirler which provides smaller length scales and less swirl intensity is a better model for a realistic possible industrial inflow condition. This swirler also gives significant reductions of HTC compared to the other cases. It is thought that the reduction of turbulent length scales compared to the turbulence grid is responsible for this. A single swirler provides the highest HTC, especially on the pressure sides and endwall. Suction side HTC shows less variation according to inlet condition than the other cases.

The detailed difference between the five cases is shown in figure 3.4 for both vane surfaces and endwalls. The turbulence grid inflow case has been used as a reference and the percentage difference

	PS HTC ($Wm^{-2}K^{-1}$)	%	SS HTC ($Wm^{-2}K^{-1}$)	%	EW HTC ($Wm^{-2}K^{-1}$)	%
Turbulence	352	-	517	-	490	-
Clean	248	-29.5	496	-4.1	407	-17.0
12 core swirl	320	-9.1	514	-0.6	423	-13.6
8 core swirl	349	-0.9	473	-8.58	489	-0.3
Single swirl	400	13.6	524	1.4	504	2.9

Table 3.1: Average HTC over the three areas of PS, SS and endwall for five different inlet conditions, along with percentage difference from turbulent case

of HTC of the other cases compared is plotted.

There is considerable re-distribution of HTC, and local variations in HTC considerably greater than the averaged values presented in table 3.1. The eight core and the single swirler results show a similar pattern of re-distribution, indicating the effect of residual swirl. Pressure side HTC near to the hub is increased, less so on the casing side. On the suction side the opposite is true, with a lowered HTC near hub and increased towards the casing. This indicates the effect of a radially non-uniform vane loading (shown further in section 4.3.3). A similar effect is visible on the endwall, HTC is increased towards one side and decreased towards the other in the upstream part. Downstream the position of the passage vortex appears to have changed, leaving a clear footprint of its shift. The clean inflow and 12-core inflow show more of a general reduction in HTC over nearly all of the endwall and pressure side surfaces. The suction side HTC is hardly changed.

The passage vortex is clearly defined in the time averaged data of the clean inflow case. However it is not nearly so distinct when a highly turbulent flow is present.

Overall, the heat transfer results show that the 12-core swirler gives a reduction of HTC of up to around 20% compared to the single swirler. This shows that it would be beneficial to NGV efficiency to design combustion chambers to have many, smaller swirlers, giving smaller length scales of turbulent structures and thus causing lower HTC in the NGV.

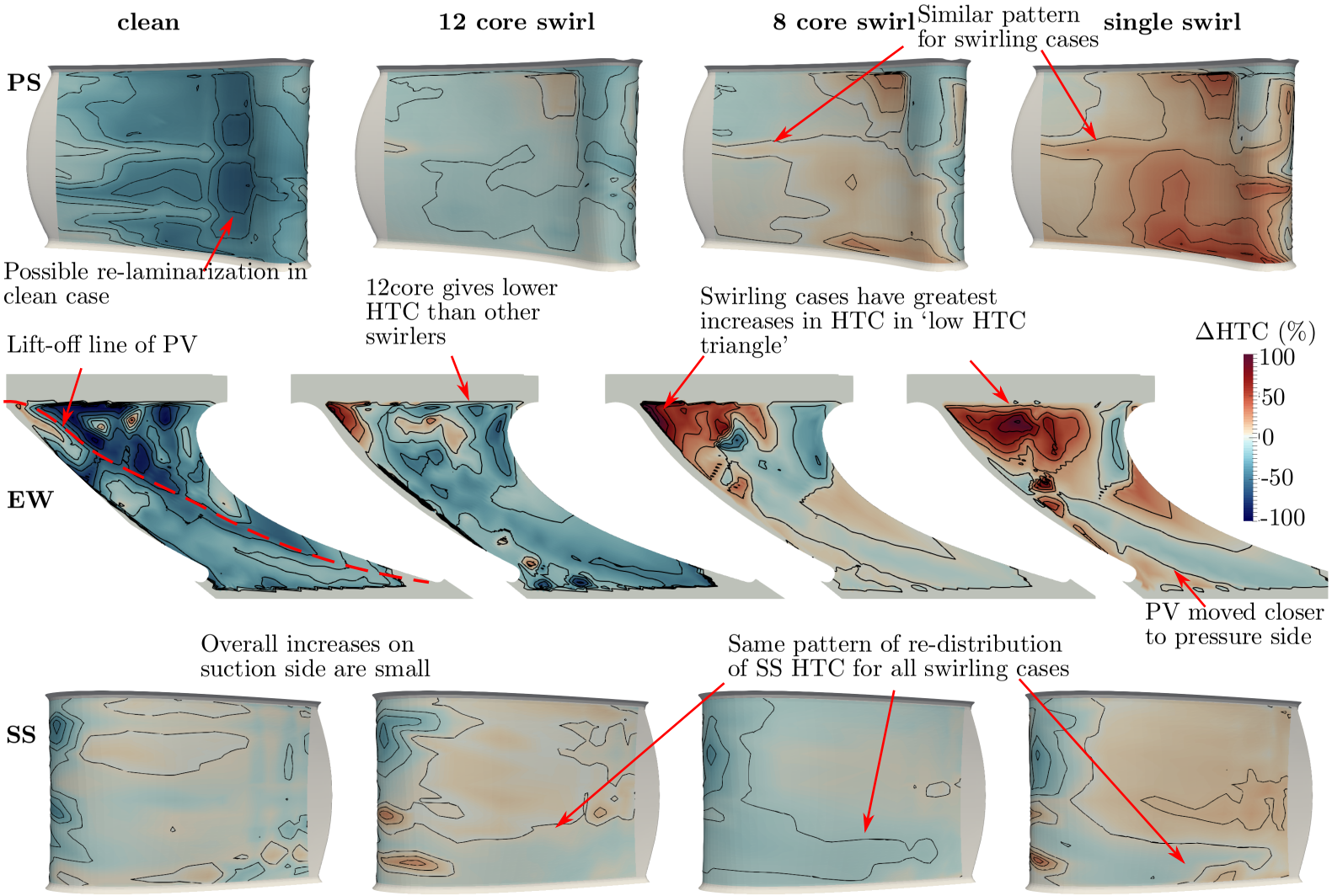


Figure 3.4: Difference in experimentally measured HTC for different inlet conditions compared to turbulence grid inflow case

3.3 New midspan secondary flow

Jacobi [14] suggested that the presence of a precessing swirl core would lead to the formation of an additional secondary flow like vortex around the vane leading edge.

In order to confirm the theory of the formation of this vortex, a CFD study is carried out using swirling inlet conditions matching experiment.

RANS CFD, using the Tblock solver, is used to investigate the critical parameters for the formation of the flow structure. Both swirling and non-swirling inlets, with various strength total pressure loss cores are used in order to investigate the factors leading to the formation of this vortex. While RANS is steady and uses the time average of the measured inlet condition as a boundary condition, it must be borne in mind that the actual, experimental swirlers create time-varying inlet flow fields. The unsteadiness is described later, along with other unsteady phenomena in chapter 4.

3.3.1 Physical explanation

The residual swirl core created in the combustion chamber causes a lower total pressure region in the centre of a passage. In the geometry under investigation, this impinges directly onto the leading edge of a NGV. When the flow impinges on the stagnation region of the vane there is a radial pressure gradient along the stagnation line, with a lower static pressure near the centre of the vane, and higher towards the endwalls. This pressure gradient results in a flow along the stagnation line from either endwall towards the centre of the vane. At the centre, these two opposing flows meet. The boundary layer separates under the reversed pressure gradient, to form a counter-rotating vortex pair, with the lift-off region in the centre. Figure 3.5 shows the static pressure gradient which causes boundary layer separation and vortex roll-up on the vanes.

This is similar to the mechanism that results in the horseshoe vortexes near each endwall, except that it is caused by the lower total pressure of the core of the swirling combustor flow, rather than by the lower total pressure of the boundary layer fluid.

This vortex pair modifies heat transfer and aerodynamic characteristics of the first vane, and could potentially have a significant effect on cooling flows.

In addition to the lower total pressure core, the overall swirl of the inlet fluid has the effect of pushing the counter-rotating vortex pair towards one side of the passage. The swirl is not a necessary component of the flow to create the vortices, the total pressure deficit core is sufficient. However it is the swirlers which are responsible for creating the central total pressure drop, as a result of the central re-circulation zone.

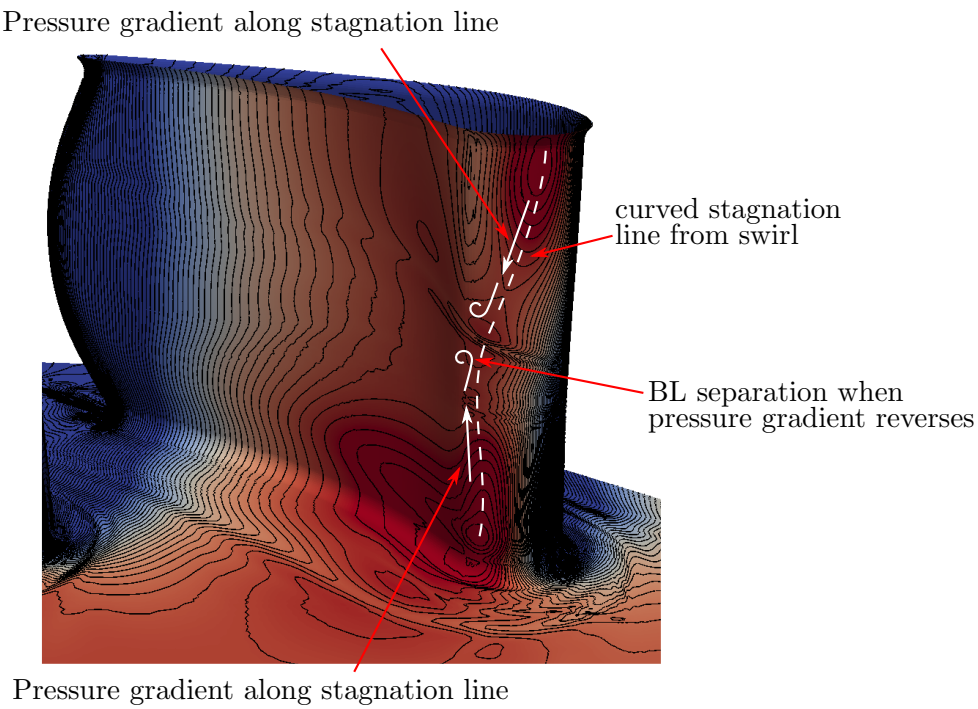


Figure 3.5: Instantaneous static pressure on leading edge causing formation of midspan vortex pair

3.3.2 RANS study

The computational domain used for CFD was intended to simulate the experimental conditions. Experimentally measured yaw, pitch and total pressure was used as the inlet boundary condition. This was scaled to create different magnitudes of total pressure loss or swirl to investigate the sensitivity of formation of the midspan vortex pair from these parameters.

A mesh of 2.5 million nodes was used for steady RANS. The solver used was a parallelised version of Tblock, as described in detail in section 2.7. A mixing length turbulence model was used.

Ten different RANS cases were run, with different inlet boundary conditions chosen to determine the sensitivity of the formation of the midspan vortex to the magnitude of the central total pressure drop, as well as swirl. The measured inlet conditions with a single swirler, and an 8 core swirler were used as baseline cases. Additionally, a uniform inlet condition was used, corresponding to the use of a turbulence grid in experiments. An inlet condition was created consisting of the same percent swirl as the single swirler case, but without any pressure drop. Another set of inlet conditions did not have any swirl, but had the same central total pressure loss core as each of the swirlers used in experiments. A further set of inlet conditions had no swirl, and the magnitude of the total pressure drop core was reduced to a half that of the experimental conditions. In all cases the mean inlet total pressure was the same.

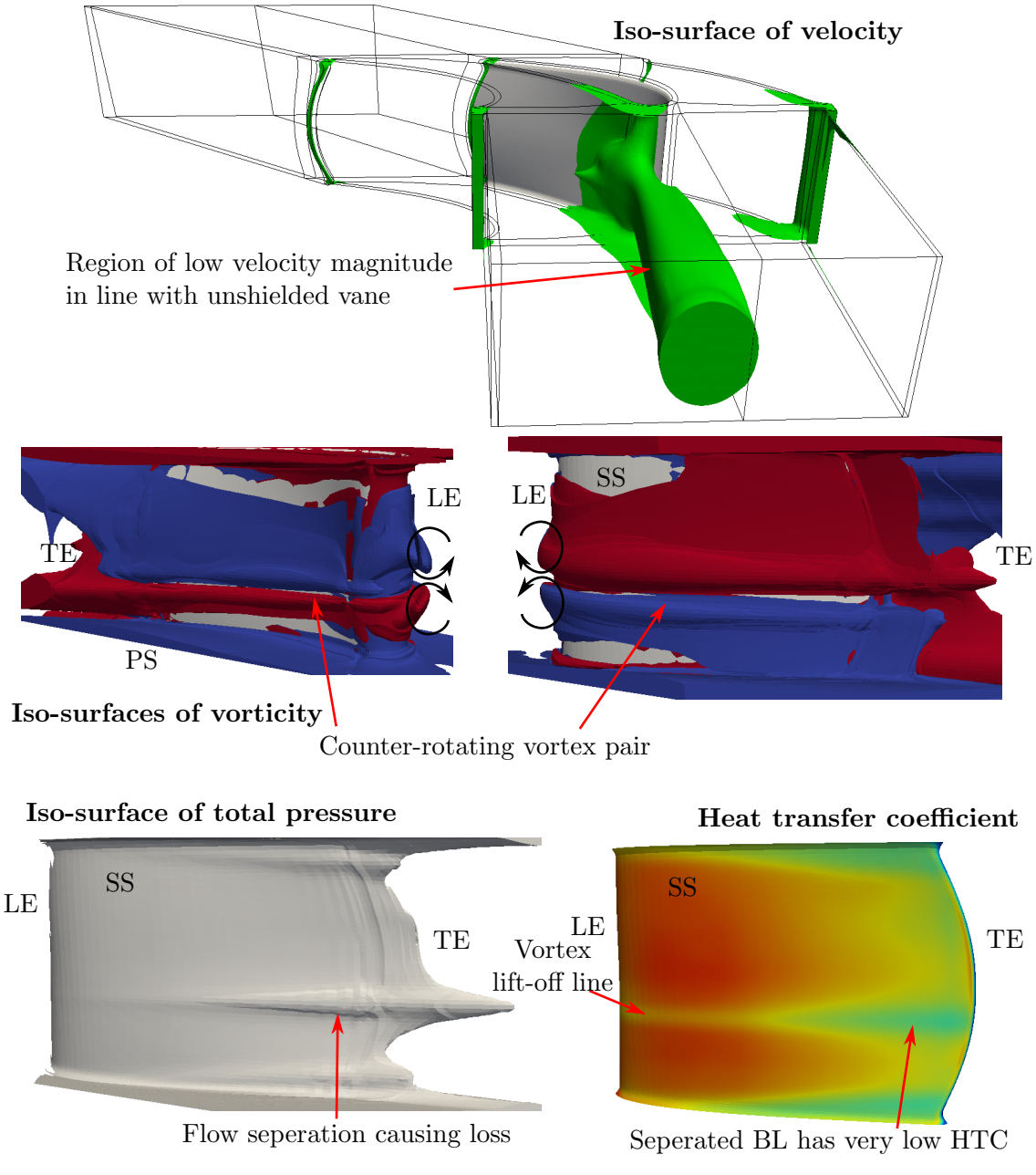


Figure 3.6: Rans CFD results of midspan vortex with loss core inlet condition without swirl

3.3.3 Detailed Analysis of pressure loss but no swirl

The simplest case is shown in detail first, to illustrate the basic interaction and its effects. The inlet condition consists of a pressure loss in the centre of the passage equal to that measured experimentally, but with no swirl present, inlet flow is purely axial.

The inlet condition and the results are shown in figure 3.6. Isosurfaces of vorticity, contours of HTC, an isosurface of total pressure and a cross section of total pressure downstream of the vanes are shown.

A pair of counter-rotating vortices on the leading edge of the NGV are formed, as explained in section 3.3.1. Due to flow turning, the vorticity which is present in the free stream due to the shear flow becomes aligned with the flow direction. The radial static pressure gradient on the stagnation line causes vortex roll-up, in a similar way to the formation of the horseshoe vortex near the leading edge. There is no swirl in this case particular case, so the vortex pair remains near the midspan of the vane.

Over most of the pressure side and the first half of the suction side, the vortex pair has little clear effect on performance. However, in the diffusion region of the suction side vane, where the flow is against the static pressure gradient, the vortex pair causes flow separation. This creates additional losses, and means that flow is being under-turned. The separated region can be seen both directly by the total pressure in figure 3.6, and also results in a distinctive footprint in HTC. The lift-off line between the vortex pair creates a line of moderately lowered HTC. Where flow separates however, this creates a much larger region of significantly reduced HTC.

The effect of the suction side flow separation is to cause a loss of total pressure and therefore entropy generation and ultimately a reduction in machine efficiency.

3.3.4 Comparison of CFD cases

Seven representative cases are shown in figure 3.7. Iso-surfaces of total pressure (loss) are shown, as this allows easy visualisation of both the location and significance in terms of losses, of the vortex pair.

It should be stressed that the loss of total pressure behind the vortex pair is not simply the inlet loss core convecting through the passage. While this does occur, the effect is less, and is not necessarily spatially co-incident with the vortex pair generated loss. This can be seen especially in the case of the single swirler, where the vortex pair has been pushed towards the hub endwall by the residual swirl, whereas the inlet loss core has convected through the centre of the passage.

In the case of inlet loss without swirl, the midspan vortex pair causes a separation near midspan

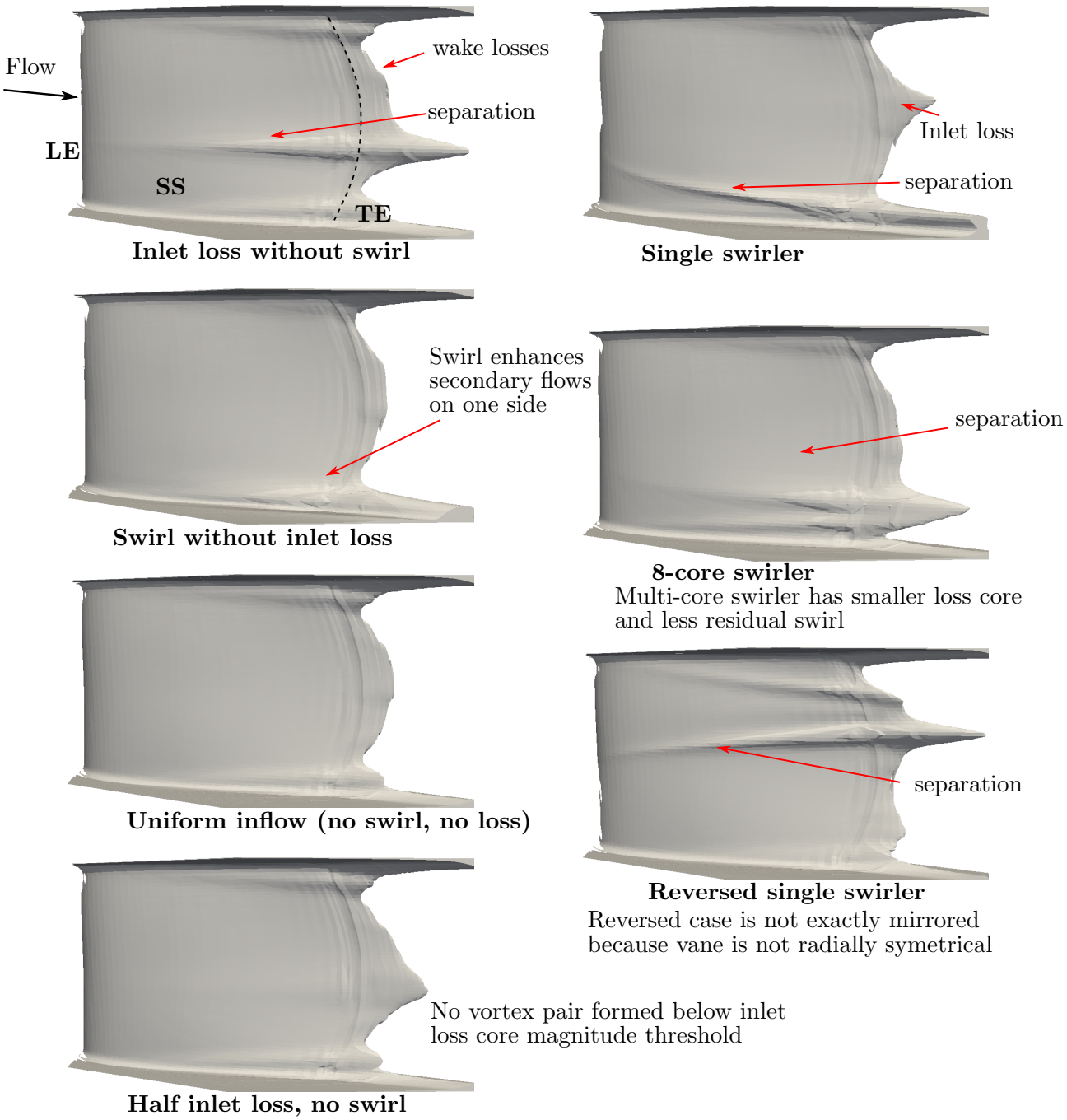


Figure 3.7: Isosurfaces of total pressure loss. Left, top to bottom: inlet loss without swirl, swirl without inlet loss, uniform inlet, half inlet loss. Right: experimentally measured inlets; top to bottom: Single swirler, multi-core swirler, reversed single swirler

in the diffusion region of the suction side, creating an additional loss.

A swirling inflow with no inlet loss core does not create any midspan vortex pair, and so there is no additional separation region caused. The passage vortex lift-off on one side is enhanced and reduced on the other.

The single swirler inflow, which corresponds exactly to experimentally measured inflow, having both a total pressure loss core and swirl, shows the vortex pair forming, then being effectively pushed towards one endwall by the effect of the residual swirl. Flow separation again occurs on the suction side, creating losses, though appearing to be almost merged with the passage vortex losses. The inlet loss core itself is convected through the centre of the passage, and does not remain co-incident with the vortex pair it created.

The multi-core swirler has a smaller, loss core, both smaller in magnitude but also more localised. The level of residual swirl is also less. This was observed to still be sufficient to cause suction side separation, and for the vortex to be pushed towards the hub endwall, where it interacts with the passage vortex. This is to a lesser extent than the single swirler case though.

The reversed swirler is an exact mirror of the single swirler, and so too are the inlet conditions. However, since the vane itself is not exactly radially symmetrical, the results appear somewhat different to the single swirler. The midspan vortex has been pushed towards the casing endwall, but not as fully as in the case of the single swirler.

The final case shown has half the magnitude of the total pressure loss core as was measured, and no residual swirl. It was found that in this case the radial static pressure gradient was insufficient to cause the boundary layer to roll up into a pair of vortices, though there must still be opposing axial vorticity on either side of the vane. Without the vortex pair forming, there was suction side flow separation, and so little additional loss. This shows that there is a threshold of total pressure loss which is required to cause vortex formation, so by appropriate combustor design this effect could be eliminated.

3.4 Summary

Heat transfer coefficients have been measured and compared between six different inlet conditions. The large variations in heat transfer dependent on inlet condition shows the benefits which could be gained from considering combustors and NGV in an integrated manner, since turbine heat transfer could be significantly reduced by combustor design. HTC is highly enhanced by inlet turbulence and swirling inflows compared to a clean inflow. This indicates a potential for great improvements to first vane heat transfer by means of improved combustor design.

In order to reduce heat transfer in the NGV, and therefore increase turbine efficiency and component life, combustors should be designed to consist of more, smaller swirlers to give smaller length scales.

To ascertain the reason for the smearing of the passage vortex lift-off line the unsteady results must be analysed, which is done in chapter 4.

An additional secondary flow like vortex structure is present at the midspan of a nozzle guide vane due to the pressure loss resulting from inlet conditions created by upstream swirlers. Below a certain threshold of inlet total pressure ratio, there is insufficient static pressure gradient on the leading edge to cause vortex roll-up, and the vortex formation is suppressed.

In the diffusion region of the suction surface, it appears that the vortex pair can trigger flow separation, causing an increase in losses. Therefore it would be beneficial if this effect was suppressed, by designing combustion chambers to not have an excessive radial total pressure gradient impinging onto the nozzle guide vanes. In reality, experimental data shows this to be a highly unsteady phenomena, as is discussed in the following chapter.

Chapter 4

Unsteady combustor turbine interactions

4.1 Introduction

The combustor-turbine interface in a gas turbine is characterised by complex, highly unsteady flows. It is the area of the turbine which faces the highest temperatures, so a detailed knowledge of flow phenomena and heat transfer is required to optimise cooling. The endwall in particular is attracting increasing interest as lean burn combustors with more homogeneous combustion result in higher temperatures near endwalls. This region has a complicated heat transfer profile with a large influence of secondary flows. In a combined experimental and LES study including realistic combustor geometry, the standard model of secondary flows in this area is found to be oversimplified. Rather than being steady-state, flow in the NGV is found to be highly unsteady. The position of the passage vortex is varied in time under the influence of the highly turbulent inflow. The horseshoe vortex at the leading edge is highly variable in time due to combustor unsteadiness. Unsteady changes in surface temperature are found to be large enough to potentially cause damage to thermal barrier coatings.

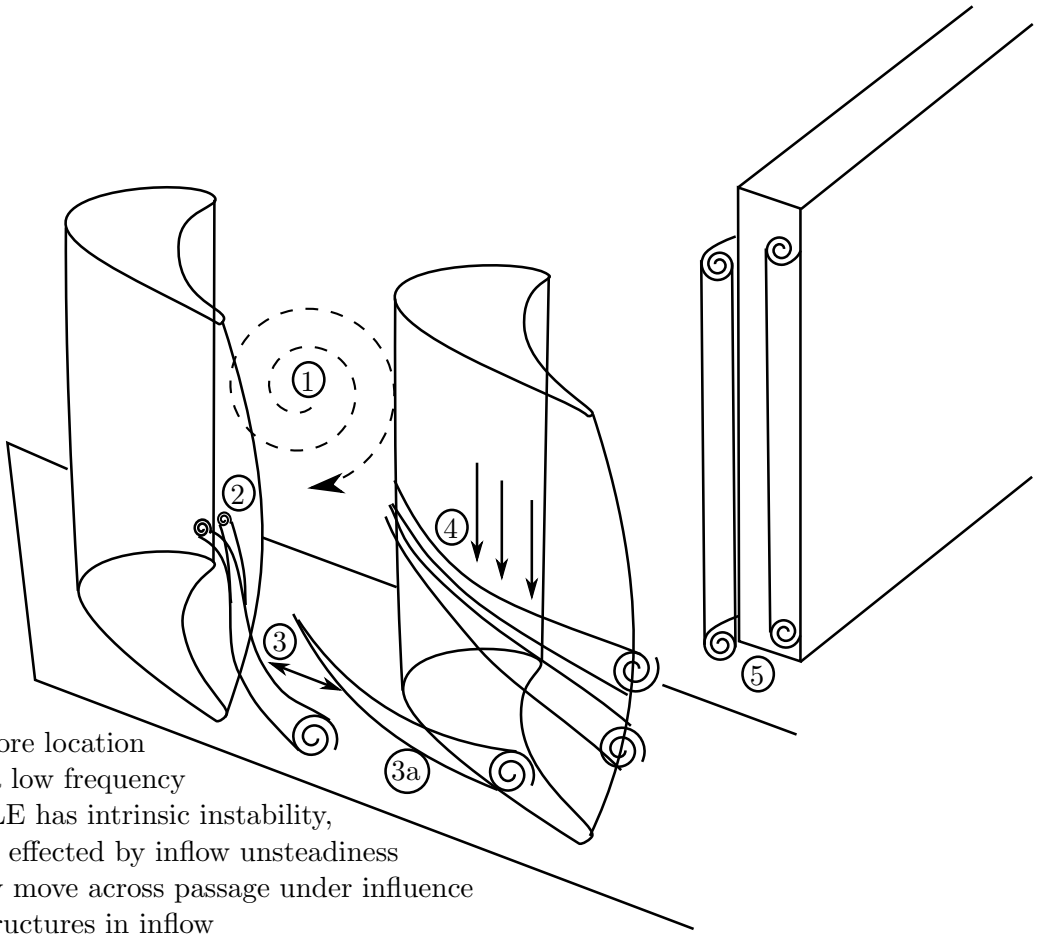
In this chapter, five unsteady phenomena are identified are described in detail. These are:

1. The precessing vortex core caused by the swirler, and the effects of the precessing vortex core on flow through the vanes. This is the main root cause of the other unsteady phenomena.

2. The horseshoe vortex at the leading edge of the vane.

3. The passage vortex within the NGV passage. This is found to be highly unsteady, and more complicated than is usually considered.

4. A new midspan secondary flow, as was described for the steady state in section 3.3, is examined



1 - Swirl core location
moves at a low frequency
2- HV at LE has intrinsic instability,
and is also effected by inflow unsteadiness
3- PV may move across passage under influence
of large structures in inflow
3a- Additional passage vortex may form
4- Midspan vorticies formed by incoming loss core
5- Vortex shedding from combustor wall

Figure 4.1: Unsteady flow features described in this chapter

in the unsteady case.

5. Vortex shedding from the combustor wall which impinges onto the vanes has been measured experimentally.

An overview of these five unsteady phenomena which will be discussed in this chapter is shown by figure 4.1.

The phenomena of the precessing vortex core is discussed first, as this aids in understanding of all subsequent results. The measurement results using thin film gauges and infra-red are presented next, followed by a detailed description of each of the remaining four main unsteady flow phenomena observed.

4.1.1 Influence of the inlet flow field on nozzle guide vanes

It has been observed by many of those involved in combustion research [54, 55, 56, 57] that the flow field leaving the combustor is characterised by time varying, large scale coherent structures.

Seo et al. [67] show that bulk flow pulsations can have a significant effect on film cooling performance. This will be investigated in terms of the unsteady pressure fields which result at the nozzle guide vanes.

Although it is often assumed that the flow around the nozzle guide vanes is essentially steady, in fact there is a highly unsteady flow field, with a range of time-scales including very low frequency interactions. The lowest frequency changes especially, could cause significant fluctuations in temperature of the NGV, and film cooling flows.

An LES study by Jacobi et al. [14], found that when this flow impinges on the first nozzle guide vane (NGV) of the turbine, a secondary flow like midspan vortex pair is created on the leading edge of the NGV. The vortex extends over the pressure and suction sides of the vane, the vortex of the pair which was aligned with the overall direction of swirl was enhanced, the other suppressed. The vortex would then migrate towards either the hub or the casing depending on swirl direction.

In an LES study Jacobi[14] found a single passage vortex that is highly unsteady in its position within the passage and migrates across the entire passage from pressure side to suction side.

There have also been indications from experimental studies that there may be significant unsteady flow effects in some areas of the NGV. Radomsky and Thole[65] measured endwall heat transfer using infra-red thermography, and based on velocimetry measurements near to the leading edge concluded that there was a significant unsteadiness in the leading edge horseshoe vortex. Praisner and Smith[68, 69] also conducted a highly detailed investigation into the horseshoe vortex at the leading edge and its effects on heat transfer, finding the vortex to be unsteady, and a local increased heat transfer where the vortex causes impingement onto the endwall.

As far as it is known, there have previously been no comprehensive studies measuring unsteady effects on heat transfer over the whole of the NGV area, as is in the present work.

4.2 Experimental and computational methods

Measurements were carried out with 384 high speed thin film heat flux gauges distributed over vane surfaces and endwalls of a NGV. Unsteady results are compared between different inlet conditions. The high resolution of measurements was such to allow direct visualisation in time of large scale turbulent structures over the endwalls and vane surfaces. Measured unsteady variation in heat transfer coefficient were scaled to engine conditions and estimated to result in fluctuations of TBC surface temperature of up to 200K. Measurements by unsteady pressure sensors and a high speed infra-red camera provide supporting data.

An LES study was carried out in order to support the experimental campaign, and provide a

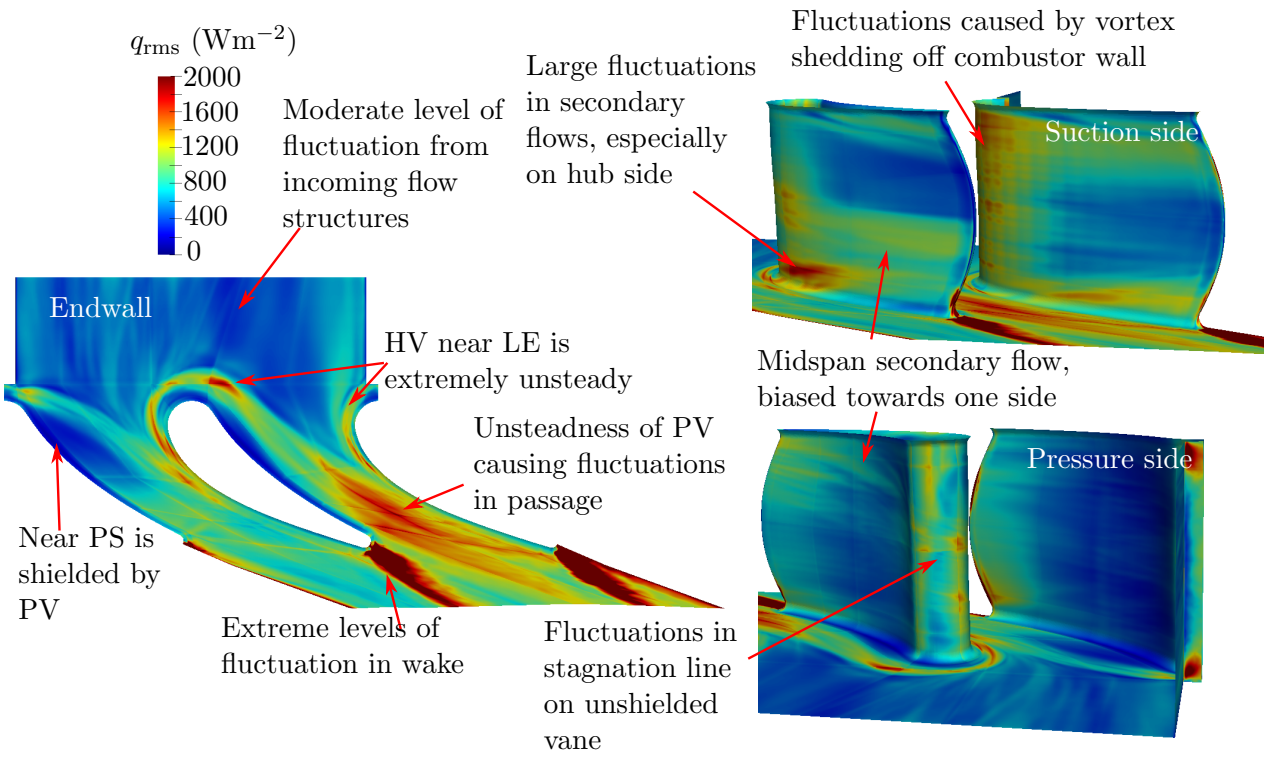


Figure 4.2: Overview of the main regions of unsteadiness on endwall and vane surfaces, calculated from LES

full flowfield dataset which can be used to investigate the physical causes of the surface phenomena observed. LES is carried out in a domain consisting of two NGV passages with an upstream swirl generators and transition duct matching experimental conditions. Details are given in chapter 2 Data reduction allowed time-varying LES data to be recorded for several cycles of the unsteady phenomena observed. LES was conducted only for the case of a single swirler, rather than for all inlet conditions, as this is the case which manifest all of the phenomena of interest.

Figure 4.2 shows the areas of unsteadiness in HTC on the vanes and endwall, calculated by LES. The causes of these unsteady interactions are described in detail, with reference to supporting experimental measurements.

4.3 Precessing swirl core

The upstream swirler creates a highly varying inflow condition which affects the unsteady behaviour of the flow in the NGV passages. The magnitude and position of the total pressure loss core varies considerably in time, with a low frequency. This can change the angle of incidence onto the vanes, and has an effect on both vane loading, and the formation of secondary flows.

While the overall levels of residual swirl remains mostly constant in angular momentum terms, the distribution is highly time-varying, such that the level of residual swirl which is split into each passage

varies in time.

The variation in inlet flow is examined mainly for the impact it has on the vanes and the flow within the vane passages. The unsteady fluctuation in inlet flow has a great deal of impact on the subsequent flow within the vane passages. LES is available for the case of a single swirler, and will be analysed here. Qualitatively similar flow fields are created in the case of multi-core swirler, at least in time-average. It appears that the levels of large scale fluctuations are less in the multi-core swirler case however.

4.3.1 Swirl core through passage

The largest unsteady flow structure in these results is the residual swirl core within the vane passage. In the machine geometry being studied, there is a two to one vane to can combustor ratio. Thus every vane either has a residual swirl core impinging on it, or a combustor wall directly upstream.

The position of the swirl core is highly variable, being centred at any point anywhere in the passage, being from time to time near the endwall by the PS, by the SS or in the centre of the passage.

Figure 4.3 shows three snapshots of locations of the swirl core, as well as the time-averaged inlet total pressure. Depending on the location, secondary flows and the horseshoe vortex is also affected.

The movement of the swirl core is a low frequency phenomena. In the time that the LES was fully recorded for, 30ms, only 1.5 full cycles occurred, giving a frequency of 50Hz. This explains well the very low frequency fluctuations observed in the experimental measurements in the case of swirling inflow, which were absent with turbulent and clean inflows.

It should be noted that regardless of which passage the swirl core is going into, both passages will still have an overall level of residual swirl, as there will be some angular momentum going into each passage. The magnitude of the angular momentum distributed between each passage varies in time, as does the loading on the vanes.

The variation of the position of the central pressure loss core upstream of the vanes is shown in figure 4.4. Three instantaneous timesteps are plotted, a well as the time-average total pressure field. The swirl core pressure loss is always present, though it varies greatly in its position. The movement of the swirl core appears quasi-random, with no clear discernible pattern to its movement for instant to instant, though it remains within an envelope and produces a smooth plot of time-average. The total pressure loss core is always present, and moves slowly through the area. A line is plotted showing the path taken by the centre of the swirl core over all timesteps of LES (calculated as the location of minimum total pressure), illustrating this quasi-random movement.

Other turbulent eddies are also present, on a range of length scales up to almost the height of the

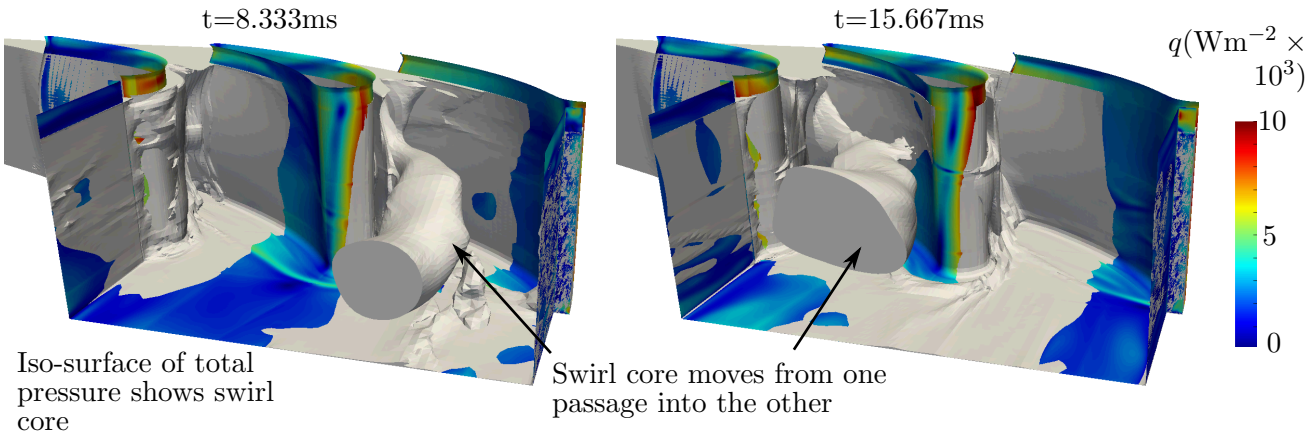


Figure 4.3: Two different timesteps showing variation in unsteady position of swirl core. In the first timestep the swirl core is entering the right hand passage. In the second timestep the swirl core is entering the left-hand passage

combustion chamber. The difference between the highest and lowest total pressure areas is significantly greater than would appear from only looking at time-averaged data.

Also shown is the variation in total pressure at the centre point of the inlet. This can be seen to vary with a low frequency, there is an approximately 330Hz fluctuation, as well as lower frequencies, such as the 50Hz noted previously. There even appears to be variation on the order of the full length of recorded time at this point, meaning <33Hz fluctuation.

4.3.2 Vane surface unsteady pressure measurements

In order to visualise the swirl core in the vane passage, and its fluctuation with time, experiments were carried out with a vane instrumented with 48 unsteady pressure sensors. These are capable of measuring unsteady content below approximately 2000Hz, as described in chapter 2.

The results of four different swirl generators are shown in figure 4.5, at equal timesteps apart. Only the suction side is shown, as the pressure side does not show so clearly the movement of the swirl core through the passage. For the purposes of visualisation the pressure is normalised by local mean static pressure: $(p - \bar{p})/\bar{p}$. Normalisation by local static pressure allows the surface fluctuations to be seen clearly over the whole surface of the vane. The amplitude of fluctuations is greater at the leading edge and less over the suction side, so that normalising by inlet dynamic head would not show large structures over the whole vane as clearly.

The first case is the same swirler as LES. There is a good agreement with LES, both in the pattern of static pressure distribution and the magnitude of static pressure change which is observed, up to 3% of absolute static pressure. The characteristic frequency of the swirl core seems to be be around 250-330Hz in the experiment, as shown by the images in figure 4.5 approximately a cycle apart.

A reversed swirl reverses the direction of the 'streaking' on the suction side, as there is a radial

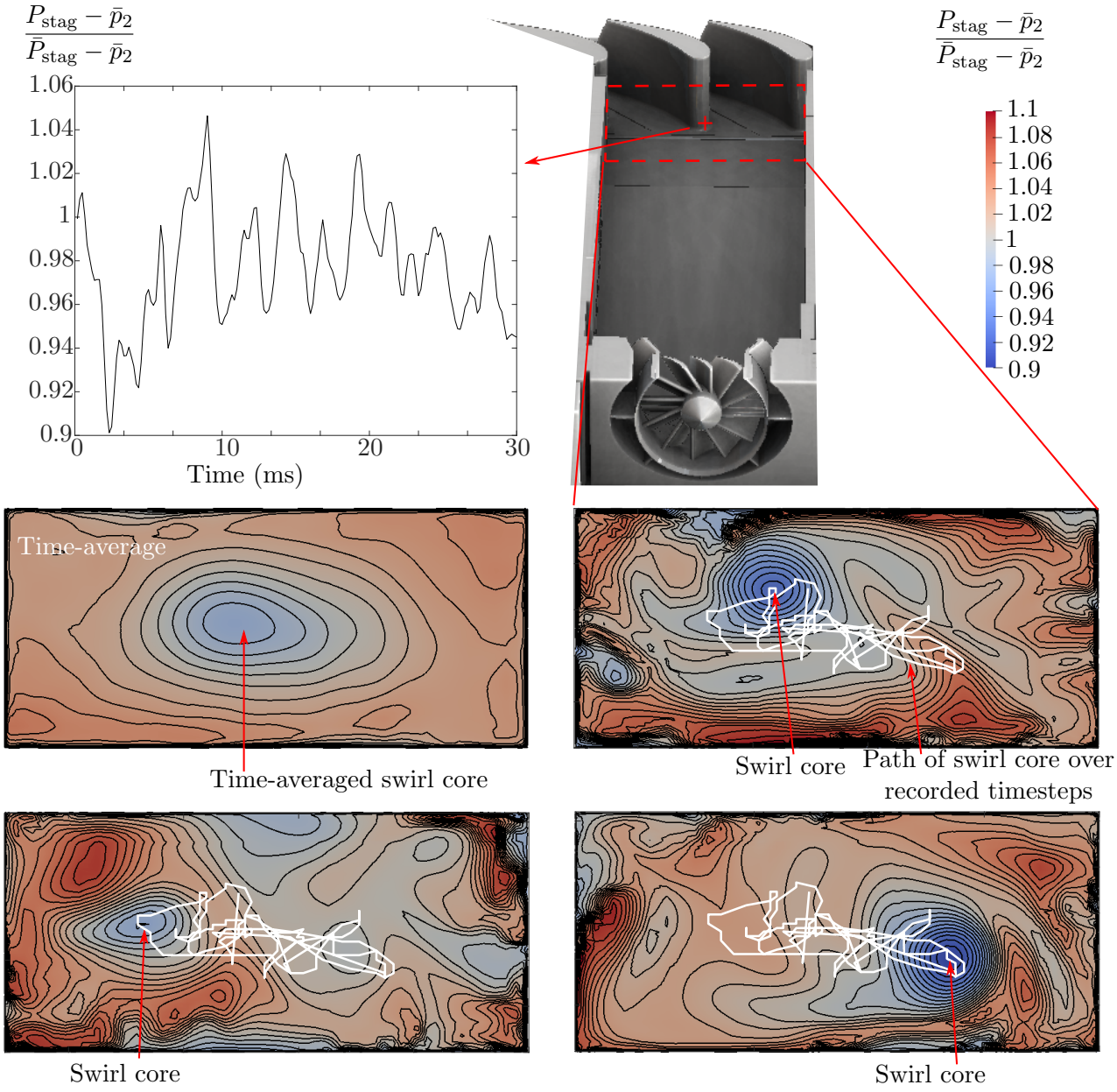


Figure 4.4: Unsteadiness of incoming flow field. Top left: total pressure at centre point of transition duct area. Middle left: Time-average total pressure contours Middle right and Bottom: instantaneous total pressure contours

component of velocity near the suction side due to the residual swirl in the passage. Otherwise the magnitude of fluctuations remains much the same.

The third case shown is that of a multi-core swirler. The overall level of residual swirl is less, and these results show also that the magnitudes of the large-scale fluctuations due to the swirl core are also less, though still present.

4.3.3 Variation in vane loading distribution

The low frequency (up to 330Hz) fluctuations in inlet total pressure have a consequent effect on vane loading distribution. The loading on the forwards part of the vane varies most dramatically. While the midspan of the vane has a loading curve with reverse pressure gradients only on the second half of the suction side of the vane, the combustor swirl has changed the angle of incidence enough to cause adverse pressure gradients over areas near the leading edge on both suction and pressure side.

The fluctuating position of the swirl core has the effect of varying the loading in time. Plots of maximum and minimum static pressure show the variance of loading which occurs. Quite significant adverse pressure gradients can occur transiently on the vane. This could be problematic for design, as compensating for the swirl at the time averaged position would still leave the vane geometry sub-optimal at other instances in time. The time scale of the fluctuations of the swirl core is much slower than the flow-through time of the vanes.

Figure 4.6 shows the loading at three different span heights. The swirl has significantly changed the loading on the vane at these different heights, and there are even regions of adverse pressure near the leading edge on both suction and pressure sides due to the changed angle of incidence caused by swirl.

This variation in static pressure on the vane surfaces could also likely affect film cooling flows, though this has yet to be investigated further.

The effect of the unsteady swirling inlet on secondary flows and other unsteady flow phenomena in the vane passages is discussed throughout the rest of this chapter.

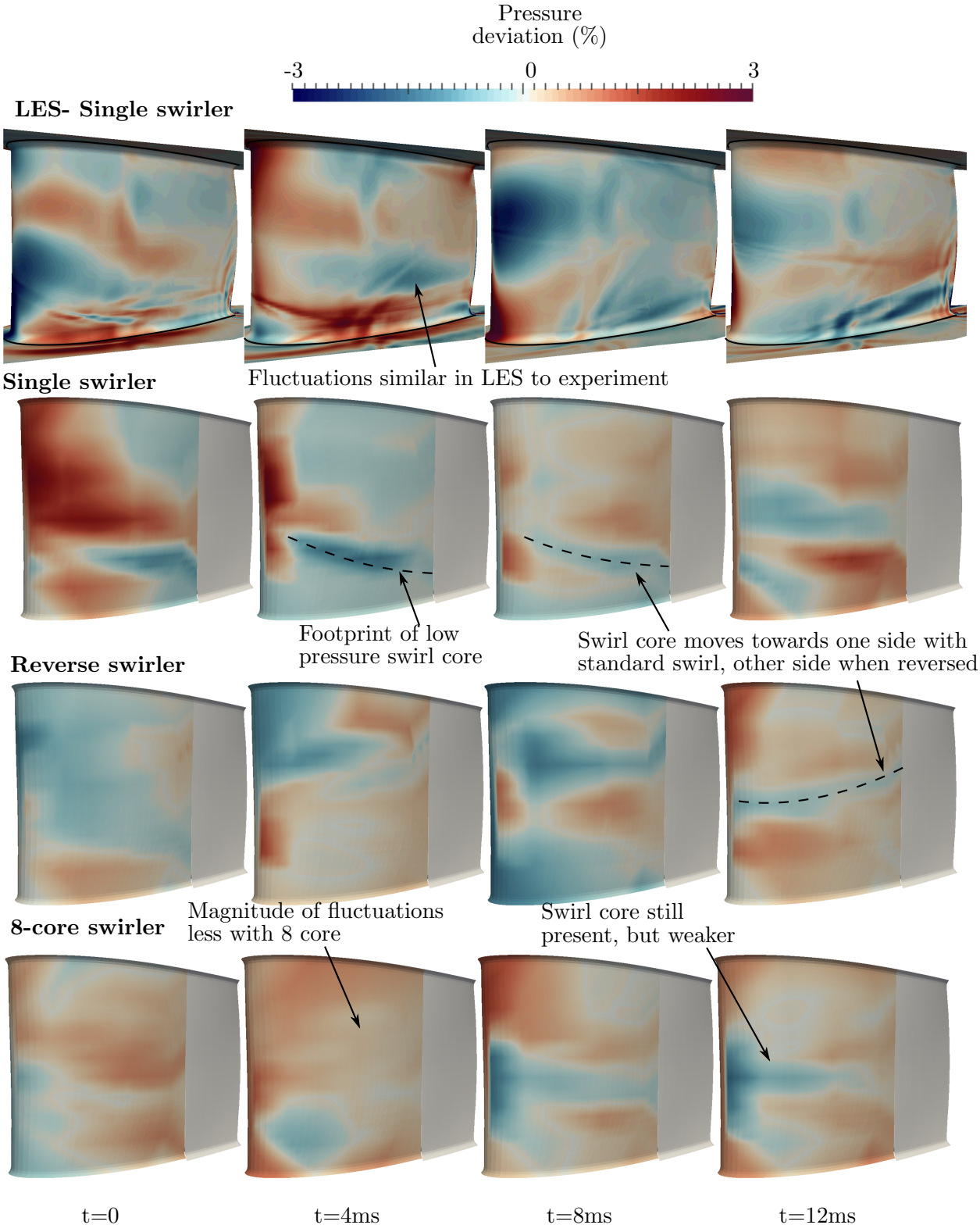


Figure 4.5: interpolated contours of normalised instantaneous pressure measured with different inlet conditions Top to bottom: Single swirler LES, Single swirler experimental, reverse single swirler, 8-core swirler

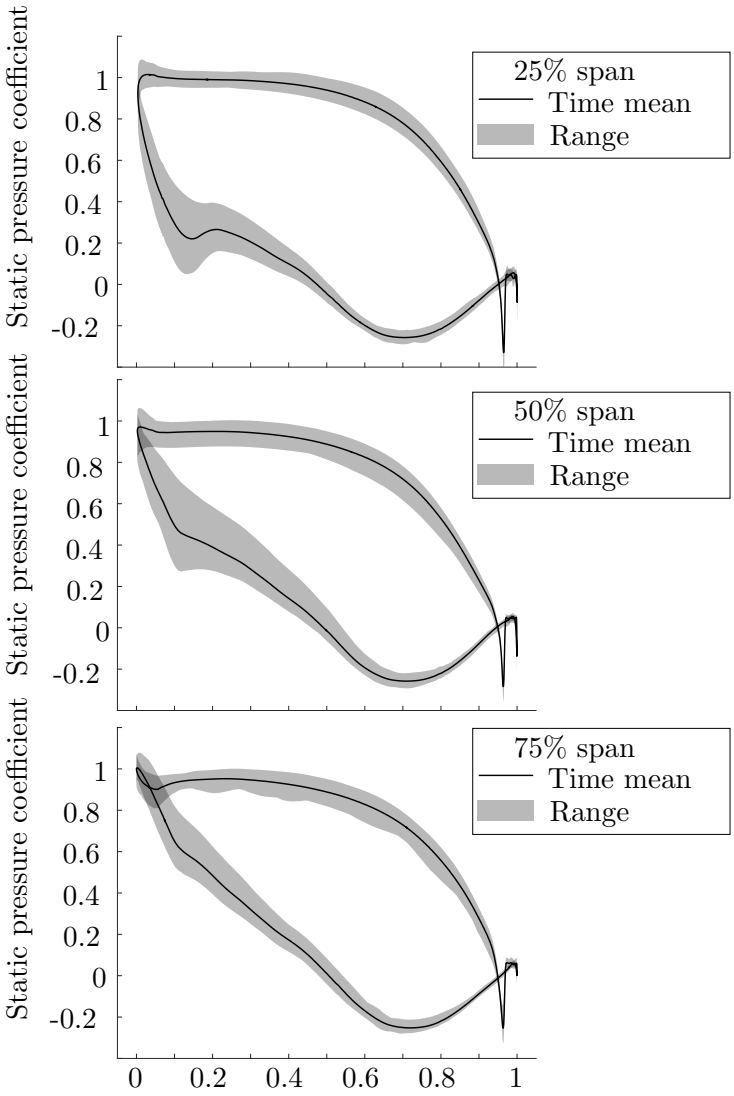


Figure 4.6: Variation of vane loading. Top to bottom: loading on vane at 25%, 50% and 75% span.

4.4 Unsteady heat transfer on vanes - measurement results

4.4.1 High speed infra-red camera

Increasingly sophisticated IR camera technology allows this to be used for measurements of unsteady heat transfer even in low-temperature, high speed facilities. The higher speed means a faster sampling speed is required, while low temperature increases the required integration time of an IR camera. With lower speed flow, or higher temperature test pieces, these IR cameras would be even more effective. Unsteady HTC can be shown in videos, and snapshots are reproduced here. High speed IR measurements were only available on the vane suction side, due to limitations of viewing angles. IR is less accurate than thin film gauges, but has the advantage of allowing full surface measurements at high spatial resolution. This allows flow structures to be seen which are difficult to see in thin film gauge plots. In the raw signals there is a large amount of camera shake. Since heat transfer calculations rely on analysing the temperature history of each pixel, for this to be accurate it is essential that the movement of the imaging area is eliminated. A Matlab script was created which used point recognition to identify features in each image frame an compare them to the same features in subsequent frames. Using this the motion between each frame could be adjusted for, allowing the accurate calculation of heat flux.

4.4.2 Comparison of swirler results

Instantaneous snapshots have been shown in figure 4.7 rather than time-averaged HTC because when viewing highly unsteady cases many of the flow features are smoothed out to the point of being invisible, whereas they can be clearly seen instantaneously. Five different experimentally measured cases are shown. The case of a non-swirling turbulence grid effectively sets the baseline case with which the others may be compared. The passage vortex lift-off lines are clear as lines of low HTC near to each endwall, and are roughly symmetrical.

The case with a single swirler has an additional large area of lowered HTC on the second half of the suction side. This is thought to be the footprint of the midspan vortex pair lift-off or separation. The vortex is pushed towards the hub endwall by the residual swirl in the passage. Towards the trailing edge the midspan vortex lift-off is very close to, and appears merged with, the lift-off of the passage vortex.

The case of a reversed swirl direction is similar, except that since the direction of residual swirl is opposite, the vortex pair is pushed towards the casing endwall instead. Again, the lift-off of the passage vortex appears effectively merged with the midspan vortex pair.

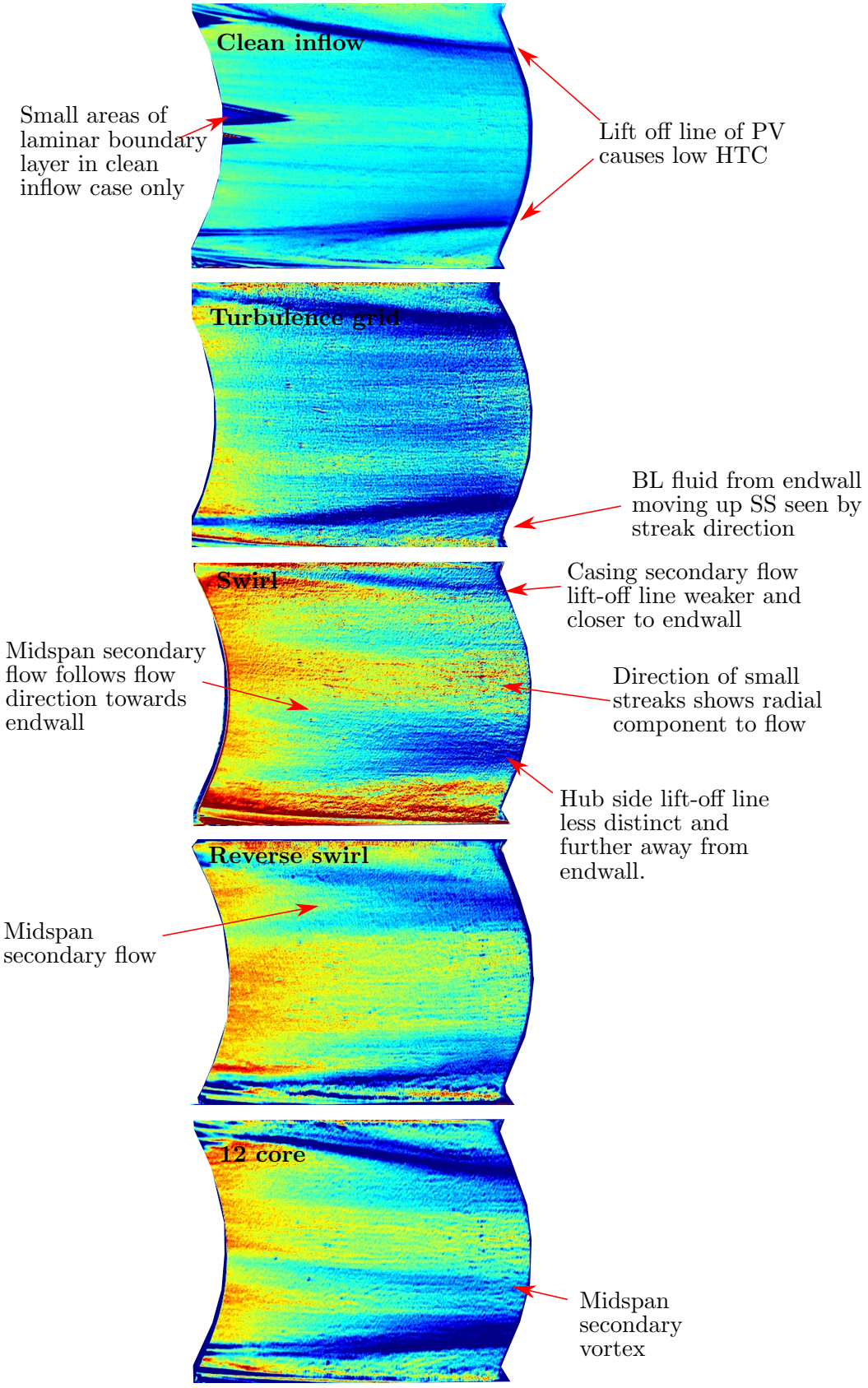


Figure 4.7: Instantaneous high speed IR HTC on suction side with different inlet conditions. This show secondary flows and flow directions caused by swirl

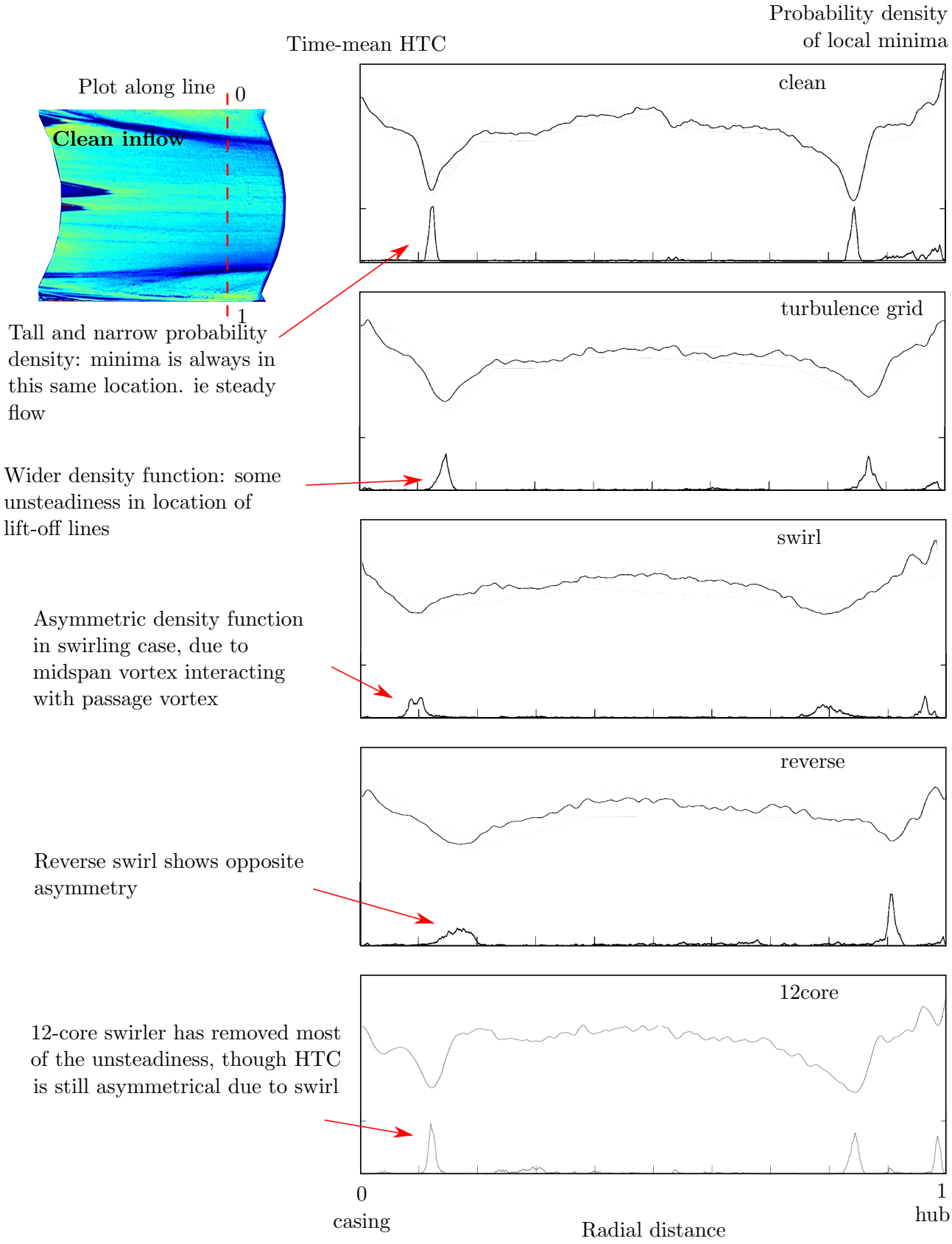


Figure 4.8: HTC and probability density of instantaneous local minima, plotted along line on suction surface showing change in passage vortex position with different inflow conditions

The 12-core swirler gives a lower level of residual swirl, and a smaller central pressure loss core. A midspan vortex pair is still formed, but it is not pushed so close to the endwall as in the case of the single swirler. The low HTC footprint also appears somewhat smaller in this case, although in all cases it is variable between timesteps. The multi-core swirler gives a lower level of unsteadiness, and the variation from timestep to timestep is much less than in the case of the single swirler.

In all swirling cases, the passage vortex lift-off line near to the midspan vortex pair is more spread out and diffuse than otherwise. It is thought that there may be some interaction between the two to cause separation over a larger area. Time averaged HTC contours do not show the effect of the vortex as clearly, because the unsteady position of the vortex results in the time-averaged HTC footprint effectively being smoothed over the surface.

Figure 4.8 shows the variation in passage vortex position depending on inlet condition. With a clear inflow passage vortex lift-off is a distinct line, which is constant in its position. A turbulence grid inflow results is passage vortex lift-off being less distinct and the position of the lift-off line is more unsteady.

As well as being useful for its own sake, HTC measurements can be used as a form of flow visualisation. The most obvious structures in figure 4.7 are the lift-off lines of the passage vortex. The passage vortex is generated as a result of flow turning in the passage, as discussed in section 3.1.2. On the suction side near to the endwall, flow has a radial velocity component up the suction surface away from the endwall. At some point the velocity vector points away from the suction surface back toward the midpassage. This is the lift-off line where flow is lifting off the surface, resulting in a low HTC. In high resolution and high sensitivity images such as those presented in figure 4.7, flow angles can be seen as streaking on the surface. In the non-swirling cases (clean and turbulence grid inflow), the flow over the rest of the vane is axial. In the swirling cases the streaks show a radial component, showing the effect of the overall swirl through the passage. In the case of reversed swirl direction this radial component is likewise reversed.

Below the passage vortex lift-off lines the surface flow direction has a large radial component, due to the passage vortex. This can be seen by the direction of surface streaking in this area.

Observing movies of time-varying HTC, it is clear that the clean inflow case appears steady flow, while a swirling case is highly unsteady. To show this difference the location of passage vortex lift-off lines, quantified as the local minima of HTC, is plotted along a line on the suction side for all timesteps. Figure 4.8 shows the probability density of the PV lift-off location, as well as time-averaged HTC along a line.

The clean inflow case is almost steady-state, with little variation in PV position. A turbulence

gird inflow, gives a greater unsteadiness, as indicated by wider probability density of PV location. In the swirling cases the locations of secondary flow lift-off lines are modified. On one side the lift-off line is much closer to the endwall. On the other, lift-off is further away from the endwall and has a larger spread. There is also evidence of an additional midspan secondary vortex, generated by the loss core of the swirling flow. In the case of reverse swirl, the directions are opposite, confirming the interpretation that swirl direction is responsible for pushing the vortex towards one side. A 12-core swirler, while showing some asymmetry in mean HTC due to swirl, shows comparatively little unsteadiness, as indicated by narrow probability density functions in figure 4.8.

4.5 Thin film gauges on vane surfaces

The high frequency and good signal to noise ratio of measurements obtained in this campaign allow time resolved heat flux to be visualised. Thin film data was acquired at a sampling rate of 10k samples/s, giving a Nyquist frequency of 5 kHz. Heat transfer coefficients have been measured over vane surfaces with 192 evenly spaced thin film gauges. Unsteady variation in HTC is plotted over the vane area. Timesteps are plotted every 0.2ms. Data was low-pass filtered to 1000Hz before plotting. A zero-phase filtering was used to ensure that no phase shifts were introduced by this process. A total of 15 timesteps (3ms) has been plotted for each case.

The spatial and temporal resolution of measurements is high enough to be able to see movement of flow structures over the vane surface. This is shown in a sequence of snapshots of data shown in figures 4.9 to 4.15. Both pressure and suction sides show this clearly.

4.5.1 Turbulence grid

Turbulence grid inflow data is shown in figures 4.9 and 4.10. Selected vortical structures have been identified by numbers and can be seen moving over the pressure side surface. Small structures near the leading edge can be seen to both move downstream, and grow in both size and strength as they do so.

On the suction side likewise heat transfer modifying structures can be seen first near the leading edge, and then being convected over the vane surface. More than on the pressure side, the effect of vortex stretching as flow accelerates can be seen. This is most clear in the pair of vortices labelled 1 in figure 4.10. From the leading edge, over the area of high HTC is seen to split into two stretched out 'filaments' over the suction side. In contrast to the observations on the pressure side, on the suction side the strength of the effect on endwall HTC is greatest near the leading edge, and lower further downstream.

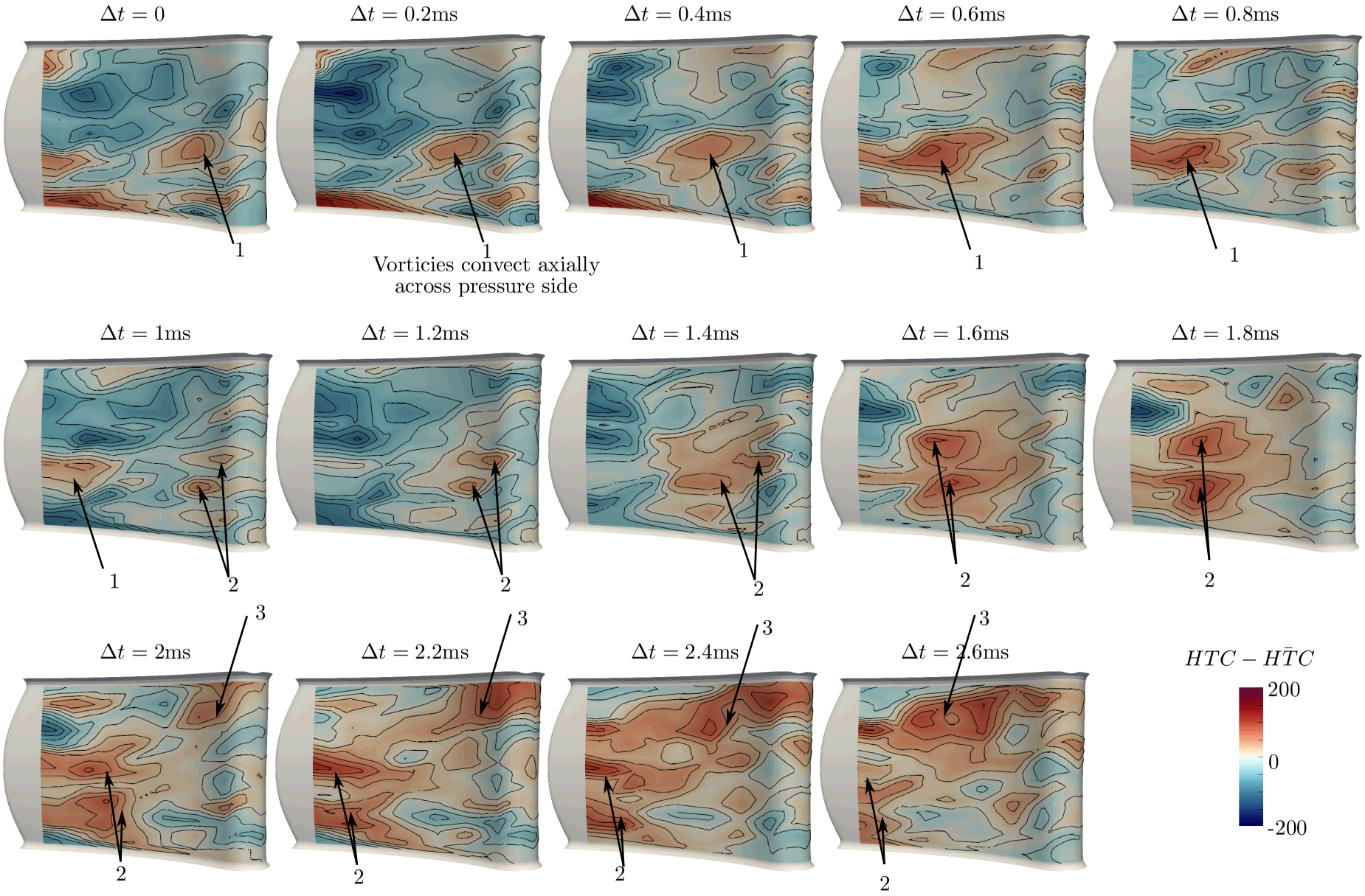


Figure 4.9: Time-varying HTC on pressure side with turbulence grid inflow. Turbulent vortex structures can be seen impinging on the vane and then flowing downstream.

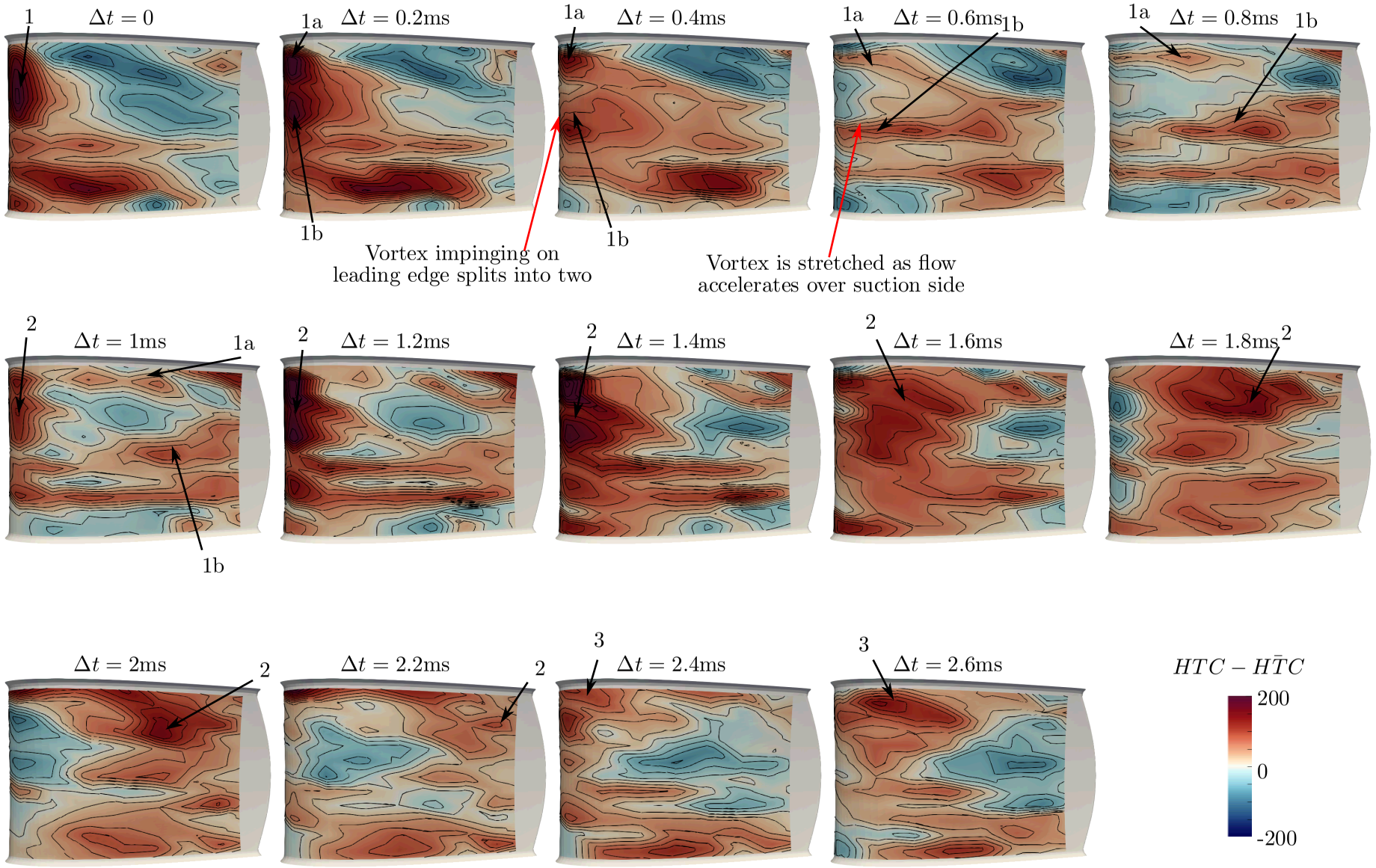


Figure 4.10: Time varying HTC on ss with turbulence grid inflow. Large turbulent structures impinge on the vane surface, and are then stretched axially by flow acceleration through passage.

4.5.2 Swirl generator

The swirling inflow case shows even larger structures than the turbulence grid inflow case. For example the structure labelled in figure 4.11 on the pressure side passes over most of the pressure side area. Unlike with a turbulent grid inflow, swirling flow the movement of some of the structures includes a radial component, from hub to casing.

On the suction side again, the swirling flow results in a radial component to the flow velocity, and larger and more coherent structures than with a turbulence grid inflow.

As well as the turbulent unsteadiness due to small, discreet vortex structures being convected through the domain, a swirling inlet also creates unsteadiness of a different sort. Large, coherent structures such as the swirl core move at a low frequency. The swirl core passing into one passage to the other creates a large footprint of HTC on the vane surfaces. This can cause both areas of increased or decreased HTC. For example figure 4.13 shows the swirl core passing into one passage causing a large area of increased HTC as the swirl core impinges onto the suction side. As the swirl core moves further a lower HTC results. This occurs in both the experiments, and in LES in figure 4.13.

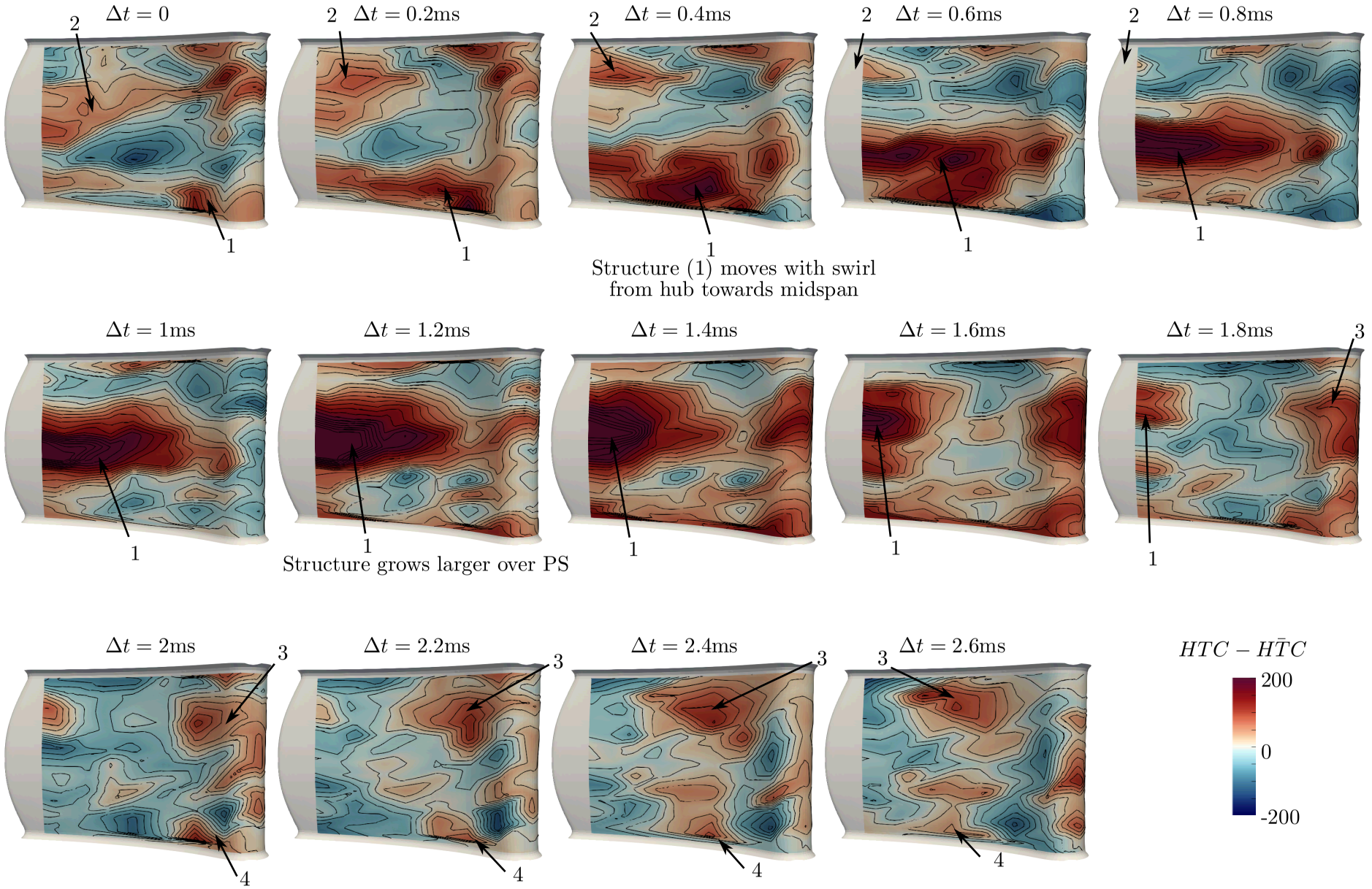


Figure 4.11: Time-varying HTC on pressure side with swirler inflow. As well as smaller turbulent structures convecting downstream similar to the turbulence inflow case, there is also the effect of the large unsteady swirl core in the passage.

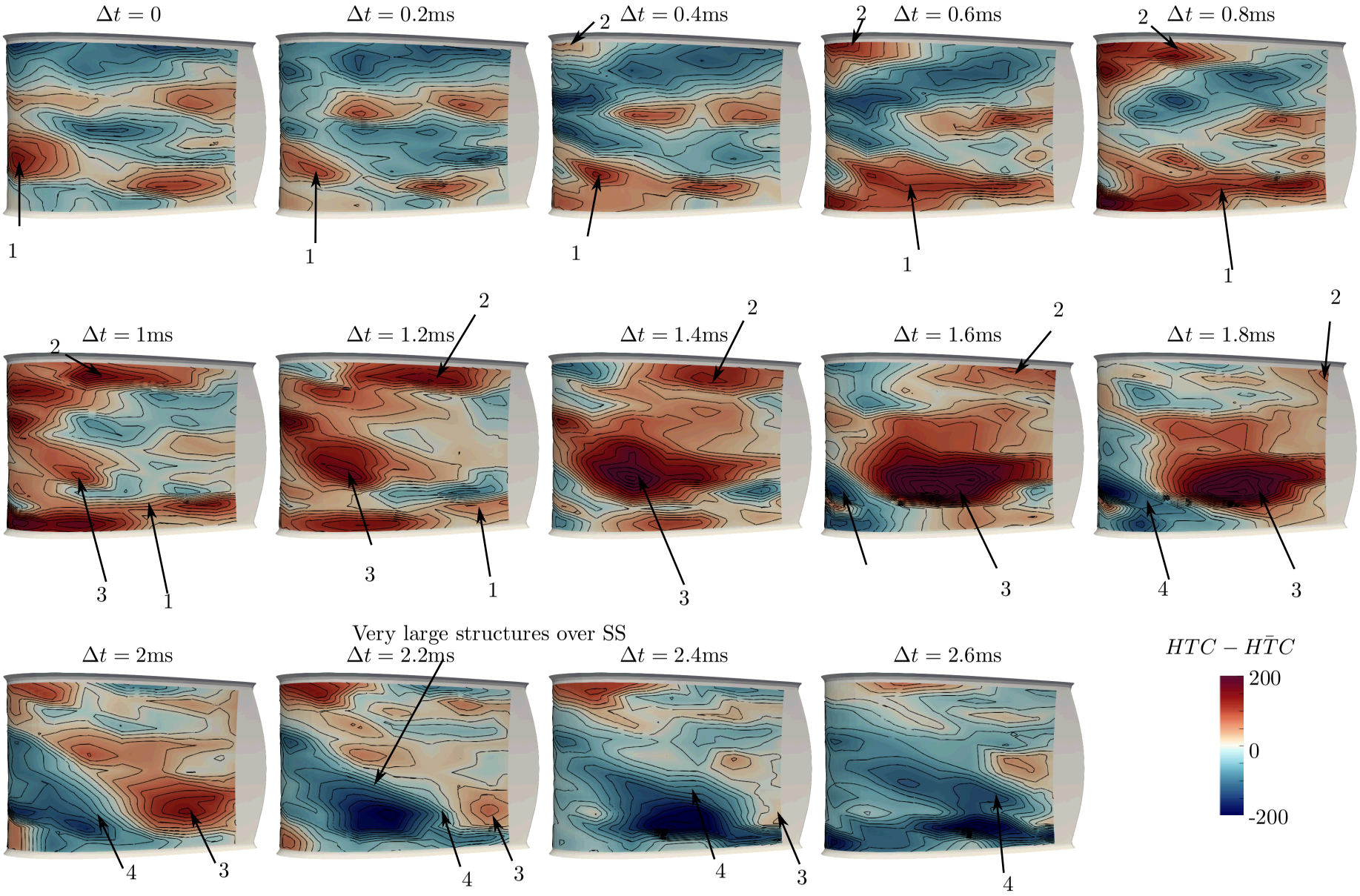


Figure 4.12: Time-varying HTC on suction surface with swirling inflow. Incoming turbulent structures are stretched axially as flow accelerates through passage. Large structure of precessing swirl core affects HTC as it moves into passage

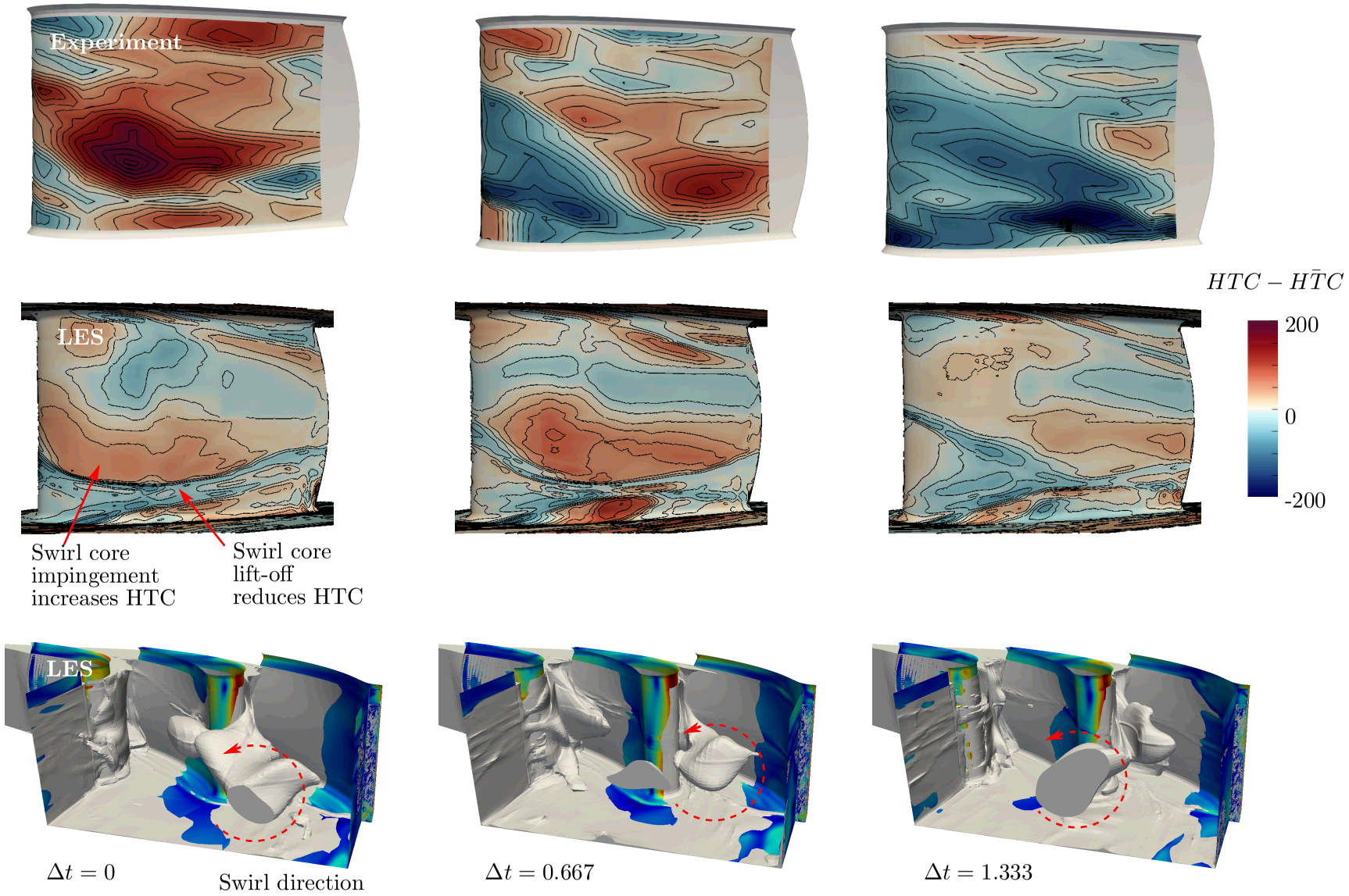


Figure 4.13: Comparison of LES to TFG measurements

4.5.3 Clean inflow

The overall magnitudes of HTC variation in time with a clean inflow do not differ much from when a turbulence grid inflow is used. In the clean inflow case, unsteady HTC structures do not appear to convect downstream with the flow direction, but are instead attached to the vane surfaces. This is thought to be indicative of vortices being generated within the vane boundary layer, and growing through the passage. In contrast, freestream turbulence convects though the passage, leaving modifying the HTC of the nearby vane surface as it passes by.

Figure 4.14 shows the fluctuations on the pressure side of the vane with a clean inflow. While near the leading edge and forwards part of the pressure side, there are small areas towards the trailing edge which show very high levels of fluctuation. Figure 4.15 shows the fluctuations on the suction side with a clean inflow. There are lower levels of fluctuation over most of the area, although near to each endwall there are greater levels of fluctuation. This is thought to be due to the instability of the suction side leg of the horseshoe vortex, discussed in section 4.6.

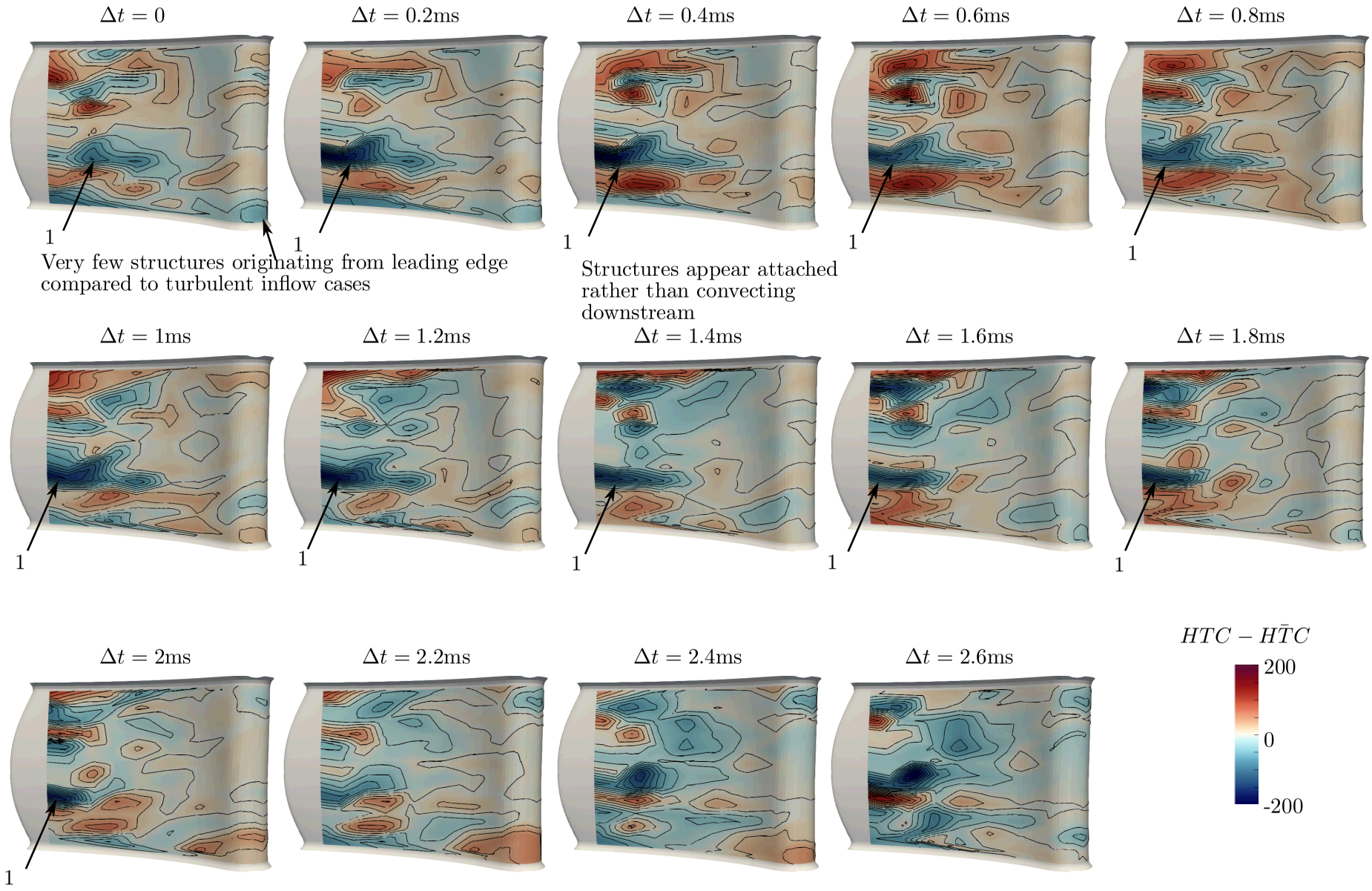


Figure 4.14: Time-varying HTC on pressure side with clean inflow condition. Unlike the high turbulence and swirling inflow cases, there are few large structure convecting from upstream. Instead attached vortices generated within the vane boundary layer can be seen

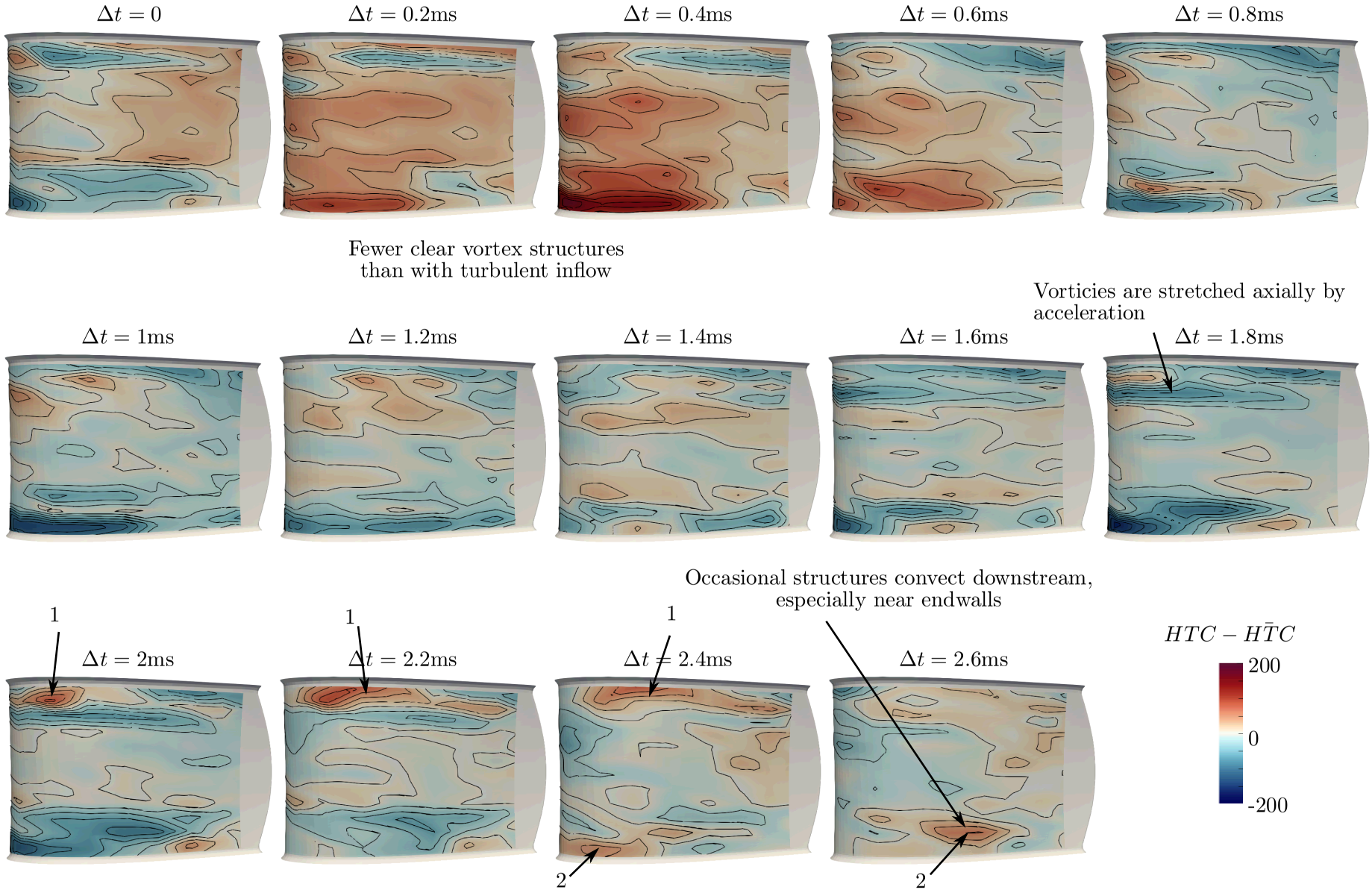


Figure 4.15: Time-varying HTC on suction surface with clean inflow. There are not large turbulent structures visible convecting from upstream. Attached vortices are stretched axially by acceleration.

4.5.4 Unsteady fluctuating heat transfer

Figure 4.16 shows the unsteadiness of HTC, quantified as the root mean square(RMS) of HTC, over the vane surfaces for the different inlet conditions.

$$\mathrm{RMS} = \sqrt{\frac{1}{P}\int_0^P (\mathrm{HTC} - \bar{\mathrm{HTC}})^2 dt} \tag{4.1}$$

Compared to a case with turbulence grid inflow, the swirler creates a distinct region of high fluctuations near the midspan, on both pressure and suction sides. This is also present, though at a lower magnitude, when the 8-core swirler inflow is used.

More surprisingly, there are a few areas in which a clean inflow gives the highest unsteadiness. On the pressure side near the throat, there is the highest unsteadiness in clean inflow cases. The features causing this can be seen in the unsteady results, figure 4.14.

4.5.5 High frequency endwall thin film gauge results

The overall RMS amplitude of the fluctuations in HTC are plotted in Figure 4.17, along with plots of relative bandpower of different frequency ranges. These frequency ranges have been chosen based on characteristic peaks in the frequency spectra of the gauges. In this way the endwall can be split into regions based on the characteristic frequencies present. This has been illustrated by the frequency spectra of a selection of individual gauges. This is shown for only the turbulence grid inflow, the results for swirling inflow and for clean inflow were very similar to turbulence grid case, and so have not been repeated.

Starting with the RMS plot: there is a high amplitude of unsteady HTC at the leading edge of the vane on the right hand side of the plot. This region also shows an extremely high HTC. This is caused by the HV intermittently causing flow impingement onto the endwall [68]. This is concentrated in a range of 1-2 kHz, though there is also a large amplitude of broadband heat flux as well.

Moving across the passage towards the pressure side, there is a significant level of fluctuation within the low HTC triangle upstream. In the spectra this is concentrated around a peak of 1800Hz.

Very close to the pressure side there is a quiescent region with almost no fluctuation in HTC. This is reminiscent of the work of Harrison [50] , who suggested that this indicated that a fresh, laminar boundary layer was being generated behind the horseshoe vortex. These results support this interpretation. Transition to turbulence occurs quickly a short distance downstream, which is to be expected given the high Reynolds number of the flow. The thin, laminar boundary layer transitioning to turbulence may partly explain the high HTC levels observed near to the pressure side. Boundary

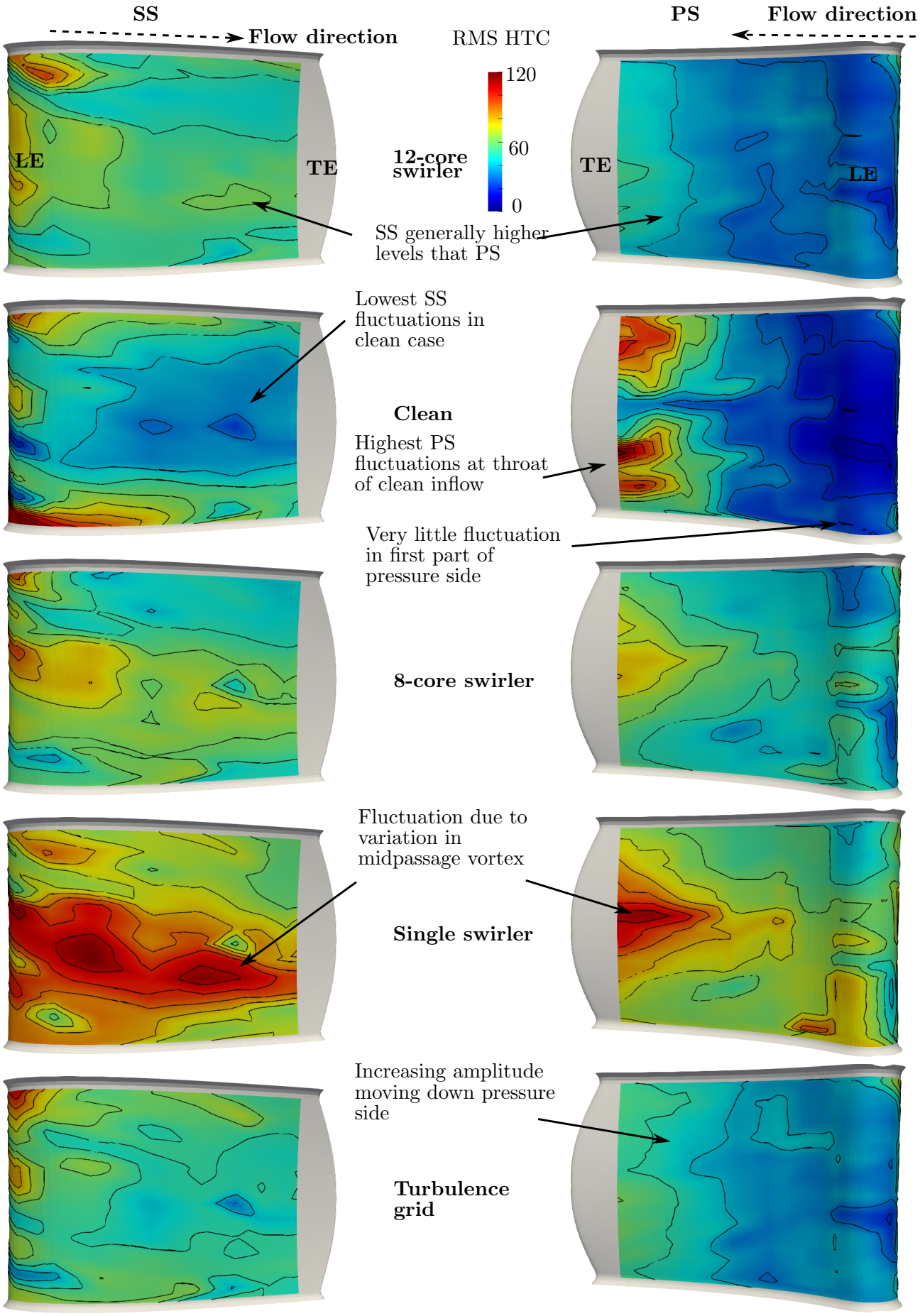


Figure 4.16: Root mean square of fluctuation in heat transfer coefficient with different inlet conditions

layer transition occurred at the same location in all cases.

Progressing along the pressure side downstream, fluctuations steadily increase, showing a characteristic frequency of 1250-1600 Hz, increasing in amplitude towards the very end of the vane. This also reflects the steady increase in HTC in this region.

Past the end of the vane in the wake there is an extremely high amplitude of broad band heat flux, as well as an extremely high time averaged HTC. This is due to the turbulent boundary layer from the vane surfaces being shed. The true von Kármán vortex street frequency was not resolved, being estimated at about 12 kHz (up to 5 kHz was measured at 10k samples/s).

Towards the suction side of the vane there is less fluctuation. An extremely sharp and distinct peak in the frequency spectra was observed at 450Hz.

An additional secondary peak was observed in the spectra of many gauges at 2250-2750Hz. Plotting the bandpower of this range shows three distinct patches along the passage.

Figure 4.18 shows the characteristic areas of the endwall, by reducing each of the plots in Figure 4.17 to a single contour line, or two contour lines for the rms plot, and overlaying them over an HTC plot.

It is not certain what the causes of all of these features are, and how they link to the time averaged HTC in each region which is of most practical importance. The experimental measurements showed frequency spectra which were not predicted by LES. The causes of all these features are not yet known.

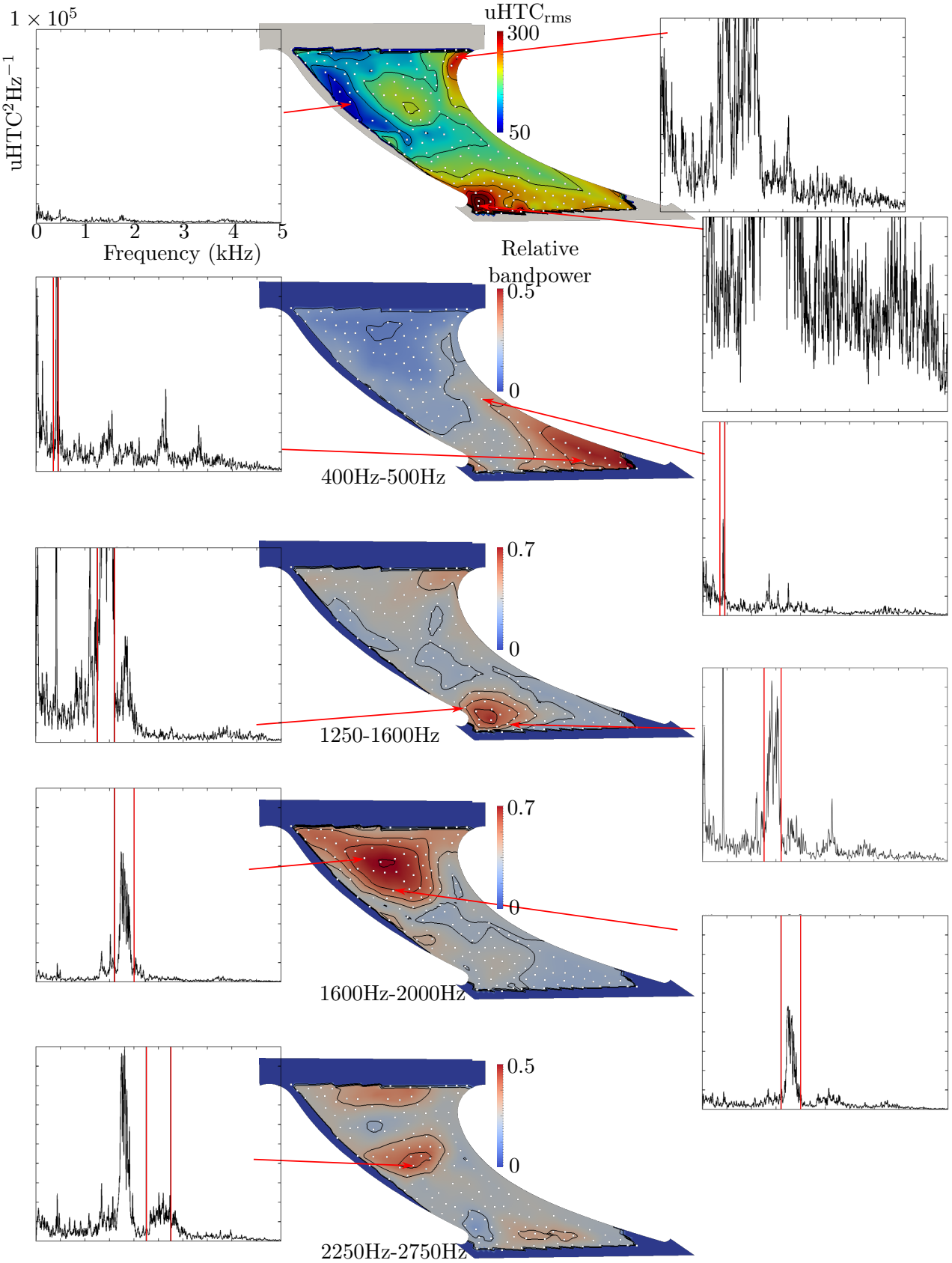


Figure 4.17: Contours of unsteady content on endwall, for different frequency range. Turbulence grid inflow data is shown, but swirling and clean inflows show similar result. Top: total rms amplitude of fluctuations in unsteady HTC. Below: relative bandpower of fluctuations for chosen frequency bands. Left and right: spectral density plots for single gauges indicated

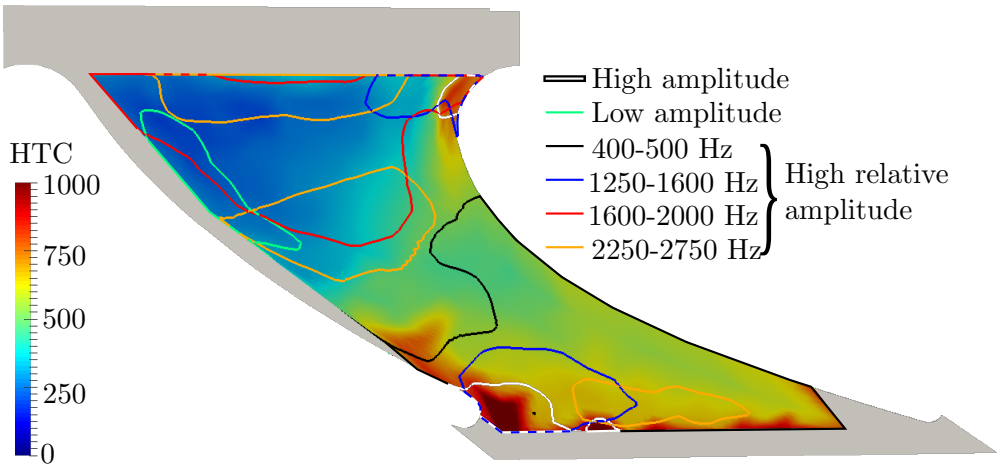


Figure 4.18: Summary of characteristic areas of endwall, overlaid on HTC

4.6 Fluctuating horseshoe vortex near vane leading edge

4.6.1 Importance of horseshoe vortex area

Figure 4.19 shows the heat transfer coefficients over a vane endwall measured using thin film gauges. The locally highest are of HTC, after the wake, is located near to the leading edge of the vane. This area of enhanced HTC is caused by the so-called horseshoe vortex (HV). The horseshoe vortex may affect cooling flows and affects secondary flows further through the passage, so it is important that it is well understood. As well as enhancing time-averaged local heat transfer, the HV is also highly unsteady, with large fluctuations in instantaneous heat transfer of up to 100% above the time-mean. As figure 4.19 shows, there is a characteristic frequency range which is associated with the HV regardless of inflow conditions, as well as additional low frequency fluctuations in the turbulent and swirling cases caused by variation in incoming flow.

Existing literature on unsteady behaviours of the HV is reviewed, before the experimental data is examined and LES is used to help explain some of the phenomena which take place with swirling inflow.

A horseshoe vortex forms near the leading edge

While this standard explanation is extremely helpful in understanding the formation of the horseshoe vortex, for many practical flows it is oversimplified. Baker [70] shows in detail the formation of the HV in laminar flows. There may not only be one main HV, but may be two, or even three distinct, co-rotating depending on flow velocity, with higher velocities forming more vortices. At even higher flow velocity the horseshoe vortex system becomes oscillatory, first periodically, and then irregularly. Thomas [71] also measured the oscillation frequency of the HV, finding a St up to 0.35, increasing

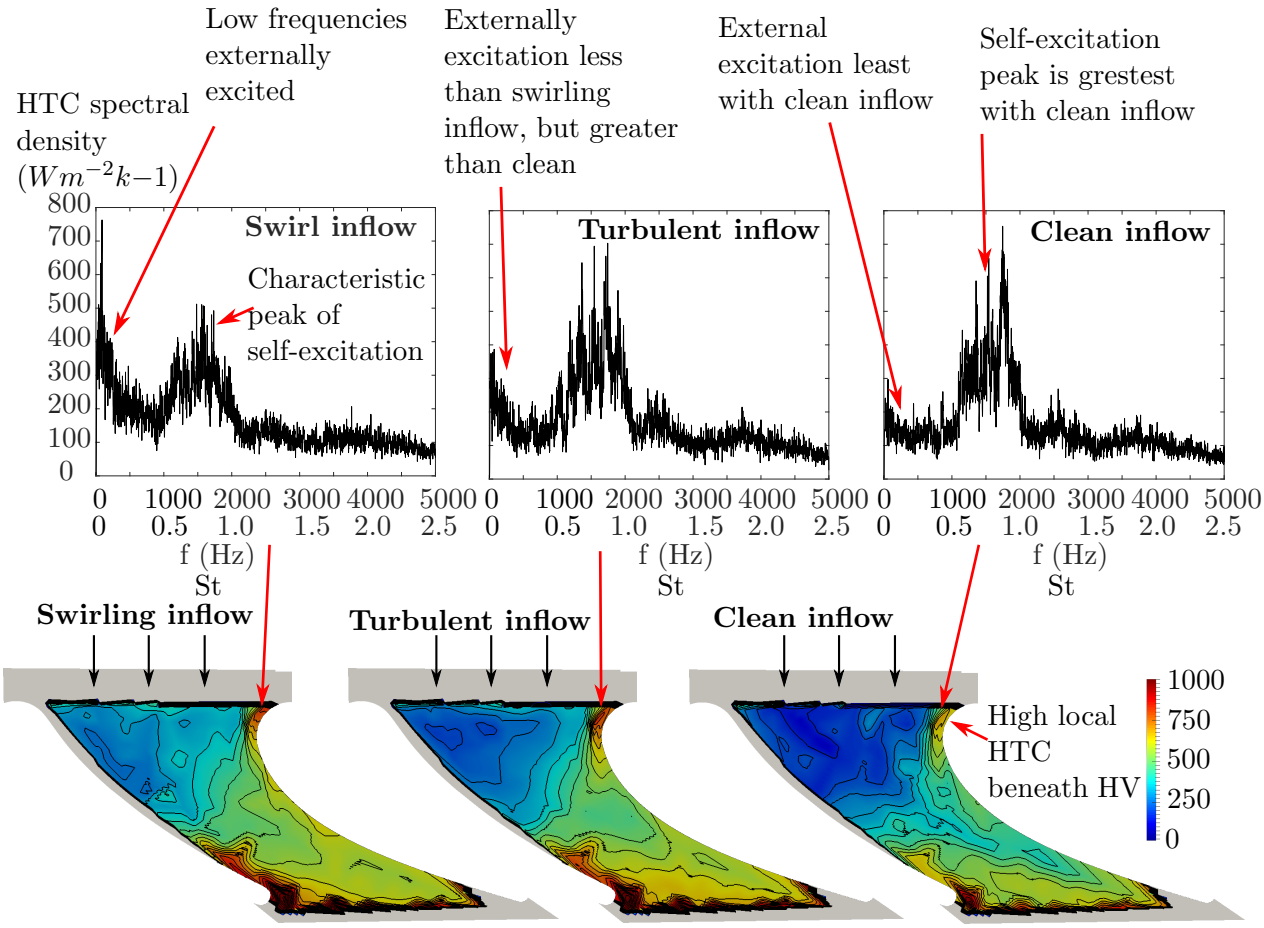


Figure 4.19: Heat transfer coefficient contours with three different inlet conditions, and spectra of fluctuations for the same gauge beneath the horseshoe vortex. The horseshoe vortex generated both a high HTC and high levels of fluctuations. The swirling inflow has the most low frequency fluctuation, while the clean inflow has slightly higher levels in the 1-2kHz range

with Re.

Unsteady oscillation of the HV are investigated in more detail by Lin et al.[72], using particle-image velocimetry (PIV). As well as steady vortex systems at low speed, what they term a periodic breakaway vortex system is measured in detail, showing a sequence of two horseshoe vortices, with the further upstream vortex growing in size and moving forwards to consume the first vortex, before in turn being swallowed by another newly formed vortex which grows upstream. The Strouhal number of this oscillation, based on boundary layer thickness, was found to be independent of Reynolds number. At even higher velocities the horseshoe vortex system becomes turbulent and irregular.

Simpson [73] reviewed the existing literature on the formation of a horseshoe vortex.

The effect of an unsteady horseshoe vortex system on endwall heat transfer was measured in detail by Praisner and Smith [68, 69]. Two bands of high heat transfer were found, corresponding to the attachment points of two distinct horseshoe vortices, which they call the HV and tertiary vortex (with secondary vortex referring to a counter-rotating vortex between them). The band of high heat transfer nearest to the LE was quite steady and constant in time, while the band further away caused by the second HV was irregular and highly fluctuating in time. By acquiring heat transfer and PIV measurements in synchronicity, heat transfer could be linked to specific flow events such as transient mainstream fluid inrush.

Launay et al. [74] also recently carried out an unsteady investigation of the horseshoe vortex, and give detailed explanations of the out of equilibrium dynamics.

There have been some suggestions to reduce the HV and its consequent detrimental effects by modification to vane geometry. While the HV formation is insensitive to the shape of the LE, from bluff to sharp to streamlined, some success has been reported by the addition of large fillets to the endwall junction. Zess and Thole, [75], showed that the HV could be reduced in this way, reducing turbulent kinetic energy generation and consequent losses. Lethander and Thole [76] further showed thermal benefits resulting from reducing the HV with a fillet.

4.6.2 Instability of horseshoe vortex near leading edge

Figure 4.19 shows experimentally measured spectra of the horseshoe vortex fluctuation. There is a clearly distinct broad peak in fluctuations around 1100-2000Hz, corresponding to a Strouhal number based on leading edge diameter of 0.55-1.0. A similar frequency spectra is seen on several of the gauges near to the leading edge, but does not resemble the spectra of any other areas of the endwall.

The frequency of oscillations was not linked to any other known forcing frequency, neither the vortex shedding from the combustor wall or any other known frequencies. An interesting observa-

tion is that this broad peak does not vary much with different inlet conditions. Comparing clean, turbulent and highly swirling inflows, the oscillation in this frequency band is in fact greatest in the low turbulence case, and less with turbulence grid inflow or swirling inflow. This was also similar in experimental cases with different inlet conditions, so is thought to be a natural, self-excited oscillation of the vortex itself.

This is broadly consistent with the work of others. The Reynolds number based on LE diameter is 1.8×10^5 in this case, according to the studies cited this would place it into the oscillatory regime. The studies by Baker [70], and Lin et al. [72], both found that above a particular Reynolds number the HV becomes oscillatory. Baker performed experiments up to $Re = 1.4 \times 10^4$, one order of magnitude lower than this case, and observed a value of $St = 0.53$ for the highest speed case, with some increase in St with Re. This agrees well with observed St of 0.55-1.0. Lin et at performed experiments up to $Re = 5000$; maximum $St = 0.35$, but again increasing with Re.

The lower frequency variations, below 1000Hz in figure 4.19, are greatest in the case of swirling inflow, and least in low turbulence inflow. This is the influence of incoming flow unsteadiness, as a similar pattern is observed in many other areas of the vane and endwalls when the swirling inflow is used. In the case of swirling inflow, these flow-excited variations cause the greatest variation in heat flux, though in the clean cases the self-excited variations are greatest.

The time-varying behaviour of the horseshoe vortex appears to be a combination of flow induced variation, caused by turbulent unsteadiness of the incoming flow, and self-excited unsteadiness, regardless of inlet flow turbulence.

4.6.3 Self-excited instability of horseshoe vortex

The nature of the self-excited instability of the horseshoe vortex is illustrated schematically in figure 4.20, along with an instance of this sequence of events occurring in LES. The horseshoe vortex at the leading edge is caused by the vane stagnating the incoming boundary layer. Once formed however, the horseshoe vortex may essentially act as a blockage itself. This can cause sufficient blockage to generate a second HV upstream of the original vortex, as if it were an actual, material blockage. Once this secondary HV has formed sufficiently, it is effectively shielding the original HV, which may consequentially reduce and 'die', allowing the secondary HV to advance towards the LE and so becomes itself the primary HV.

Areas of high heat flux occur when mainstream flow impinges onto the surface, while vortex lift-off results in a lowered heat flux. While vectors are shown in a plane normal to the vortex, the HV is of course a three dimensional structure. Changes to the position and form of the vortex do not apply to

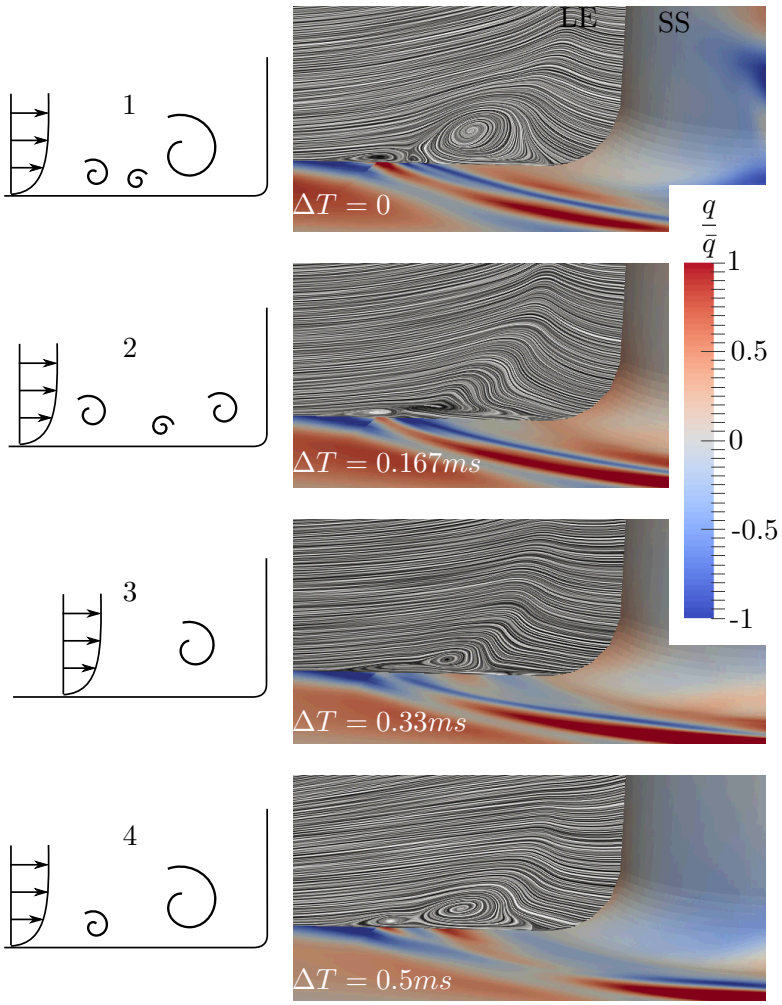


Figure 4.20: Explanation of behaviour of HV system in high Re flow. Sketch of mechanism of evolution of unsteady HV system, along with example timesteps from LES. LES velocities visualised using LIC, along with surface heat flux deviations.

the entire vortex simultaneously, but begin at the leading edge, and propagate around the vane along the vector of vorticity. This can be seen by the movement of the heat flux 'footprints' of the vortex convecting from frame to frame in figure 4.20.

While the evolution of the HV sometimes follows this regular progression as illustrated, it also often deviates from it, and varies in an irregular fashion. Small vortices often form and then disappear, or are absorbed into the main vortex, this sometimes appears to be linked to changes in the incoming flow, and at other times appears to be spontaneous.

It seems probable that mainstream turbulence 'interfering' with the natural evolution of the HV is why the self-excited frequencies are less strong measured with swirling or turbulence grid inflow than a with clean inflow.

4.6.4 Influence of incoming flow on horseshoe vortex of unshielded vane

In addition to the intrinsic unsteadiness of the high Re horseshoe vortex, the large scale unsteady flow structures coming from the inlet flow can have a significant impact on the horseshoe vortex. The incoming flow field has large scale, slow fluctuations due to the large structures created by the upstream swirl generator, and in particular, the swirl loss core, as is discussed in section 4.3. Concerning the horseshoe vortex, the most important features of the incoming flow are the boundary layer thickness and the flow velocity, or in non-dimensional terms, the Reynolds number with respect to boundary layer thickness, and Reynolds number with respect to geometrical length scale. In this flow however, these two properties both vary greatly with time, in the vicinity of the vane-endwall junction.

The impinging boundary layer thickness is mostly influenced by the position of the swirl core. The vane is placed directly behind the swirl generator, so when examining time averaged results the swirl core appears to impinge directly onto the central vane, however, the position of the swirl core is extremely unsteady in both its strength and position; this is described in detail in section 4.3. As the swirl core moves from one side of the passage to the other, the boundary layer thickness of the flow impinging onto the central vane changes, and so affects the formation of the horseshoe vortex. Similarly, the axial velocity in the vicinity of the vane endwall junction also varies greatly, leading to changes in the strength of the HV.

This is illustrated in figure 4.21. The time averaged inlet total pressure is shown, showing the thickening of the boundary layer on the upwash side of inlet swirl, and thinning on the opposite side. Four different instantaneous timesteps are shown illustrating the different near junction flow and the HV which results. In timestep (a), the local mainstream velocity is high, and there is also an off-centre swirl core. The high velocity means there is a greater amount of circulation in the incoming flow, while

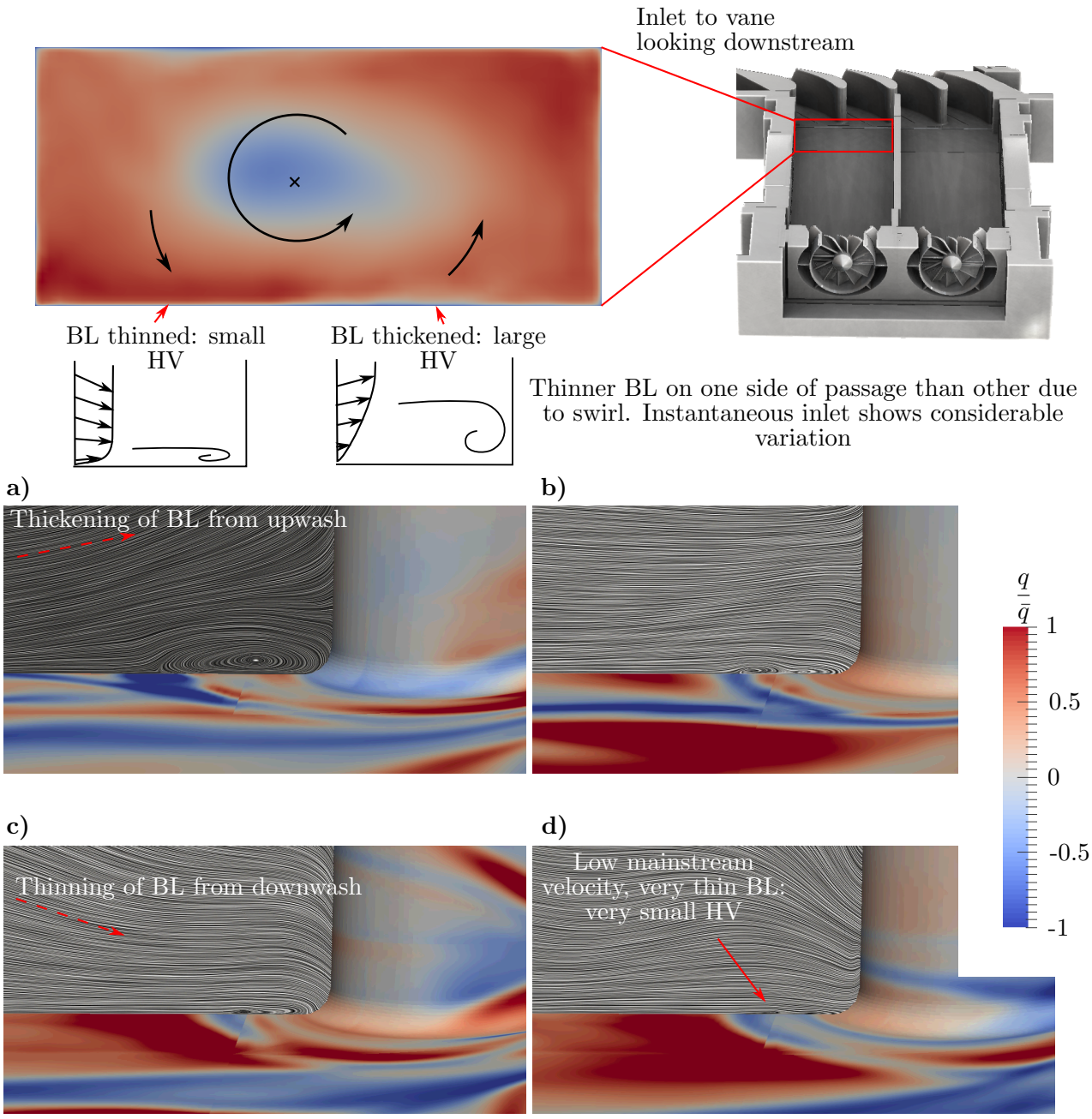


Figure 4.21: Large scale changes to horseshoe vortex as a result of large structures in mainstream flow in front of the unshielded vane

the position of the swirl core is causing the radial component of velocity, indicated with a dashed line. This causes a thickening of the boundary layer. Together these effects result in an extremely large and strong horseshoe vortex. In timestep (b), there is no significant radial component of velocity, and the boundary layer is thin. The local mainstream velocity is not as high, and so the horseshoe vortex is weaker. In timestep (c), the flow velocity is higher, which results in a strong HV. in timestep (d), the swirl core has moved to the other side of the vane, and so there is a radial component of velocity in the opposite direction. This accelerates the flow near to the wall, and so there is only a very thin boundary layer to form the horseshoe vortex, resulting in an extremely small vortex. This case also has the lowest local HTC on the endwall, as a result of the smaller vortex.

The effects of mainstream flow variation is greatest by the leading edge of the unshielded vane. The shielded vane does not experience such large scale influences on incoming boundary layer thickness because the swirl core does not impinge directly onto it.

4.7 Analysis of unsteady passage vortex

From the leading edge, the pressure side leg of the horseshoe vortex extends through the passage, and is merged with the boundary layer vorticity of the turning flow, forming a passage vortex. Typically this passage vortex straddles the passage to the suction side of the adjacent vane. The passage vortex is often considered as a steady state phenomena, and experiments indicate that with low turbulence inflows it is, but when there is a highly turbulent and swirling inflow, there is a great deal of unsteadiness present. The passage vortex is both extremely mobile, from time to time sweeping across the whole of the passage, and is also highly variable in size. While at most times the passage vortex is continuous with the pressure side leg of the leading edge horseshoe vortex, at other times a secondary passage vortex may form in addition.

Figure 4.22 gives an indication of how much variation in secondary flow there can be from time to time. While the first image shows a strong lift-off line and the strong radial component of velocity can be seen by surface streak-lines below the lift-off line. In the second, representing a fraction of a second later in the same run, no evidence can be seen of the suction side secondary flow or passage vortex lift-off by the same endwall. The flow continuously switches between these and intermediate states throughout the run.

4.7.1 Passage vortex and secondary flow unsteadiness

Recently, there have been more studies making use of LES for investigations of the passage vortex and secondary flows. Jacobi et al. [14] found that the passage vortex may be unsteady when inflow

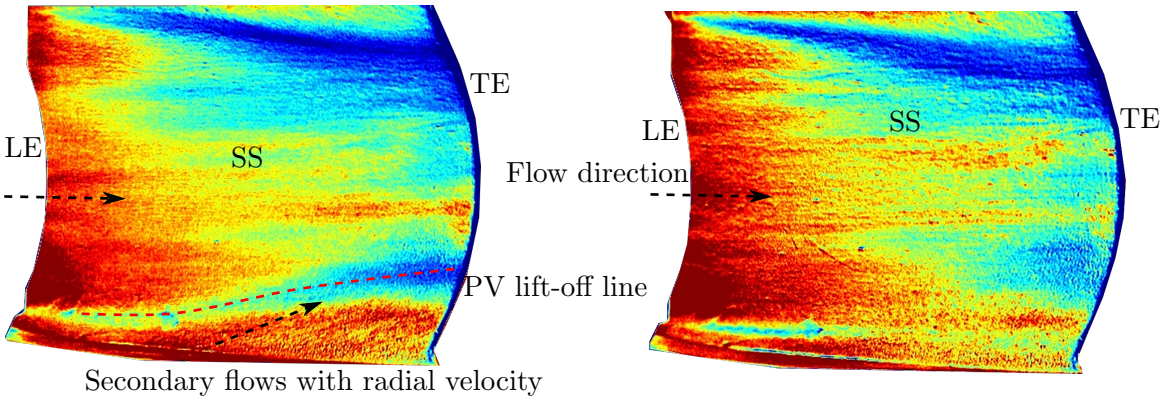


Figure 4.22: Two instantaneous instances of unsteady HTC on suction side of vane, measured by high speed IR, showing extremes of unsteady variation in secondary flows. Left: suction side secondary flows are strong, PV lift-off line is far away from endwall. Right:barely any evidence of SS secondary flow visible; no lift-off contour, and surface streak-lines appear axial even close to endwall.

is highly turbulent and swirling, and can sweep across the entire passage. It was speculated that this could lead to the periodic removal of film cooling. More detailed investigations were called for to gain a full understanding of the phenomena.

Cha et al. [66] suggested that with the extremely high turbulence levels the conventional passage vortex system breaks down, as there is more vorticity in the freestream turbulent eddies than in the boundary layers.

There have been to date few comprehensive experimental studies of the unsteady behaviour of the passage vortex. While in many cases the passage vortex may be a mostly steady phenomenon, it has been observed here that incoming flow turbulence may be sufficient to switch from a steady to an unsteady behaviour.

4.7.2 Passage vortex on endwall

The endwall heat transfer was measured at high frequency using a high density array of thin film gauges, described in detail in section 2.4.

Time averaged HTC contours are shown in figure 4.19 for three different inlet conditions. In the case of clean inflow there is a streak of lowered HTC which is thought to be the footprint of the horseshoe vortex and then the passage vortex lift-off. This extends from near the leading edge downstream towards the suction side of the second vane. In the high turbulence and swirling inflow cases, there is still a lowered HTC in this area, but in a broad u-shaped contour, rather than a distinct line. This is thought to indicate that the passage vortex is either more diffuse in these cases, giving a less distinct lift-off line; or that the passage vortex remains instantaneously distinct, but has some variance in its position, and so when time-averaged the footprint is spread over the passage.

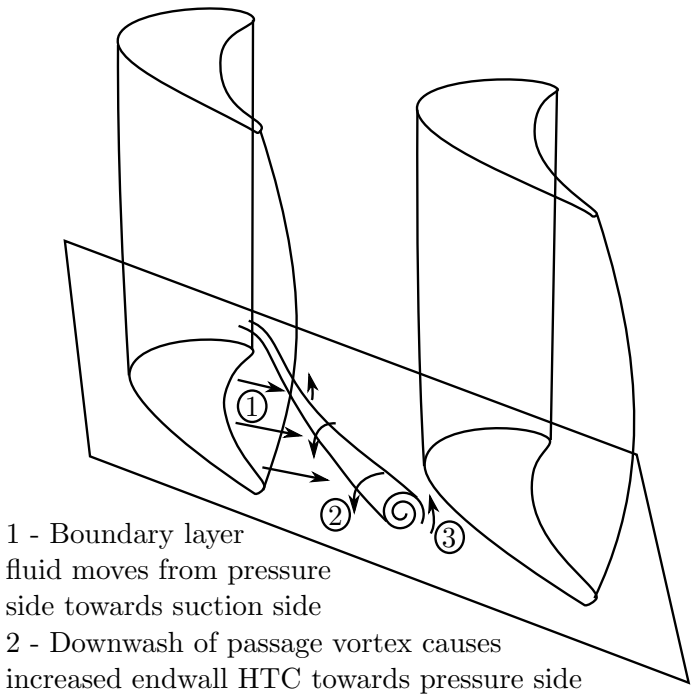


Figure 4.23: Simplified illustration of passage vortex impingement and lift-off causing enhancement of endwall HTC

The time varying position of the passage vortex can be seen by examining the instantaneous unsteady HTC. Both absolute values of unsteady HTC and the percentage deviation of HTC from the time averaged value is presented, for the same timesteps in each case. This data is shown for the swirling inflow cases in figure 4.24. The normalised heat flux is around a mean of zero, while the time mean of the unsteady HTC is equal to the steady HTC shown in figure 4.19. In all images, the likely position of the passage vortex has been identified when possible. The sense of rotation of the passage vortex is such to create a line of lowered HTC towards the suction side, with higher HTC towards the pressure side, due to the impingement and lift-off on each side of the vortex, as sketched in figure 4.23. This has been done by looking for streamwise-aligned contours of heat flux, indicative of the passage vortex lift-off, as in the steady state case. Each pair of HTC and Δq plots are the same instance, but plotting both aids understanding, as both absolute levels and deviations can be seen together.

Axially aligned flows are overwhelmingly dominant in the relative heat flux, especially in the downstream sets of plots. These unsteady, streamwise heat flux contours are caused by the instantaneous position of passage vortex lift-off.

The PV does remain as a distinct structure within the flow, but one which is unstable in its position. This based on the observation that the contours of instantaneous HTC for a given snapshot show the enhancing effect behind the PV just as distinctly in the highly turbulent cases (both swirling inflow and turbulence grid inflow) and as for the clean inflow. After being time averaged, the HTC

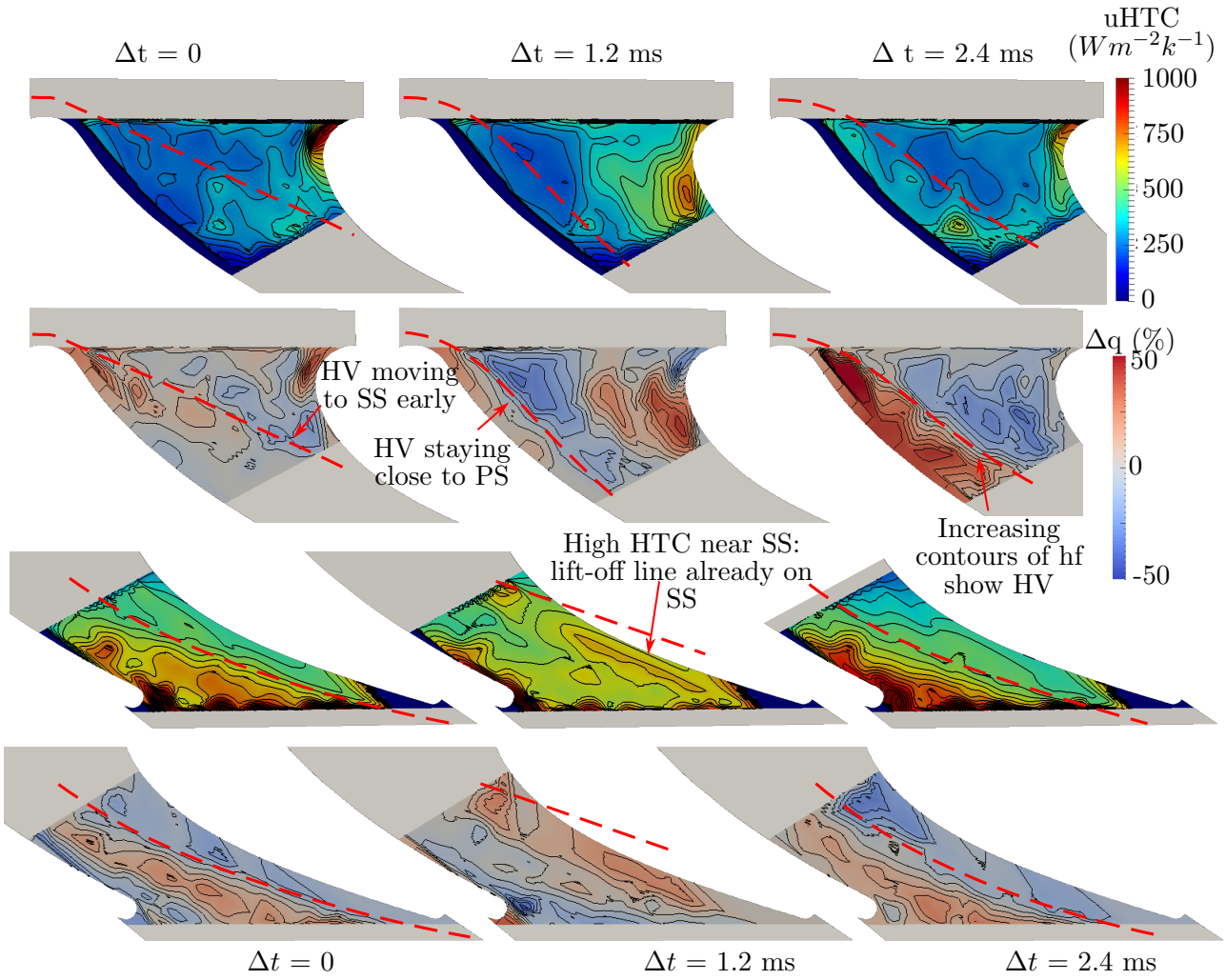


Figure 4.24: Unsteady experimental measurements with swirling inflow. Top to bottom row: uHTC upstream, Δq upstream, uHTC downstream, Δq downstream. Position of the PV/HV marked.

contours have been smoothed out in the swirling and turbulence grid case, but remain distinct only in the clean inflow case as the PV has been steady in its position.

The unsteady passage vortex at various times appears to traverse nearly the entirety of the passage, from its own pressure side to the suction side of the adjacent vane. In some instances in the case of the swirling inflow, there is no clear instantaneous footprint on the downstream section, for example the second timestep in figure 4.24. This may be indicative of a vortex which has moved across to the suction side especially early, as seems to have happened in the first timestep of the upstream measurements in figure 4.24.

The time taken to move from one side of the passage to another is around 3-3.6ms, giving a characteristic frequency of a full cycle of around 150Hz. However, it must be emphasised that the behaviour of the vortex is a stochastic process caused by random large eddies generated by the swirler or turbulence grid, so any time scales should be considered an average, rather than a regular interval.

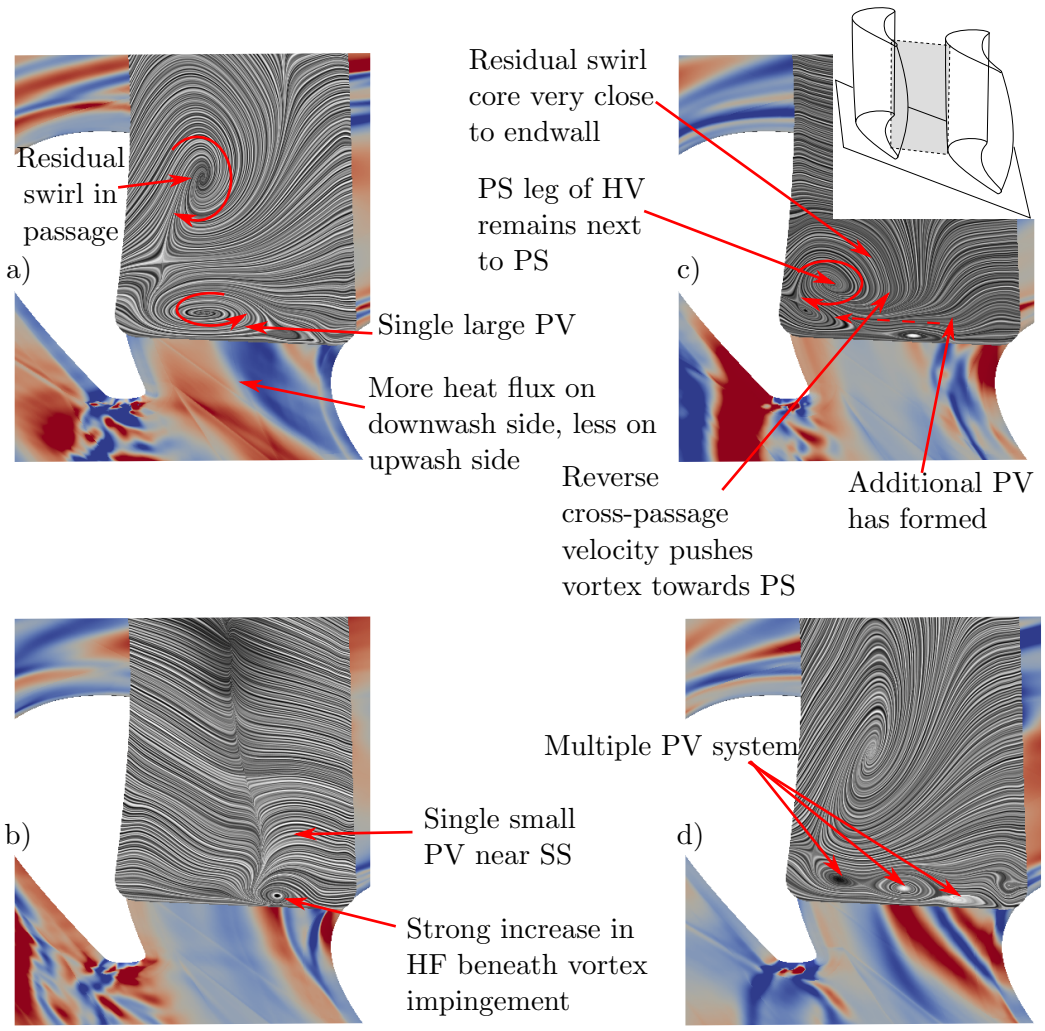


Figure 4.25: Snapshots of streamlines in passage showing various positions of passage vortex and swirl core

4.7.3 Large eddy simulation results showing unsteady passage vortex

LES helps to give additional insight into the state of the unsteady flow. Figure 4.25 shows the different positions the passage vortex can take at various times, and its effect on heat transfer. Figure 4.25 (a) shows a large PV in the middle of the passage; there is enhanced heat transfer on the downwash side and reduced heat transfer on the upwash, as expected. The large size of this PV corresponds to the extremely large HV which is generated at the LE at this time (see figure 4.21).

In figure 4.25 (b) there is a small and localised PV, nearby to the SS, as is expected in the ordinary model. Just as the over large PV previously mentioned derived from the over-large HV at the LE, the very small and localised PV in this timestep corresponds to a small HV at the LE.

In figure 4.25 (c) the swirl core has moved very close to the endwall and pressure side of this passage. There is an ordinary HV/PV nearer to the SS; very close to the PS an additional vortex has formed, counter-rotating with the swirl core.

Finally figure 4.25 (d) shows a system in which multiple streamwise aligned passage vortices have formed.

Figure 4.26 shows for one timestep the conditions which have resulted in the horseshoe vortex momentarily becoming attached to the pressure side of the vane, rather than crossing towards the adjacent vane suction side. The swirl core has moved towards one side of the transition duct, so that there is a very large residual swirl concentrated in one passage. This swirl means that rather than being purely axial, the inlet flow has a large circumferential velocity near the endwalls. This leads to a large radial pressure difference on the vanes, especially the pressure side, as the flow near the hub has to be turned much more than near the casing. Since there is a radially varying pressure on the vane pressure side, fluid near the pressure side follows this pressure gradient, such that there is a radial flow of the near pressure side fluid from hub to casing. This is resulting in the pressure side of the horseshoe vortex remaining attached to the vane pressure side.

Meanwhile, there is clearly also a pressure gradient from pressure side to suction side, as this is necessary to turn the flow. However, due to swirl, near to the hub endwall there is a circumferential component of velocity, flowing from suction side towards the pressure side. Since this is against the pressure gradient, the endwall boundary layer separates, rolling up into a passage vortex. This passage vortex is separate from the pressure side leg of the horseshoe vortex. This passage vortex goes towards the suction side of the vane as normal, with the original boundary layer fluid going into this vortex, and the boundary layer vorticity becomes aligned with the flow as fluid is turned through the passage.

Midspan vortex

Section 3.3 showed how a low total pressure swirl core created in the combustion chamber can lead to the formation of an additional midspan secondary flow-like vortex pair. The effect of this vortex on heat flux can also be seen in high-speed IR measurements, in section 4.7.

The inlet flow field impinging on the vanes shows a great deal of fluctuation, as was shown in section 4.3. However, the lowest total pressure point is not necessarily in the centre of the passage at any point in time, rather it moves about, and is at times more or less intense. This is in contrast to the RANS cases which were run with steady inlet conditions.

LES shows the formation and evolution of the midspan vortex pair. Figure 4.27 shows the vortex pair forming on the leading edge, and its effects on heat flux for four selected instantaneous timesteps of LES. As the total pressure loss core moves towards either the hub or casing, the leading edge vortex pair likewise moves radially along the NGV leading edge, corresponding to the location of lowest total pressure. At some times, the total pressure loss core is not impinging directly on the central vane,

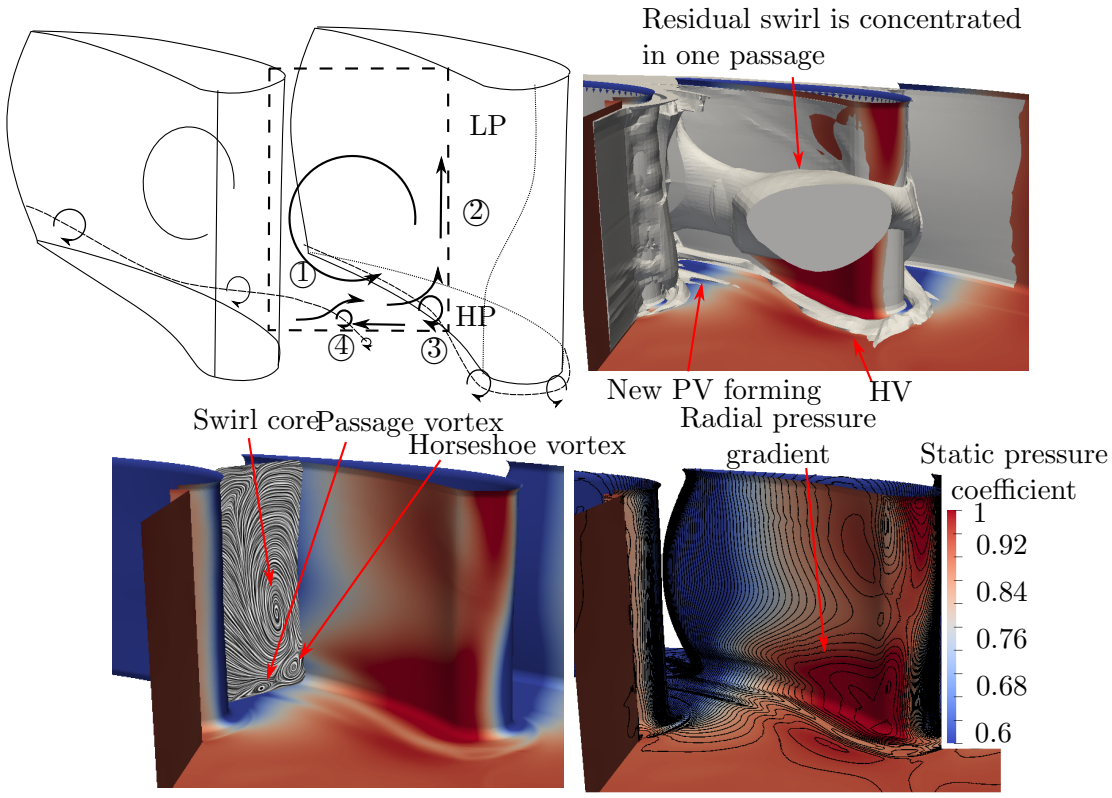


Figure 4.26: Pressure side leg of horseshoe vortex can remain attached to pressure side, and secondary HV forms

1. Residual swirl core in passage causes additional cross passage velocity and radial pressure gradient

2. Because of shift in stagnation line, radial pressure gradient on vane PS. Near pressure side there is radial velocity from hub to casing

3. This causes pressure side HV to remain attached to pressure side, instead of moving out into passage

4. angular momentum of residual swirl causes near endwall flow from SS to PS. This is against pressure gradient so BL separates and rolls up into passage vortex. BL vorticity becomes aligned with flow as flow turns through passage.

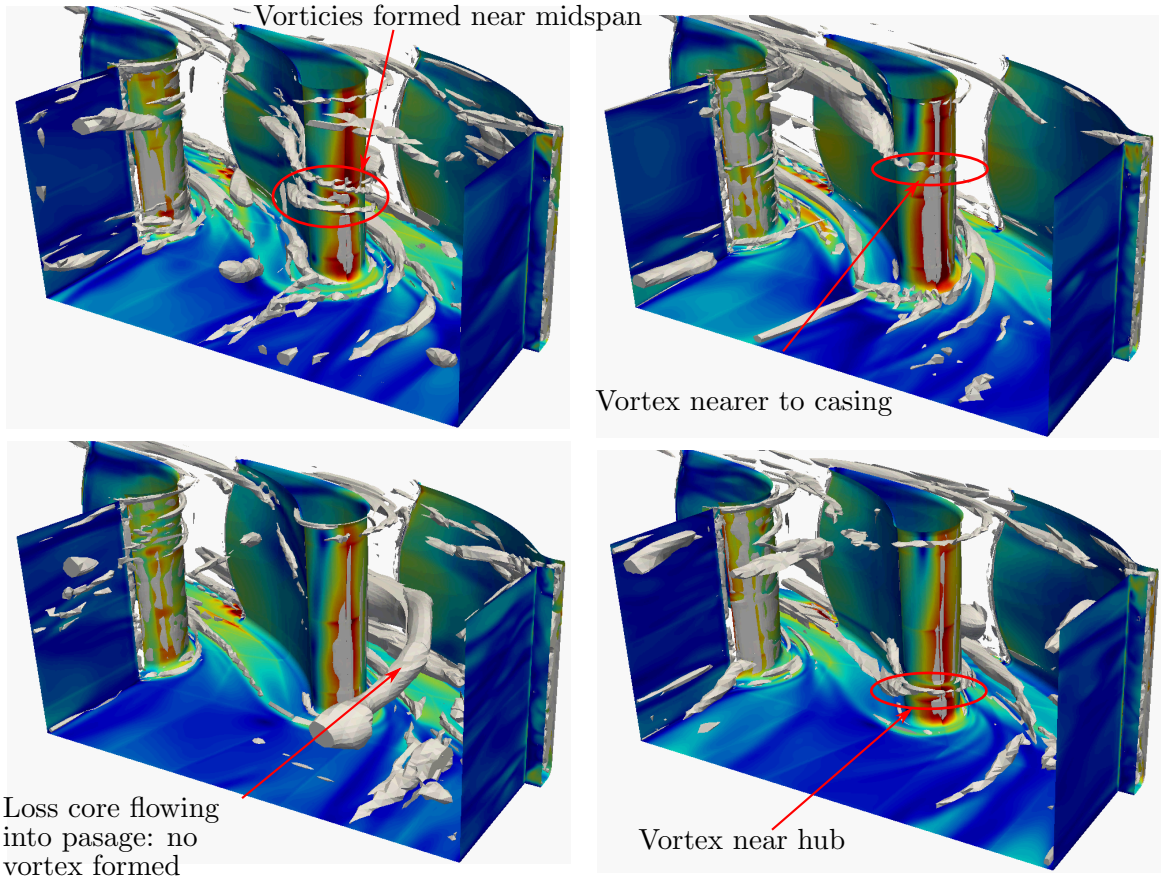


Figure 4.27: Q criterion and heat flux of snapshot of LES domain. Selected timesteps show the range of leading edge vortex formation which occurs. Fluctuations are driven by fluctuations in inlet flowfield

but has moved circumferentially so that it convects directly into one passage or the other. When this occurs, the midspan vortex pair does not form.

From its position of formation the vortex is wrapped around either side of the vane, and is pushed towards one side, as shown in previous sections. Likewise, on the pressure side of the vane, the vortex pair is pushed towards the opposite endwall, due to the residual swirl acting on the other side of the vane.

4.8 Vortex shedding from combustor wall

The can combustor walls extend very close to the leading edge of the NGV. Some NGV are therefore 'shielded' by the nearby combustor wall, this may provide some reduction in heat transfer, as the boundary layer fluid from the combustor wall may be transferred onto the vane. On the other hand, there is also an increase in turbulence directly behind the combustor wall, which may have detrimental effects. Since the leading edge of the vane uses the most cooling air, it is important that these phenomena are well understood.

The effect of combustor wall including the effect of 'clocking' the vanes in different circumferential

positions relative to the combustor, was investigated experimentally and with CFD by Aslanidou[19], and Jacobi [13] in the same facility as the present study. Heat transfer coefficients were slightly less on the leading edge of the shielded vane than unshielded vanes. In this study, the clocking position which gave the best (lowest) heat transfer is used throughout, compared to a vane which does not have the combustor wall before it.

Rosic et al. [77] suggested the use of integrated vanes, replacing the nozzle guide vanes with extensions to the combustor walls which would achieve the same levels of flow turning and acceleration. Jacobi and Rosic [78, 79], investigated this with experiments and CFD, showing that improvements to both aerodynamics and heat transfer are achieved.

Aslanidou et al.[80, 16], investigated an intermediate, so-called 'shielded vane' concept, whereby every other vane in the 2-1 vane-combustor configuration is replaced with a vane integrated with the combustor wall, with intermediate vanes conventional.

Although the integrated vane concept seems extremely promising, there are perhaps concerns that limiting the combustor-vane ratio to be exactly 2-1 or 1-1 would overly constrain the design space of the machine. It is still therefore worth investigating the impact of the combustor wall on NGV, and ways to ensure that there is no detrimental effects.

It appears that one of the major effect of the combustor wall is that it results in vortex shedding. Mazzoni et al. [81] showed using LES that vortex shedding from the combustor wall can be expected to have a detrimental effect on leading edge film cooling, by periodically removing cooling flow and altering the coolant flow rates though the cooling holes. This has an overall effect of reducing time-averaged cooling effectiveness for a vane behind the combustor wall.

In a RANS CFD study, Saw [82] confirmed that leading edge film cooling flows are negatively affected by vortex shedding using the present vane and combustor geometry, with showerhead cooling including the interior of cooling holes.

Vortex shedding and its suppression is a well known problem in structural engineering. Suppression of vortex shedding usually takes the form of introducing additional three-dimensional effects, which prevents regular vortex shedding; for example tall chimneys will often have a helical strake that introduces three-dimensionality into the flow and prevents vortex shedding. Although flow around a chimney may appear very different to flow inside a gas turbine, in fact Reynolds numbers may be similar. Zdravkovich [83] gives a review of the formation of vortex shedding around a cylinder, and methods by which it may be suppressed.

Concerning flow around a cylinder, the vortex shedding regime depends on where transition to turbulence occurs. When Reynolds numbers are large enough that flow is fully turbulent well before

the separation point, then regular vortex shedding re-occurs, similar to a fully laminar case. In the case of flow off the combustor wall, the boundary layer has fully transitioned to turbulence, despite Re being relatively low.

4.8.1 Can combustor geometry

In the machine considered, every second vane has a combustor wall directly in front of it.

Vortex shedding is usually characterised by Strouhal number, which is effectively a non-dimensional frequency. In the well-studied case of a cylinder in cross-flow, the length scale used is the cylinder diameter. In this case, the combustor wall width is used as a length scale.

$$St = \frac{fL}{v} \tag{4.2}$$

Reynolds number of the combustor wall is calculated using the combustor wall thickness as a length scale, and mean flow velocity through the combustor exit plane.

$$Re_c = \frac{\rho v L}{\mu} = 1.1 \times 10^{-5} \tag{4.3}$$

This means of calculating Reynolds number is probably best for comparison to vortex shedding around cylinders. However, there are some significant points in which it may differ from other cases at similar Reynolds numbers: the boundary layer is fully turbulent, and the separation points are fixed at the sharp corners of the square-ended combustor wall.

4.8.2 Leading edge measurements

A pair of instrumented nozzle guide vanes were used to measure unsteady content behind the combustor wall. A vane instrumented with unsteady pressure tappings, and an vane instrumented with thin film gauges were used. These are described in detail in section 2.4.

Each vane was placed in both the shielded, and the unshielded positions, and the results compared.

Figure 4.28 shows unsteady measurements of vortex shedding off the combustor wall, with both heat flux and unsteady pressure measurements agreeing well with each other. There is a clear dominant frequency at $St = 0.17$, which is not present in the unshielded vane. The value measured of $St = 0.17$ is close to the common approximation that $St = 0.2$ for a cylinder in cross-flow.

Other than at this specific peak, the vanes show similar frequency spectra whether in shielded or unshielded position.

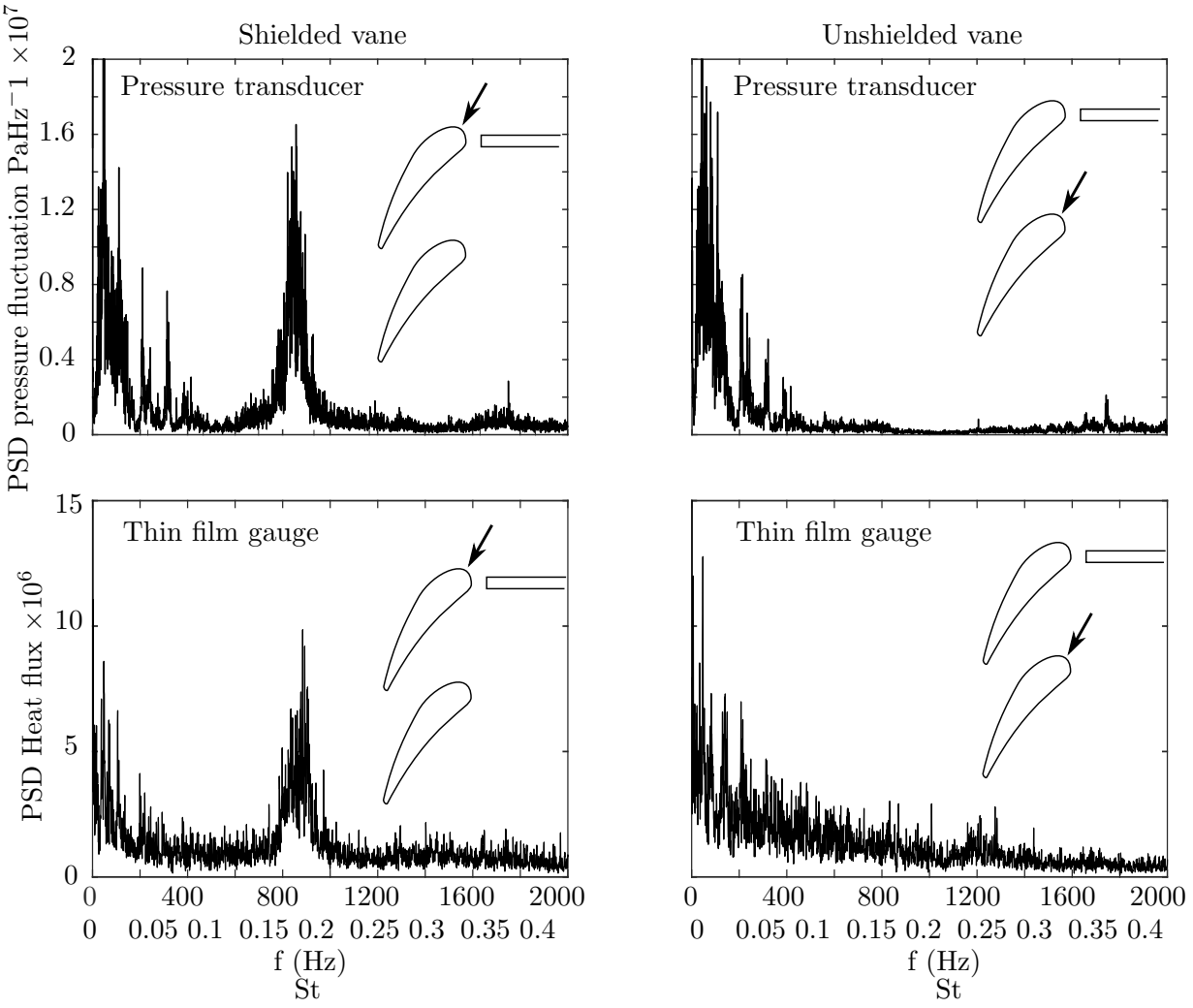


Figure 4.28: Top: unsteady pressure measured near the leading edge, left: shielded vane, right: unshielded vane. Bottom: unsteady heat flux measured using TFGs. left:shielded, right:unshielded. Both these methods show a distinct peak around 850Hz in the case of shielded, but not unshielded vane. This is result of vortex shedding from the combustor wall

Distribution of unsteady content over leading edge and vane

The distinct frequency peak caused by vortex shedding is only observed very close to the leading edge of the vanes. On both the pressure side and suction side, very little peak in pressure fluctuations can be observed by the time the flow passes over the second row of pressure tappings on either the pressure side or suction side. The distribution of unsteady bandpower over the vane is shown measured by unsteady pressure tappings in figure 4.29. There is an asymmetry in the distribution of vortex shedding, with the hub side showing it more clearly in all cases. This is due to the fact that the vane itself is not symmetrical.

There is quite clearly no significant bandpower of unsteady content in this frequency range on the unshielded vane in any cases, confirming that this is due to the effect of the combustor wall. Strouhal number confirms this to be vortex shedding, and this is also confirmed by comparison to CFD studies which show the same frequency [82].

Effect of swirler on vortex shedding

The vortex shedding persists when a multi-core swirler which gives a moderate level of swirl is employed. When using a large, single swirler however, vortex shedding is largely suppressed. This is thought to be due to the highly three-dimensional nature of the flow when this larger swirler is used, and the large scale of unsteady structures meaning that periodic shedding never becomes established (See Section 4.3). There is however still a broad band unsteadiness generated by the combustor wall, compared to the unshielded vane. It is not clear whether this broad band turbulence would have a greater or lesser effect on cooling than the regular vortex shedding observed in the other inflow cases.

Since the trend in combustor design is towards smaller length scales and more homogeneous mixing, vortex shedding from combustor walls as demonstrated here may become increasingly significant.

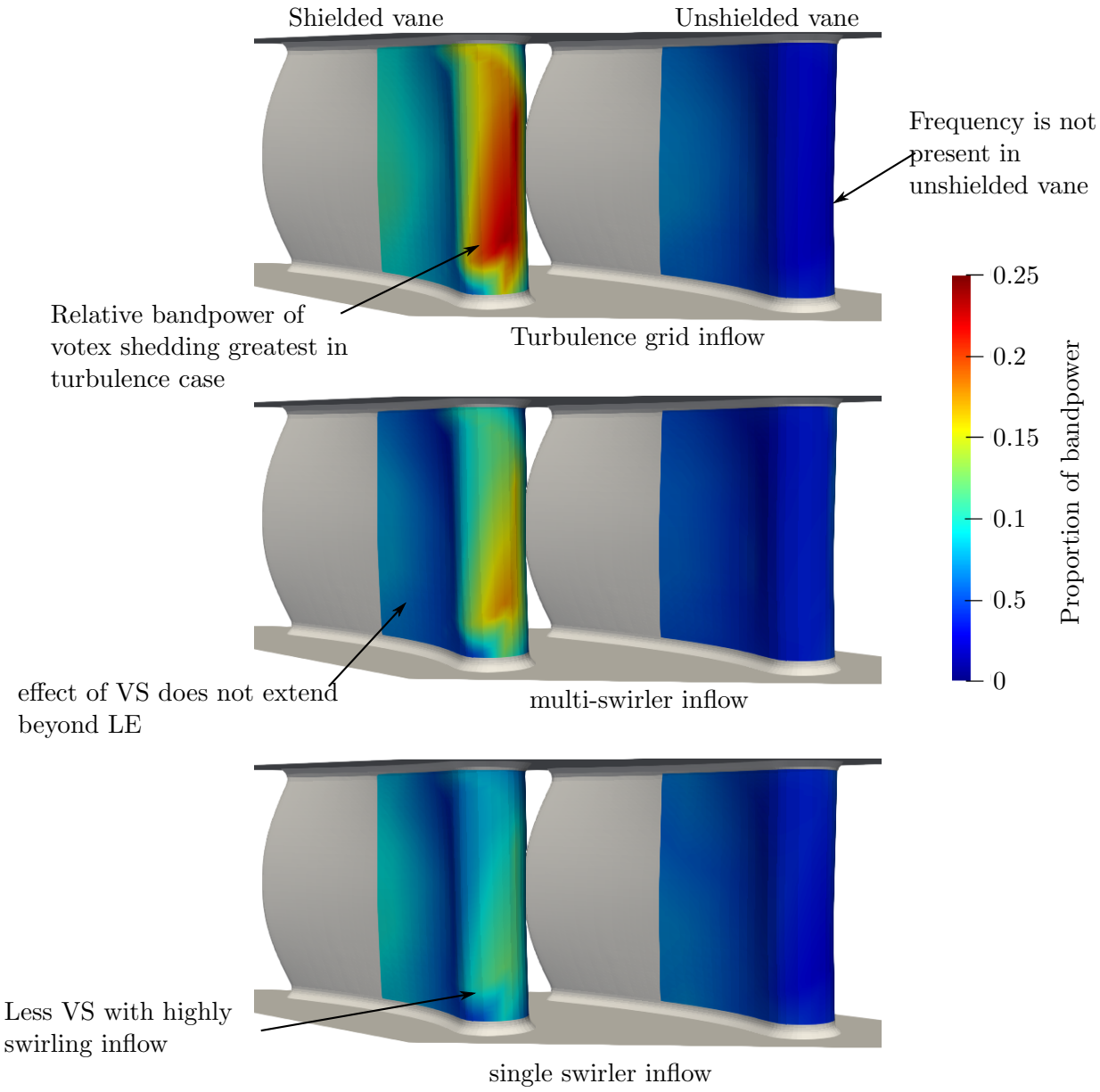


Figure 4.29: Measurements of distribution vortex shedding influence for three different inlet conditions, measured using unsteady pressure sensors. The effect of vortex shedding is less distinct when a swirling inflow is used. There is some asymmetry in where the greatest effect is.

4.9 Summary and conclusion

This combined experimental and computational study shows some of the many complex flow interactions which are often overlooked in simplified studies. While the NGV are often thought of as a 'steady flow' area, in fact there is a great deal of unsteadiness resulting from the time-varying combustor outflow. This is not simply high turbulence, but coherent structures such as the swirl core, which persist in time, but vary in position. Many of these flow interactions are highly unsteady in nature, and are not picked up by steady state CFD, or even unsteady CFD if it does not have the correct time-varying inlet conditions. The ordinary view of secondary flows in the NGV as being essentially steady structures is shown to be oversimplified. These unsteady interactions create a great difference in the flow field, and may effect losses and cooling. Vane loading is also highly variable in time.

The method of using high density thin film gauges to measure and visualise large scale turbulent flow structures has been demonstrated. The high resolution, simultaneously in time and space, of the heat flux measurements allows for direct visualisation and study of the movement of heat transfer modifying structures over the endwall. Large scale turbulent structures can be measured and visualised, as well as larger scale coherent structures created by swirling inflow.

High frequency measurements show several distinct regions on the endwall with different characteristic behaviour. A quiescent region behind the horseshoe vortex indicates the creation of a thin laminar boundary layer, which then results in an increased HTC downstream as it transitions to turbulence. High magnitudes of broadband unsteadiness accompany the highest HTC areas of the wake and the suction side horseshoe vortex.

There is a highly unsteady flow field generated by the single swirler impinging onto the NGVs. This flow field is dominated by a low total pressure loss core which is caused by vortex breakdown of the swirling flow in the transition section. LES shows a good agreement with unsteady pressure measurements, in both magnitude, distribution and frequency of pressure variations of the inlet flow. The large scale unsteadiness of the inlet occurs at a low frequency in the order of 10-330Hz. This unsteady swirl core has a significant effect on vane loading distribution.

It has been found that the effect of inlet turbulence in this geometry was to modify the passage vortex from a steady state phenomena in the clean inflow case to being highly unsteady when turbulent or swirling inflow was used. The passage vortex appears to remain as a distinct structure, but one which is unsteady in its position. This consequentially changes also the time averaged pattern and magnitude of HTC. This can be caused by the fluctuating swirl core position and residual swirl in the passage. Though the observation that it also occurs with a turbulence grid shows it can be caused by random turbulent eddies as well. It does not occur in the case of a low turbulence inflow. Speculatively,

it is quite possible that attempts at manipulating the passage vortex by endwall contouring, or jets or other techniques, may be made more difficult as the location of the passage vortex cannot be relied upon at any point in time.

The horseshoe vortex near the leading edge was also found to be highly unsteady, in all inlet cases, confirming the findings others had made in low speed flows. This is though to be partly a self-excited instability independent of the unsteadiness of the inflow, and partly a response to the varying inflow conditions.

The midspan secondary flow that was analyses in a steady-state manner in chapter 3 was found to in fact be highly unsteady and variable in time.

The presence of the combustor wall causes vortex shedding, which created an additional high-frequency unsteadiness on the NGV.

The fact that such large effects occur in the first vane shows the importance of designing combustors and first vanes in an integrated manner, as there can be great benefits to the first vane flow field resulting from changes to the combustor.

Chapter 5

Effects of unsteady heat flux on component life

5.1 Introduction

Turbine components exposed to the hot gas path typically fail by temperature mediated effects, such as corrosion, erosion or creep. These effects have non-linear dependence on temperature, so that mean temperature does not matter so much as peak temperature reached. So if, for example, a TBC material has an allowable working temperature of 1000C, and it is exposed to a fluctuating temperature between 900-1100C, then it would be no surprise if failed prematurely, even if the mean temperature did not exceed the allowable limit.

The effects of unsteady heat flux on component life are often considered negligible, with only the time-averaged values of heat flux being of interest to designers. In fact, it is shown in this chapter, these unsteady effects can cause significant surface temperature fluctuations, which could contribute to failure.

In this chapter, a method is derived to scale up unsteady heat transfer coefficients, measured experimentally, to calculate surface temperature fluctuations at real engine conditions, using real engine materials.

Secondly, the experimental measurements are also analysed to ensure that the assumption that unsteady heat flux is a result of a true unsteady HTC, and scales with temperature difference. It is shown that this assumption is justified, for these experiment data at least.

5.1.1 Thermal barrier coating literature

It is now common for thermal barrier coatings to be used to protect hot-gas path components in gas turbines. Padture et al. [84] gave an early review of of the use of thermal barrier coating in gas turbine applications. The thermal barrier coating typically consists of a bond coat, a thermally grown oxide layer which develops in use, and the ceramic top-coat, which provides the thermal insulation. Failure is often caused by thermally induced stresses, which cause crack growth until spallation occurs.

Gleeson [85] reviewed thermal barrier coatings for aero-engine applications, with a focus on vapour deposition TBC. The main failure modes were reported to be cracking in the intermediate thermally grown oxide, or cracking and delamination caused by CMAS infiltration at the surface of the top-coat.

TBC for gas turbine applications were again reviewed by Clarke et al. [86]. Failure can occur by several routes, including chemical and phase changes which occur in the ceramic topcoat. These are thermally activated processes so are expected to increase exponentially with temperature. CMAS infiltration is also an increasing concern with higher temperatures, as dust and other fine particulates can form a molten glass which fills the porosity in the TBC, having a detrimental effect on thermal and mechanical properties. This is described by Levi et al. [87].

The structure and manufacturing of TBC is described by Sampath et al. [88]. TBC used in industrial turbines are typically atmospheric plasma sprayed (APS). Molten droplets of ceramic are sprayed onto the part at atmospheric conditions, resulting in layers of 'splats', each formed from a individual droplet of ceramic. This reduces thermal conductivity normal to the surface, and also results in a significant porosity.

Kumar and Balasubramanian [89] made a comprehensive review of the failure mechanisms of TBC. At high service temperatures, TBC can undergo sintering and phase transformation, which negatively modify the TBC structure and can contribute to failure. Hot corrosion and CMAS infiltration are also major failure modes.

The thermal properties of yttria stabilised zirconia (YSZ), a common TBC material, have been reported by Winter and Clarke [90]. The values reported have been used as the basis of the thermal properties quoted later.

5.1.2 High frequency change in surface temperature

In order to estimate the effects of a time-varying heat flux on temperature of a gas turbine component, the simplified model shown in figure 5.1 is first solved for the case of sinusoidally varying heat transfer coefficient. It is assumed that transverse temperature gradients are small compared to those normal to the surface, such that conduction can be assumed to be one dimensional. Additionally, it is assumed

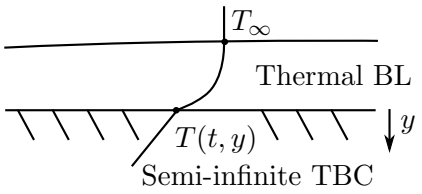


Figure 5.1: Model used for transient conduction into thermal boundary layer.

that the substrate is semi-infinite, so that the periodic temperature fluctuations will never reach the back surface of the substrate. The values of penetration depth calculated show that this is a valid assumption for a TBC surface of reasonable thickness.

Fourier's law of conduction, neglecting radiative heat transport effects and assuming no internal heat generation is:

$$\frac{\partial T}{\partial t} = \alpha \nabla^2 T \tag{5.1}$$

Taking conduction to be one-dimensional into the substrate, this simplifies to:

$$\frac{\partial T}{\partial t} = \alpha \frac{\partial^2 T}{\partial y^2} \tag{5.2}$$

The boundary condition is of a varying heat transfer coefficient,h, as has been measured in cascade tests. To simplify the solution, the fluctuating part of h will be taken to be purely sinusoidal, with an amplitude of H:

$$q = (T_\infty - T) \cdot h \tag{5.3}$$

$$h = \bar{h} + H \sin \omega t \tag{5.4}$$

$$k \frac{\partial T}{\partial y}_{y=0} = (T_\infty - T) \cdot (\bar{h} + H \sin \omega t) \tag{5.5}$$

From the superposition principle, due to the fact that the heat equation is a linear equation, the steady state part and the fluctuating parts can be solved separately. Since the boundary condition itself contains the variable of interest, this makes the solution difficult. As an approximation, if small changes in surface temperature are assumed, then the value of T in equation 5.5 can be replaced by $\bar{T}$ where $\bar{T}$ is the time-mean surface temperature and is treated as a constant. This allows the formation of a conventional boundary condition, as a periodic forcing heat flux:

$$k \frac{\partial T}{\partial y}_{y=0} = (T_\infty - \bar{T}) \cdot H \sin \omega t \tag{5.6}$$

Since the forcing is purely periodic, with no given start time, the solution must also be purely periodic in time. Since the forcing is sinusoidal, it might be natural that the response will be similar.

Allowing for a phase difference between heat flux and temperature, and a phase lag dependent on depth into the surface, a trial solution is attempted as given in equation 5.7, where A, B, C and D are constants to be found, and ω can take any value.

$$T = Ae^{-By}\sin(\omega t + Cy + D) \tag{5.7}$$

$$\frac{\partial T}{\partial t} = A\omega e^{-By}\cos(\omega t + Cy + D) \tag{5.8}$$

$$\frac{\partial T}{\partial y} = Ae^{-By}\big(C\cos(\omega t + Cy + D) - B\sin(\omega t + Cy + D)\big) = \frac{q}{k} \tag{5.9}$$

$$\frac{\partial^2 T}{\partial y^2} = Ae^{-By}\big((B^2 - C^2)\sin(\omega t + Cy + D) - 2BC\cos(\omega t + Cy + D)\big) \tag{5.10}$$

Combining equation 5.9 with the boundary condition, equation 5.6 allows the constants to be found:

$$A\big(C\cos(\omega t + D) - B\sin(\omega t + D)\big) = (T_\infty - \bar{T})\cdot H\sin\omega t/k \tag{5.11}$$

Using trigonometric identities and equating coefficients of $\sin\omega t$ and $\cos\omega t$:

$$-AC\sin D - AB\cos D = (T_\infty - \bar{T})H \tag{5.12}$$

$$C\cos D - B\sin D = 0 \tag{5.13}$$

Substituting equations 5.8 and 5.10 into equation 5.2 gives:

$$A\omega e^{-By}\cos(\omega t + Cy + D) = Ae^{-By}\big((B^2 - C^2)\sin(\omega t + Cy + D) - 2BC\cos(\omega t + Cy + D)\big) \tag{5.14}$$

Again equating coefficients of sin and cos terms gives:

$$B^2 - C^2 = 0 \tag{5.15}$$

$$2BC\alpha = \omega \tag{5.16}$$

Using the property that $B >= 0$, in order to avoid exponentially increasing temperature, and solving equations 5.12, 5.13, 5.15 and 5.16 gives the values of the constants:

$$B = \sqrt{\frac{\omega}{2\alpha}} = -C \tag{5.17}$$

$$D = \frac{\pi}{4}, \frac{5\pi}{4} \tag{5.18}$$

material	k	$\alpha \times 10^{-6}$	f	Δh	ΔT	$d_{0.5} \times 10^{-6}$	δT
YSZ porous	0.8	0.32	10	2000	500	70	89.21
YSZ porous	0.8	0.32	50	2000	500	31	39.89
YSZ porous	0.8	0.32	1000	2000	500	7.0	8.92
YSZ non-porous	2.3	0.6	50	2000	500	42	19.00
YSZ non-porous	2.3	0.6	1000	2000	500	9.6	4.25
Inconel 625	25	7.3	50	2000	500	150	6.10
Inconel 625	25	7.3	1000	2000	500	33	1.36

Table 5.1: Example temperature fluctuations which may arise from different materials and conditions

$$A = (T_\infty - \bar{T})H\sqrt{\frac{\alpha}{\omega}} \cdot \frac{1}{k} \tag{5.19}$$

The solution with constants substituted is thus:

$$T(y,t) = (T_\infty - \bar{T})H\sqrt{\frac{\alpha}{\omega}} \cdot \frac{1}{k} e^{-\sqrt{\frac{\omega}{2\alpha}}y} \sin\left(\omega t - \sqrt{\frac{\omega}{2\alpha}}y + \frac{\pi}{4}\right) \tag{5.20}$$

The value of B given in equation 5.17 can be thought of as a measure of penetration depth of the temperature fluctuations into the surface. By examination of equation 5.20, the depth at which there is a temperature fluctuation which is 50% that of the surface can be given as:

$$d_{0.5\delta T} = \sqrt{\frac{2\alpha}{\omega}} \cdot \ln 2 \tag{5.21}$$

The value of A, given in equation 5.19, is the amplitude of surface temperature fluctuations. The effect of unsteady HTC on temperature is frequency dependent, with lower frequencies having a greater effect on surface temperature, and a greater penetration depth. This equation breaks down for very low values of ω, as the assumption that $T_{y=0} \approx \bar{T}$ is no longer valid. As this solution has been derived for a pure sinusoid of frequency ω, the solution to any time-varying HTC will be given by the superposition of the solution to each frequency component of a Fourier transform.

It can be seen that higher diffusivity, lower conductivity, and lower frequency result in higher fluctuations in surface temperature. Some realistic example values are shown in table 5.1l material values, and fluctuating heat flux values found in these experiments, scaled to engine conditions. In future, the trend is towards further reducing the thermal conductivity of TBC materials, which will further increase the surface temperature fluctuations.

The blade passing frequency of the rotating row is around 2000Hz, and so would not be expected to result in significant surface temperature fluctuation. The nozzle guide vanes however, feature flow fields which fluctuate at very low frequencies, even below 100Hz, and these low frequency fluctuations could result in larger surface temperature changes.

Since the heat equation is time invariant, *sin* may be replaced by *cos* in the derivation above, since they differ only in a phase shift. Also given that the heat equation is linear, any valid solutions may be superposed to give a valid solution. The equation derived above is valid for any value of ω, so that the temperature fluctuation due to any periodic fluctuations of heat transfer coefficient may be given as a Fourier series. For a function of period P expressed as a Fourier series:

$$h(t) = \bar{h} + \sum_{n=1}^{N} a_n \cos\frac{2\pi n}{P}t + b_n \sin\frac{2\pi n}{P}t \tag{5.22}$$

Where $\omega = \dfrac{2\pi n}{P}$ is the frequency of that component. Then the surface temperature resulting will be:

$$T(t,0) = \bar{T} + (T_\infty - \bar{T})\frac{\sqrt{\alpha}}{k}\sum_{n=1}^{N}\frac{a_n}{\sqrt{P/2\pi n}}\cos\left(\frac{2\pi n}{P}t + \frac{\pi}{4}\right) + \frac{b_n}{\sqrt{P/2\pi n}}\sin\left(\frac{2\pi n}{P}t + \frac{\pi}{4}\right) \tag{5.23}$$

Following this, a Matlab function has been written to calculate from any time-varying HTC, the fluctuations in surface temperature which result.

5.1.3 Non-dimensional numbers and engine scaling

To be applicable, the values measured experimentally must be scaled to real engine conditions. The relevant values are the Reynolds number (Re), Strouhal number (Str), Stanton number (Stn), and Nusselt number (Nu). The relationships are summarised in table 5.2. Reynolds number in the experiments is slightly less than half that in the real machine. Lengths have been scaled down to 62% of real engine scale. Mach number is identical to real engine conditions. Experiments are carried out at around room temperature (300K), while turbine inlet temperatures of industrial gas turbines are exceeding 1700K. Velocities are scaled according to the temperature in order to keep Mach number constant.

The Strouhal number (Str) is effectively non-dimensional frequency; it is assumed that for unsteady effects Str will be the same between experiments and the real machine. Although the real machine is larger than the experimental cascade, which would tend to reduce frequencies, velocities are also higher such that frequency will be increased slightly compared to experimental measurements.

Stanton number (Stn) characterises forced convection heat transfer. Stanton number is a weak function of Reynolds number, so since Reynolds number is of the same order of magnitude between experiments and the real machine, it has been approximated that Stn is the same in experiments and the real machine. Consequentially Nusselt number (Nu) is increased proportionally to the increase in Re (with changes to Prandlt number (Pr) assumed to be negligible). After accounting for the large

quantity	formula	relationship to experimental quantity	notes
Re	$\frac{\rho U L}{\mu}$	$Re_{eng} = 2.35 Re_{exp}$	
L	-	$L_{eng} = 1.61 L_{exp}$	
M	$\frac{U}{\sqrt{\gamma R T}}$	$M_{eng} = M_{exp}$	Equal by design
T	-	$T_{eng} = 5.6 T_{exp}$	
U	$M\sqrt{\gamma R T}$	$U_{eng} = M\sqrt{\gamma R T_{eng}} = U_{exp}\sqrt{\frac{T_{eng}}{T_{exp}}} = 2.4 U_{exp}$	
Str	$Str = \frac{fL}{U}$	$Str_{eng} = Str_{exp}$	Assumed to be equal
Stn	$\frac{Nu}{Re \cdot Pr}$	$Stn_{eng} = Stn_{exp}$	Assumed to be equal
Pr	$\frac{c_p \mu}{k}$	$Pr_{eng} = Pr_{exp}$	
Nu	$\frac{hL}{k}$	$Nu_{eng} = Stn \cdot Re_{eng} \cdot Pr = Nu_{exp} \cdot \frac{Re_{eng}}{Re_{exp}} = 2.35 Nu_{exp}$	
k	$k(T)$	$k_{eng} = 3.8 k_{exp}$	
h	$Nu \cdot \frac{k}{L}$	$h_{eng} = \frac{k_{eng}}{L_{eng}} \cdot Nu_{eng} = \frac{Nu_{eng}}{Nu_{exp}} \frac{k_{eng}}{k_{exp}} \frac{L_{exp}}{L_{eng}} h_{exp} = 5.5 h_{exp}$	
f	$\frac{Str \cdot V}{L}$	$f_{eng} = \frac{Str \cdot U_{eng}}{L_{eng}} = f_{exp} \cdot \frac{U_{eng}}{U_{exp}} \cdot \frac{L_{exp}}{L_{eng}} = 1.5 f_{exp}$	

Table 5.2: Dimensional and non-dimensional numbers of real engine as function of experimental quantities.

increase in conductivity at elevated temperatures, this means that real heat transfer coefficients are expected to be 5.5 times those measured in the cascade. It has been assumed that the unsteady portion of heat transfer coefficient follow this same scaling.

5.1.4 Increase in surface temperature due to measured unsteadiness

In order to estimate the effect of the unsteady components of heat transfer on peak surface temperature, unsteady heat transfer coefficients measured in a cascade endwall using thin film gauges were used. The measured cascade unsteady heat transfer coefficient has been scaled to engine conditions, and equation 5.23 applied to the fast Fourier transform of the heat transfer, and then returned to the time domain by an inverse fast Fourier transform. In calculating peak temperatures, it is important that phase information is retained correctly, and care has been taken to ensure this is the case.

To calculate peak temperature increase, the 99th percentile of temperature has been used, rather that the single maximum temperature. This was thought to be a better measure as it should not be dependant on the total length of data sampled, whereas maximum temperature would continually increase with longer lengths of sampled data. This is illustrated in figure 5.2 for a single set of gauge data, the red lines show the values of the 1st, 50th (mean) and 99th percentiles of temperature.

The increase in peak surface temperature over the endwall, scaled to engine conditions, compared to a steady HTC is shown in figure 5.3. In the area most affected by unsteady effects, the wake, the

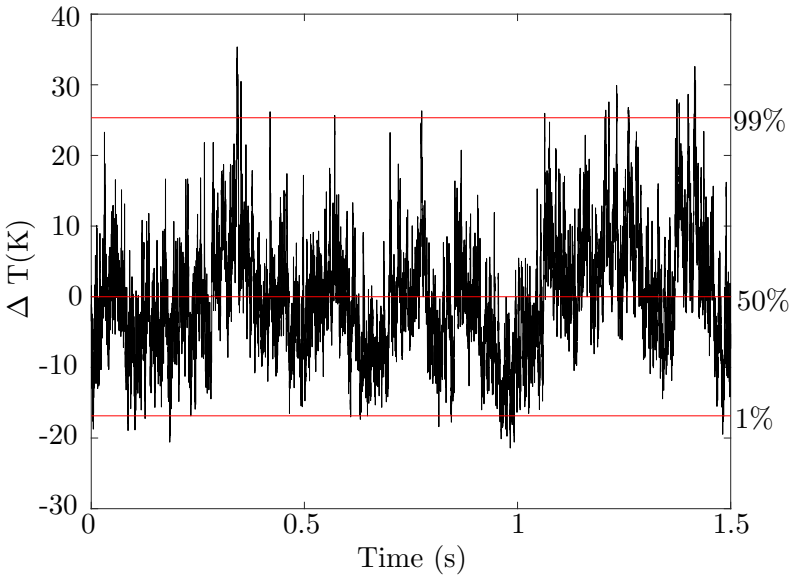


Figure 5.2: Variation in surface temperature and the 99th percentiles, calculated from experimentally measured unsteady heat transfer coefficients scaled to engine conditions.

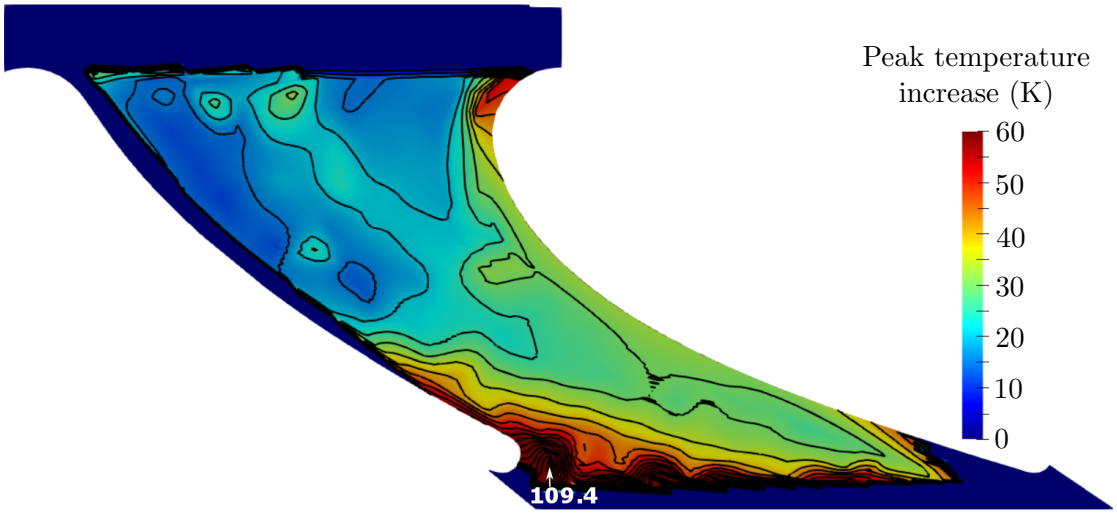


Figure 5.3: Increase in peak temperature as a result of unsteadiness, in the case of a swirling inflow

peak surface temperature is 109K above the mean surface temperature. Over large areas there is peak temperature >25K above the mean surface temperature.

5.1.5 Effect of temperature fluctuation on component life

The deterioration mechanisms of TBC are complicated, and involve the interaction of chemical and mechanical processes. The temperature fluctuations estimated will only affect a very thin layer on the surface of a TBC.

However, by increasing the peak temperature seen, deterioration mechanisms which begin on the surface, such as CMAS infiltration and phase change YSZ, will be accelerated. The exact relationship between temperature and failure is not know in detail for each particular TBC. However, it would be expected that the peak temperature seen would be more important than the mean temperature, and

therefore a cyclic temperature variation would increase deterioration faster than a steady temperature of the same mean value.

If temperature fluctuations are large enough it is possible that thermal gradients near to the surface may cause sufficient stress to cause high-cycle fatigue. If this is the case then a cyclic temperature may be even more damaging than even an elevated steady temperature.

The unsteady effects on heat transfer occur at a low enough frequency to have a significant effect on component peak temperature. In some areas this could be as much as 100K increase in peak surface temperature above time-mean temperature. This could have a detrimental effect on component life, depending on what failure mechanism is dominant.

5.2 Separating unsteady HTC from unsteady temperature fluctuations

In the preceding analysis, it was assumed that the fluctuating part of the unsteady heat flux was due to a unsteady component of heat transfer coefficient, such that unsteady heat flux could be scaled by temperature difference to give unsteady heat flux in a real machine. However, there is also a component of unsteady heat flux which is caused instead by local fluctuations in fluid temperature, and which is observed even when there is no temperature difference between fluid and the wall.

Measured surface heat flux may be split into three components, the steady state heat flux, unsteady heat flux proportional to temperature difference, and unsteady heat flux independent of temperature difference.

$$q = \Delta T \cdot \bar{H} + \Delta T \cdot H^* + q^* \tag{5.24}$$

While the steady state part of q may be easily separated from the fluctuating components, it is more difficult to separate the fluctuating parts.

Consider the measured unsteady heat flux gauge data shown in figure 5.4. With T plotted against q, there is a steady state component of heat flux, an unsteady component proportional to ΔT, and additional unsteadiness even once adiabatic temperature has been reached.

The residual unsteady heat flux q^* is likely made up of several component. A small part of this is measurement noise, discussed in section 2.4.3. The greater part is due to local temperature fluctuations of the fluid. The magnitude of peak to peak temperature fluctuations is on the order of 0.3K for a typical gauge in this cascade, so even very small freestream temperature fluctuations may be detected and feed into apparent unsteadiness. The temperature fluctuations likely arise from several different sources, and it is not clear how these could all be scaled from rig to engine conditions.

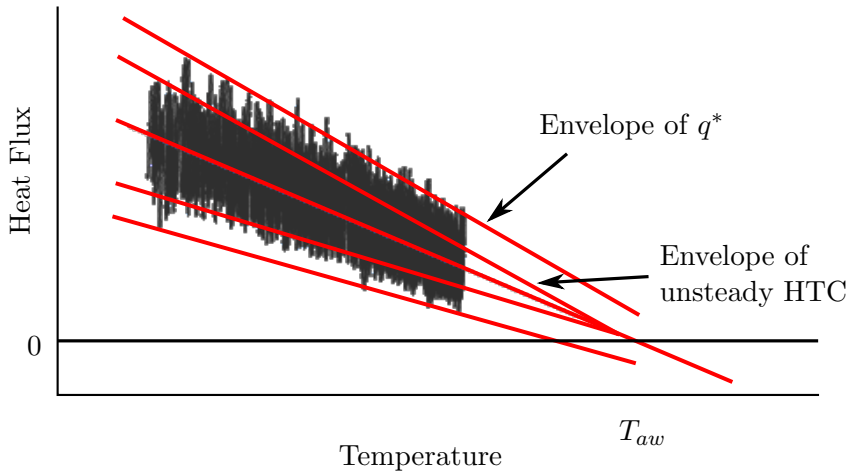


Figure 5.4: Unsteady heat flux gauges data showing the different components of heat flux

5.2.1 Separation technique

Heat flux was separated into the components in the frequency domain using the discreet Fourier transform, and each frequency component analysed separately. The heat transfer coefficient can then be found for each frequency component individually, as the gradient of $\hat{q}$ against ΔT, where $\hat{q}$ is the amplitude of that frequency component. The value of $\hat{q}$ when $\Delta T = 0$ is then q^*, the component of q which is independent of ΔT.

$$q(t) = \sum \hat{q}_n e^{i\omega t} \tag{5.25}$$

$$\hat{q}_n = \hat{q}^* + \hat{H}\Delta T \tag{5.26}$$

To achieve this, a windowed fft has been used. As the window is passed over the length of the signal, the mean ΔT, and the amplitude of each frequency component is calculated. For each frequency component, a regression is used to estimate $\hat{H}$ and q^*, as shown in figure 5.5.

The result of this can be plotted overall for each gauge, and compared. RMS values of HTC can also be compared to HTC calculated assuming $q^* = 0$, so that the validity of this approximation in previous sections may be assessed.

To verify the algorithm, as well as measured data a synthetic dataset consisting of pure sine waves or broadband noise was constructed. The algorithm could correctly distinguish heat flux data which was proportional to a temperature difference to that which was not.

The exact algorithm used to implement this was written in Matlab, and is reproduced from reference in appendix A.

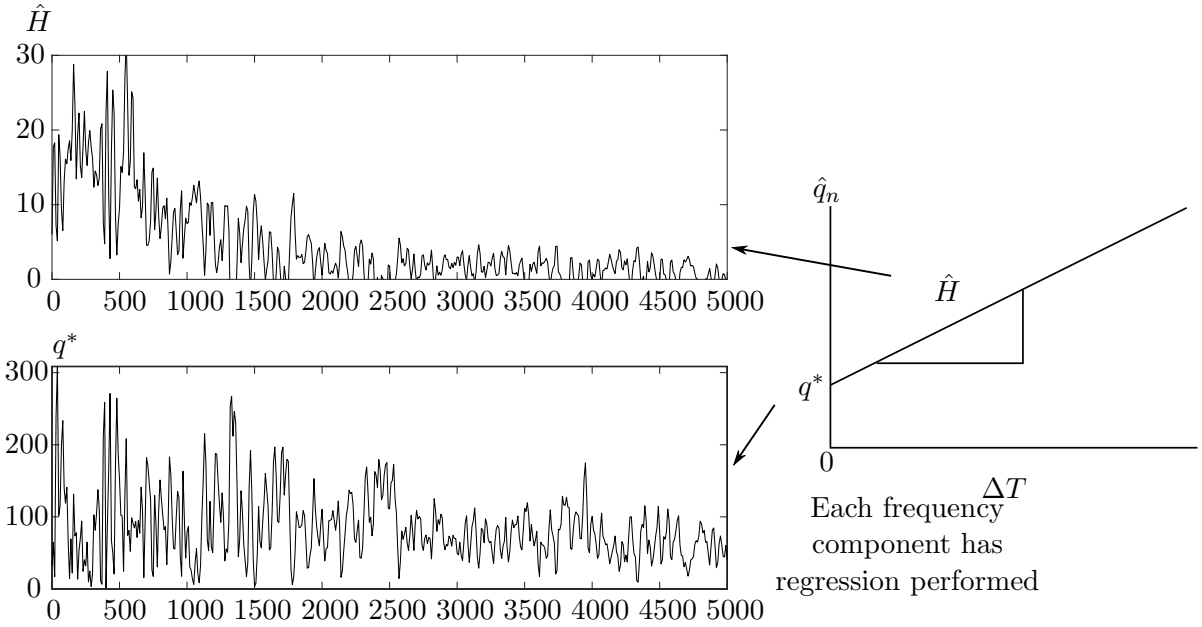


Figure 5.5: Regression to find unsteady HTC amplitude for each frequency component. Measured data from single gauge

5.2.2 Application to measured data

Comparing RMS of unsteady HTC by this calculation method, compared to the simple method used elsewhere, it was found that unsteady HTC by this method was on average 80% of that indicated by the simple calculation. This indicates that the majority of unsteady heat flux measured was indeed due to fluctuations in heat transfer coefficient, rather than fluid temperature fluctuations. Calculated values are unfortunately quite sensitive to window functions chosen however, so there is a great deal of uncertainty in this value.

Unfortunately, in this procedure phase information is lost, so that exact unsteady heat transfer coefficients with spurious unsteady heat flux removed, cannot be reconstructed in time. This means that the analysis of surface temperature excursions in section 5.1 cannot be repeated exactly with corrected data. However, the results show that the majority of measured unsteady heat flux is indeed proportional to temperature difference and so is true unsteady heat transfer coefficient. Therefore the broad method and conclusions of section 5.1 is justified, though exact values are probably slightly overestimated.

5.2.3 Possible future improvements to method

There are several possible improvements to the method which could be implemented to improve results. Firstly, the window function used could be optimised; a Gaussian window was used for simplicity, but other windowing functions could be used. Additionally, the results show some sensitivity to the length

of the window, and this required further investigation.

Also, if the method was modified to ensure that phase information was retained, this would allow the separated unsteady heat transfer coefficient signal to be reconstructed in the time domain.

The accuracy of regression to calculate $|q|$ as function of ΔT could be improved by increasing the length of signal sampled, by using steady state adiabatic signals to fix the value of q^*, and by using the reversed heat flux state when the heater mesh is switched off to increase the span of the regression line.

Chapter 6

Flow within the midpassage gap

In order to increase gas turbine efficiency, higher inlet temperatures are being employed along with reduced cooling flows. Lean burn combustion also leads to more uniform turbine inlet temperatures and higher heat load on vane endwalls. The need to optimise performance requires investigation into detailed aspects of turbine geometry, which have often been neglected in the past. In this case, the midpassage gap.

Typically, gas turbine blades and vanes are manufactured as a single or small number of blades, along with endwalls, as one piece. These are then assembled around the annulus of the turbine. For both assembly purposes, and to allow for thermal expansion in operation, there is a clearance between adjacent blade platforms, as well as between combustor and first vane, and vane and blade rows. This is called the midpassage gap, also referred to as platform gap or slashface gap.

Figure 6.1 shows the midpassage gap in the nozzle guide vanes of an industrial turbine. The midpassage gap reduces turbine efficiency and causes up to 20% additional heat load into the vane platform, as well as changing the distribution of endwall heat transfer and film cooling.

Traditionally, there has been significant purge flow out of these gaps, thereby preventing hot gas ingestion. In modern, large industrial turbines however, there is a trend towards reducing purge flow rates. This increases efficiency, but raises the possibility of hot gas ingestion into the gap, causing damage to components.

In this chapter, experiments carried out in a high speed linear cascade using thin film heat transfer gauges, static pressure tappings and a five-hole probe traverse are reported. A parametric measurement campaign was carried out to investigate the effect of gap width on heat transfer and aerodynamic losses. This was supported by a RANS CFD study.

A one-dimensional model has been derived, and is shown to agree well with experiments and CFD. Using this, the effects of the gap can be quantified based only on geometric features.

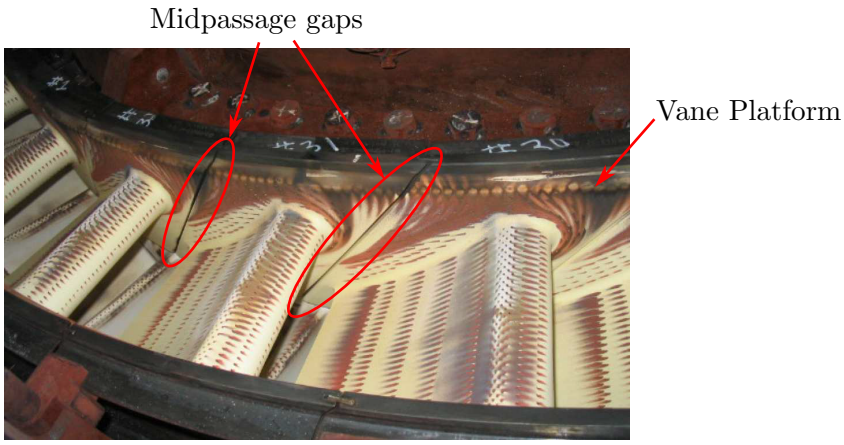


Figure 6.1: Gas turbine vanes and mid-passage gap [11]

It is found that at present there are significant losses and a large proportion of heat load caused by the gap, but that with modified design this could be reduced to negligible levels. Approximations are given to asses the impact of gaps in other machines.

Purge flows into the gap are investigated analytically and with CFD, although experiments were carried out with zero purge. An ideal distribution of purge flow can fully cool the gap with only a small amount of cooling air required. This ideal purge distribution can be calculated directly, with no need for iterative optimisation.

Recommendations are given for targets that turbine designers should work towards in reducing the adverse effects of the midpassage gap.

While this chapter focuses on a large industrial turbine, similar features are also found in smaller machines and aero-engines. The analytical model developed is generic and should apply to all rotor and stator blades which posses a similar mid-passage gap. A method to estimate the effect of gap flow is presented, so that for any machine the significance of the gap may easily be assessed.

6.1 Midpassage gap literature review

The midpassage gap reduces turbine efficiency, causes additional heat transfer into the vane platform, and changes the distribution of endwall heat transfer and film cooling. Despite this, no comprehensive explanation of the fundamental flow phenomena of importance, or mitigating design measured has been found.

Reid et al. [91] measured a significant reduction in stage efficiency of 1.5% in a cascade in a combined experimental and numerical investigation. The presence of the gap causes this reduction in efficiency even with zero purge flow. Increasing purge flow was found to have only a small additional impact on efficiency. Even with relatively large purge flow rates of 1% of mainstream, there was still

ingress of mainstream fluid into the gap. Angling the gap or controlling which direction purge flow came from was investigated as a means to improve efficiency [92], but was found to have only minor benefits.

Heat transfer may be increased, or decreased over different areas of the endwall as a result of gap flow. purge flow from the gap may also provide some endwall film cooling. There have been a number of investigations on these effects, in various experimental facilities.

Piggush and Simon [93, 94] experimentally investigate the effect of the gap on endwall heat transfer, including the effect of misalignment of adjacent vane platforms. They found a redistribution of endwall HTC as a result of the gap. It was also found that higher blowing from the gap results in higher aerodynamic losses.

Lynch and Thole[95], Lynch et al. [96] and Lange et al. [97], Hada and Thole[98], Cardwell et al. [99, 100] showed that the midpassage gap can increase endwall heat transfer downstream of the gap. A vortical structure was found downstream of the gap which particularly was responsible for increasing heat transfer. IR imaging of a constant heat flux surface was used to determine heat transfer on the endwall surface. Heat transfer within the gap itself was not measured. A particular area of concern on the endwall had enhanced HTC, but low cooling effectiveness from purge flow, giving a potential for high metal temperatures. Flow was ingested in upstream part of the gap, and expelled downstream.

Liu et al. [101] carried out experiments and computational studies to optimize endwall geometry including the effects of the midpassage gap. It was found that the gap increases aerodynamic losses and increasing net leakage flow rates further increases losses. The presence of the gap also removed the benefits of a contoured endwall which had been optimised for the no-gap case.

Chowdhury [102] investigated using midpassage gap purge to cool the endwall, however it was observed that cooling from the gap was concentrated over only a small area near the throat, such that it is unlikely to be optimal. The heat transfer coefficient was not measured leaving the possibility of overall detrimental effects, as was observed by Cardwell [99, 100].

Roy [103] confirmed the overall view of flow ingestion at the upstream part of the gap and ejection in the downstream half. Both endwall cooling effectiveness and HTC were measured and combined into heat heat flux reduction at engine conditions. Some areas of the endwall were found to have a net heat flux reduction, other areas to have an increase in net heat flux.

There has been very little study of the flow within the gap itself. This is of fundamental importance to understanding the causes of the mostly undesirable effects of the gap, and understanding what must be done to reduce these effects.

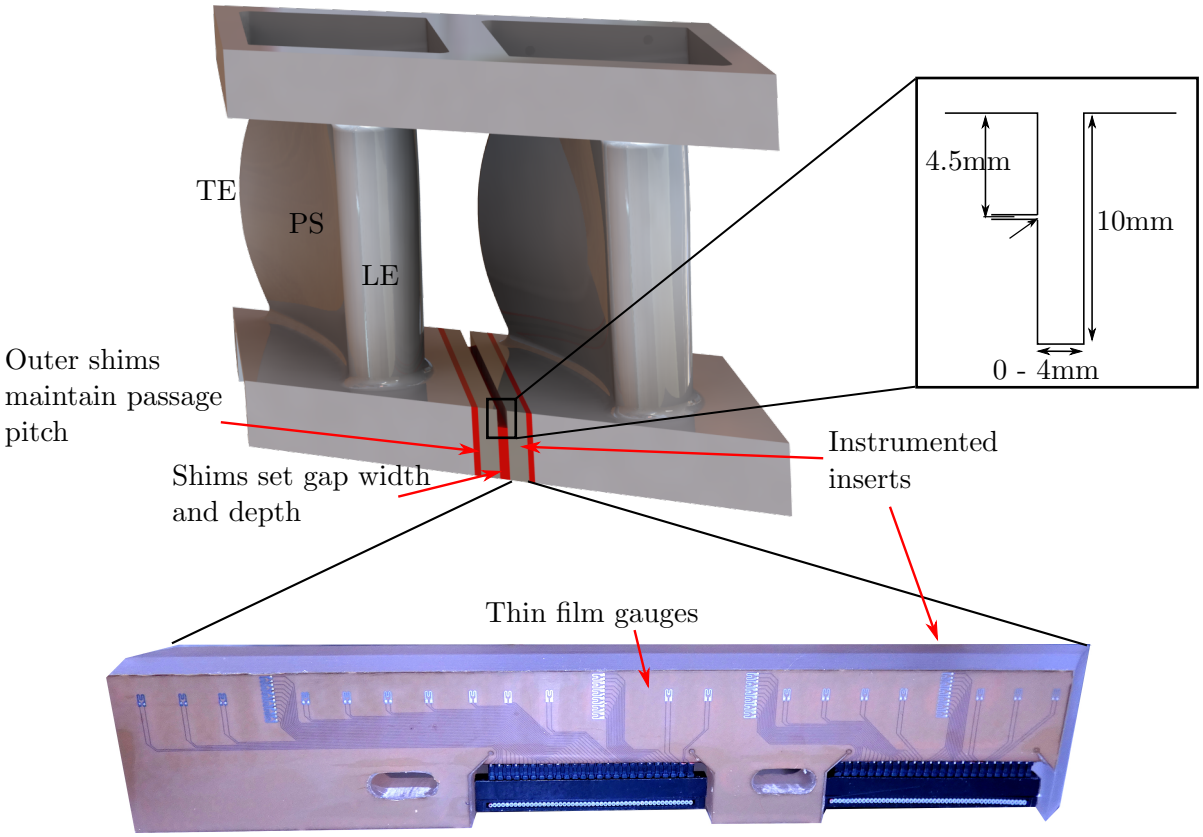


Figure 6.2: Test piece used for measurements of midpassage gap

6.2 Experimental set up

In order to investigate methods of minimising gap ingestion and heat transfer into the gap, experiments were carried out in the MHI High Speed Linear Cascade. A flexible platform for studying a mid-passage gap without purge was constructed. A pair of NGV were constructed using SLA (3-D printing), with a replaceable insert in the mid-passage where the gap would be located. This insert can be replaced with various instrumented inserts, to measure static pressure, or heat transfer, for various geometries in a flexible yet repeatable manner. The inserts are securely bolted in place before running, with the size of the gap set by the use of specially shaped shims. These shims allow the size of the gap to be adjusted, in increments of 0.1mm. Since the shims are made of soft paper or plastic, and are under compression when assembled, they also function as a seal to prevent any leakage flow. Measurement with a micrometer after assembly confirmed that the shims had a consistent thickness after compression. The assembly is illustrated in figure 6.2. Shims are also placed on both sides of the inserts to keep the total passage width constant while adjusting the width only of the gap; in this way different gap geometries and different instrumentation can be used in an otherwise identical cascade.

Gap geometry consists of a straight sided gap, fully sealed at the bottom with no purge flow. The width of the gap was varied between 0.2mm and 3mm. The depth of the gap was kept a constant

10mm, equivalent to 16.7mm at engine scale, for this set of experiments, although the depth of this gap could be varied in future. Test pieces were available to either include a chamfer, reflecting industrial practice, or be sharp cornered. The chamfer is present in the real engine due to the difficulty of cooling sufficiently a sharp corner being heated on both sides. Static pressure measurements were made using both a sharp cornered gap geometry and a chamfered gap geometry, to ascertain whether this changed the flow dynamics. Static pressure was measured using drilled tappings communicating with an array of pressure sensors via pneumatic tubing.

Thin film gauges were chosen to measure heat transfer coefficients within the gap, as the lack of optical access to the inside the gap made using an infra-red camera impossible. Thin film gauges consist of a thin film of platinum on a polyimide substrate, which act as high speed resistance temperature detectors. The manufacture and use of thin film gauges the measure heat transfer coefficient is described in section 2.4.

A second experimental campaign was carried out to investigate aerodynamic losses resulting from the midpassage gap. This was carried out at lower speed, using a blower. This allowed longer experimental run times than were possible using a compressed air supply. The Reynolds number at lower speed was 6×10^5, compared to 1.6×10^6 at high speed. Exit Mach number is reduced from 0.65 to 0.24 in the lower speed case. This was necessary in order to carry out detailed traverses to measure aerodynamics. The traverse was carried out using a flattened Pitot probe which was able to take measurements close to the endwall.

6.3 CFD simulation of midpassage gap

A steady CFD simulation was run in order to assist with visualisation and investigation of flow physics, as well as to investigate cooling flows which was beyond the scope of the experimental campaign. Several different gap sizes were analysed to provide a comparison to the analytical model over a range. The same mesh topology was used for all cases, only the width of the gap was changed.

CFD was performed using a modified version of Denton's Tblock, modified to run using multiple CPUs. This is described in detail in section 2.7. A multiblock structured grid was used of 1.5M cells in 9 blocks. Each gap consists of one block with 18 nodes uniformly spaced across. A mixing length turbulence model was used, where mixing length is taken as wall distance near walls, and a maximum value equal to a proportion of passage width in the mainstream flow path away from walls. This is established practice for turbomachinery flows using this solver. Within the gaps mixing length is strictly wall distance. All boundary layers were assumed to be fully turbulent. The main purpose of CFD for this study was to give insight into the physical mechanism for flow in the gap as a complement

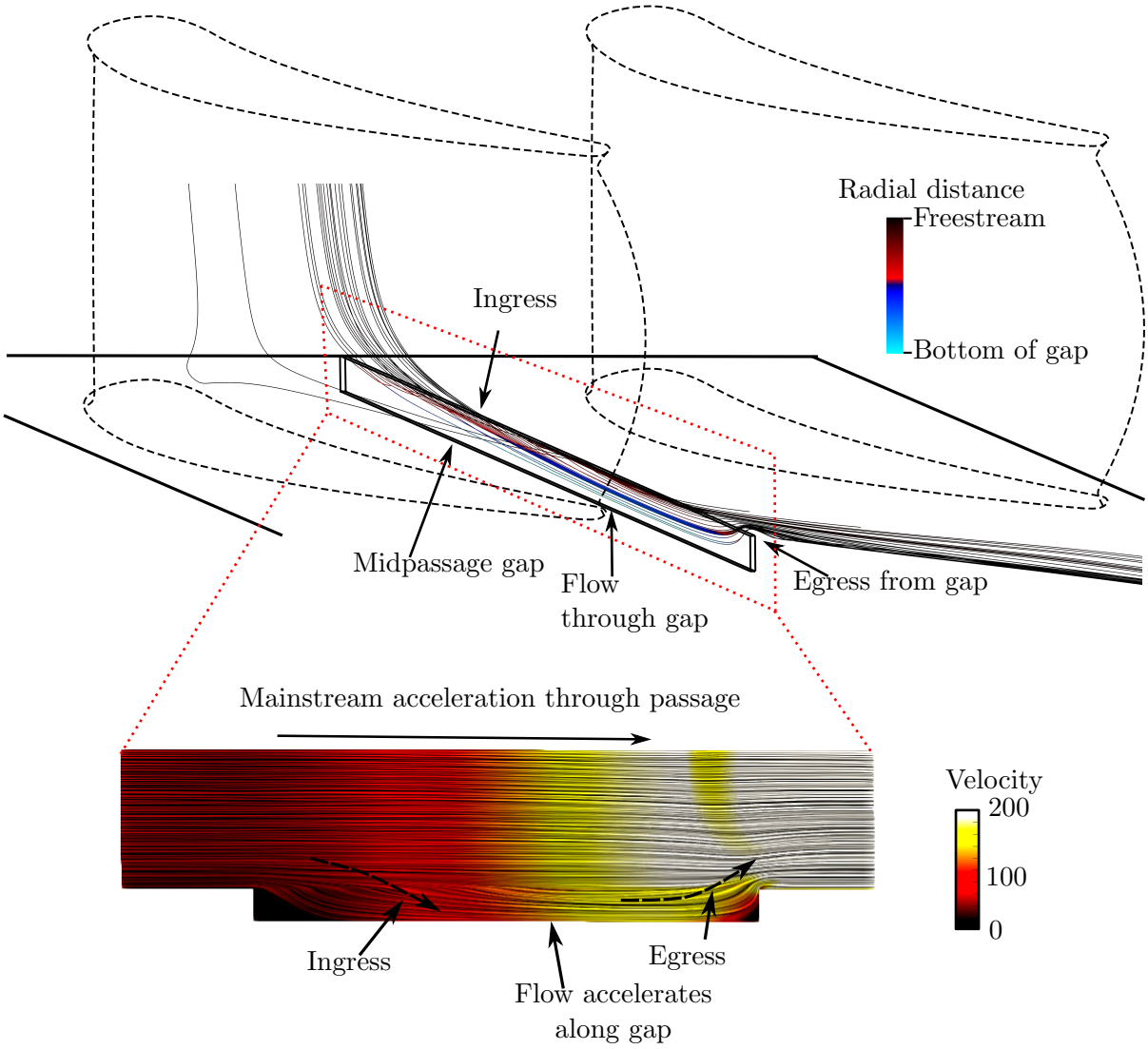


Figure 6.3: Streamlines of flow into and out of gap from CFD. Streamlines have been seeded from the top of the gap, both forwards and backwards to show both the flow entering, within, and leaving the gap. Streamlines are coloured by radial co-ordinate to aid visualisation. Below: LIC of flow through gap

to experiments.

The results of this CFD agree well with experiment, and also are consistent in character with the results of the works mentioned in the introduction, performed by several different groups using a variety of different geometries and techniques.

6.4 Overview of flow within gap

The physical mechanism dominating the flow within the midpassage gap is simple and fundamental, but is not obvious and has not been stated explicitly in any of the preceding literature.

The midpassage gap spans from a short distance upstream of a blade or vane to a short distance downstream. Between these two endpoints there is a relatively large pressure difference, in the case focused on in this study there is a pressure ratio of about 1.6. Since the gap is open along its whole length, we would expect that the pressure at any point will be very similar in magnitude to the freestream static pressure above that point, for if it is not fluid will ingress or egress to equalise the pressure.

Given the opportunity, mainstream fluid enters the gap and travels down this pressure gradient from high pressure to low pressure, bypassing the main passage.

For approximately the first 75% of the gap length (depending on geometry) flow is entering the gap. For the last 25% flow exits the gap. Flow into, through and finally out of the gap is shown using streamlines in figure 6.3.

Due to the extremely high pressure gradient down the length of the gap, flow within the gap accelerates to a high velocity, comparable to the freestream velocity. This in turn results in a high heat transfer coefficient between the flow and the sides of the gap, and consequentially a high heat load into the sides of the vane platforms. In the case with no purge studied here, 20% of platform heat load is a result of the gap (calculated simply as area times average HTC). If flow ingress into the gap could be reduced or eliminated, or HTC significantly reduced, this would represent a significant reduction of the total heat load on the vane.

There is also a potential to reduce the significant aerodynamic losses associated with the gap. Since the gap is simply a straight passage with no turning or change in area, taking the fluid from the high pressure to low pressure, before mixing with the free stream again, any flow through the gap represents a loss of aerodynamic efficiency.

It is shown in figure 6.4 that the pressure within the gap is mostly fixed to the static pressure in the freestream. Near the end of the gap, there is some deviation from the freestream static pressure. This is due to the high velocity gap flow being forced to rapidly egress to satisfy continuity.

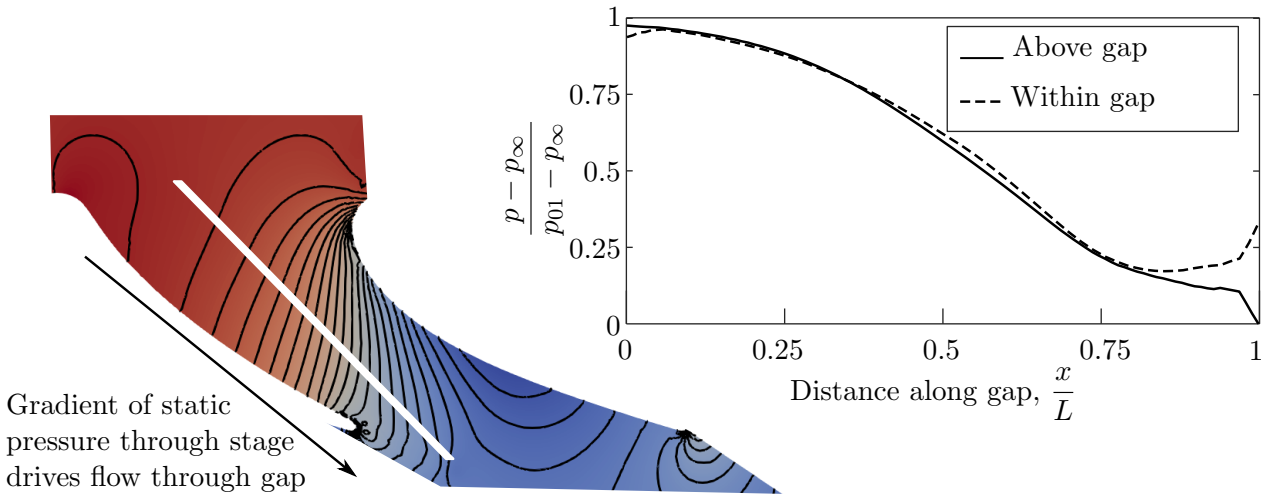


Figure 6.4: Pressure within the gap is fixed by the static pressure field in the freestream over the majority of the length.

The ingress and egress of fluid into the gap also has an effect on endwall heat transfer, causing a re-distribution of HTC, with some areas of the endwall having increased HTC, and other areas reduced. When purge flow is used there may also be some cooling effectiveness on the endwall.

6.5 Low order analysis of flow in gap

A simplified model of the flow within the gap, using a one-dimensional ordinary differential equation(ODE), can be constructed and gives significant insight into the factors affecting the flow. The equation is based on consideration of momentum, static pressure forces, and wall shear forces in the gap. Many further refinements are possible to give more accurate results, until the limit of solving the 3-D Navier-Stokes equations with a turbulence model, but when analysing these more complicated results it is easy to lose sight of the fundamentals which drive the flow field, and the effects of the fundamental geometric parameters. The 1-D model shows the most important driving forces on the flow, and which geometrical parameters should be changed to give a beneficial effect. Despite the extreme simplification of the model used here, it gives a good agreement with CFD and experimental data, and is expected to be useful for design.

6.5.1 Derivation of equation for mass flow within midpassage gap

Assumptions and approximations

The fluid properties at a plane normal to the gap axis are considered to be everywhere equal to the average at that plane. Fluid may enter of leave the gap, so mass flow along the gap is not conserved,

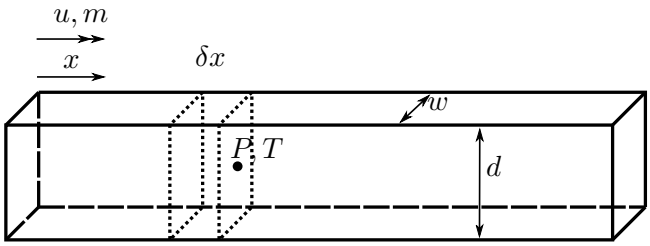


Figure 6.5: Model used to derive 1-D equation for gap flow. This model gave good agreement with CFD and experimental measurements.

but the change in momentum flux as a result of fluid ingress or egress is taken account of in the equation described. The mainstream flow is considered to be entirely unaffected by the flow in the gap. It is assumed that the static pressure inside the gap is fixed to be equal to the static pressure in the mainstream above that point; this is justified based on the observations of CFD and experiments.

Fluid is assumed to be an ideal gas. The equation is derived for compressible flow, with static temperature dependant on velocity and total temperature. Total temperature may be treated as a constant for adiabatic flow, or a second ODE can be added to calculate the total temperature subject to heat transfer. The gap is assumed to be much greater depth than width, $d >> w$. Cross-sectional area of the gap is assumed to be constant.

Derivation of equation

Figure 6.5 illustrates the physical assumptions used to derive a 1-D equation. Mass flux, m, and momentum flux, I, are defined at a control surface. Differentiating with respect to x gives change in momentum flux, I'. Momentum flux at control surface, I:

$$m = \rho u A \tag{6.1}$$

$$I = mu\,\mathrm{sgn}(u) \tag{6.2}$$

$$I' = m'u + u'm \tag{6.3}$$

$$\frac{m'}{m} = \frac{\rho'}{\rho} + \frac{u'}{u} \tag{6.4}$$

Combining equations 6.3 and 6.4 gives the equation for change in momentum flux:

$$I' = 2u'm + mu\frac{\rho'}{\rho} \tag{6.5}$$

Change in momentum flux over length δx, with an ingressing mass flux δm^*

$$\frac{dI}{dx}\delta x = \underbrace{-A\frac{dp}{dx}\delta x}_{\text{Pressure force}} - \underbrace{F_\tau \delta x}_{\text{Wall shear force}} + \underbrace{m' u^\star \delta x}_{\text{Momentum flux of ingressing fluid}} \tag{6.6}$$

Between two control surfaces, there will be mainstream fluid ingress, injecting additional momentum flux into the cavity. u^* is the velocity of free stream fluid above the cavity, when fluid is ingressing, or if mass flux is leaving the gap, $u^* = u$.

Combining equations 6.5 and 6.6 and re-arranging gives an expression for change in velocity through the gap.

$$u' = \frac{\frac{F_\tau - Ap'}{m} + \frac{\rho'}{\rho}(u^* - u)}{\left(2 - \frac{u^*}{u}\right)} \tag{6.7}$$

For a compressible flow, ρ must be allowed to change as a function of static temperature.

$$\frac{\rho'}{\rho} = \frac{p'}{p} - \frac{T_0'}{T} + \frac{uu'}{c_p T} \tag{6.8}$$

Substituting this into equation 6.7 and re-arranging gives an equation for change in velocity along the length of the gap.

$$u' = \frac{\frac{F_\tau - Ap'}{m} + \left(\frac{p'}{p} - \frac{T_0'}{T}\right)(u^* - u)}{1 + \left(1 - \frac{u^*}{u}\right)\left(1 + \frac{u^2}{c_p T}\right)} \tag{6.9}$$

Shear stress is not known exactly, but may be estimated as equation 6.10, where $C_\tau = 6$ for fully developed laminar flow, or $C_\tau = 16$ for 7th power law fully developed turbulent flow. This approximates that flow through the gap is always fully developed.

$$F_\tau = 2d\frac{C_\tau u \mu}{w} \tag{6.10}$$

6.5.2 Solution of equation for mass flow within midpassage gap

Equation 6.9 was solved numerically from an initial condition in MATLAB using an explicit marching scheme. The code used to solve the 1-D equation is given in appendix B.3. This 1-D model of the flow gives good agreement with fully 3D RANS CFD. This gives confidence that the physical explanation given in section 6.5, on which the 1-D model is based, is indeed the dominant mechanism forcing the flow in this region.

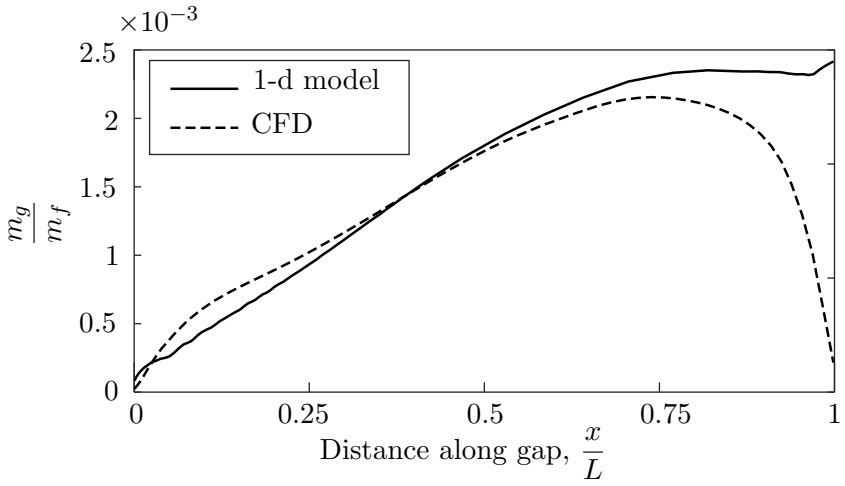


Figure 6.6: Mass flow calculated from CFD and from 1-D model using external static pressure as input. For the first 3/4 of the gap this gives good results

Figure 6.6 shows the calculated mass flow and velocity using 1-D model, compared to RANS CFD using 21k nodes in the gap alone, and 1.5M nodes in total for the whole domain. While the velocity and mass flow is too high at the far end of the gap, due to there being insufficient degrees of freedom in the equation to impose the necessary boundary condition, for most of the passage the mass flows and velocity are remarkably accurate.

The solution of the ODE was found to be quite robust and insensitive to initial conditions. It must be emphasised that this result is from an entirely analytical consideration, with no parameters requiring tuning to match the results. The only parameter available for adjustment in the model is the value of the shear stress coefficient C_τ. In practice it is not certain what value this should take. A value of 16, corresponding to fully developed turbulent flow, gave good agreement to CFD, but the CFD itself assumed all boundary layers to be fully turbulent, so agreement is not unexpected. The Reynolds number within the gap is sufficiently small that transitional or laminar flow might be expected over some areas.

The magnitude of the mass flow is such that 0.2% of mainstream mass flow is bypassing the passage and flowing through the gap, in this geometry with baseline gap width.

6.5.3 Derivation of critical threshold for gap flow

To help gain insight into the most important parameters affecting gap flow, an even more simplified model is derived, of a 1-D ODE with constant coefficients. From this, a set of 0-D solutions can be obtained, allowing approximation of gap flow from the basic operating conditions.

Firstly, heat transfer is neglected, so that $T_0' = 0$, and compressibility is considered negligible so that $u^2/(c_p T) \ll 1$. Rather than p' as a function of position, a constant value of $p' = \Delta p/L$ is used. An effective ingress length $L = 0.6L_{\text{true}}$ was used to account for the fact that continuity forces flow to

egress somewhat before the end of the gap, as seen in figure 6.6. The natural values of u^* to choose are either the freestream velocity above that point along the gap, or a lower value on the basis that ingested fluid will be from the boundary layer and will have a low velocity. To calculate this exactly would require a full 3-D CFD, negating the value of a simplified model. For the sake of calculation simplicity, a natural choice of value would be either $u^* = u$, or $u^* = 0$. Taking $u^* = 0$ was found to give good agreement with experimental results, and this value is used in the following section. This can be justified by considering that the fluid entering the gap is from the boundary layer and so will have a low velocity.

Using these approximations, and put in terms of gap mass flow, equation 6.9 can be simplified to equation 6.11 below.

$$\frac{dm}{dx} = \frac{Bm^2 + Cm + D}{m} \tag{6.11}$$

$$B = -\frac{p'}{p} \tag{6.12}$$

$$C = -\frac{2dC_\tau \mu}{w} \tag{6.13}$$

$$D = -A^2 p' \rho \tag{6.14}$$

Equation 6.11 is difficult to solve analytically, but approximate solutions can be found for different situations.

Inviscid solution: $C = 0$ and $x = L$;

$$m = \sqrt{\frac{D}{B}} \sqrt{e^{2Bx} - 1} \tag{6.15}$$

Viscosity dominated, with shear stress balancing pressure force:

$$m = -\frac{D}{C} = \frac{\rho d p' w^3}{2C_\tau \mu} \tag{6.16}$$

Equations 6.15 and 6.16 can be used to estimate the upper bound of what is expected mass flow through the gap. Mass flow will be the minimum of these two upper bounds.

The point at which viscosity becomes dominant can be calculated by comparing which of these

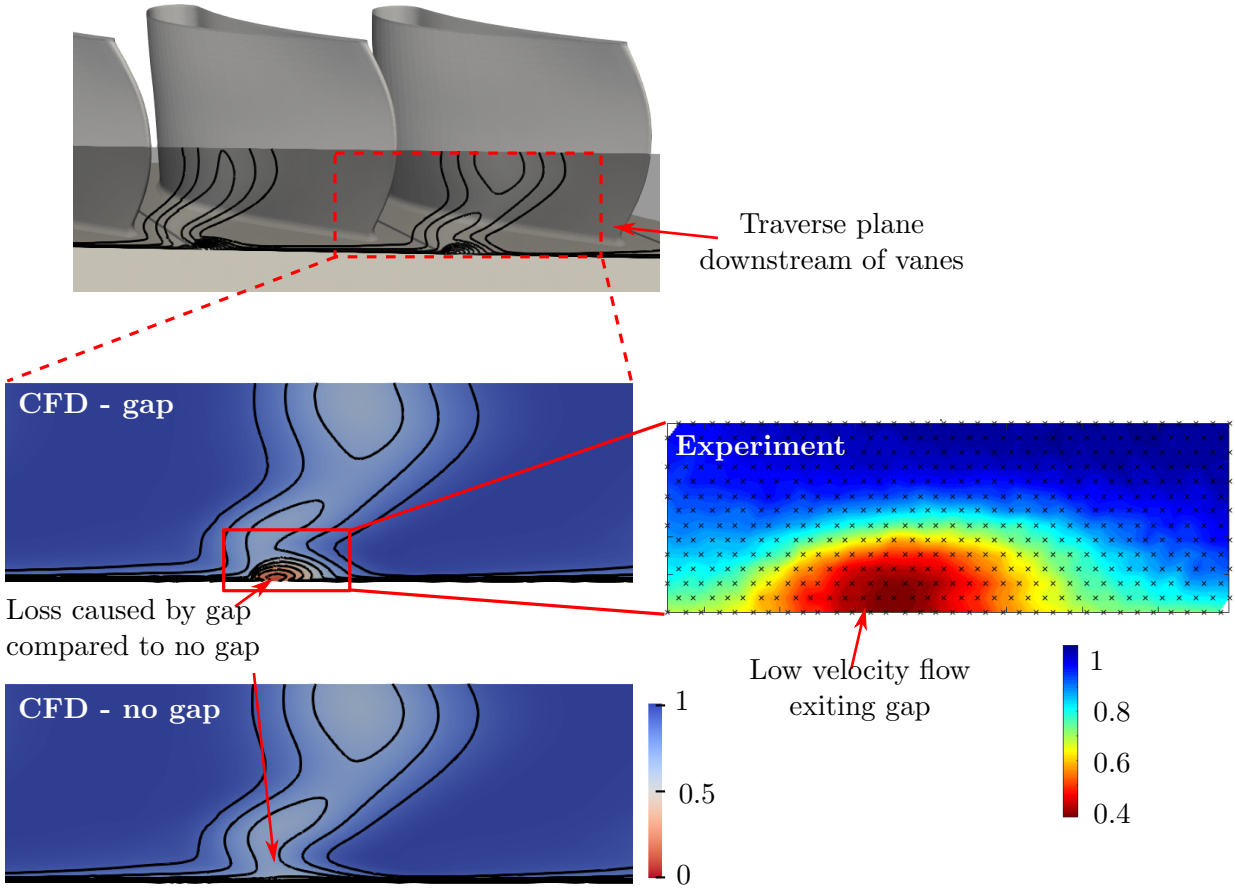


Figure 6.7: Total pressure downstream of gap, measured using a 2-axis traverse. Flow which has passed through the gap creates a distinct loss core.

two solutions is greater.

$$\frac{D}{C} < \sqrt{\frac{D}{B}}\sqrt{e^{2BL}-1} \tag{6.17}$$

$$\ln\left(1+\frac{BD}{C^2}\right) < 2BL \tag{6.18}$$

$$\frac{BD}{C^2} < 2BL \tag{6.19}$$

$$\frac{w^2\sqrt{\rho\Delta p}}{4LC_\tau\mu} < 1 \tag{6.20}$$

Equation 6.20 can be used as a non-dimensional value characterising whether the gap is viscous dominated or not, with smaller values being desirable.

6.6 Aerodynamic losses due to midpassage gap

Since flow is bypassing the main passage and flowing through the gap, there is a corresponding loss of stage efficiency. Loss is examined using the methodology popularised by Denton [46] of considering

entropy generation as a measure of loss. Entropy loss coefficient is defined as:

$$\zeta = \frac{T_2 \Delta s}{h_{02} - h_2} \tag{6.21}$$

It is assumed that mainstream flow through the passage has a constant total pressure $p_{0f} = p_{01}$. A total mass flow remains constant, but is split between freestream and gap flow: $m = m_f + m_g$. Gap flow is split from the mainstream, and rejoins at some location with a different velocity and at a flow angle α. After some distance the flows will be well mixed again to give flow conditions u_2, p_{02} etc. It is assumed that mixing takes place at a constant pressure in a constant cross-sectional area duct. Applying conservation of momentum total pressure downstream can be calculated.

$$u_f m_f + u_g m_g \cos\alpha = u_2 m \tag{6.22}$$

$$p_{01} = p + 1/2 \rho u_f^2 \tag{6.23}$$

$$p_{02} = p_{01} - 1/2 \rho u_f^2 + 1/2 \rho u_2^2 \tag{6.24}$$

$$p_0 = p_{01} - \rho \frac{m_g}{m_f} u_f \left(u_f - u_g \cos\alpha + \frac{m_g}{m_f} u_g \cos\alpha \right) \tag{6.25}$$

From this change in total pressure, entropy generation Δs can be calculated.

$$\Delta s = -R \ln \left(\frac{p_0}{p_{01}} \right) \tag{6.26}$$

$$\Delta s = -R \ln \left(1 - \frac{\rho u_f^2}{p_{01}} \frac{m_g}{m_f} \left(1 - \frac{u_g}{u_f} \cos\alpha + \frac{m_g}{m_f} \frac{u_g}{u_f} \cos\alpha \right) \right) \tag{6.27}$$

$$\Delta s \approx R \cdot \frac{\rho u_f^2}{p_{01}} \frac{m_g}{m_f} \left(1 - \frac{u_g}{u_f} \cos\alpha + \frac{m_g}{m_f} \frac{u_g}{u_f} \cos\alpha \right) \tag{6.28}$$

$$\zeta \approx 2 \frac{p}{p_{01}} \frac{m_g}{m_f} \left(1 - \frac{u_g}{u_f} \cos\alpha \right) \tag{6.29}$$

For a given machine p/p_{01} will be fixed, so loss coefficient due to the effect of the gap will be proportional to gap mass flow ratio. It is possible to recover some of the loss from the gap if velocity leaving the gap is high and aligned with mainstream flow.

This loss analysis assumed gap flow exited with a uniform velocity. The vast majority of gap flow does exit over a short distance past the throat, and so this assumption appears reasonable.

For the cascade being studied, this indicated a 0.3% loss of stage efficiency due to the presence of the gap. The mass flow through the gap has been shown to be enormously sensitive to the gap width however, so this may be increased several times, or reduced to negligible levels by adjusting the gap width, all within the realistically expected tolerances of the real machine.

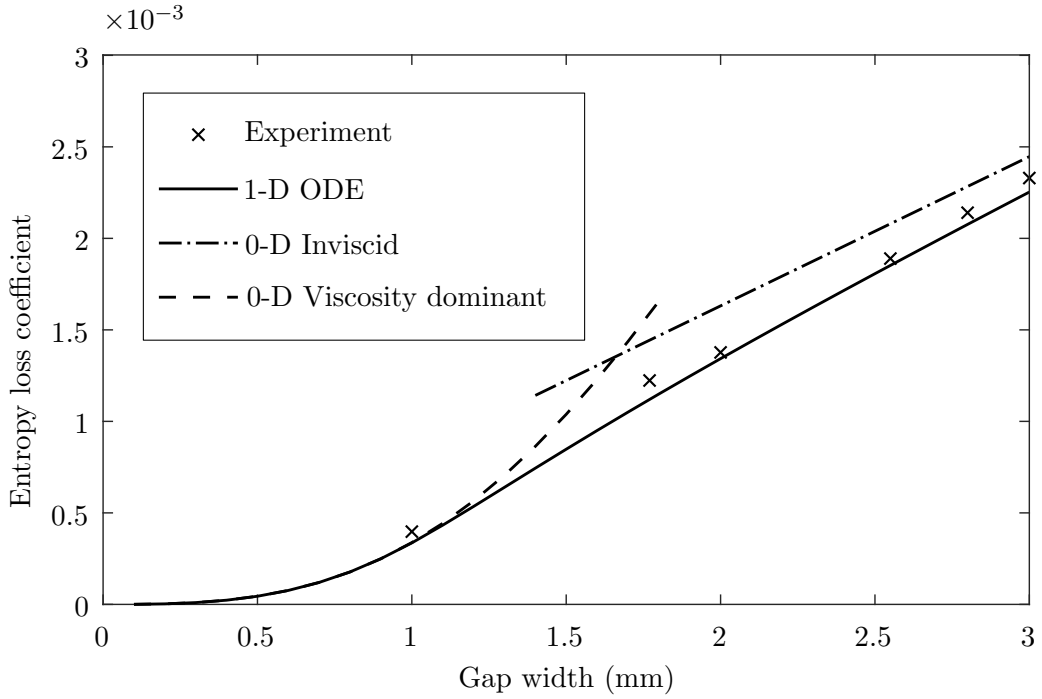


Figure 6.8: Mixed out losses due to gap: experiment and approximations

6.7 Comparison of predicted loss to experiments

To compare losses a series of low speed tests were performed using a blower. Total pressure was measured using a one-hole probe traverse over a small area. These experiments were all carried out with straight sided gap with no chamfer.

An example of the traverse measurement is shown in figure 6.7. The loss core due to the presence of the gap can clearly be seen by comparing the case with a gap to the case without the gap. Although it only covers a small area of the passage, the intensity of the loss core is greater than any of the secondary flow or wake losses. Using equation 6.23, the total mixed out loss is calculated.

Figure 6.8 shows the mixed out loss for a low-speed flow measured with a one hole probe traverse, compared to approximations of the solution to the 1-D analysis. The one-dimensional model gives a remarkably good prediction for losses in this case, showing the power of this model for predicting gap flows. While a large gap may cause considerable losses, this can be reduced to negligible levels by reducing the gap width sufficiently.

6.8 Additional heat load to vane platform due to gap

Mainstream fluid flowing through the midpassage gap results in an additional heat load to the vane platforms. Heat transfer to the vane platforms both reduces thermodynamic efficiency, and reduces component life. In some vane designs the area of the gap walls is as much as 20% of the endwall

area. A wide gap has a similar heat transfer coefficient to the endwall, so that the gap may account for almost 20% of the total heat load into the platform. This may be reduced by using a purge flow through the gap to prevent ingress, but we will show in this section that it may also be reduced to very low levels by modifying the geometry of the gap, such that purge flows may be unnecessary.

Fluid heat capacity upper bound

Heat transfer coefficient is defined as:

$$h = \frac{q}{A_w \Delta T} \tag{6.30}$$

There is a limited possible heat flux into the gap given by the heat capacity of the fluid entering:

$$q_{\max} = m c_p \Delta T \tag{6.31}$$

Combining these two equations gives the maximum mean heat transfer coefficient in the gap, due to gap flow, neglecting turbulent diffusion through the top of the gap.

$$\bar{h}_{\max} = \frac{m c_p}{A_w} \tag{6.32}$$

So if m can be reduced to an acceptably low level, then so too can heat transfer coefficients in the gap. This is a maximum level for narrow gaps, larger gaps will have an HTC of a similar magnitude to the main passage endwall HTC.

For a viscosity dominated gap, then this can be combined with equation 6.16 to give an upper bound of heat transfer.

$$\bar{h}_{\max} = \frac{\Delta p \rho c_p}{\mu L^2 C} \cdot w^3 \tag{6.33}$$

Therefore, in general the best method to reduce heat transfer into the gap is to reduce the gap width. By reducing the gap width to sufficiently low levels, HTC can be reduced to negligible levels even in the absence of purge flow.

Dittus-Boetler upper bound

The local heat transfer coefficient can be found using established correlations. The Dittus-Boetler equation[104] is a simple correlation to give Nusselt number as a function of Reynolds number and

Prandlt number:

$$\mathrm{Nu}^* = 0.023\mathrm{Re}_w^{0.8}\mathrm{Pr}^{0.3} \tag{6.34}$$

$$h^* = 0.023\left(\frac{\rho u}{\mu}\right)^{0.8} Pr^{0.3} k \cdot D_h^{-0.2} \tag{6.35}$$

In this correlation, the length scale used in Re and Nu is the hydraulic diameter. For a narrow rectangular channel hydraulic diameter $D_h = 2w$. This gives the local heat transfer coefficient, with respect to the fluid temperature in the gap. For larger gaps, this can act as an upper bound to true heat transfer coefficient, with respect to freestream temperature.

Ordinary differential equation for heat transfer

A more detailed 1-D analysis is given below.

For simplicity, for now we will use the freestream inlet temperature as reference temperature.

An second ODE can be derived for temperature in the gap. Total internal energy flux through a control surface:

$$U = mc_pT \tag{6.36}$$

Change in internal energy flux

$$(mc_pT)' = 2dh(T_w - T) + c_pT_fm' \tag{6.37}$$

Rearranging and substituting $u = c_pT$ gives:

$$T' = \frac{2dh^*(T_w - T) + c_pT_fm' - m'c_pT}{c_pm} \tag{6.38}$$

Real heat transfer coefficient is then calculated as:

$$h = \frac{q}{2d(T_f - Tw)} = \frac{h^*(T_g - T_w)}{(T_f - T_w)} \tag{6.39}$$

Alternatively, heat transfer coefficient can be defined as the change in wall heat flux with respect to a change in temperature:

$$h = \frac{q_2 - q_1}{2d(T_{f2} - T_{f1})} \tag{6.40}$$

These two methods give almost identical results, differing by less than 1 in 10^6.

Equation 6.38 was solved as an uncoupled equation, with mass flow calculated first. It is also possible to solve for temperature with a coupled ODE. This makes little difference to the results in

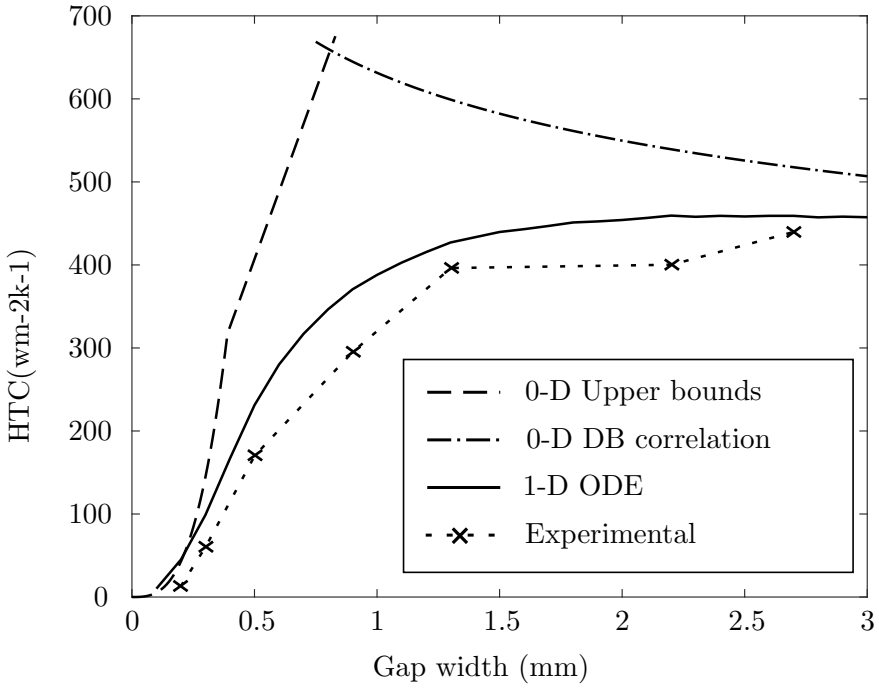


Figure 6.9: Measurements and results of 1-D analysis for different gap widths from 0.2mm to 1mm. Heat transfer coefficients in the gap and losses can be reduced to almost zero levels by reducing gap width

this case, but has been included in appendix B.2 for reference.

The results of this are shown for a variety of gap widths in figure 6.9. By reducing gap width to a low enough value, heat transfer into the gap can be reduced to essentially zero levels. For example in this machine, a gap width of 0.2mm would have a negligible level of heat transfer coefficient.

6.8.1 Measured distribution of heat transfer coefficient within gap

Experiments were carried out with a set of thin film gauges to measure the distribution of HTC along the length of, and through the depth of the gap.

Figure 6.10 shows the distribution of HTC over the internal surface of the gap. There is a high HTC through the whole depth of the gap, and along the whole length. The fact that HTC is roughly uniform through the depth of the gap gives confidence to the idea that a 1-D model should be sufficient to analyse gap heat transfers.

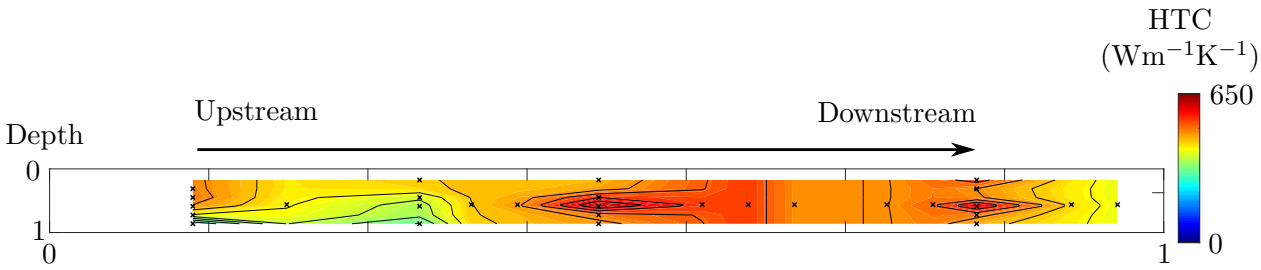


Figure 6.10: Heat transfer distribution over the internal surfaces of the gap.

6.9 Control of ingress using purge flows

While it has been shown that the best case scenario is a narrow gap, with viscous forces dominant and thus a low velocity and negligible heat transfer into the gap and losses, in practice this may be difficult to achieve. Purge flow may then be used to prevent ingestion and so prevent excessive heat load into the vane platform. However, with naive purge flow schemes, such as a uniform purge flow, or allowing a leaky seal, there may be large areas inside the gap which are not effectively cooled. Additionally, these purge regimes use a large excess of cooling flow with consequent reduction in efficiency. To minimise the required purge flow, the distribution of the introduced purge is critical.

A modified 1-D ODE to take into account addition of purge flow can be derived. m' is considered to consist of the sum of ingress, m'_i and purge flow, m'_p.

$$m' = m'_i + m'_p \tag{6.41}$$

$$-Ap' - F_\tau + m'_i u^* = 2m'u - \frac{\rho'}{\rho} mu \tag{6.42}$$

This gives the required ODE:

$$m'_p + m'_i(1 - \frac{u^*}{2u}) = \frac{m\rho'}{2\rho} - \frac{Ap' + F_\tau}{2u} \tag{6.43}$$

By setting $m_i = 0$, the purge flow rate to ensure zero mainstream ingress is found:

$$m'_p = \frac{m\rho'}{2\rho} - \frac{(Ap' + F_\tau)}{2u} \tag{6.44}$$

This gives the minimum purge flow required to prevent any ingress into the gap. A cooling effectiveness of purge flow within the gap is defined:

$$\eta = \frac{T_f - T}{T_f - T_c} \tag{6.45}$$

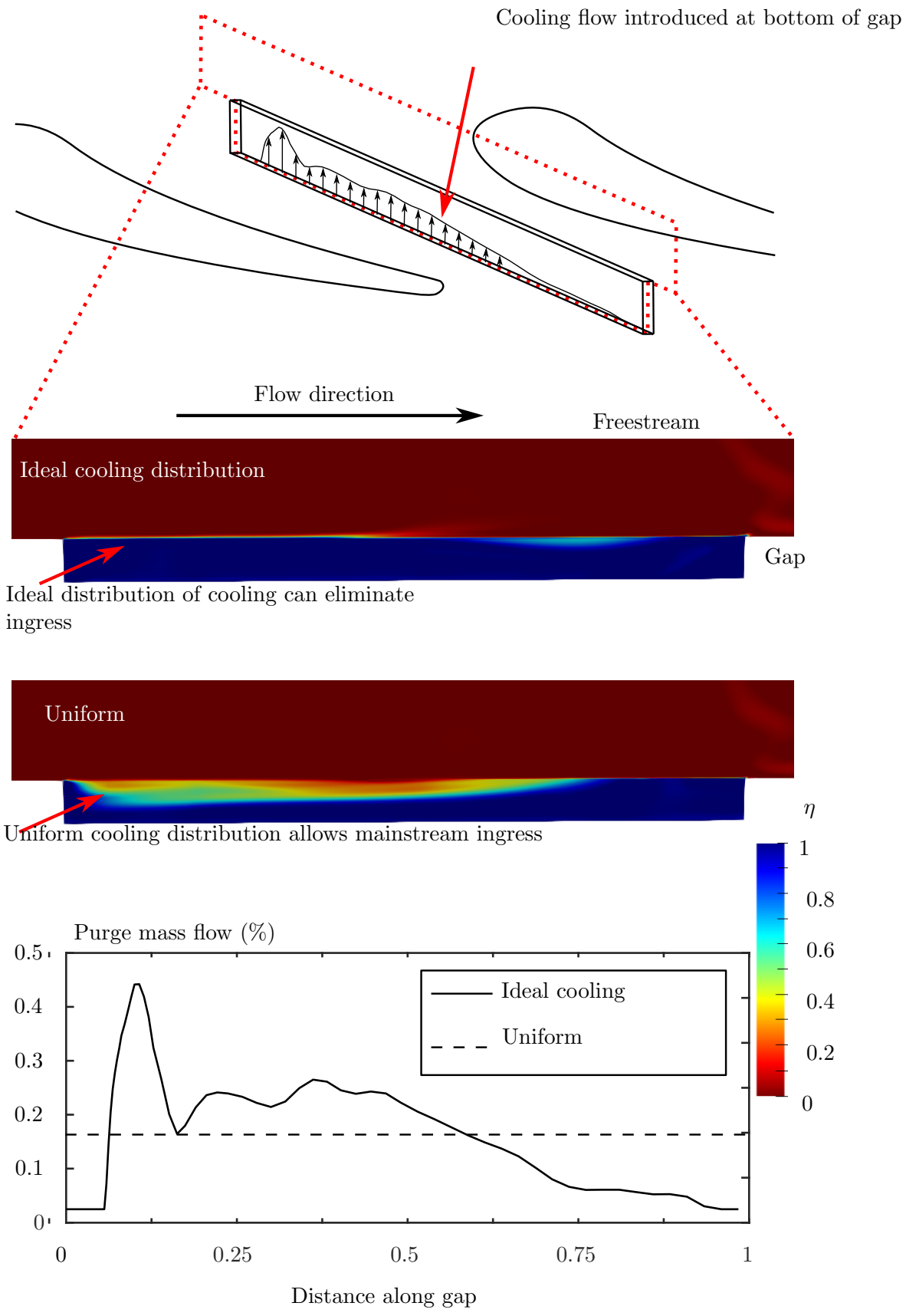


Figure 6.11: Ideal purge flow to cool a 1mm wide midpassage gap, calculated using 1-D ODE and verified with CFD. This is calculated directly from the 1-D model with no iteration required.

With purge flow present, a cooling effectiveness very close to 1 can be achieved within the gap. Figure 6.11 shows that the gap may be almost perfectly cooled by a modest amount of cooling air, 0.17% of mainstream cooling air, when distributed optimally. The purge flow distribution shown in figure 6.11 did not require any iterative optimisation, but rather was calculated using the 1-D ODE equation 6.44. If the same amount of cooling air is distributed uniformly along the length of the gap, then there are some areas with significant mainstream ingress which are not well cooled. If purge flow were to be introduced by means of a leaky seal along the length of the gap, then most purge flow would enter at the lowest pressure areas downstream, which is exactly the opposite situation to the optimal case. This is both ineffective at protecting from ingress, and uses an excessive amount of purge flow. The ideal purge flow distribution can be achieved in practice by non-uniform spacing of cooling holes within the gap, with more purge flow directed into the upstream part of the gap.

If it is desired to use some purge flow to act as endwall cooling, then equation 6.43 can be used to calculate the purge flow required to achieve this.

6.10 Effect of gap flow on endwall HTC

The gap may have a significant effect on the distribution of HTC over the endwall. The exact nature of the redistributing effect will likely depend on the exact gap geometry, and may be positive or negative.

In the test case studied here, the overall effect on HTC was generally neutral. The endwall HTC with and without the gap are shown calculated by CFD in figure 6.12. Some areas has an increased HTC, as boundary layer fluid was entrained into the gap, leaving behind a thin boundary layer and consequentially a higher HTC. This was balanced however by areas of lowered HTC where fluid was egressing. It bears repeating however, that although the effect on the endwall itself may be neutral, there is additional heat transfer taking place in the gap itself.

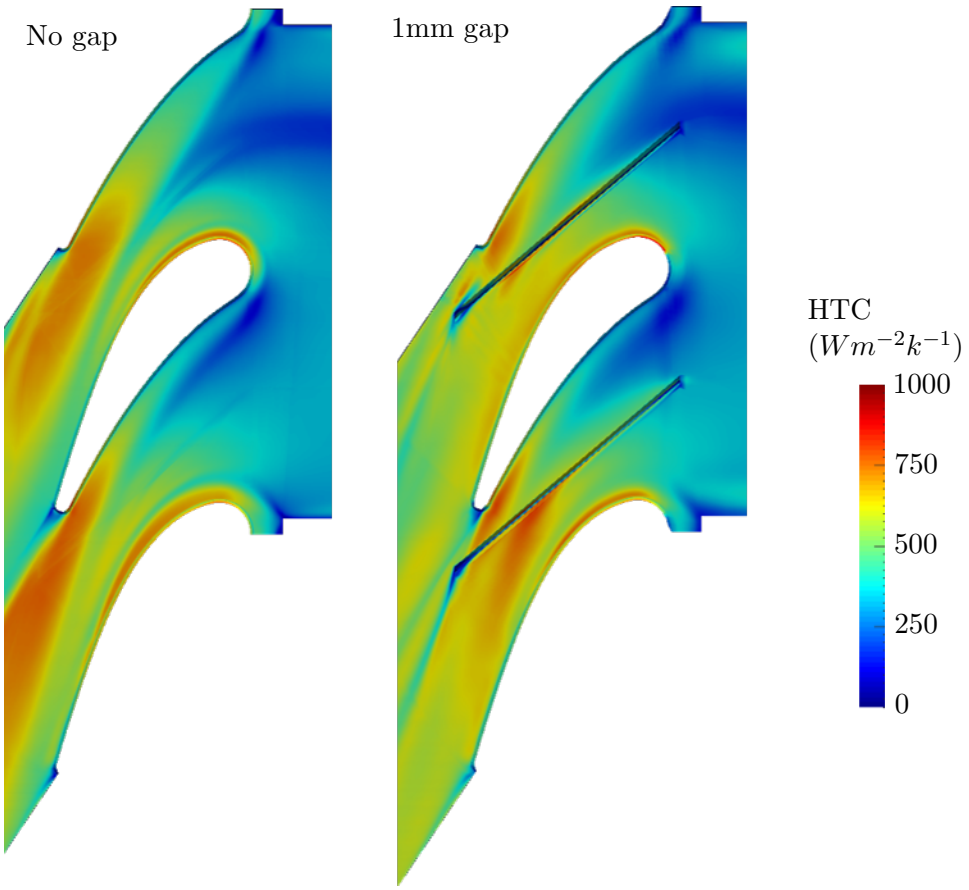


Figure 6.12: Endwall HTC with and without midpassage gap (RANS)

6.11 Effect of chamfered edges and other geometrical modifications

As has been shown, the flow through the gap is caused by the externally imposed static pressure gradient. The detailed geometry of the top of the gap makes only a negligible difference to this.

In some machines there is a chamfer at the top of the gap. The addition of a chamfer at the top of the gap adds to the gap flow, as there is effectively a larger gap area. This increases losses and total heat transfer. It would be better for efficiency if the size of the chamfer was minimised.

Figure 6.13 shows the static pressure measured within the gap with and without a chamfer. Although the difference is measurable, it is too small to make any significant difference to the flow within the gap.

Likewise, changing the slot angle of the gap is not likely to make any great difference to the flow.

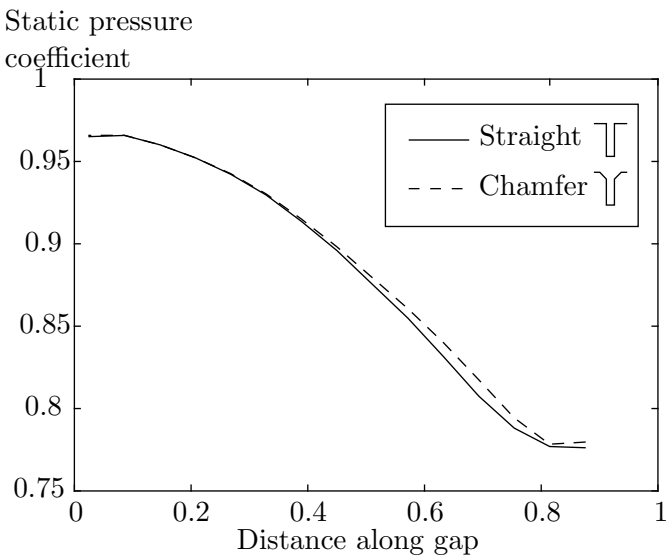


Figure 6.13: Static pressure within the gap with and without a chamfered edge. The difference is not enough to significantly change the flow physics.

6.12 Estimate of gap influence

To summarise, the influence of the gap can be estimated for a generic turbine stage using the following process:

1. Check viscous flow parameter

$$G = \frac{w^2\sqrt{\rho\Delta p}}{4LC_\tau\mu} \tag{6.46}$$

   If $G \ll 1$, then gap flow is highly viscous dominated and is unlikely to be problematic. If instead $G \sim 1$ or $G > 1$, then there will be high velocity flow through the gap which may cause losses and excessive heat transfer.

2. Estimate mass flux through the gap. For $G < 1$

$$m = 2GA\sqrt{2\Delta p\rho} \tag{6.47}$$

   Or for $G > 1$

$$m_g = A\sqrt{\Delta p\rho}\sqrt{e^{\Delta p/p} - 1} \tag{6.48}$$

3. An estimate of stage efficiency loss may then be estimated by

$$\zeta \approx 2\frac{p}{p_{01}}\frac{m_g}{m_f}\left(1 - \frac{m_g A_f}{m_f A_g}\cos\alpha\right) \tag{6.49}$$

4. An upper bound of gap internal heat transfer may be given as

$$\bar{h} = \min\left(\frac{m_g c_p}{2dL}\ ,\ 0.023\left(\frac{m}{\mu A}\right)^{0.8} Pr^{0.3} k \cdot D_h^{-0.2}\right) \tag{6.50}$$

These approximations will of course not give a completely accurate assessment of every possible machine, but should be sufficient to check whether or not a fuller analysis is warranted.

6.13 Conclusions and recommendations

There is a potentially extremely high heat load into the blade or vane platform through the midpassage gap, as well as causing aerodynamic loss and modification of endwall HTC, so it is an area which should not be neglected in design.

Flow through the gap is driven by the static pressure gradient imposed by the mainstream. This may accelerate fluid to a velocity near to the mainstream velocity. Heat transfer coefficients of the gap will be similar to the endwall HTC. Since flow is effectively bypassing the main passage there is also a loss associated with the gap flow.

If the gap width can be reduced below a critical threshold, flow though the gap can be dramatically reduced, with consequential improvements to both heat load and efficiency. This is of course subject to manufacturing constraints, but it is shown to be a worthy goal for designers to attempt.

The presence of a chamfer on the gap causes additional losses, so the size of the chamfer should be reduced as far as is practical. Chamfers and other minor geometrical features have a negligible impact on the pressure forces which drive the gap flow.

In real machines there is often an excessive amount of purge flow used to seal the gap and prevent hot gas ingress. With an ideal distribution of purge flow, hot gas ingress may be eliminated with a fraction of flow rates currently used.

The demonstration case for this study was the nozzle guide vane of a large frame industrial gas turbine, but the same principles will apply to all rotor and stator blades which posses a similar mid-passage gap.

A method to estimate the effect of gap flow is presented, so that for any machine the significance of the gap may be assessed.

Chapter 7

Ingress into stationary ring segment cavity

7.1 Introduction

Industrial gas turbines have a cavity between adjacent ring segments. The hub cavity consists of a stationary ring segment adjacent to a rotating ring segment. For reasons of assemblability, there is a cavity also between stationary ring segments on the casing side. There have been instances in MHI gas turbines of localised component damage which appears to be due to hot gas ingestion into the ring segment cavity. This chapter investigates the local effects of mainstream ingress causing heat transfer into the vane platform, and whether this may be reduced without excessive cooling air usage.

Experiments were carried out on a simplified geometry in a high speed linear cascade. The geometry investigated consisted of a set of Nozzle guide vanes with a cavity downstream. The geometry to be tested was supplied by MHI, based on their F-class gas turbine.

RANS CFD was carried out in order to help gain physical insight into the flow phenomena present. Use of purge flow to prevent ingress is also investigated with CFD. A method to reduce mainstream ingress by means of focusing cooling flows is suggested, and is demonstrated in a CFD study.

The area of the gas turbine under test is shown schematically in figure 7.1. There is a can combustion chamber, followed by the stator vanes, each formed of one piece with its own platform. Following the stator vanes is the turbine rotor. On the hub side the rotor platform is formed as one piece with the rotor blade. The casing is formed from separate stationary ring segments. Between stator vane platforms and rotor platforms and ring segments there are cavities through which flow may ingress.

All of these components include internal and external(film) cooling. Some of the stator platform

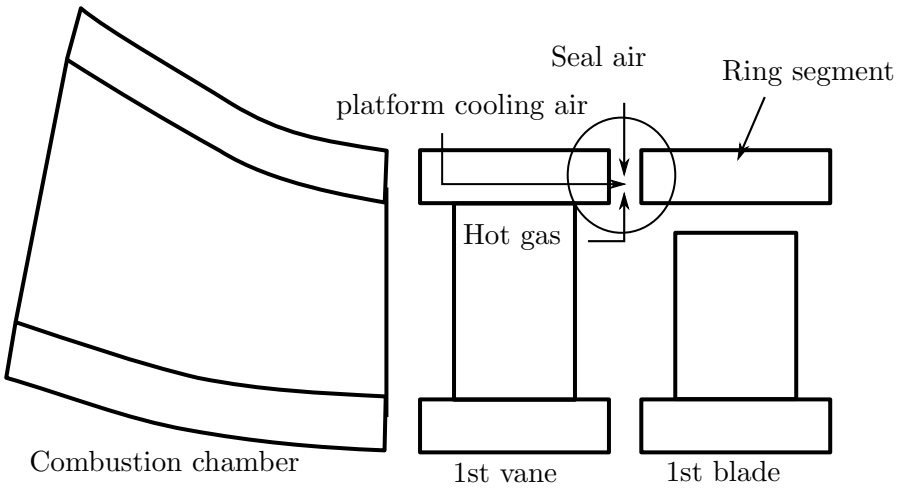


Figure 7.1: Schematic of flow domain showing stationary ring segment under investigation. Similar effects may apply in rotating segments as well however

internal cooling air is exhausted into the stator vane platform-ring segment cavity, where it is ideally expected to provide some degree of sealing of this area. As well as this, some additional sealing air may be deliberately introduced to prevent hot gas ingress. It is desirable to reduce as much as possible the use of additional sealing air in this area, in order to increase efficiency.

It should be emphasised that this study is concerned with the stationary ring segment, as a rotating ring segment will have quite different physics, due to the radial pump effect (centrifugal force on the boundary layer) of the rotating segment. Qualitatively, the results may still have some applicability to rotating ring segments. The focus is on the interaction of the main flow with the cavity and ingestion which occurs, rather than details of sealing. It is believed that these are the first detailed measurements of heat transfer within the ring segment to be carried out.

In addition, this study was carried out in a linear cascade, but in a annular domain there will be additional forces in the polar reference frame, for example centrifugal force due to the circumferential velocity component. The downstream rotating blade row is also not included in this study.

7.2 Turbine ring cavity literature review

There is plentiful literature on the subject of hot gas ingestion into turbine ring cavities. However, most existing studies consider the ring cavity to be circumferentially uniform. The rotor pumping is of course circumferentially uniform, and rotor blade passing speeds are fast enough that it is reasonable to consider only the time averaged effect of these. However, the stator vane potential field extends some way both upstream and downstream of the vanes themselves. This means that there is a non-uniform circumferential pressure field. A purge flow calculated on the basis of preventing ingestion in the case of a uniform pressure field will thus be excess in regions of lower static pressure, and insufficient in

the regions of higher pressure, allowing hot gas ingress.

Many studies have been carried out on ingestion into the turbine wheelspace by the Bath group [105, 106, 107, 108]. By use of trace gas sampling ingestion into the wheelspace can be determined at different levels of purge flow. Sophisticated models have been developed to help quantify the ingestion. Gentilhomme et al.[109] measured experimentally and modelled rim seal ingestion between the NGV and rotor disc, including measurements of the effect of including rotational effects compared to modelling NGVs alone. It was found that modelling the vanes alone produced very similar results to modelling the entire turbine stage.

Owen[105, 106] details the modelling of ingestion by means of orifice equations. These are based on inviscid equations, with empirical discharge coefficients used to account for viscous effects. Externally induced ingress occurs over that area where the mainstream static pressure is greater than the internal pressure, and egress occurs when mainstream pressure is lower.

Scobie et al.[107] reviewed the research into ingress into rim seals. In general, ingress is caused by circumferentially non-uniform pressure caused by the presence of blades and vanes, and also by the centrifugal pumping effect of the rotating disk. As mentioned, in the present work rotational effects are not considered. Relatively simple orifice models are often used to estimate the amount of hot gas ingestion which occurs. Sealing effectiveness is often measured experimentally in test facilities by using tracer gas concentration measurements within the wheel space. Seal geometries featuring various axial and radial clearances are typically used along with a net purge flow rate to try to eliminate mainstream ingress. Scobie et al. identified several unanswered questions of importance, including the effect of ingress on heat transfer and what effect the egressing fluid has on blades downstream.

Scobie et al.[108] carried out detailed concentration measurements within the seal clearance, at different circumferential positions. The results confirmed the importance of the circumferential pressure variation on flow ingress. Sealing flow concentration was also shown to vary circumferentially with pressure downstream of the seal, showing the circumferential variation in egress. Within the rim seal region, the effectiveness was little effected by the seal configuration used inboard to protect the wheelspace; this indicates that the present study may also have a wider applicability even though an inboard seal is not modelled.

Clark et al.[110] investigated experimentally the effects of purge hole configuration on sealing effectiveness. Two different densities of uniformly spaced holes were investigated, with the higher density of holes found to give better sealing effectiveness.

No studies appear to attempt to introduce circumferentially non-uniform purge flows to counter the circumferentially non-uniform externally induced ingress. This will be demonstrated in the present

work using CFD and a simplified geometry, we suggest that this would be a interesting method to investigate in those more specialised rigs which have been built for rim seal investigations.

7.3 Experimental setup

Experiments were carried out in the MHI High Speed Linear Cascade. A new set of nozzle guide vanes was manufactured for the purpose of carrying out these tests, using an extended length cascade working section which has sufficient space downstream to allow the inclusion of a downstream cavity and instrumentation.

The modelled flow domain is shown in figure 7.2. Three full vanes are used including the downstream cavity, and well as two end pieces which do not include a downstream cavity. The middle vane is directly behind a combustor wall, and it is this vane which is always instrumented, to maximise periodicity of the cavity.

Measurements were taken using both an infra-red camera and thin film gauges for heat transfer measurements, and a static pressure was measured through tappings. IR gives full surface coverage, and requires less specialised manufacturing, but cannot measure areas to which there is no optical access. To measure heat transfer within the cavity itself, thin film gauges were used.

Vanes were constructed out of SLA resin. To make the cavity, a replaceable section downstream was manufactured. This section was separated from the main section by shims, allowing the cavity spacing to be precisely set. Shims are used to set separation and then the downstream piece is securely bolted into place. This design was also intended to allow a future parametric study to vary the cavity spacing and measure the effects. A set of four vanes was fabricated, one painted to be suitable for infra-red measurements. A second vane was instrumented with 96 thin film gauges within the cavity.

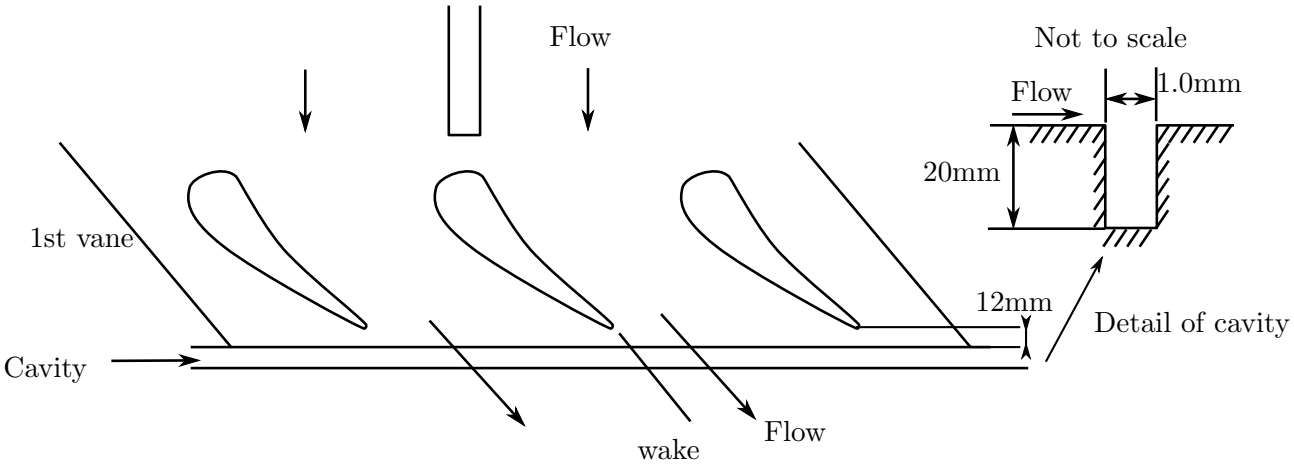


Figure 7.2: Experimentally measured flow domain. Four passages were used rrepresenting two can combustors and four vanes. A circumferential cavity was behind the vanes

A third vane was made with 64 pressure tappings within the cavity. These are shown in figure 7.3. A fourth vane did not include a cavity, but included pressure tappings at the same location as the cavity, to give a baseline measure of static pressure.

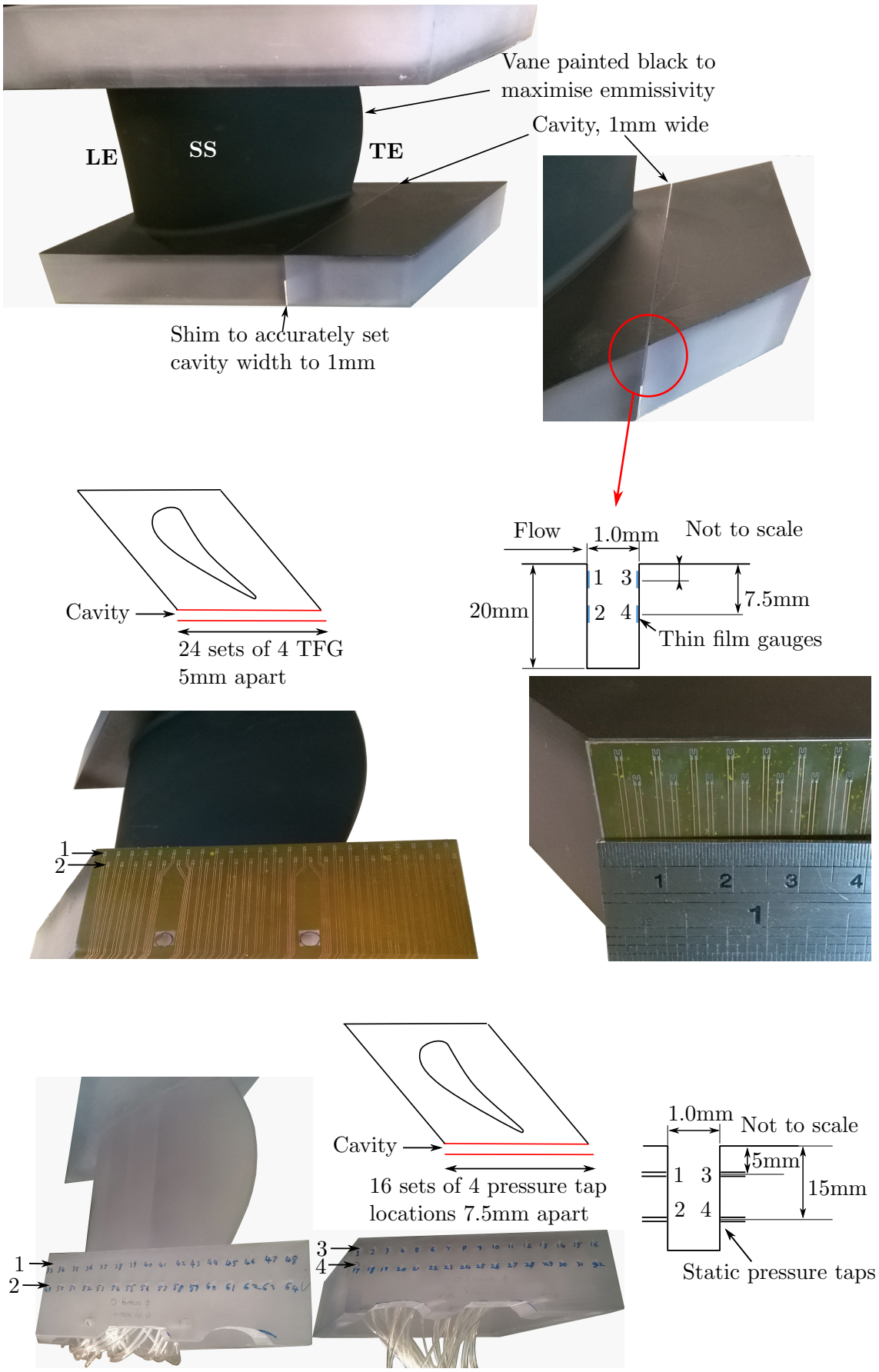


Figure 7.3: Test pieces used for cavity study experiments. Top: Vane used for IR. Middle: Vane instrumented with TFG in cavity. Bottom: Vane with static pressure tappings.

7.4 CFD domain

CFD was carried out using a parallelised version of Denton's Tblock solver, as described in section 2.7. The cavity consisted of 18 elements uniformly spaced across the gap. Due to the structured meshing, these elements propagate across the main passage, so increasing this number led to high aspect ratio cells perpendicular to the flow, which causes instability. The total number of cells was 2.8 million. RANS CFD was carried out using a mixing length turbulence model.

Two passages were modelled, with one vane downstream of a combustor wall. This leads to a slight difference in the pressure field behind the two vanes, which in turn leads to different ingress behaviour into the downstream cavity.

Initially, no seal air was used, to give a baseline which could be compared to experiments. Then a uniform cooling was added downstream of the vane platform. This reflects industrial practice, whereby air which has been used for internal cooling of the vane platform is exhausted into the cavity. This is intended to provide sealing and ideally provide some film cooling to downstream. A non-uniform distribution of platform cooling air has also been used to provide superior sealing and film cooling distribution.

7.5 Experimental and CFD results within cavity

7.5.1 External heat transfer coefficient

Heat transfer coefficient (HTC) on the endwall is shown for both experiments and CFD in figure 7.4. There is a good qualitative agreement between CFD and experiment. As flow passes over the cavity, HTC abruptly increases in some areas and decreases in others. This is due to ingress and egress from the cavity. Where flow ingresses, it is the boundary layer fluid which ingresses first, so that behind the cavity a new, thin boundary layer forms. This results in a higher HTC. From areas of ingress fluid flows through the cavity to lower pressure areas, where it egresses from the cavity. The low velocity egressing fluid adds to the boundary layer and results in a thicker boundary layer downstream. This results in a lower heat transfer coefficient.

7.5.2 Pressure within cavity

The static pressure within and above the cavity was measured. This is shown in figure 7.5. Pressure on the lower row of tappings are higher, showing the streamline curvature towards the top of the cavity, as flow moves from ingress to egress. The variation in static pressure above the cavity is the driving factor which causes fluid ingress and egress. There is no apparent way to reduce this driving

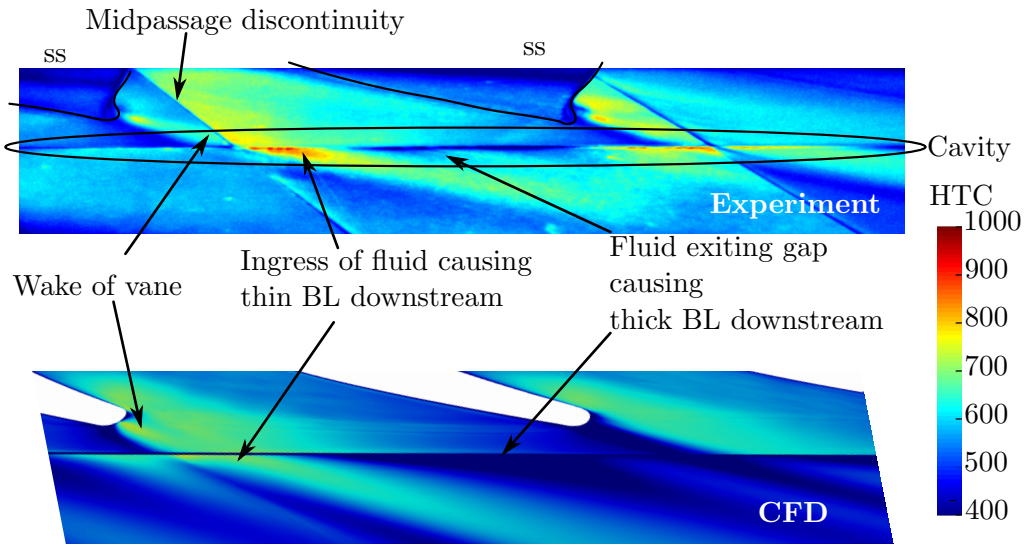


Figure 7.4: Top: IR measurements of htc in the vicinity of cavity. Bottom: CFD predictions of HTC. There is a good agreement downstream the cavity, areas of higher HTC show ingress, while areas of lower htc showing egress are present in both CFD and experimental data, and locations match.

pressure, without gross redesign of the stator vanes. The pressure within the cavity may be more amenable to modification to prevent ingress.

Alternatively, if cavity width was reduced, the levels of ingress would be reduced further; this is dependent on design and manufacturing constraints of course.

7.5.3 Heat transfer coefficient within cavity

Figure 7.6 shows the internal heat transfer coefficients within the cavity, measured using thin film gauges. The highest levels of HTC are around the same levels as freestream HTC. However, there are also areas of low velocity where HTC is almost zero.

There is a wide range of HTC measured within the cavity, with HTC going from almost zero over a significant area of the cavity, up to the same as the freestream magnitude over other areas. Many gauges, arranged in different sets agree on this variation and the locations where each occurs, lending confidence to the results. The very high levels of local HTC explain the damage which has been observed in real machines.

The upper row of gauges shows higher HTC, as would be expected given that there be a higher velocity in this area. The level of HTC measured by the lower row is still significant however, showing that ingressing fluid penetrates to a significant depth in to the cavity. The locations of measured high HTC correspond to the locations of ingress identified by external IR measurements.

The very high levels of HTC which occur show the importance of knowledge of flow in this area, as excessive heat transfer may easily occur if not properly managed.

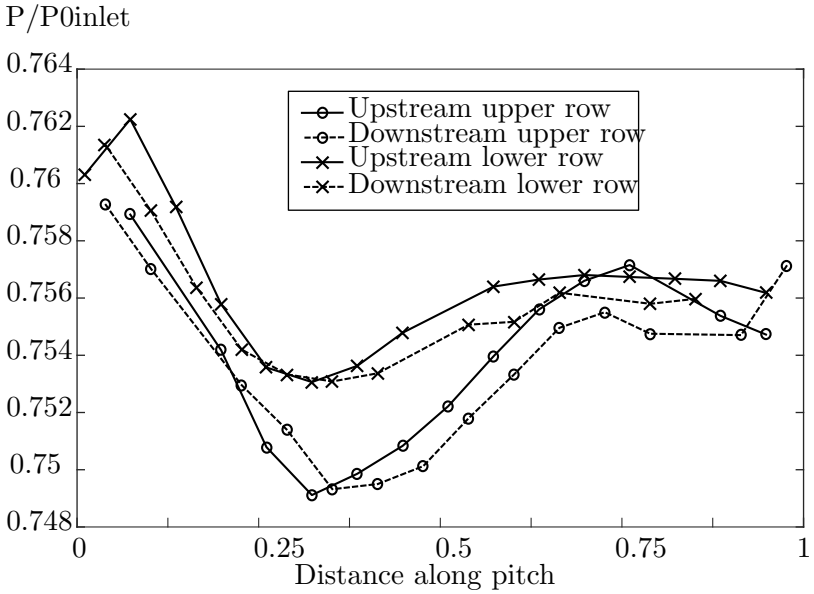


Figure 7.5: Static pressure within the cavity. The static pressure difference between freestream and cavity drives flow ingress and egress. Variation in cavity pressure is less within cavity than in the freestream above.

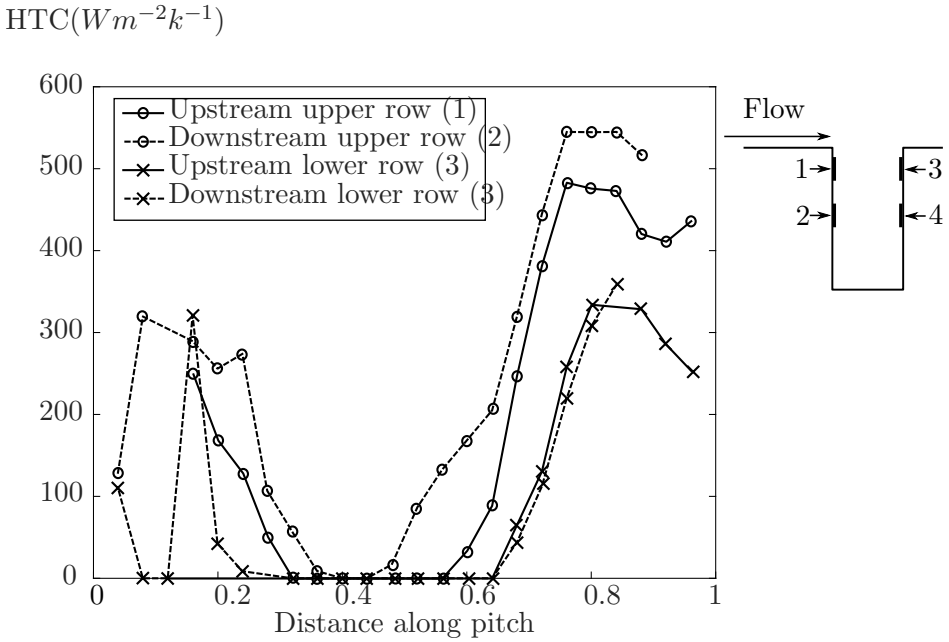


Figure 7.6: HTC within cavity measured using TFGs. Maximum HTC is up to the same levels as freestream HTC, but other areas have almost zero HTC where there is low flow velocity.

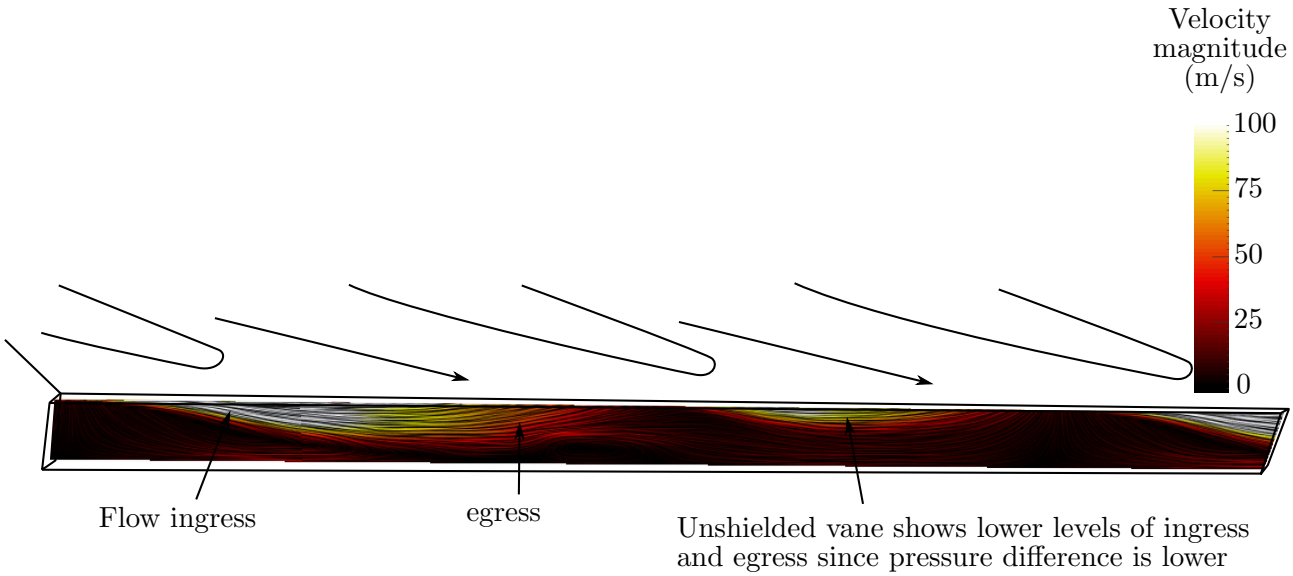


Figure 7.7: Velocity distribution and streamlines (LIC) from CFD show locations of very high velocity and other are of almost zero velocity, which explains measured heat transfer results. Some areas show flow velocities up to 100m/s, while in other areas it is zero

7.5.4 Flowfield within cavity

CFD results without cooling agree well with experimental data, and explains the flow physics that leads to ingress, and agrees with theoretical predictions.

Mainstream fluid ingresses into the cavity in some areas, and egresses elsewhere. Within the cavity, flow reaches very high local velocities, as shown in figure 7.7. High velocity within the cavity only occurs in localised areas. This explains the locally high HTC that was measured experimentally. Those areas which see high velocity ingressing mainstream fluid have a very high HTC, while other areas have low flow velocities and no ingress, and so have low HTC.

Flowfield from CFD is shown in figure 7.8, with streamlines seeded from a uniform line source just upstream of the cavity. Flow is ingested into the cavity mainly just behind the wake and pressure side of the vanes. Flow through the cavity causes high levels of local heat transfer where flow velocity is high, explaining the experimental HTC measurements, which showed very high levels of HTC in some areas, and almost zero levels elsewhere. Flow exits the cavity over a relatively small area, the thickened boundary layer so caused is clearly visible in surface HTC plots. This can also be seen in streamlines in figure 7.8. If purge flow is used then this effectively acts as film cooling on the downstream platform.

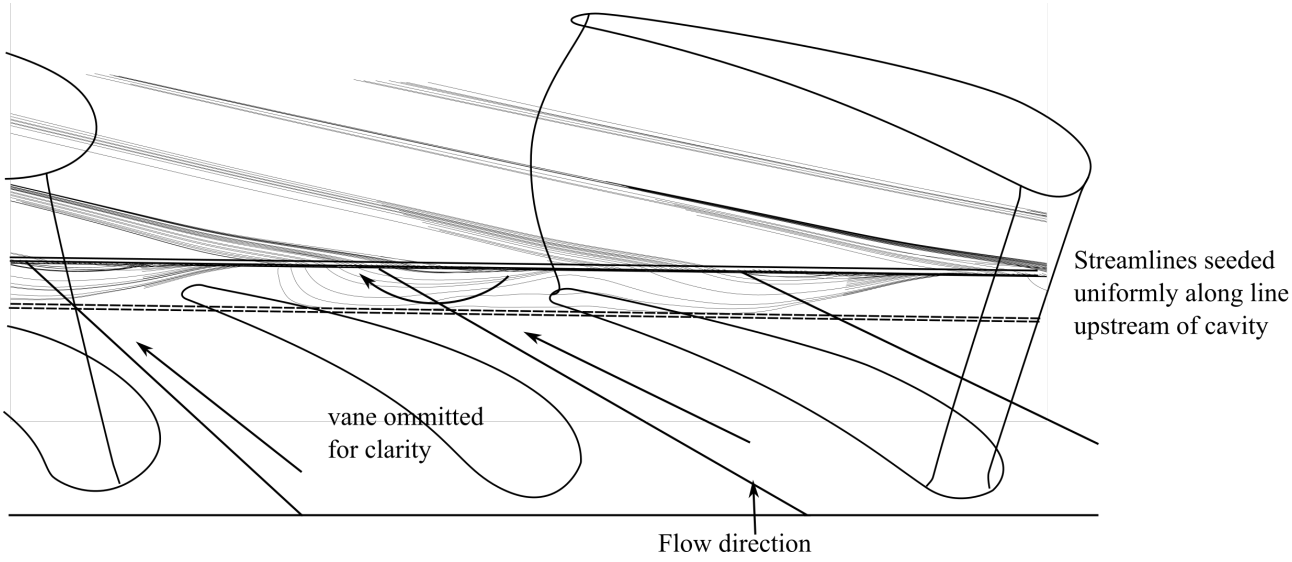


Figure 7.8: Flow ingress and egress from downstream cavity shown using streamlines from CFD

7.6 Explanation of flow into and out of cavity

The flow into and out of the cavity is caused by the static pressure field created by the vanes. In areas of higher pressure flow ingresses into the cavity. Flow then moves through the cavity and egresses in areas of lower pressure.

The circumferential velocity component is also extremely important to the flow field, and leads to large circumferential velocity within the cavity. Flow is turned through 70° by the NGVs, so that the main component of velocity is parallel to the cavity. When flow ingresses, the circumferential component of velocity ensures flow continues in the same circumferential direction before egressing, rather than spreading in both directions.

It is notable that there is a significant difference in flow ingress between the two vanes. This is due to the different downstream static pressure caused by the shielded compared to the unshielded vane, caused by the combustor wall upstream.

7.7 Downstream cavity with purge flows

A CFD simulation was carried out to investigate the effect of purge flow on the cavity. In the machine used as the model for this study, there is cooling air blown out of a uniformly spaced row of holes

Case	mass flow to prevent ingress	as % of mainstream
uniform	0.012	0.96
non-uniform	0.008	0.64
angled	0.006	0.48

Table 7.1: Cooling flow required to prevent cavity ingress with different cooling schemes. Cooling requirements can be halved compared to a uniform cooling distribution.

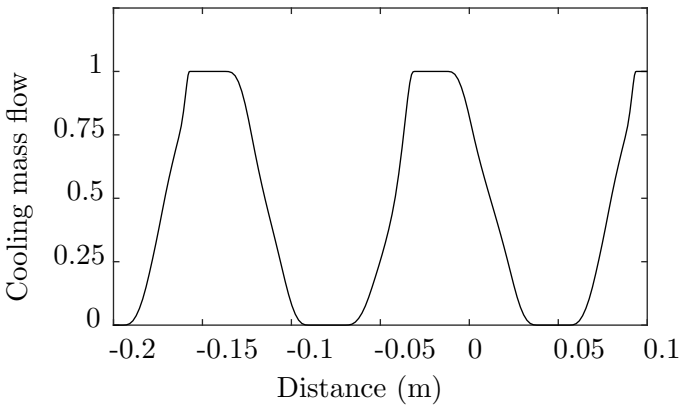


Figure 7.9: Circumferentially non-uniform cooling distribution used in cavity to prevent ingress. Cooling flow may be reduced 50% compared to a uniform cooling flow

within the cavity in the downstream side of the vane platform. This has been simulated with Tblock, using a uniform coolant patch and a realistic mass flow of 1% of mainstream flow.

A coolant patch is used over a large area, instead of modelling each hole individually. In reality discreet holes would be used for such small quantities of coolant, but the modelling is sufficiency to demonstrate the idea.

While this does reduce the levels of mainstream ingress, it does not eliminate it completely, there is still some ingress in the higher pressure areas behind the vanes. Moreover, this uses excessive amounts of cooling air, as most of the cooling air is exhausted out of areas which would not see any mainstream ingress anyway.

It was investigated whether concentrating the flow of cooling air more locally, concentrating on the areas of ingress, could reduce mainstream ingress while minimising cooling air usage.

Tblock was modified to allow non-uniform cooling flows to be specified. A Matlab script was created to generate the Tblock inlet files including non-uniform cooling. By means of this Matlab script cooling air could iteratively be added to the areas where there is ingress. In this way the cooling air locations could be optimised. The optimisation procedure was relatively crude, but is sufficient to show the large improvement which can be gained above a uniform cooling flow.

A further improvement may be gained by angling the cooling holes, so that ingress may be prevented with a smaller quantity of cooling air. If pressure inside the cavity is greater than that outside, then no ingress will occur.

0.5% of coolant mass flow was required to prevent ingress with the modified, non-uniform cooling scheme. This is approximately the amount currently exhausted from the vane platform in existing machines, so that sealing may be achieved by this without any additional seal air.

When this same coolant is distributed uniformly, it is insufficient to prevent mainstream ingress.

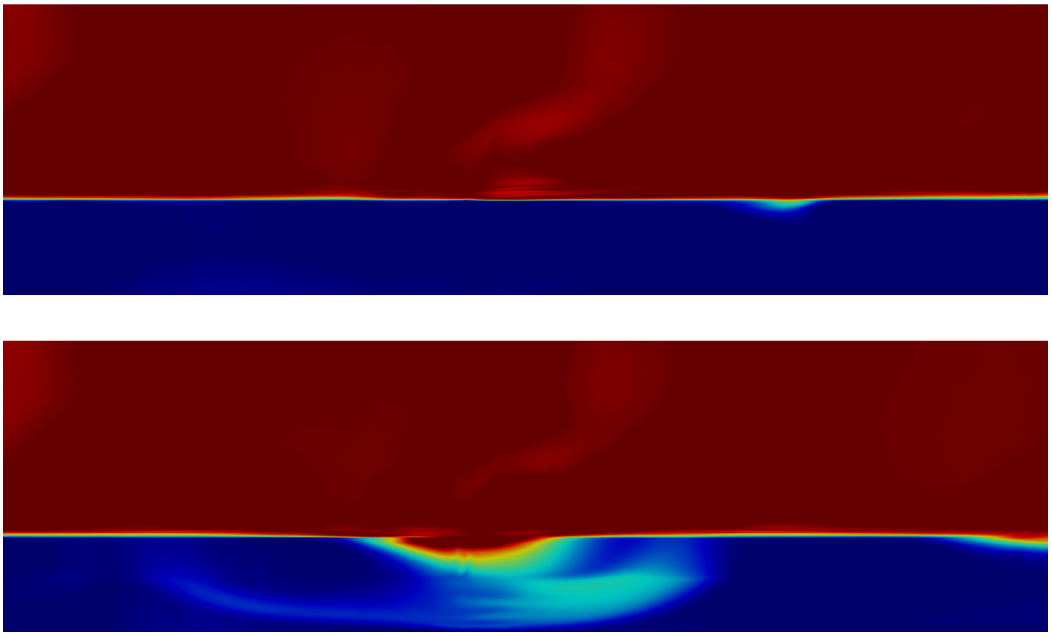


Figure 7.10: Temperature field due to ingress with optimum cooling compared to uniform cooling

When uniformly distributed, 1% of mainstream mass flow as required to prevent ingress. When non-uniformly distributed this can be reduced by a third to only 0.65% of mainstream mass flow required to prevent ingress.

Further improvements may be made by using angled cooling holes to blow air out of high static pressure areas. This can further reduce cooling air requirements, but it is perhaps more sensitive to cavity width and raises the possibility of instead entraining mainstream air from elsewhere. These schemes are summarised in table 7.1.

By using a cooling scheme of actively blowing air against ingress, required sealing flow rates were found to be less than half of a uniform sealing flow into the cavity, and complete sealing could be achieved. The circumferential distribution of cooling air in the cavity is shown in figure 7.9. The scheme is relatively simple, and has deliberately not been 'over optimised' in a very exact system which would likely to be sensitive to small changes in conditions.

This cooling strategy also has the secondary effect of spreading coolant over the ring segment downstream of the cavity. With a uniform coolant distribution, this coolant coverage is extremely uneven. With an optimised, non-uniform coolant distribution is employed, the downstream coolant coverage is more uniform.

While this investigation has been conducted only using stationary ring segments, the same principle should apply also to externally induced ingress between rotating segments. When ingress is being driven by circumferentially non-uniform pressure forces, the sealing flows opposing this ingress ought to have a corresponding circumferential non-uniformity.

Figure 7.10 shows the ingress which occurs when uniform cooling is used, but which can be eliminated by using non-uniformly distributed cooling.

7.8 Conclusion

Experiments and CFD have been carried out and found to be in reasonable agreement. Local HTC measurements in the rim cavity area have been carried out for the first time.

Most areas have hardly any fluid flow and very low HTC, ingress in concentrated in small areas of the cavity where there is the highest vane static pressure. Seal air, if any, can be concentrated into small areas of ingress. The results of this study are consistent with and explain observed damage in gas turbines.

This study shows the potential for localised seal flow as a method to reduce ingress. Since ingress is caused by locally higher pressure, it makes sense to also use locally concentrated seal flows to counter this, rather than uniformly applying sealing flows. This is very much dependent on machine geometry, but in the machine modelled and many others there is a platform cooling flow which is available for the purpose, so that additional seal flows may be minimised or eliminated.

By using non-uniform sealing flows, sealing flow rates could be halved compared to a circumferentially uniform flow giving the same level of sealing.

Further experiments could be carried out in future to test the proposed cooling scheme, and to test sensitivity to cavity width. This could be carried out in the existing facility without any major modification. More detailed studies including rotational effects and detailed seal geometry are probably better suited to purpose-built facilities such as those mentioned in the literature review.

These have been the first published results of heat transfer in this area, and show the extremely high levels of heat transfer which can occur locally, potentially causing damage to components even if sealing flows are sufficient to prevent ingress into wheelspaces and other secondary flow areas of the machine.

Chapter 8

Surface texturing to reduce heat transfer

8.1 Introduction

In this chapter, it is found that directional surface finish is an important factor for heat transfer, and so directionality must be accounted for in design using novel textured materials, such as ceramic matrix composites.

Furthermore, the heat transfer of the best case surface texture alignments is in fact lower than a smooth case. This suggests the possibility of deliberately engineering surface texture as a means of reducing heat transfer.

Use of novel materials with higher allowable working temperatures offers the possibility of a step change in efficiency of gas turbines. Many ceramics have melting points far higher than even the superalloys currently used for gas turbine hot path components. However, to date the generally low fracture toughness of ceramics have made them unsuitable for use in gas turbines. The development of ceramic matrix composites (CMC) may overcome these limitations and allow their use in gas turbine applications. A CMC consists of ceramic fibres embedded in a ceramic matrix. Often the matrix material is the same material as the fibres, so there is no reduction in melting point, but the fact that fibres can pull out of the matrix increases the crack propagation energy and so dramatically increases fracture toughness.

In common with other composite materials, CMC may often have a distinct surface texture of aligned grooves due to the fibres. The effect of this surface texture on heat transfer in a gas turbine application is investigated.

Previous work by Parfett [111] had found that the use of streamlined 'micro-contouring' of turbine



Figure 8.1: CMC samples. Left: without EBC. Right: with EBC

endwalls reduced heat transfer coefficients (HTC) by around 15%, and also reduced secondary flow losses. It was hypothesised that this was due to grooves inhibiting the cross-passage migration of boundary layer fluid, thus both reducing secondary flow losses and reducing HTC.

An experimental investigation was carried out to find whether the natural surface texture of CMC is an important consideration for design, and secondarily, whether this surface texture could be exploited to actually give beneficial effects.

8.2 Experimental specification and methods

This investigation was carried out to find whether orientation of the CMC surface texturing effects performance, especially heat transfer.

Experiments were carried out in the MHI High Speed Linear Cascade using a pair of scaled NGVs with a replaceable endwall, shown in figure 8.2. This test piece provides a flexible platform for testing many different endwall geometries easily and repeatably, and has been used successfully for several different studies in the past [111]. Instead of entire vanes being manufactured, only new endwall inserts need be made to test different geometries.

Eight different endwall geometries were made, corresponding to a smooth case, grooves following the streamlines, and straight grooves at six different orientations. The size of the grooves corresponds to CMC surface texture provided by MHI. Two samples are shown in figure 8.1. With environment barrier coating (EBC) added, the surface texture can be modelled as 1d sinusoidal texture with wavelength of 3mm and amplitude of 0.1mm. This was scaled by 60% in the experiments to match Reynolds numbers (as is the entire vane).

The as built test pieces were examined with an optical microscope to ensure that the groove geometry was as specified. The results of this examination are shown compared to nominal in figure

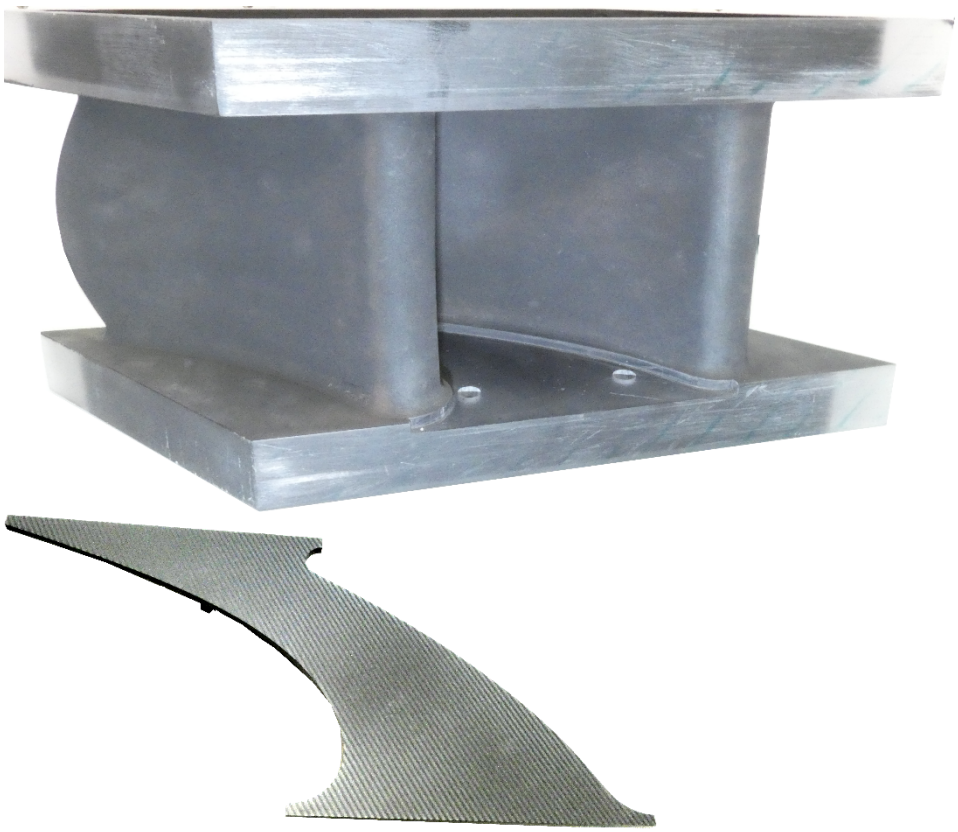


Figure 8.2: Test pieces used in experiment. Top: vane platform for endwall study. Bottom: replaceable endwall piece with angled grooves

8.3, and were judged to be satisfactory. The geometries chosen were a case with axial grooves, and at angles up to 135° to axial. It should be remembered while considering the results, that axial does not mean aligned with the flow along most of the passage. Flow begins axial, then is turned by about 70°, so axial grooves have an angle of incidence to the high speed flow in the second half of the passage of 70°. In order to achieve the specified tolerance, the endwall inserts were machined from ABS.

Heat transfer measurements were carried out using and infra-red (IR) camera using a transient method, as described in section 2.3. However, only selected viewpoints were possible, so only a portion of the endwall could be measured.

Figure 8.4 shows the view field of the IR camera and some example HTC results on the endwall. The endwall from the throat onwards had HTC measured. This is the area with highest HTC. Several IR runs were carried out for each case to ensure repeatability, the results shown here are averaged over these separate runs.

All tests were carried out using an upstream turbulence grid which gives approximately 12% turbulent intensity.

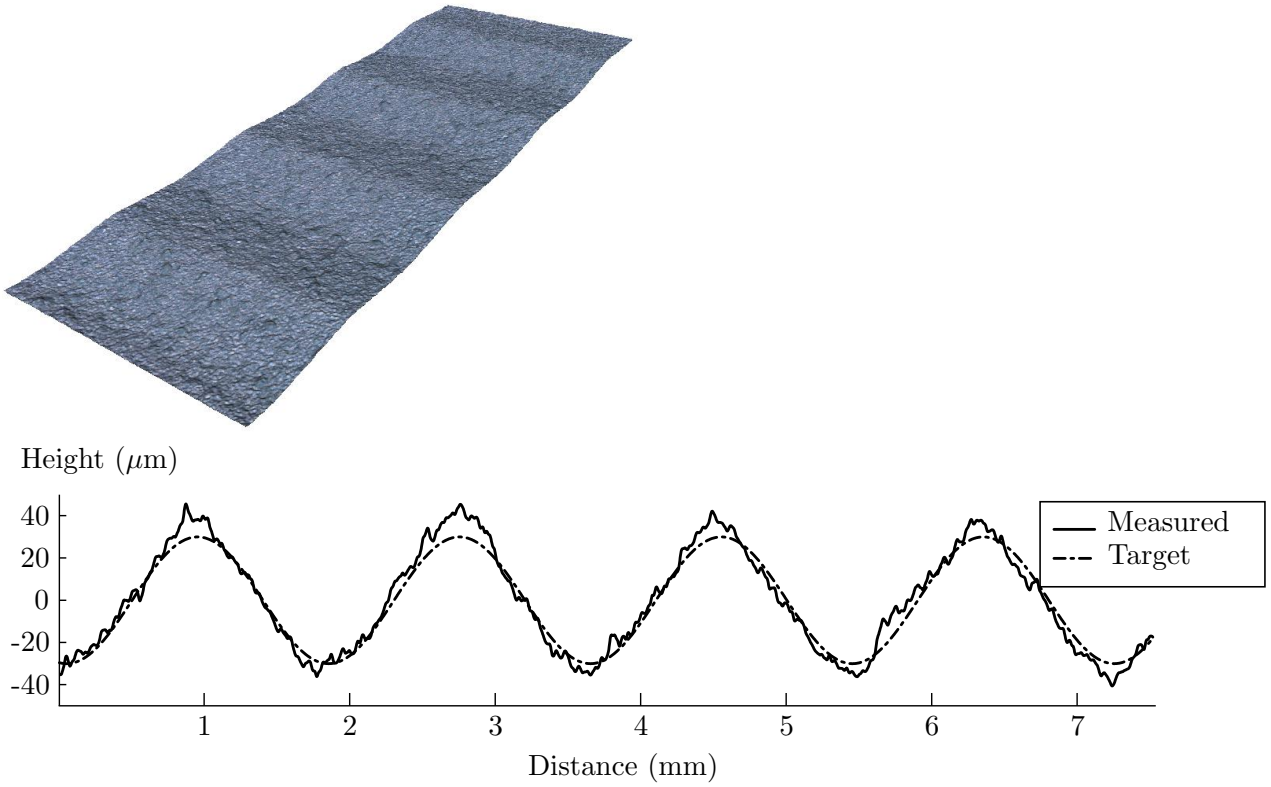


Figure 8.3: Measured surface texture of test pieces as built

8.3 Results

Figure 8.5 shows the variation of HTC with groove angle, as well as the flat and streamlined cases. It is clear from this that the groove angle chosen is of great importance, as it can increase HTC by 24% comparing the best to the worst cases. The best cases are in fact superior to the flat case. The streamlined case is about equal to the best of the straight grooved cases, but it seems likely that it might give superior performance if the whole of the endwall could be measured, rather than a limited area.

As well as the magnitude of HTC being affected, there is also some change in the distribution of HTC. In most cases the highest HTC is near the trailing edge where the wake of the vane passes over. In the axial case however, the highest HTC is near to the centre of the passage instead.

It is thought that there are two phenomena at play which are sometimes working in contrary directions. The first is the inhibition of migration of endwall boundary layer fluid from pressure to suction side that the grooves can cause. The second effect is that flow across grooves will disrupt the boundary layer and increase mixing with the free stream.

The highest HTC occurs between 135-0° grooves. This is unsurprising since flow is nearly perpendicular to the grooves, wo the effect will be to promote mixing of the boundary layer with freestream, and so increase HTC. The lowest HTC is the 45° grooves, which gives improvement even over the flat

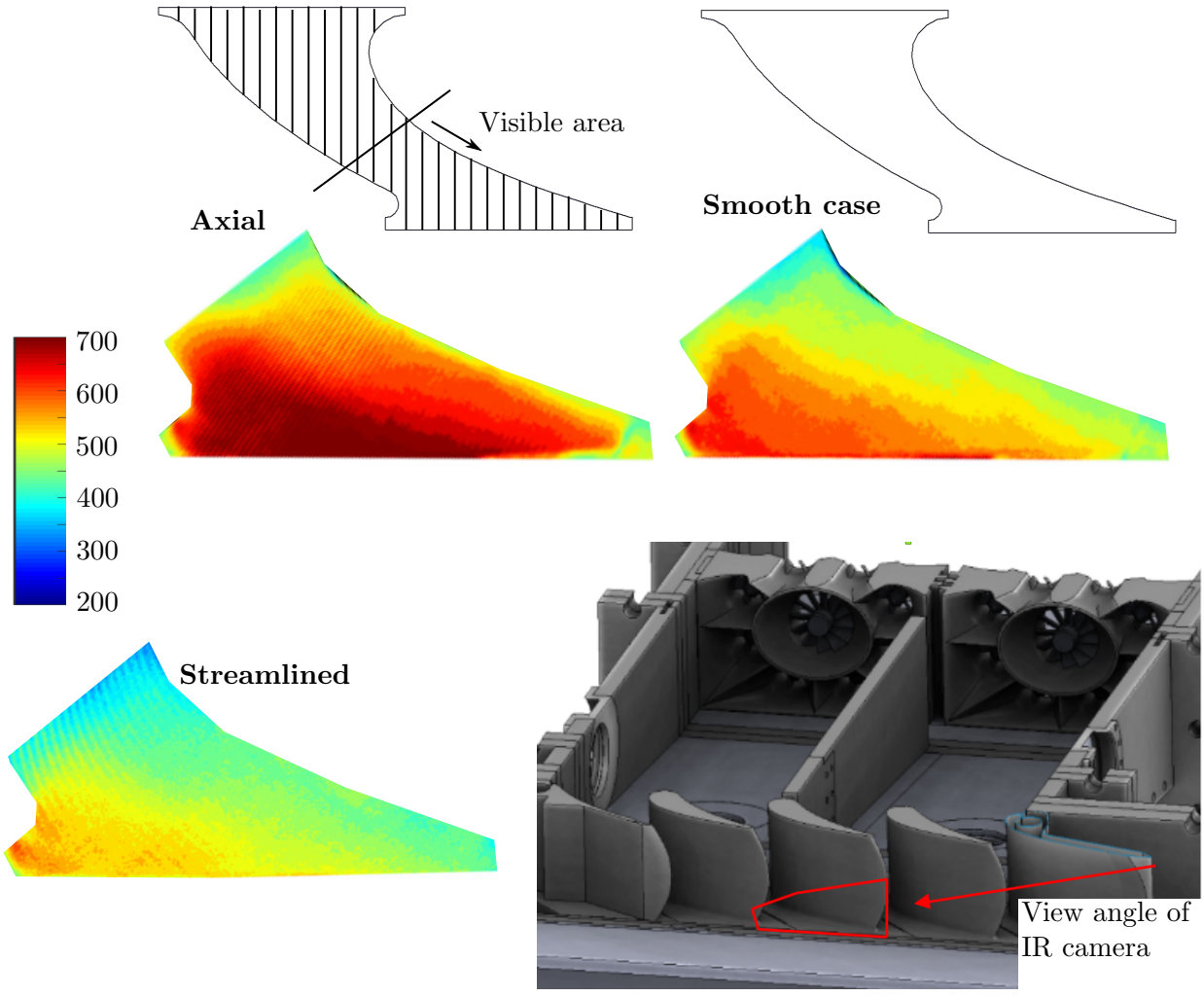


Figure 8.4: Heat transfer results. Flat endwall case, axially aligned groove case and streamlined geometry , viewpoint of IR camera.

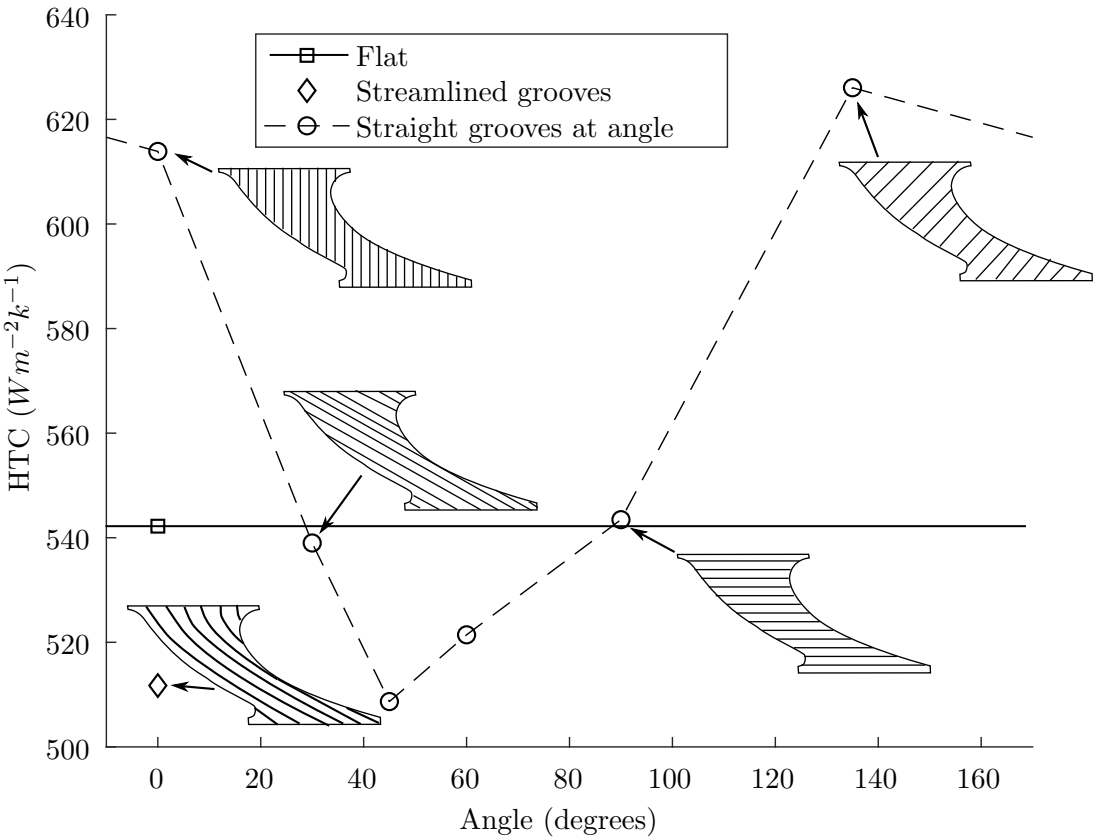


Figure 8.5: Variation of HTC with groove angle and flat and streamlined cases

case. This is thought to be the effect of grooves inhibiting cross-passage migration of boundary layer fluid, and so leading to a thicker endwall boundary layer and so a low HTC.

8.4 Discussion

This study shows that grooves, or micro-contouring, of the NGV endwall can have a significant effect on performance, and that orientation of these grooves is critical. The effect may be either beneficial or harmful depending on orientation. Changing orientation of grooves may modify HTC by up to 24%, between the best and worst cases. Therefore if CMCs are to be used in turbines, orientation of surface texture should be taken into account in design.

Both the streamlined case and the optimally angled case gave large reductions in HTC compared to a flat case. This is due to reduced secondary flows leading to a thicker downstream boundary layer, combined with a small incidence angle between the grooves and flow at all points. Although the streamlined test case would not be possible using CMCs, it does indicate an interesting possibility for reducing HTC in other situations, such as with bare metal vanes which could be machined to have streamlined micro-contours.

As well as the direct application of these results to the use of CMC in gas turbines, the reduction of

HTC below the level of a flat cases raises possibility of wider use of surface texturing for reduction of HTC in turbines and other applications. A reduction of 7% in heat transfer was observed over the flat case, and this was using an unoptimised groove size and geometry. While the use of riblets and other surface features are widely used for enhancing heat transfer, it is not currently usual to deliberately use surface texturing for reducing heat transfer.

Chapter 9

Conclusion

9.1 Introduction

The project was supported by Mitsubishi Heavy Industries, in order to support their development of a new generation of ultra high efficiency power generation turbines. These newer gas turbines feature higher turbine inlet temperatures, but with reduced cooling flows. The part of the gas turbine which faces the most arduous conditions is the combustor-turbine interface and nozzle guide vanes.

As the high temperature conditions within the combustor turbine interface make accurate instrumentation of a real machine impractical, CFD and measurements of scale models have been used to investigate flows and heat transfer in NGV.

For this thesis, it was set out to develop instrumentation and measurement techniques to investigate heat transfer, and then to apply this to the problem areas identified in real machines. In this, a close industrial partnership was crucial to identify areas of investigation. Regular meetings with turbine designers ensured that the results of these investigations were rapidly communicated back to turbine design teams, and that investigations could be focused on priority areas in the development of the next generation of turbines.

This final chapter reviews to what extent the thesis objectives were achieved, summarises the outcomes of each investigation and gives suggestions for future work and applications.

9.2 Experimental techniques

Further increases in gas turbine efficiency must increasingly be made by improvements to component efficiency. Using extensive and detailed instrumentation can reveal behaviour which is difficult to simulate with standard RANS methods.

Thin film gauges

Thin film gauge technology was developed for this thesis to give high resolution, time-resolved heat transfer measurements. Unsteady heat transfer coefficients have been calculated. This has the advantage that errors in calibration are cancelled out in the calculation.

Up to 384 gauges were instrumented on a single vane. The high resolution allowed direct visualisation of turbulent structures over surfaces. Thin film gauges were also used for areas which do not have optical access, such as the midpassage gap.

Changes to fabrication have made thin film heat flux gauges much quicker to instrument and use. This includes the use of surface mount connectors and using multi-layer flex circuit technology. These developments have made experiments in this facility much quicker and more reliable.

In futures, further development to increase sensitivity can be undertaken, as well as to further increase density. In addition, thin film gauges could be used for a wide range of other applications for sensitive heat transfer measurements.

High speed IR camera

Newer models of commercially available IR cameras were demonstrated to be useful for unsteady measurement of heat transfer.

The limitation of thin film gauges is that they require extensive design an fabrication for each area of measurement, and also give a limited number of measurement points. The newest state of the art IR cameras are capable of high speed data acquisition at high resolution, though with lower speed and accuracy than thin film gauges. This technology seems well suited for measurements in cascades, and is recommended for use in this facility and others in future.

Even in situations where heat transfer is not of interest in itself, the high resolution of measurements effectively allows heat transfer to be used as a form of flow visualisation. Unsteady flow directions can be seen by examination of heat flux videos. It has also been attempted to automate this process, mainly for the sake of giving objective results. This could be used for flow visualisation in a wide variety of high speed flows, so long as there is optical access, some surface roughness, and a means of creating a temperature difference between the flow and the test piece. Unlike oil flow visualisation, or use of tufts, this technique can show unsteady flows.

Unsteady pressure sensors

A vane was instrumented with pressure sensors close to the surface, allowing measurements at up to 2000Hz. The technique of unsteady pressure sensors proved to be successful, and produced informative

results, and may be well worth using in future in this facility and others.

In future it is planned to instrument the transition duct with unsteady pressure transducers, to investigate combustor flows and stability. The techniques developed here would be well suited for this, as the frequency is not too high, and a much larger number of measurement points could be used than with conventional fast response pressure transducers.

9.3 Applications of experimental techniques to nozzle guide vanes

Unsteady combustor turbine interactions

Experiments were carried out in the High Speed Linear Cascade using thin film gauges, IR camera, and unsteady pressure sensors. A variety of inlet conditions were used to simulate the effect of combustion chamber geometry on the NGV. The inlet condition had a important effect on both unsteady and mean heat flux. LES was run with a swirl generator inlet, and experiments were performed with many different inlet conditions to test these effects.

Some of unsteady flow structures are described with the help of LES. A swirling inflow condition created large flow structures, particularly the precessing swirl core, which impacts upon the NGVs. Vane loading was unsteady, and also varied radially along the vane. Pressure fluctuations of up to 3% were observed both experimentally and in LES. The horseshoe vortex at the leading edge fluctuated under the influence of inflow unsteadiness, and also had an intrinsic unsteadiness regardless of inflow. The passage vortex is steady state in the case of low turbulence inflow, but is found to fluctuate in its position due to inflow unsteadiness. A midspan vortex is generated but the low total pressure swirl core, and in likewise unsteady, making its difficult to observe in time averaged experimental data, but is clearly present when time resolved experimental data is examined.

The main recommendation for future work is to extend measurements to include film cooling. The experimental rig has recently been upgraded to include a film cooling supply, and an investigation to include the effects of film cooling is beginning in the Oxford Thermofluids Institute.

It has been shown using a small number of example designs that the combustor geometry can have an important effect on NGV heat transfer. In particular, by using an increased number of smaller swirlers, instead of a single large swirler, heat transfer in the NGV is reduced. HTC was reduced by using an 8-core swirler compared to a single swirler, and was futher reduced beyond this by using a 12-core swirler with even smaller length scales.

As a future study there should be a comprehensive investigation to find combustor designs which satisfy combustion requirements of homogeneous mixing and flame stability and so on, while also

leading to reduced heat transfer and losses in the nozzle guide vanes.

A significant caveat on this study was the lack of reactive flow in the combustion chamber, which may change the nature of the unsteady structures generated, as well as resulting in a non-uniform temperature profile and increasing turbulence levels. If possible, this should be investigated, though it is unclear how this could reasonably be achieved in a test facility. An LES investigation may be possible using reactive flow, but the difficulty of meshing and post-processing such large domains means that a comprehensive study comparing many different geometries would be a significant undertaking. However the importance of the phenomena discovered in this study may justify such an effort.

The several unsteady flow phenomena which affected heat transfer should also be investigated in the presence of film cooling. In particular, the low frequency fluctuations caused by swirler inflow could likely cause a reduction in film cooling effectiveness, if the fluctuations allow mainstream flow to periodically impinge directly onto component surfaces.

Effect of unsteady heat transfer of component life

The magnitude of unsteady heat transfer fluctuations measured experimentally with thin film gauges were scaled up to engine conditions. It was found that unsteady heat fluxes in the absence of cooling are potentially damaging to thermal barrier coatings when scaled up to engine conditions. It would be important to measure what this effect would be in the presence of film cooling.

TBC are now commonly used to protect hot gas path components. Increasing thickness of TBC reduce cooling requirements, but lead to increased TBC surface temperatures. Due to the low thermal conductivity of TBC, there is a high temperature gradient across the TBC. A locally high HTC may result in a higher surface temperature which may cause failure. This is in contrast to a traditional metal vane in which the ability of internal cooling flow to remove heat is the limiting factor.

A low frequency unsteady heat flux may cause significant surface temperature fluctuations of a TBC. Using measured unsteady HTC scaled up to engine conditions, it was found that surface temperature fluctuations up to 100°C above time-mean temperature could occur on the NGV endwall. This will reduce the apparent maximum operating temperature accordingly. If unsteady heat flux, and thus surface temperature, can be reduced then thicker TBC and higher inlet temperatures could be employed. As thermal barrier coating thickness continues to increase, bond layer temperatures will reduce while surface temperatures will increase. TBC surface temperature will eventually become a limiting factor in heat transfer design. Surface temperature fluctuations must then be controlled to prevent damage.

Midpassage gap

A midpassage gap between adjacent vane platforms was investigated using a specially constructed test vane, instrumented with thin film gauges. Initially the focus was on heat transfer, as it was observed by MHI that there may often be damage to real machines in this area. It was found that there are significant impacts for aerodynamic efficiency as well. The gap appears to have received very little attention in the past, yet may be significant in many machines. For example, in the F-class turbines used as a model, it is estimated to account for 20% of platform heat load.

A 1-dimensional model was constructed from the basic flow physics of the system, and this was found to agree well with experimental and CFD data. A threshold below which designers should reduce gap width is calculated, and estimates of losses and heat transfer can be calculated. Optimal purge flow distribution to eliminate ingress into the gap can be calculated from this 1-d model, and this have been successfully validated with CFD.

The analysis of the midpassage gap is quite complete, and is already quite generic, although validation with different vane and rotor geometries may be useful.

The effect of the gap is shown to be significant for both losses and heat load in this case of a power generation turbine. Calculations should be performed to check the magnitude of these effects in other turbines including in aero-engines. Quantification of the size of these gaps during operation is crucial, as a small uncertainty in gap size may lead to excessive losses and heat load.

The most important next stage is to apply the conclusions of the study to turbine design. There are several measures which could be taken. Conceptually the simplest, and the most effective solution is to reduce the width of the gaps to below the critical threshold where losses and heat transfer will be negligible. If this is not possible, then cooling flow can be distributed optimally to eliminate ingress. The number of such gaps can be reduced by welding several vane platforms together, though this may impact other areas of manufacturing, assembly and maintenance. The approximations given can be used to assess whether such measures are justified.

The analytical analysis undertaken could be extended to include the effects of similar gaps in compressor stages, and the aerodynamic losses which result.

Downstream cavity

A cavity between stationary ring segments was investigated using thin film gauge and IR measurements and CFD. The downstream cavity is shown to lead to a significant localised heat transfer, which corresponds to observed damage in real machines. A non-uniform circumferential pressure field drives ingress into the cavity. This causes locally high heat loads.

A circumferentially non-uniform cooling scheme has been proposed and tested with CFD. A non-uniform cooling can seal the cavity with half the cooling air of a uniform cooling flow. This should be experimentally verified in the future. It is suggested that a non-uniform seal flow of this kind could be applied to sealing of rotor-stator gaps also, as ingress in driven by a similar circumferentially varying pressure field. A cascade with a full annulus should really be used to verify this, and ideally rotating blades included as well.

A non-uniform cavity cooling could be implemented in real vanes by changing the distribution of cooling holes already present in this area. This study was limited by the use of a linear rather than annular cascade, as well as the lack of rotating blades. This will likely affect the total amount of ingress into the cavity. However, it is believed that the overall conclusions recommending the use of circumferentially non-uniform sealing flows would still be valid.

Surface texturing effect on heat transfer

Surface texturing mimicking the texture of ceramic matrix composite was applied to the endwall of NGV, to discover whether this is an important consideration if CMC are to be used in turbine vane construction in the future. Test pieces were constructed with a surface texture at a range of orientations, and heat transfer measured using IR. It was found that the angle at which the texturing was applied was critical, and could dramatically increase or decrease heat transfer. This means that angle of surface texturing must be taken into account in heat transfer calculations if CMC are to be applied.

In addition, it was discovered that the best case heat transfer was in fact less than that with a smooth surface. This suggests the possibility of deliberately engineering surface finishes to reduce heat transfer in other contexts, even when CMC are not used.

A project to take this further, with a full experimental and CFD investigation into surface texturing to reduce HTC, has already begun in the Oxford Thermofluids Institute.

9.4 Final remarks

A close correspondence between numerical work, experiments and industrial observation can produce useful results without excessive resources. There is still a great capacity to increase gas turbine efficiency by means of component optimisation. Several ways to reduce heat transfer and losses have been discovered in the course of this project. There are doubtless still further optimisations to be found.

Appendix A

Temperature fluctuations appendix

Separate unsteadiness

Matlab function to separate effect of temperature fluctuations from fluctuations in htc in thin film data

```
function ratio=seperate_htc_(all_q,all_T,Fs,all_htc_inst)
[~,N]=size(all_q);
fig=figure;

for m=1:N % Loop through each gauge individually

 q=all_q(:,m);
 T=all_T(:,m);
 Ta=all_Ta(m);
 htc_inst=all_htc_inst(:,m);
```

High-pass q to remove overall change (this is already accounted for in htc)

```
 qhp=prepare_unsteady(q,10,Fs);
```

Create window and perform windowed fourier transform

```
 window=gausswin(1000,3.5);
 window=window(:);
 window=window/(trapz(window));
 skips=1;
 T_windowed=windowedmovingaverage(T,window,skips); %window T and find average T
 [magsinglesided, freq]=windowed_fft(qhp,window,skips,Fs); % window q and apply fft
```

Perform Regression of amplitude q against deltaT

```
 [N,~]=size(magsinglesided);
 p1=zeros(1,N);
 p2=p1;
 for n=1:N
  p=polyfit(Ta-T_windowed,magsinglesided(n,:),1);
  p1(n)=p(1);
```

```
  p2(n)=p(2);
 end
```

Find RMS value

```
 rms_htc=sqrt(trapz(freq,p1));
 ratio(m)=rms_htc/rms(htc_inst);
```

Plot to check

```
 title(['gauge number ' m] )
 subplot(2,1,1)
 plot(freq,p1)
 ylim([0 30])
 subplot(2,1,2)
 plot(freq,abs(p2))
 saveas(fig,['gauge' num2str(m) '.png'])

end % End loop
end % End function
```

Local functions

```
function [magsinglesided, freq]=windowed_fft(data,window,skips,Fs)

windowlength=length(window);
n=1;
dataarray=zeros(windowlength,ceil(floor(length(data)-windowlength)/skips));

for index=1:skips:floor(length(data)-windowlength)
 dataarray(:,n)=data(index:index+windowlength-1);
 n=n+1;
end
window=window*windowlength;
datawindowed=bsxfun(@times,dataarray,window);
mag=fft(datawindowed);
[L,~]=size(datawindowed);
freq = Fs*(0:(L/2))/L;

P2 = abs(mag/L);
P1 = P2(1:L/2+1,:);
magsinglesided=P1;
magsinglesided(2:end-1,:) = 2*P1(2:end-1,:);
end

function data_smoothed=windowedmovingaverage(data,window,skips)
windowlength=length(window);
n=1;
dataarray=zeros(windowlength,ceil(floor(length(data)-windowlength)/skips));

for index=1:skips:floor(length(data)-windowlength)
 dataarray(:,n)=data(index:index+windowlength-1);
 n=n+1;
end
datawindowed=bsxfun(@times,dataarray,window);
```

```
data_smoothed=sum(datawindowed);
end
```

Appendix B

Midpassage gap appendices

B.1 Alternative ODE derivation

It may be noted that the 1-D model of gap flow given in equation 6.7 becomes non-physical for values of $u^* = 2u$. An alternative derivation can be made by using slightly different assumptions in setting up the model.

$$\frac{dI}{dx}\delta x = \underbrace{-A\frac{dp}{dx}\delta x}_{\text{Pressure force}} - \underbrace{F_\tau \delta x}_{\text{Wall shear force}} + \underbrace{m^* u^\star \delta x}_{\substack{\text{Momentum flux} \\ \text{of ingressing fluid}}} \tag{B.1}$$

Between two control surfaces, there will be mainstream fluid ingress, injecting additional momentum flux into the cavity. The amount of mainstream ingress is approximated as being set by the change in area of a constant mass flow control volume. u^* is the velocity of free stream fluid above the cavity, when fluid is ingressing, or if mass flux is leaving the gap, $u^* = u$. Given a fixed amount of fluid with mass flux m_1, and properties u_1, ρ_1 etc.:

$$A_1 = \frac{m_1}{\rho_1 u_1} \tag{B.2}$$

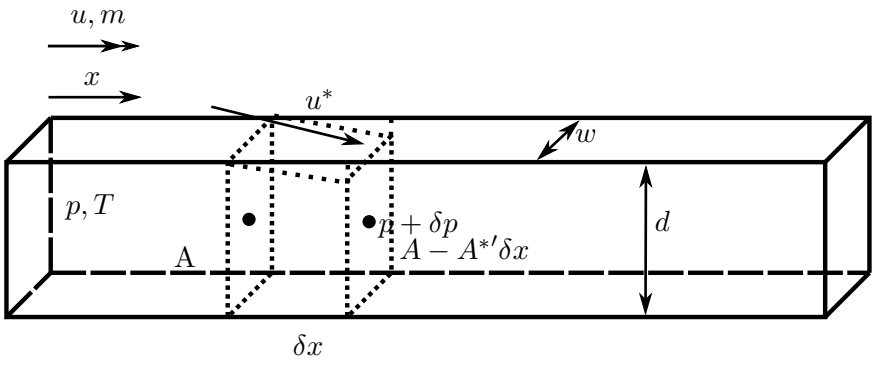


Figure B.1: Alternative model used to derive 1-d equation for gap flow. This model is identical to the original for $u^* = u, 0$

$$\delta A^* = A\left(\frac{u_1'}{u_1} + \frac{\rho_1'}{\rho_1}\right)\delta x \tag{B.3}$$

$$I_1' = m_1 u_1' = -Ap' - F_\tau \tag{B.4}$$

$$u_1' = \frac{-Ap' - F_\tau}{m} \tag{B.5}$$

Over a small section of gap length δx, the ingresses mass flux will therefore be:

$$\delta m^* = \rho^* u^* A\left(\frac{-Ap' - F_\tau}{mu} + \frac{\rho_1'}{\rho_1}\right)\delta x \tag{B.6}$$

It is assumed that after a distance δx, flow is again fully mixed out and uniform. Substituting equations B.4 and B.6 into equation B.1 and re-arranging for u' gives the overall equation for gap velocity:

$$u' = \frac{-Ap' - F_\tau}{m} \cdot \frac{u^2 + u^{*2}}{2u^2} + \frac{\rho'}{\rho} \cdot \frac{u^{*2} - u^2}{2u} \tag{B.7}$$

For a compressible flow, ρ must be allowed to change as a function of static temperature. In the case of incompressible flow, static temperature may be approximated to be equal to a constant total temperature. In either case, temperature may be solved as a separate equation, which is investigated in section B.2.

$$\rho = \frac{p}{RT} \tag{B.8}$$

$$\frac{\rho'}{\rho} = \frac{p'}{p} - \frac{T_0'}{T} + \frac{uu'}{c_p T} \tag{B.9}$$

Substituting this into equation B.7 and re-arranging:

$$u' = \frac{1}{Z}\left[\frac{-Ap' - F_\tau}{m} \cdot \frac{u^2 + u^{*2}}{2u^2} + u\left(\frac{p'}{p} - \frac{T_0'}{T}\right) \cdot \frac{u^{*2} - u^2}{2u^2}\right] \tag{B.10}$$

$$Z = 1 - \frac{u^2}{c_p T} \tag{B.11}$$

In many ways gap mass flow m_g, is a more useful quantity than velocity.

$$m' = \frac{mu'}{u} + \frac{m\rho'}{\rho} \tag{B.12}$$

$$m' = \frac{-Ap' - F_\tau}{u} \cdot \frac{u^2 + u^{*2}}{2u^2} + m(\frac{u^{*2} - u^2}{2u^2} + 1)\frac{\rho'}{\rho} \tag{B.13}$$

It should be noted that in the cases of $u^* = 0$, or $u^* = u$, this is identical to the equation derived previously.

B.2 Coupled temperature equation

Temperature and heat transfer in the midpassage gap may be solved by first solving the equation for flow through the gap with T_0' assumed to be zero, and then solving the ODE 6.38 for T with mass flow fixed. However, a more accurate method would be to create a second ODE which can be solved simultaneously with equation 6.9 in a coupled manner. In practice, it was found that there was negligible difference in results using these two methods, but the full ODEs are shown here for completeness.

When solving simultaneously, u' and T_0' are unkowns to be solved for. Two equations are available, 6.9 and 6.38 for u' and T_0' respectively, so the system is fully defined. The equation for each of these unknowns includes the other, so some re-arrangement is neccessary to produce an equation for T_0' in terms of known flow quantites only. The value of T_0' found can then be substituted into equation 6.9 for u' while these two ODEs are solved for simultaneously.

$$W = \frac{F_\tau - Ap'}{mu} \tag{B.14}$$

$$X = \frac{u^* - u}{u} \tag{B.15}$$

$$Y = \frac{2dh^*}{mc_p} \tag{B.16}$$

$$Z = 1 + \frac{u^2}{c_p T} \tag{B.17}$$

Z is the same definition as has been used previously.

$$(mc_pT_0)' = 2dh(T_w - T) + c_pT_{0f}m' \tag{B.18}$$

$$T_0'\left(1 + \frac{\Delta T}{T}\right) = T(T_w - T) + \Delta T\left(\frac{p'}{p} + Z\frac{u'}{u}\right) \tag{B.19}$$

$$\frac{u'}{u} = \frac{W + \left(\frac{p'}{p} - \frac{T_0'}{T}\right)X}{1 - XZ} \tag{B.20}$$

Substituting for $\frac{u'}{u}$:

$$T_0'\left(a + \frac{\Delta T}{T}\right) = Y(T_w - T) + \Delta T\left[\frac{p'}{p} + Z\left(\frac{W + X\left(\frac{p'}{p} - \frac{T_0'}{T}\right)}{1 - XZ}\right)\right] \tag{B.21}$$

Re-arranging:

$$T_0' = \frac{Y(T_w - T) + \Delta T\left(\frac{p'}{p} + ZW\right)}{1 + \left(1 + XZ\frac{\Delta T}{T}\right)} \tag{B.22}$$

This gives an equation for compressible flow, with heat addition from the gap walls. Although it contains many terms, it is simply a 1st order ODE, with all right hand side terms being known flow quantities.

B.3 Numerical solution to equation with Matlab

Numerical integration of 1-d open channel flow for gap study

First order ODE for mass flow in gap. All numerical values are in base SI units

```
function [mout,uout,xout,hout,Tout]=one_d_numerical(xin,pin,w,ode)
```

Set parameters not given in function call

```
if nargin<1
 xspan=[0.0001 0.15];
else
 xspan = [min(xin) max(xin)];
end
if nargin<2
 p_case='linear';
else
 p_case='input';
end
if nargin< 3
 w=1e-3;
end
if nargin<4
 ode='1_u';
end
```

Set other parameters

```
u_0=5; % Initial condition must be seeded >0
d=0.01;
A=w*d;
T_0=1700;
Tw=900;
Tf=T_0;

p_0=getps(xspan(1));
rho_0=p_0/(R*T_0);
m_0=u_0*rho_0*A;
mi=0;
switch ode
```

```
 case '1_m_inc'
  y0=m_0;
  ode_function=@ode_1_order_m_simple;
 case '1_u'
  ode_function=@ode_1_order_u_adiabatic;
  y0=u_0;
 case '1_m_purge'
  ode_function=@ode_1_order_m_purge;
  m_0=u_0*rho_0*A;
  y0=[m_0;m_0];
 case '2_u_T'
  ode_function=@ode_2_order_u_T;
  y0=[u_0;T_0];
end
```

Solve equation

```
[xout,yout] = ode45(ode_function,xspan,y0);

pout=getps(xout);
switch ode
 case '1_m_inc'
  mout=yout;
  Tout=T_0*ones(size(xout));
  rhoout=pout./(R*Tout);
  uout=mout./(rhoout*A);
 case '1_u'
  uout=yout;
  Tout=T_0*ones(size(xout));
  rhoout=pout./(R*Tout);
  mout=uout.*(rhoout*A);
 case '1_m_purge'
  mout=yout(:,1);
  Tout=T_0*ones(size(xout));
  rhoout=pout./(R*Tout);
  mpout=yout(:,2);
  uout=mout./(rhoout*A);
 case '2_u_T'
  uout=yout(:,1);
  T0out=yout(:,2);
  Tout=T0out-0.5*uout.^2/cp;
  rhoout=pout./(R*Tout);
  mout=uout.*(rhoout*A);
end

if strcmp(ode,'2_u_T')
hout=get_h_DB(rhoout,uout,w);
qout=2*d*hout.*(Tout-Tw);
hsout=qout/((Tf-Tw)*2*d);
else
hout=get_h_DB(rhoout,uout,w);
Toutunc=uncoupled_htc(xout,mout,hout,Tw,d,T_0);
qout=2*d*hout.*(Toutunc-Tw);
hsout=qout/((Tf-Tw)*2*d);
```

```
end
```

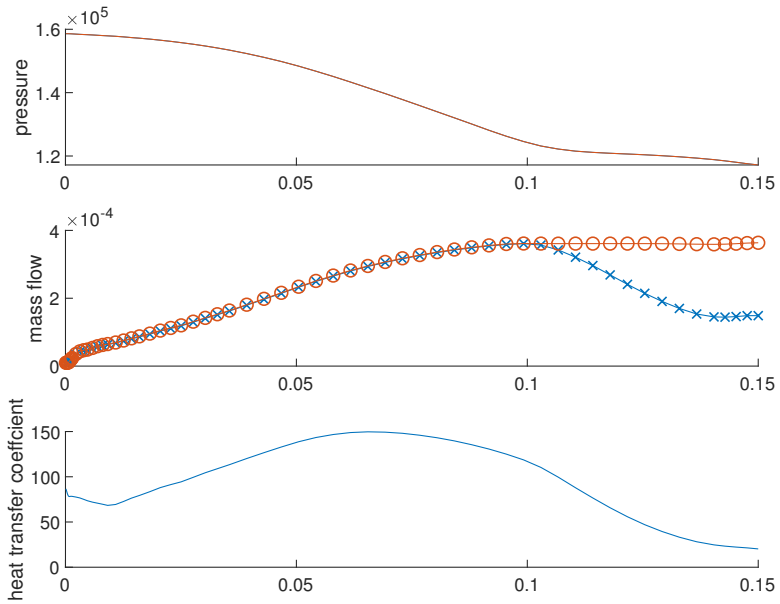
Plot results

```
figure
subplot(3,1,1)
hold on
plot(xout,getps(xout))
plot(xout,pout)
ylabel('pressure')

subplot(3,1,2)
hold on
plot(xout,mout,'x-')
if exist('mpout','var')
 plot(xout,mpout,'o-')
end
ylabel('mass flow')

subplot(3,1,3)
hold on
plot(xout,hsout)
ylabel('heat transfer coeffcient')

%%%%%%%%%%%%%%%%%%%%%%%%%%%%%%%%%%%%%%%%%%%%%%%%%%%%%%%%%%%%%%%%%%%%%%%%%%%%%%%
```



Define odes

```
function dy=ode_1_order_m_simple(x,y)
% ODE solved in terms of mass flow (m). Incompressible, adiabatic, no
% purge flows. Approximation that u*=0;
m=y;
T=T_0;
p=getps(x);
rho=p/(R*T);
dp=d_bydx(x,@getps);
```

```
B=-dp/p;
Ct=16;
C=-2*d*Ct*mu_air/w;
D=-A^2*dp*rho;
dm=(B*m^2+C*m+D)/m;

dy=dm;
end

function dy=ode_1_order_u_adiabatic(x,y)
% ODE solved in terms of velocity (u). Compressible, adiabatic, no purge
% flows.
u=y;
T=T_0-0.5*u^2/cp;
p=getps(x);
rho=p/(R*T);
dp=d_bydx(x,@getps);
m=rho*u*A;

us=getus(p);
%us=u;
%us=0;
Ft=tauforce(u);

Z=1+u^2/(T*cp);
Zs=1-(u^2/(T*cp));
W=(-A*dp-Ft)/(m*u);

if us>u
 du=(1/Zs) * ((W*u^2+us^2) + (us^2-u^2)*(dp/p))/(2*u);
else
 du=(W*u+(dp/p)*(us-u)) /(1+(1-(us/u))*Z);
end
dy=du;
end

function dy=ode_1_order_m_purge(x,y)
% solve for m to give targeted egress
% Assume purge flow does not contribute any momentum to flow
% Incompressible and adiabatic
T=T_0;
m=y(1);
p=getps(x);
rho=p/(R*T);
u=m/(rho*A);
Ft=tauforce(u);
dp=d_bydx(x,@getps);
us=u;

W=(-A*dp-Ft)/(m*u);
mp=m*W/2+m*(dp/p)/2-mi*(1-(us/(2*u)));
if mp<0
 mp=0;
```

```
 dm=m*(W+(dp/p))/(2-(us/u));
else
dm=mp+mi;
end


dy(1)=dm;
dy(2)=mp;
dy=dy(:);
end

function dy=ode_2_order_u_T(x,y)
% ODE solved in terms of velocity (u) and total temperature T0.
% Compressible, heat transfer, no purge flows.
% For use with us<=u only
u=y(1);
T0=y(2);
T=T0-0.5*u^2/cp;
p=getps(x);
rho=p/(R*T);
dp=d_bydx(x,@getps);
m=rho*u*A;

%us=getus(u,p,1);
us=u;
%us=0;
Ft=tauforce(u);
hs=get_h_DB(rho,u,w);
DT=Tf-T0;
W=(-A*dp-Ft)/(m*u);
X=(us-u)/u;
Y=2*d*hs/(m*cp_air);
Z=1+u^2/(T*cp);

dT0=(Y*(Tw-T) + DT*((dp/p)+Z*W))/(1+(1+X*Z*(DT/T)));
du=u*(W + X* ( (dp/p) -(dT0/T)  )  ) /  (1-X*Z);

dy(1)=du;
dy(2)=dT0;
dy=dy(:);
end

%%%%%%%%%%%%%%%%%%%%%%%%%%%%%%%%%%%%%%%%%%%%%%%%%%%%%%%%%%%%%%%%%%%%%%%
```

Define tau as function of velocity

```
function tauforceout=tauforce(u)
Ctau=16; % Ctau=6 for laminar fully devloped, 16 for ^7 turbulent fully developed.
tauforceout=2*d*Ctau*u*mu_air/w;
end
```

Define p as function of x

```
function pout=getps(x)
```

```
switch p_case
case 'linear'
 pout=160e3-x*200e3; % linear decrease in p between start and end pressures
case 'input'
 pout=interp1(xin,pin,x,'spline');
end
end
```

Define us: the velocity of fluid entrained into passage

```
function usout=getus(p)
```

Velocity above cavity based on static pressure

```
%p1=pin(1);
p01=160e3;
rho=p/(R*330);
us=sqrt( 2*(p01-p)/rho );
usout=us;

end

end
```

End of nested functions

Define dp/dx as function of x

Use simple central difference to get gradient. Input function to be interpolated must be smooth. 'func' is handle to function to have gradient calculated. Example call: dpbydx=d_bydx(x,@func_getp)

```
function d_bydxout=d_bydx(x,func)
h=0.00001;
p1=func(x-h/2);
p2=func(x+h/2);

d_bydxout=(p2-p1)/h;
end
```

Get h with Dittus-Boelter correlation

```
function h=get_h_DB(rho,v,w,Pr,mu,k)

% if fluid properties are undefined, assume air
if nargin <4
 Pr=Pr_air;
 mu=mu_air;
 k=k_air;
end

dh=2*w; % Hydraulic diameter of rectangular channel
h=0.023* (rho.*abs(v)*dh./mu).^0.8*Pr^0.3*k/dh;

% use laminar value if greater
 for i=1:length(h)
  h(i)=max([h(i) (2*k/w)]);
 end
```

```
end
```

Calculate gap HTC uncoupled

Calculate the gap HTC given gap velocity and pressure field, assuming temperature changes are not sufficient to significantly change mass flow

```
function Tout=uncoupled_htc(xinp,minp,hinp,Tw,d,T01)

xspan=[min(xinp),max(xinp)];
Tf=T01;
[x,Toutunc] = ode113(@ode_function,xspan,T01);
Tout=interp1(x,Toutunc,xinp,'spline');
```

Temperature ODE

```
function dT =ode_function(x,T)
h=get_h(x);
m=interp1(xinp,minp,x,'spline');
dm=getdm(x);
dT=(2*d*h*(Tw-T)  +subplus(cp_air*Tf*dm) -(dm+subplus(-dm))*cp_air*T) /(m*cp_air);
end

function mout=getdm(x)
 dminp=gradient(minp)./gradient(xinp);
 mout=interp1(xinp,dminp,x,'spline');
end

function hout=get_h(x)
 hout=interp1(xinp,hinp,x,'spline');
end

end
%%%%%%%%%%%%%%%%%%%%%%%%%%%%%%%%%%%%%%%%%%%%%%%%%%%%%%%%
```

Bibliography

[1] OECD, "Outlook for electricity demand and supply," *World Energy Outlook*, 2018.

[2] S. Hada, K. Takata, Y. Iwasaki, M. Yuri, and J. Masada, "High-efficiency gas turbine development applying 1600 C class "J" technology," *Mitsubishi Heavy Industries Technical Review*, vol. 52, no. 2, p. 2, 2015.

[3] T. Hashimoto, K. Sakamoto, Y. Yamaguchi, K. Oura, K. Arima, and T. Suzuki, "Overview of integrated coal gasification combined-cycle technology using low rank coal," *Mitsubishi Heavy Industries Technical Review*, vol. 48, no. 3, pp. 19–23, 2011.

[4] K. Fujimoto, Y. Fukunaga, S. Hada, T. Ai, M. Yuri, and J. Masada, "Technology application to MHPS large flame F series gas turbine," in *ASME Turbo Expo 2018: Turbomachinery Technical Conference and Exposition*, pp. V003T08A010–V003T08A010, American Society of Mechanical Engineers, 2018.

[5] M. Nose, T. Kawakami, H. Arakai, N. Senba, and S. Tanimura, "Hydrogen-fired gas turbine targeting realization of CO2-free society," *Mitsubishi Heavy Industries Technical Review*, vol. 55, no. 4, 2018.

[6] M. Yuri, J. Masada, K. Tsukagoshi, E. Ito, and S. Hada, "Development of 1600 C-class high-efficiency gas turbine for power generation applying J-type technology," *Mitsubishi Heavy Industries Technical Review*, vol. 50, no. 3, pp. 1–10, 2013.

[7] E. Ito, K. Tsukagoshi, Y. Sakamoto, J. Masada, K. Saito, and S. Takiguchi, "Key technologies for ultra-high temperature gas turbines," *Mitsubishi Heavy Industries Technical Review*, vol. 52, no. 2, pp. 15–23, 2015.

[8] D. G. Bogard and K. A. Thole, "Gas turbine film cooling," *Journal of propulsion and power*, vol. 22, no. 2, pp. 249–270, 2006.

[9] S. Mizukami, M. Isono, N. Nagai, and K. Saitoh, "Simulation and measurment technology of combustion and heat transfer for development of high-efficiency gas turbines," *Mitsubishi Heavy Industries Technical Review*, vol. 52, no. 4, pp. 15–21, 2015.

[10] M. H. P. Systems, "Our technology," 2019.

[11] T. Ai, C. Koeneke, H. Arimura, and Y. Hyakutake, "Development of an air cooled G class gas turbine (the M501GAC)," in *ASME Turbo Expo 2009: Power for Land, Sea, and Air*, pp. 961–968, American Society of Mechanical Engineers Digital Collection, 2009.

[12] R. S. Bunker, "Gas turbine heat transfer: Ten remaining hot gas path challenges," *Journal of Turbomachinery*, vol. 129, no. 2, pp. 193–201, 2007.

[13] S. Jacobi, "Influence of lean premixed combustor geometry on the first turbine vanes' aerothermal performance," Master's thesis, Swiss Federal Institute of Technology (ETH), Zurich, 2013.

[14] S. Jacobi, C. Mazzoni, B. Rosic, and K. Chana, "Investigation of unsteady flow phenomena in first vane caused by combustor flow with swirl," *Journal of Turbomachinery*, vol. 139, no. 4, p. 041006, 2017.

[15] S. Luque, V. Kanjirakkad, I. Aslanidou, R. Lubbock, B. Rosic, and S. Uchida, "A new experimental facility to investigate combustor–turbine interactions in gas turbines with multiple can combustors," *Journal of Engineering for Gas Turbines and Power*, vol. 137, no. 5, p. 051503, 2015.

[16] I. Aslanidou and B. Rosic, "Aerothermal performance of shielded vane design," *Journal of Turbomachinery*, vol. 139, no. 11, p. 111003, 2017.

[17] K. Chana, "Gas turbine combustor swirl and first vane aerodynamic interactions," Master's thesis, University of Oxford, 2015.

[18] P. Roach, "The generation of nearly isotropic turbulence by means of grids," *International Journal of Heat and Fluid Flow*, vol. 8, no. 2, pp. 82–92, 1987.

[19] I. Aslanidou, *Combustor and Turbine Aerothermal Interactions in Gas Turbines with Can Combustors*. PhD thesis, University of Oxford, 2015.

[20] F. Papa, U. Madanan, and R. J. Goldstein, "Modeling and measurements of heat/mass transfer in a linear turbine cascade," *Journal of Turbomachinery*, vol. 139, no. 9, p. 091002, 2017.

[21] B. Laveau, R. S. Abhari, M. E. Crawford, and E. Lutum, "High resolution heat transfer measurements on the stator endwall of an axial turbine," *Journal of Turbomachinery*, vol. 137, no. 4, p. 041005, 2015.

[22] N. Harvey and T. Jones, "Measurement and calculation of end wall heat transfer and aerodynamics on a nozzle guide vane in annular cascade," in *ASME 1990 International Gas Turbine and Aeroengine Congress and Exposition*, pp. V004T09A035–V004T09A035, American Society of Mechanical Engineers, 1990.

[23] M. Spencer, T. Jones, and G. Lock, "Endwall heat transfer measurements in an annular cascade of nozzle guide vanes at engine representative reynolds and mach numbers," *International Journal of Heat and Fluid Flow*, vol. 17, no. 2, pp. 139–147, 1996.

[24] M. Barringer, K. Thole, and M. Polanka, "An experimental study of combustor exit profile shapes on endwall heat transfer in high pressure turbine vanes," *Journal of Turbomachinery*, vol. 131, no. 2, p. 021009, 2009.

[25] I. Qureshi, A. D. Smith, and T. Povey, "HP vane aerodynamics and heat transfer in the presence of aggressive inlet swirl," *Journal of Turbomachinery*, vol. 135, no. 2, p. 021040, 2013.

[26] F. E. Ames, P. A. Barbot, and C. Wang, "Effects of aeroderivative combustor turbulence on endwall heat transfer distributions acquired in a linear vane cascade," in *ASME Turbo Expo 2002: Power for Land, Sea, and Air*, pp. 981–992, American Society of Mechanical Engineers, 2002.

[27] S. P. Lynch, N. Sundaram, K. A. Thole, A. Kohli, and C. Lehane, "Heat transfer for a turbine blade with non-axisymmetric endwall contouring," in *ASME Turbo Expo 2009: Power for Land, Sea, and Air*, pp. 887–898, American Society of Mechanical Engineers, 2009.

[28] P. Giel, G. VanFossen, R. Boyle, D. Thurman, and K. Civinskas, "Blade heat transfer measurements and prediction in a transonic turbine cascade," 1999.

[29] R. Martinez-Botas, G. Lock, and T. Jones, "Heat transfer measurements in an annular cascade of transonic gas turbine blades using the transient liquid crystal technique," in *ASME 1994 International Gas Turbine and Aeroengine Congress and Exposition*, pp. V004T09A024–V004T09A024, American Society of Mechanical Engineers, 1994.

[30] A. Epstein, G. Guenette, R. Norton, and Y. Cao, "High-frequency response heat-flux gauge," *Review of Scientific Instruments*, vol. 57, no. 4, pp. 639–649, 1986.

[31] S. Jacobi, *Development and Aerothermal Investigation of Integrated Combustor Vane Concept*. PhD thesis, University of Oxford, 2016.

[32] M. Collins, K. Chana, and T. Povey, "New technique for the fabrication of miniature thin film heat flux gauges," *Measurement Science and Technology*, vol. 26, no. 2, p. 025303, 2015.

[33] K. Chana, D. Cardwell, and T. Jones, "A review of the oxford turbine research facility," in *ASME Turbo Expo 2013: Turbine Technical Conference and Exposition*, pp. V03CT14A026–V03CT14A026, American Society of Mechanical Engineers, 2013.

[34] C. Sieverding, T. Arts, R. Dénos, and J.-F. Brouckaert, "Measurement techniques for unsteady flows in turbomachines," *Experiments in Fluids*, vol. 28, no. 4, pp. 285–321, 2000.

[35] M. Oldfield, "Guide to impulse response heat transfer signal processing: Version 2," *OUEL Report*, vol. 2233, no. 2000, p. 13, 2000.

[36] M. Oldfield, "Impulse response processing of transient heat transfer gauge signals," *Journal of Turbomachinery*, vol. 130, no. 2, p. 021023, 2008.

[37] E. Bertolazzi, L. Battisti, and F. Trivellato, "Numerical processing of thin-film thermometer data for determining transient heat fluxes," *Applied Mathematical Modelling*, vol. 36, no. 8, pp. 3645–3662, 2012.

[38] G. Fralick, J. Wrbanek, and C. Blaha, "Thin film heat flux sensor of improved design," *48th International Instrumentation Symposium*, 2002.

[39] A. Zribi, M. Barthès, S. Bégot, F. Lanzetta, J. Y. Rauch, and V. Moutarlier, "Design, fabrication and characterization of thin film resistances for heat flux sensing application," *Sensors and Actuators A: Physical*, vol. 245, pp. 26–39, 2016.

[40] D. L. Schultz and T. Jones, "Heat-transfer measurements in short-duration hypersonic facilities.," tech. rep., ADVISORY GROUP FOR AEROSPACE RESEARCH AND DEVELOPMENT PARIS (FRANCE), 1973.

[41] E. Piccini, S. Guo, and T. Jones, "The development of a new direct-heat-flux gauge for heat-transfer facilities," *Measurement Science and Technology*, vol. 11, no. 4, p. 342, 2000.

[42] R. Ainsworth, R. Miller, R. Moss, and S. Thorpe, "Unsteady pressure measurement," *Measurement Science and Technology*, vol. 11, no. 7, p. 1055, 2000.

[43] C. M. Mazzoni, S. Luque, and B. Rosic, "Capabilities of thermal wall functions to predict heat transfer on the ngvs of a gas turbine with multiple can combustors," in *ASME Turbo Expo 2015: Turbine Technical Conference and Exposition*, pp. V02AT38A035–V02AT38A035, American Society of Mechanical Engineers, 2015.

[44] C. Klostermeier, *Investigation into the capability of large eddy simulation for turbomachinery design*. PhD thesis, University of Cambridge, 2008.

[45] B. Cabral and L. C. Leedom, "Imaging vector fields using line integral convolution," tech. rep., Lawrence Livermore National Lab., CA (United States), 1993.

[46] J. D. Denton, "Loss mechanisms in turbomachines," in *ASME 1993 International Gas Turbine and Aeroengine Congress and Exposition*, pp. V002T14A001–V002T14A001, American Society of Mechanical Engineers, 1993.

[47] E. M. Greitzer, C. S. Tan, and M. B. Graf, *Internal flow: concepts and applications*, vol. 3. Cambridge University Press, 2007.

[48] C. Sieverding, "Recent progress in the understanding of basic aspects of secondary flows in turbine blade passages," *Journal of Engineering for Gas Turbines and Power*, vol. 107, no. 2, pp. 248–257, 1985.

[49] L. Langston, "Secondary flows in axial turbines—a review," *Annals of the New York Academy of Sciences*, vol. 934, no. 1, pp. 11–26, 2001.

[50] S. Harrison, "Secondary loss generation in a linear cascade of high-turning turbine blades," in *ASME 1989 International Gas Turbine and Aeroengine Congress and Exposition*, pp. V001T01A021–V001T01A021, American Society of Mechanical Engineers, 1989.

[51] J. Denton and G. Pullan, "A numerical investigation into the sources of endwall loss in axial flow turbines," in *ASME Turbo Expo 2012: Turbine Technical Conference and Exposition*, pp. 1417–1430, American Society of Mechanical Engineers, 2012.

[52] R. Gaugler and L. Russell, "Comparison of visualized turbine endwall secondary flows and measured heat transfer patterns," *Journal of Engineering for Gas Turbines and Power*, vol. 106, no. 1, pp. 168–172, 1984.

[53] T. Simon and J. Piggush, "Turbine endwall aerodynamics and heat transfer," *Journal of propulsion and power*, vol. 22, no. 2, pp. 301–312, 2006.

[54] Y. Huang and V. Yang, "Dynamics and stability of lean-premixed swirl-stabilized combustion," *Progress in Energy and Combustion Science*, vol. 35, no. 4, pp. 293–364, 2009.

[55] M. Vigueras-Zuñiga, A. Valera-Medina, and N. Syred, "Studies of the precessing vortex core in swirling flows," *Journal of applied research and technology*, vol. 10, no. 5, pp. 755–765, 2012.

[56] K. Oberleithner, S. Terhaar, L. Rukes, and C. O. Paschereit, "Why nonuniform density suppresses the precessing vortex core," *Journal of Engineering for Gas Turbines and Power*, vol. 135, no. 12, p. 121506, 2013.

[57] N. Syred, "A review of oscillation mechanisms and the role of the precessing vortex core (PVC) in swirl combustion systems," *Progress in Energy and Combustion Science*, vol. 32, no. 2, pp. 93–161, 2006.

[58] S. Terhaar, K. Oberleithner, and C. Paschereit, "Key parameters governing the precessing vortex core in reacting flows: An experimental and analytical study," *Proceedings of the Combustion Institute*, vol. 35, no. 3, pp. 3347–3354, 2015.

[59] M. D. Turrell, P. J. Stopford, K. J. Syed, and E. Buchanan, "CFD simulation of the flow within and downstream of a high-swirl lean premixed gas turbine combustor," in *ASME Turbo Expo 2004: Power for Land, Sea, and Air*, pp. 31–38, American Society of Mechanical Engineers, 2004.

[60] S. Pyliouras, H.-P. Schiffer, E. Janke, and L. Willer, "Effects of non-uniform combustor exit flow on turbine aerodynamics," in *ASME Turbo Expo 2012: Turbine Technical Conference and Exposition*, pp. 1691–1701, American Society of Mechanical Engineers, 2012.

[61] G. Schmid, A. Krichbaum, H. Werschnik, and H.-P. Schiffer, "The impact of realistic inlet swirl in a 1 1/2 stage axial turbine," in *ASME Turbo Expo 2014: Turbine Technical Conference and Exposition*, pp. V02CT38A045–V02CT38A045, American Society of Mechanical Engineers, 2014.

[62] H. Werschnik, M. Schneider, J. Herrmann, D. Ivanov, H.-P. Schiffer, and C. Lyko, "The influence of combustor swirl on pressure losses and the propagation of coolant flows at the large scale turbine rig (lstr): Experimental and numerical investigation," *International Journal of Turbomachinery, Propulsion and Power*, vol. 2, no. 3, p. 12, 2017.

[63] H. Werschnik, J. Hilgert, M. Wilhelm, M. Bruschewski, and H.-P. Schiffer, "Influence of combustor swirl on endwall heat transfer and film cooling effectiveness at the large scale turbine rig," *Journal of Turbomachinery*, vol. 139, no. 8, p. 081007, 2017.

[64] L. Giller and H.-P. Schiffer, "Interactions between the combustor swirl and the high pressure stator of a turbine," in *ASME Turbo Expo 2012: Turbine Technical Conference and Exposition*, pp. 1401–1415, American Society of Mechanical Engineers, 2012.

[65] R. Radomsky and K. Thole, "High freestream turbulence effects on endwall heat transfer for a gas turbine stator vane," in *ASME Turbo Expo 2000: Power for Land, Sea, and Air*, pp. V003T01A009–V003T01A009, American Society of Mechanical Engineers, 2000.

[66] C. M. Cha, P. T. Ireland, P. A. Denman, and V. Savarianandam, "Turbulence levels are high at the combustor-turbine interface," in *ASME Turbo Expo 2012: Turbine Technical Conference and Exposition*, pp. 1371–1390, American Society of Mechanical Engineers, 2012.

[67] H. Seo, J. Lee, and P. Ligrani, "Effects of bulk flow pulsations on film cooling from different length injection holes at different blowing ratios," *Journal of turbomachinery*, vol. 121, no. 3, pp. 542–550, 1999.

[68] T. Praisner and C. Smith, "The dynamics of the horseshoe vortex and associated endwall heat transfer—part i: Temporal behavior," *Journal of Turbomachinery*, vol. 128, no. 4, pp. 747–754, 2006.

[69] T. Praisner and C. Smith, "The dynamics of the horseshoe vortex and associated endwall heat transfer—part ii: Time-mean results," *Journal of Turbomachinery*, vol. 128, no. 4, pp. 755–762, 2006.

[70] C. Baker, "The laminar horseshoe vortex," *Journal of fluid mechanics*, vol. 95, no. 2, pp. 347–367, 1979.

[71] A. S. Thomas, "The unsteady characteristics of laminar juncture flow," *The Physics of fluids*, vol. 30, no. 2, pp. 283–285, 1987.

[72] C. Lin, P.-H. Chiu, and S.-J. Shieh, "Characteristics of horseshoe vortex system near a vertical plate–base plate juncture," *Experimental Thermal and Fluid Science*, vol. 27, no. 1, pp. 25–46, 2002.

[73] R. L. Simpson, "Junction flows," *Annual Review of Fluid Mechanics*, vol. 33, no. 1, pp. 415–443, 2001.

[74] G. Launay, E. Mignot, N. Rivière, and R. Perkins, "An experimental investigation of the laminar horseshoe vortex around an emerging obstacle," *Journal of Fluid Mechanics*, vol. 830, pp. 257–299, 2017.

[75] G. Zess and K. Thole, "Computational design and experimental evaluation of using a leading edge fillet on a gas turbine vane," in *ASME Turbo Expo 2001: Power for Land, Sea, and Air*, pp. V003T01A083–V003T01A083, American Society of Mechanical Engineers, 2001.

[76] A. T. Lethander, K. A. Thole, G. Zess, and J. Wagner, "Optimizing the vane-endwall junction to reduce adiabatic wall temperatures in a turbine vane passage," in *ASME Turbo Expo 2003, collocated with the 2003 International Joint Power Generation Conference*, pp. 711–721, Citeseer, 2003.

[77] B. Rosic, J. D. Denton, J. H. Horlock, and S. Uchida, "Integrated combustor and vane concept in gas turbines," *Journal of Turbomachinery*, vol. 134, no. 3, p. 031005, 2012.

[78] S. Jacobi and B. Rosic, "Development and aerothermal investigation of integrated combustor vane concept," *Journal of Turbomachinery*, vol. 138, no. 1, p. 011002, 2016.

[79] S. Jacobi and B. Rosic, "Thermal investigation of integrated combustor vane concept under engine-realistic conditions," *Journal of Turbomachinery*, vol. 139, no. 2, p. 021005, 2017.

[80] I. Aslanidou, B. Rosic, V. Kanjirakkad, and S. Uchida, "Leading edge shielding concept in gas turbines with can combustors," *Journal of Turbomachinery*, vol. 135, no. 2, p. 021019, 2013.

[81] C. M. Mazzoni, C. Klostermeier, and B. Rosic, "Influence of large wake disturbances shed from the combustor wall on the leading edge film cooling," *Journal of Engineering for Gas Turbines and Power*, vol. 136, no. 8, p. 081503, 2014.

[82] J. Saw, "Gas turbine vane film cooling for engine-realistic combustor flows," Master's thesis, University of Oxford, 2017.

[83] M. Zdravkovich, "Review and classification of various aerodynamic and hydrodynamic means for suppressing vortex shedding," *Journal of Wind Engineering and Industrial Aerodynamics*, vol. 7, no. 2, pp. 145–189, 1981.

[84] N. P. Padture, M. Gell, and E. H. Jordan, "Thermal barrier coatings for gas-turbine engine applications," *Science*, vol. 296, no. 5566, pp. 280–284, 2002.

[85] B. Gleeson, "Thermal barrier coatings for aeroengine applications," *Journal of Propulsion and Power*, vol. 22, no. 2, pp. 375–383, 2006.

[86] D. R. Clarke, M. Oechsner, and N. P. Padture, "Thermal-barrier coatings for more efficient gas-turbine engines," *MRS bulletin*, vol. 37, no. 10, pp. 891–898, 2012.

[87] C. G. Levi, J. W. Hutchinson, M.-H. Vidal-Sétif, and C. A. Johnson, "Environmental degradation of thermal-barrier coatings by molten deposits," *MRS bulletin*, vol. 37, no. 10, pp. 932–941, 2012.

[88] S. Sampath, U. Schulz, M. O. Jarligo, and S. Kuroda, "Processing science of advanced thermal-barrier systems," *MRS bulletin*, vol. 37, no. 10, pp. 903–910, 2012.

[89] V. Kumar and K. Balasubramanian, "Progress update on failure mechanisms of advanced thermal barrier coatings: A review," *Progress in Organic Coatings*, vol. 90, pp. 54–82, 2016.

[90] M. R. Winter and D. R. Clarke, "Thermal conductivity of yttria-stabilized zirconia–hafnia solid solutions," *Acta Materialia*, vol. 54, no. 19, pp. 5051–5059, 2006.

[91] K. Reid, J. Denton, G. Pullan, E. Curtis, and J. Longley, "The interaction of turbine inter-platform leakage flow with the mainstream flow," *Journal of Turbomachinery*, vol. 129, no. 2, pp. 303–310, 2007.

[92] K. Reid, J. Denton, G. Pullan, E. Curtis, and J. Longley, "Reducing the perfomance penalty due to turbine inter-platform gaps," in *ASME turbo expo 2006: Power for land, sea, and air*, pp. 799–808, American Society of Mechanical Engineers, 2006.

[93] J. Piggush and T. Simon, "Heat transfer measurements in a first-stage nozzle cascade having endwall contouring: Misalignment and leakage studies," *Journal of Turbomachinery*, vol. 129, no. 4, pp. 782–790, 2007.

[94] J. Piggush and T. Simon, "Flow measurements in a first stage nozzle cascade having endwall contouring, leakage, and assembly features," *Journal of Turbomachinery*, vol. 135, no. 1, p. 011002, 2013.

[95] S. Lynch and K. Thole, "The effect of combustor-turbine interface gap leakage on the endwall heat transfer for a nozzle guide vane," *Journal of Turbomachinery*, vol. 130, no. 4, p. 041019, 2008.

[96] S. P. Lynch and K. A. Thole, "The effect of the combustor-turbine slot and midpassage gap on vane endwall heat transfer," *Journal of Turbomachinery*, vol. 133, no. 4, p. 041002, 2011.

[97] E. Lange, S. Lynch, and S. Lewis, "Computational and experimental studies of midpassage gap leakage and misalignment for a non-axisymmetric contoured turbine blade endwall," in *ASME*

Turbo Expo 2016: Turbomachinery Technical Conference and Exposition, pp. V05AT13A001–V05AT13A001, American Society of Mechanical Engineers, 2016.

[98] S. Hada and K. A. Thole, "Computational study of a midpassage gap and upstream slot on vane endwall film-cooling," in *ASME Turbo Expo 2006: Power for Land, Sea, and Air*, pp. 839–848, American Society of Mechanical Engineers, 2006.

[99] N. Cardwell, N. Sundaram, and K. Thole, "Effect of midpassage gap, endwall misalignment, and roughness on endwall film-cooling," *Journal of Turbomachinery*, vol. 128, no. 1, pp. 62–70, 2006.

[100] N. Cardwell, N. Sundaram, and K. Thole, "The effects of varying the combustor-turbine gap," *Journal of Turbomachinery*, vol. 129, no. 4, pp. 756–764, 2007.

[101] H. Liu, C. Hu, X. Shen, X. Zhu, H. Yang, and Z. Du, "The aerodynamic optimization design of turbine cascade nonaxisymmetric endwall and the midgap influence assessment," *Proceedings of the Institution of Mechanical Engineers, Part G: Journal of Aerospace Engineering*, vol. 232, no. 15, pp. 2760–2774, 2018.

[102] N. H. Chowdhury, C.-C. Shiau, J.-C. Han, L. Zhang, and H.-K. Moon, "Turbine vane endwall film cooling with slashface leakage and discrete hole configuration," *Journal of Turbomachinery*, vol. 139, no. 6, p. 061003, 2017.

[103] A. Roy, S. Jain, S. V. Ekkad, W. Ng, A. S. Lohaus, M. E. Crawford, and S. Abraham, "Heat transfer performance of a transonic turbine blade passage in the presence of leakage flow through upstream slot and mateface gap with endwall contouring," *Journal of Turbomachinery*, vol. 139, no. 12, p. 121006, 2017.

[104] R. H. Winterton, "Where did the Dittus and Boelter equation come from?," *International Journal of Heat and Mass Transfer*, vol. 41, no. 4-5, pp. 809–810, 1998.

[105] J. M. Owen, "Prediction of ingestion through turbine rim seals—part ii: Externally induced and combined ingress," *Journal of Turbomachinery*, vol. 133, no. 3, p. 031006, 2011.

[106] J. M. Owen, "Theoretical modelling of hot gas ingestion through turbine rim seals," *Propulsion and Power Research*, vol. 1, no. 1, pp. 1–11, 2012.

[107] J. A. Scobie, C. M. Sangan, J. M. Owen, and G. D. Lock, "Review of ingress in gas turbines," *Journal of Engineering for Gas Turbines and Power*, vol. 138, no. 12, p. 120801, 2016.

[108] J. A. Scobie, F. P. Hualca, C. M. Sangan, and G. D. Lock, "Egress interaction through turbine rim seals," *Journal of Engineering for Gas Turbines and Power*, vol. 140, no. 7, p. 072504, 2018.

[109] O. Gentilhomme, N. Hills, A. Turner, and J. Chew, "Measurement and analysis of ingestion through a turbine rim seal," *Journal of Turbomachinery*, vol. 125, no. 3, pp. 505–512, 2003.

[110] K. Clark, M. Barringer, D. Johnson, K. Thole, E. Grover, and C. Robak, "Effects of purge flow configuration on sealing effectiveness in a rotor–stator cavity," *Journal of Engineering for Gas Turbines and Power*, vol. 140, no. 11, p. 112502, 2018.

[111] A. Parfett, "Nozzle guide vane endwall heat transfer for varying endwall geometries," Master's thesis, University of Oxford, 2016.